Study of Seal Glass for Solid Oxide Fuel/Electrolyzer Cells

Manoj Kumar Mahapatra

Dissertation submitted to the Faculty of the Virginia Polytechnic Institute and State University in partial fulfillment of the requirements for the degree of

Doctor of Philosophy

in

Materials Science and Engineering

Committee Members:

Kathy Lu, Chair

William T. Reynolds, Jr.

Jeremiah T. Abiade

Robert J. Tracy

December 2, 2009

Blacksburg, VA 24061

Keywords: Solid oxide fuel/electrolyzer cell, Seal glass, Thermal properties, Metallic interconnect alloy, Interface, Sealing performance

Study of Seal Glass for Solid Oxide Fuel/Electrolyzer Cells

Manoj Kumar Mahapatra

ABSTRACT

Seal glass is essential and plays a crucial role in solid oxide fuel/electrolyzer cell performance and durability. A seal glass should have a combination of thermal, chemical, mechanical, and electrical properties in order to seal different cell components and stacks and prevent gas leakage. All the desired properties can simultaneously be obtained in a seal glass by suitable compositional design. In this dissertation, SrO-La_2O_3-Al_2O_3-B_2O_3-SiO_2 based seal glasses have been developed and composition-structure-property relationships have been investigated. B_2O_3 free SrO-La_2O_3-Al_2O_3-SiO_2 based seal glass is the most suitable and its compatibility with the metallic interconnects and sealing performances have been evaluated.

A seal glass should be stable for 5,000-40,000 hrs in the oxidizing and reducing atmospheres at 600-900°C but both the thermal and chemical stability is a persistent problem. The effect of Al_2O_3 on a SrO-La_2O_3-Al_2O_3-B_2O_3-SiO_2 based seal glass has been studied to improve the thermal properties, such as glass transition temperature, softening temperature and thermal expansion coefficient, and the thermal stability. Al_2O_3 improves the thermal stability but does not significantly affect the thermal properties of the seal glass.

Comprehensive understanding of composition-structure-property relationships is needed to design a suitable seal glass. The thermal properties and stability of a borosilicate seal glass depend on the B_2O_3:SiO_2 ratio in the composition. The role of B_2O_3:SiO_2 ratio on the glass

thermal stability were correlated with the glass network structure and the calculated network connectivity. This study shows that the thermal properties degrade with increasing B_2O_3:SiO_2 ratio due to increase in the non-bridging oxygen and decrease in the network connectivity. High B_2O_3:SiO_2 ratio induces BO_4 and SiO_4 structural unit ordering, increases micro-heterogeneity, and subsequently degrades thermal stability. B_2O_3 free SrO-La_2O_3-Al_2O_3-SiO_2 seal glass shows the best combination of the thermal properties and thermal stability among the studied glasses.

Nickel or nickel oxide is added into a seal glass to modify the thermal properties depending on the specific composition. The role of nickel as a network former or modifier and its effect on the thermal properties and thermal stability of the SrO-La_2O_3-Al_2O_3-B_2O_3-SiO_2 based seal glasses have been investigated. Nickel is a modifier in this glass system and does not improve the thermal properties but degrades thermal stability by decreasing network connectivity and inducing micro-heterogeneity.

The interconnect-seal glass interface stability is the most crucial for solid oxide fuel/electrolyzer cell. Crofer 22 APU and AISI 441 alloys are the preferred interconnects. The interfacial stability of the SrO-La_2O_3-Al_2O_3-SiO_2 based seal glass with these alloys have been studied as a function of time (0-1000 hrs), temperature (700-850°C), atmospheres (air, argon, and H_2O/H_2) using scanning electron microscopy (SEM), energy dispersive spectroscopy (EDS), and X-ray diffraction analysis (XRD). Complementary analytical techniques such as wave length dispersive spectroscopy (WDS) and SEM of thin samples were also carried out for selected samples. This study shows good interfacial stability of the SrO-La_2O_3-Al_2O_3-SiO_2 based seal glass with these alloys for the studied conditions.

A suitable seal glass should be hermetic and withstand 100-1000 thermal cycles for practical application. Sealing performances of the SrO-La_2O_3-Al_2O_3-SiO_2 based seal glass have

been evaluated by pressure-leakage method. The seal glass is hermetic for at least 2000 hrs and withstands 100 thermal cycles. Overall, present work shows that the SrO-La_2O_3-Al_2O_3-SiO_2 based glass has all the desired properties and suitable for solid oxide fuel/electrolyzer cell seal.

DEDICATION

This dissertation is dedicated to The Almighty who decides the destiny.

ACKNOWLEDGEMENTS

Many generous people came across during my study and without their kind help I could not pursue my Ph. D. degree. I am grateful to all who have supported me during my entire academic career. My study at Virginia Tech is the most effective and enjoyable from learning aspect.

I would like to express my sincere gratitude to my advisor, Prof. Kathy Lu, for giving me the opportunity to study in the Department of Materials Science and Engineering in Virginia Polytechnic Institute and State University and pursue Ph. D. under her supervision. I am fortunate to get a chance to work under Prof. Kathy Lu, an energetic advisor, who always encourages and helps her students to implement their own ideas rather than just following her instructions. I have learned a lot from her to improve research skill, critical thinking and technical writing. I am grateful to Prof. Kathy Lu for her tireless effort to grow me as a more matured researcher. Apart from learning research and science based knowledge, Prof. Lu's advices and guidance must help me to become a successful research professional. I do not know any suitable word but simply say 'Thank you' for everything she did for me.

I would like to thank Prof. Bill Reynolds, Prof. Robert Tracy, and Prof. Jeremiah Abiade for being my graduate committee members, their suggestions and discussions during this dissertation. I am also grateful to Prof. Reynolds and Prof. Tracy for their advice and discussion about analytical work with great patience and valuable time.

Financial support from the Department of Energy under the grant number DE-FC07-06ID14739 during this dissertation is sincerely acknowledged. I would like to acknowledge Mr. Charles Farley and Prof. Robert Bodnar, Department of Geoscience, Virginia Tech, for their help

during Raman spectroscopy experiment, and Prof. Sabyasachi Sen, Department of Chemical Engineering and Materials Science, University of California, Davis for the NMR experiment.

I am indebted to Mr. Junwei Wu and Prof. Xingbo Liu, West Virginia University, Dr. Zhenguo "Gary" Yang, Pacific Northwest National Laboratory, Richland, Washington, and Dr. James Rakowski, ATI Allegheny Ludlum, USA for providing interconnect materials for this work.

My appreciation goes to Mr. Stephen McCartney, Mr. John McIntosh, and Dr. Mitsuhiro Murayama, Nanoscale Characterization and Fabrication Laboratory, Virginia Tech for their kind help during microscopy works and Mr. Devid Berry and Dr. Carlos Suchicital for their help during experiments. I am also thankful to all the staffs of the Materials Science and Engineering Department, Virginia Tech for their help during my study.

The countless and generous help of Mr. Tongan Jin, my colleague, and Mr. Christopher Story, my former colleague, during experiments is sincerely appreciated. Thanks to them so much.

I would like to take this opportunity to express my sincere gratitude to my former teachers, Prof. Om Parkash, Prof. Devendra Kumar, Dr. P. K. Biswas, Prof. Sunanda Mukhopadhyay, and Prof. Monica Katiyar for their teaching and constant encouragement to pursue Ph. D.

I am grateful to my friends Raghunath Rao Thridandapani, Abhoy Kumar, Prasenjit Barick, and Dibyendu Chakravarty for their support and real friendships. Thanks to many other friends for their kindness and patience to entertain me.

The ultimate admiration and respect are for my parents and elder sister, who are the source of my inspiration for everything. I specially owe to my father, a noble teacher and humanitarian, for teaching me to graciously accept both success and failure.

Table of contents

LIST OF FIGURES

LIST OF TABLES

CHAPTER ONE

INTRODUCTION

Fuel cells are electrochemical devices that convert hydrogen or hydrocarbon into electricity to fulfill the exponentially increasing demand without any pollution. When hydrogen is used as a fuel, water is the by-product. Example fuel cells are phosphoric acid fuel cell, proton exchange membrane fuel cell, molten carbonate fuel cell, solid oxide fuel cell, and alkaline fuel cell. Among these different fuel cells, solid oxide fuel cells (SOFCs) are the most preferred due to their higher efficiency (45-85%) [1,2], fuel flexibility, and cost effectiveness. However, SOFCs have to be operated at high temperatures (500-1000°C) to realize these advantages. When a SOFC is operated in the reverse mode, it is called solid oxide electrolyzer cell (SOEC) and can generate hydrogen by splitting water. The SOFC/SOEC working principle is shown schematically in Fig. 1-1. Thus electrical energy and hydrogen fuel can be produced simultaneously by proper design. In addition, the heat loss in nuclear plant and gas-turbines can also be used to operate SOFC/SOEC.

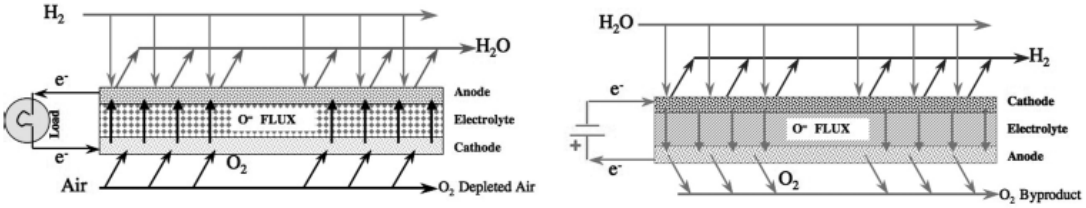

(a) (b)

Fig.1-1. Schematics of a) SOFC and b) SOEC principle [3].

A SOFC mainly consists of electrodes (anode and cathode), electrolyte, and interconnect. Oxygen gas from air is ionized to oxygen ions at the cathode side. The oxygen ions then migrate

to the anode side through solid oxide electrolyte and combine with the fuel at the anode side. The interconnect collects current and provides integrity to the cell stacks.

SOFCs have great potentials for stationary and mobile applications such as residential, power grid, military, long duration mobile devices, and remote communication electronics. SOFC can be classified into three types according to operating temperatures: high temperature SOFC (900-1000°C), intermediate temperature SOFC (700-900°C), and low temperature SOFC (500-700°C). Typical SOFC operating temperature is ~ 800°C. Most of the research has been carried out for intermediate temperature SOFCs. Reducing the operating temperature to 500-600°C requires new electrolytes with high oxygen ionic conductivity, active catalysts for oxidation at the anode and reduction at the cathode, and electrode materials with suitable ionic and electronic conductivities. To produce electrical power in kilowatt to megawatt range, many cells need to be stacked through interconnect materials. With the understanding that the cathode in the SOFC mode acts as the anode in the SOEC mode and the anode in the SOFC mode serves as the cathode in the SOEC mode, five components are essential in a cell stack. Using SOFC configuration for discussion convenience, they are electrolyte, cathode, anode, interconnect, and seal. Fully dense and high ionic conductivity cubic ZrO_2 is the electrolyte. Lanthanum manganite, lanthanum strontium cobaltite, and lanthanum strontium cobaltite ferrite have been used as the cathode [4]. Ni-ZrO_2 cermet is used as the anode [5]. Iron-based alloys with high chromium content are used as the interconnect [6].

There are mainly two designs for SOFCs: tubular and planar. Planar designs are preferred due to: 1) high power density, 2) a wide range of operating temperatures, 3) potential for both stationary and mobile applications, 4) design flexibility and ease of fabrication, and 5) lower cost [7]. For example, a current density of 3468 $A \cdot m^{-2}$ can be obtained from a planar design compared

to 2890 $A \cdot m^{-2}$ from a tubular design at the same operating condition [8]. For planar design, sealing is required along the edges of cell components [7]. The locations of seals in planner SOFCs are illustrated in Fig. 1-2. A seal material is a critical component of planar SOFCs because it seals the cells/stacks and prevents gas leakage and mixing. The efficiency of SOFCs degrades proportionally to the gas leakage rate because of less utilization of input fuels. Mixing of reducing and oxidizing gases also accelerates cell performance degradation and can cause explosion [9,10]. Development of a suitable seal material is the focus of this dissertation.

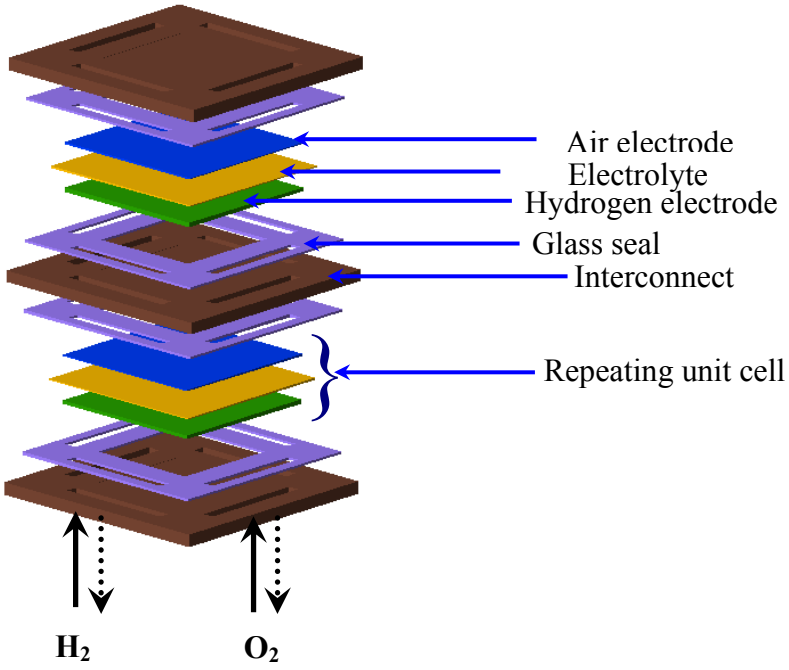

Fig. 1-2. Schematic illustration of seal positions in a planar SOFC for an anode supported cell stack using H_2 as the fuel.

1.1. Functional requirements of seals for solid oxide cells

In planar SOFCs, gas-tight sealing is required along the edges of the electrodes, electrolyte, and interconnect as well as between individual cells as shown in Fig. 1-2 depending

on specific cell configuration such as anode supported, electrolyte supported, cathode supported, or metal supported cell. There are two basic needs for a sealing material. First, it needs to seal the adjacent cell components. Second, the seal needs to be stable over long term cell operation. The requirements of a seal are listed in Table 1-1 [11,12]. Lack of suitable seal materials is the main shortcoming for the advancement of planar SOFCs.

Table 1-1. Properties and fabrication requirements of a SOFC/SOEC seal.

Properties	Requirements
Thermal properties	• Thermal expansion coefficient (CTE) at 9.5 12.0 × 10^{-6}/°C • Thermally stable for ~ 5,000 hrs for mobile applications and for ~ 50,000 hrs for stationary applications at 650-900°C cell operating temperatures
Chemical properties	• Resistant to vaporization and compositional change in stringent oxidizing and wet reducing atmospheres at 650-900°C • Limited or no reaction with other cell components
Mechanical properties	• Withstand external static and dynamic forces during transportation and operation • Resistant to thermal cycling failure during start-up and shut-down of cell stacks

Electrical properties	• Electrical resistivity ≥ 10^4 Ω·cm at operating temperature
Sealing ability	• Sealing load < 35 kPa • Withstand differential pressure up to 14-35 kPa across a cell or stack. • Total fuel leakage < 1% for the duration of the cell life.
Fabrication flexibility	• Flexible design, low processing cost, and high reliability

1.2. Classification of seals

There are three types of seals: compressive, compliant, and rigid. Mica and mica-based hybrid materials, metal-brazes, and glass/glass-ceramic materials are used as compressive, compliant, and rigid seals, respectively [7,13]. At cell operating temperatures, compressive seals require an applied load, which complicates cell design and increases fabrication cost. Compliant seals do not bond well with the SOFC components, are prone to oxidation and 'hydrogen embrittlement', and are electrically conductive. Glass and glass-ceramic seals are rigid seals amd have many advantages compared to compressive and compliant seals. Glass and glass-ceramic seals rigidly bond to the cell components, can prevent leakage and mixing of gasses, and are electrically insulating. Additionally, glass and glass-ceramic seals are flexible in design, easy to fabricate, and cost-competitive [7,11-13]. A wide range of material properties required for sealing can be achieved in a glass or glass-ceramic seal by suitable compositional adjustment. Seal glasses are preferred due to these advantages. Seal glasses are studied in this dissertation.

1.3. Design criteria of glass seal

Various physical and chemical properties and thermal stability should be obtained simultaneously in a glass seal material for proper SOFC/SOEC operation. The most important physical properties include glass transition temperature (T_g), thermal expansion coefficient (CTE), and electrical resistivity. Chemical properties include resistance to vaporization and degradation at cell operating temperatures (500-1000°C) in oxidizing (cathode side) and wet reducing (≥ 50 vol% H_2O, anode side) atmospheres. A seal material should be compatible with the interfacing components to avoid pores and cracks which are gas leakage paths. Since SOFCs need to operate continuously for ≥ 5,000 hrs for mobile applications and ≥ 40,000 hrs for stationary applications, and undergo thousands of thermal cycles between room temperature and operating temperature [14], a seal material should be stable and withstand thermal cycling without substantial property degradation for the entire period. Additionally, a seal glass should withstand thermal and mechanical stresses arising from material property differences, temperature gradient, and various loads during operation and transportation. The electrical resistivity of a seal glass must be high to prevent SOFC from electrical shunting. Simultaneous fulfillment of these requirements is the main challenge in developing a suitable seal material [7,10,12-14].

Glass is defined as ‘an amorphous solid completely lacking in long range periodic atomic structure and exhibiting a region of glass transformation behavior’ [15]. Seal glasses contain network formers, network modifiers, intermediates, and additives. Network formers are oxides of high field strength (1.0-2.0) and low coordination number (3-4), which form polyhedral units in a glass network structure [16,17]. Common network formers for seal glasses are SiO_2 and B_2O_3. Network modifiers are oxides of low field strength (≤ 0.35) and high coordination number (8)

[16,17]. They disrupt glass network structure, occupy random positions in-between the polyhedra, and maintain local charge neutrality [15,16]. Modifier oxides create non-bridging oxygen which do not link the polyhedral units [15-17]. Common network modifiers are alkaline oxides and alkaline earth oxides. Intermediate oxides have field strength (0.84-1.04) and coordination number (4-6) in-between those of the network formers and modifiers [16]. They can either be a glass former or a modifier depending on the specific glass composition. Al_2O_3 is the most commonly used intermediate oxide in seal glasses. Rare earth oxides (such as La_2O_3) and transition metal oxides (such as NiO, TiO_2, and ZnO) are often added into a seal glass to tailor the desired properties and known as additives [18]. A schematic illustration of glass structure is shown in Fig. 1-3.

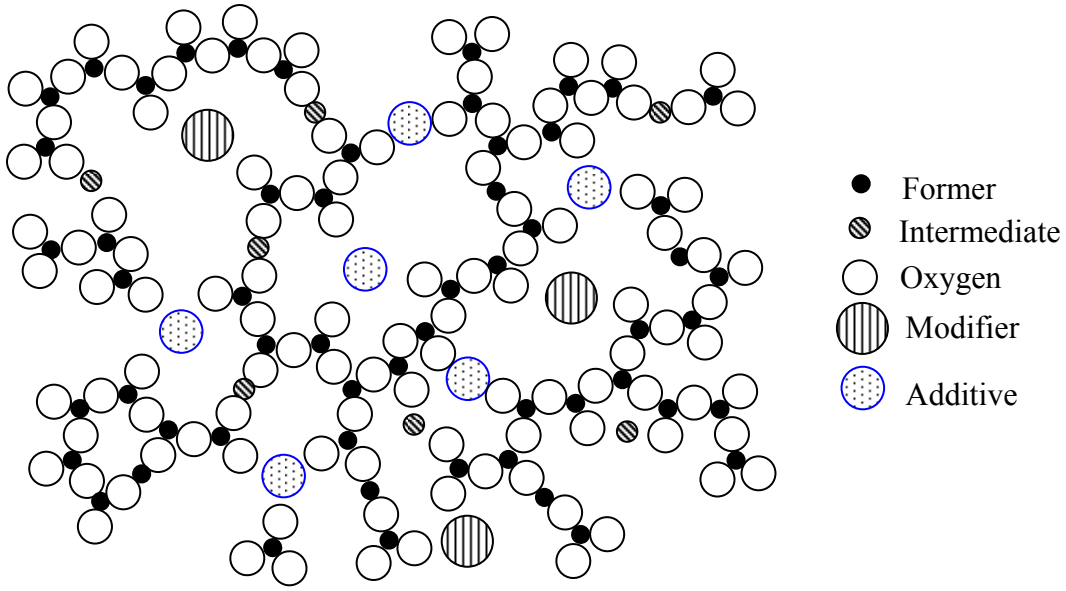

Fig. 1-3. Schematic illustration of a glass network structure.

Glass from pure glass forming oxides does not have the required properties suited for SOFC/SOEC seal. For example, silica glass is the most thermally stable glass but has high T_g

(1203°C), T_s (> 1400°C), and low CTE (0.5× 10^{-6}/°C) and unsuitable for SOFC seal [16]. However, the desired properties of SOFC glass seal can be tailored by compositional design. Glass composition design is generally based on the properties of individual oxides in a particular glass system [15,16,19]. Designs of seal glass compositions are mainly based on the knowledge of the field strength of the constituent cations and the 'additive rule'. Field strength, F, of an oxide is expressed as [16,19]:

$$F = \frac{z}{r^2} \qquad (1\text{-}1)$$

where 'z' is the valency of the cation and 'r' is the interatomic distance between cation and oxygen.

The desired properties of a seal glass (Table 1-1) are often not achieved based on this compositional design due to three reasons: deviation of 'additive rule' due to 'combined ion effect', 'boron anomaly', and lack of understanding of glass composition-structure-property relations. According to the 'additive rule', seal glass properties, C, can be modified by varying constituents in a glass composition according to [19]

$$C = m_i C_i + a \qquad (1\text{-}2)$$

where C is any property, m_i is the molar concentration of oxide i, C_i is the corresponding property of glass composition i, and a is a constant that depends on the particular glass system. However, deviation of 'additive rule' is frequently observed due to short-range interaction between different types of modifiers [15,19,20]. This phenomenon is known as 'combined ion effect'. From a different aspect, B_2O_3 is a common constituent in most of the seal glass compositions. Modifier cations change the glass properties anomalously by converting planar boroxyl structural groups to borate structural groups in B_2O_3-containing glasses. This phenomenon is known as 'boron anomaly' [15,16]. The properties of a seal glass depend not

only on the cationic field strength but also on the coordination number of cations, cation-oxygen bond length and bond angles, local ordering in the network structure, and the degree of network connectivity. Heterogeneity due to local ordering can occur at the atomic level in a multi-component seal glass [18,21-23].

For SOFC/SOEC seal application, three types of glass system have been investigated: silicate, borate, and borosilicate glasses. These studies are carried out mainly to modify the thermal properties. Even though the thermal properties have been achieved in these studied glasses, long-term stability and sealing performances remain a persistent problem due to the lack of understanding the composition-structure-property relation.

1.4. Properties of glass seal

1.4.1. Thermal properties

There are three important thermal properties to consider for a SOFC seal glass: glass transition temperature (T_g), glass softening temperature (T_s), and thermal expansion coefficient (CTE). T_g can be defined as 'on heating, the temperature at which a glas transforms from an elastic to a viscoelastic materials characterized by the onset of a rapid change in thermal expansivity' [24]. Glass softens and becomes flowable at T_s. CTE is the volume change of glass during heating or cooling. Generally linear thermal expansion is used as the CTE since glass is an isotropic material.

1.4.1.1. Glass transition and softening temperature

Glass is brittle below T_g. The T_g value of a seal glass should be slightly below the cell

operating temperature to relieve thermal stress and self-heal cracks [25,26]. T_s value should be higher than the cell operating temperature to avoid excessive glass flow but below 1000°C to maintain the oxidation resistance of the metallic interconnects during sealing. T_g and T_s should be in the temperature ranges of 650-750°C and 700-900°C, respectively. T_g and T_s of a seal glass depend on the compositions.

A seal glass generally contains 40-70 mol% network formers. T_g in 675-725°C temperature range and T_s in 725-825°C temperature range have been obtained for silicate glasses [27-32]. T_g and T_s generally increase with SiO_2 content because of high T_g and T_s of vitreous SiO_2. T_g in 500-580°C temperature range has been achieved for borate glasses [29-32]. Presence of planar boroxyl structural groups and low T_g of pure B_2O_3 (~ 275°C) lead to low T_g for these glasses [16,19]. For borosilicate glasses, T_g of 480-740°C and T_s of 600-750°C are obtained [29,33-41]. T_g and T_s decrease by 50-100°C with the increase of B_2O_3/SiO_2 ratio as shown for borosilicate glasses [29,33,42].

A seal glass generally contains 20-45 mol% network modifiers. A wide range of T_g and T_s have been obtained in alkaline earth oxide containing seal glasses. T_g of 500-675°C and T_s of 650-750°C are obtained in BaO-containing borosilicate glasses [27,29,34,36-38,40,42]. T_g of 625-700°C and T_s of 700-775°C are obtained in SrO-borosilicate seal glasses [33,35,41]. T_g of 610-720°C are obtained for CaO-containing and MgO-containing borosilicate glasses [29,36,43]. Modifier oxides decrease T_g and T_s in a silicate glass. The field strength of modifier ions can modify the T_g and T_s. The field strength of modifier cations are: K^+ (0.17) <Na^+ (0.19) <Li^+ (0.23) for alkaline oxides and Ba^{2+} (0.24) <Sr^{2+} (0.27) <Ca^{2+}(0.33-0.35) <Mg^{2+} (0.45-0.51) for alkaline earth ions [15,16]. The T_g and T_s of a seal glass increase in the same order when these species are involved. T_g and T_s of alkaline earth oxide containing glasses are higher than those of

alkaline oxide containing glasses because of the higher field strength and lower mobility of alkaline earth ions. For example, T_g decreases by ~ 110°C (from 685°C to 562°C) as the alkaline oxide content ($Na_2O + K_2O$) increases from 8 to 16.6 mol% by replacing alkaline earth oxide (MgO + CaO) in a borosilicate seal glass [44].

Al_2O_3 is the most commonly used intermediate oxide, generally at 5-10 mol% in a seal glass composition. Al_2O_3 is a network former if the coordination number of Al^{3+} is four and is a network modifier if the coordination of Al^{3+} is five or six [15,16,21]. In general, T_g and T_s increase if Al_2O_3 is a network former but decrease if Al_2O_3 is a network modifier. For example, 10 mol% increase in the Al_2O_3 content (6.9 mol% to 17.0 mol%) decreases T_g by 30°C (from 638°C to 608°C) in a CaO-MgO-borosilicate glass [43].

Several additives such as rare earth metal oxides and transition metal oxides are used in seal glass compositions to tailor the thermal properties. La_2O_3, a rare earth metal oxide, is commonly used in seal glass compositions. Less than 10 mol% La_2O_3 is sufficient to increase the T_g by 30-50°C although more than 20 mol% has been used in some seal glasses [33,41,44]. ZrO_2, TiO_2, NiO, ZnO, and Y_2O_3 are the transition metal oxides used in seal glass compositions. The effect of the transition metal oxides on T_g and T_s depends on the specific glass composition [18,23]. T_g and T_s increase when these oxides are network formers and decrease or unchanged when these oxides are network modifiers. For example, 2 mol% ZrO_2 addition has no effect on T_g in MgO-borosilicate glasses [36] but 3 mol% ZrO_2 addition increases T_g by 15-20°C in a BaO-borosilicate glass [37] and T_s by 50-70°C in an alkaline and alkaline earth oxide containing silicate glass[32]. Similar anomaly have been observed for TiO_2, Ni, and ZnO when they are added in silicate and borosilicate glasses [29,36,37,45-48].

1.4.1.2. Thermal expansion coefficient

The CTE of a seal glass should not differ by more than 1×10^{-6}/°C with the interfacing SOFC components in order to obtain pore- and crack-free interface [49]. CTE mismatch between the seal glass and the adjoining SOFC components can cause tensile ($CTE_{component} > CTE_{glass}$) or compressive ($CTE_{component} < CTE_{glass}$) thermal stress at the interface [50]. The CTEs of SOFC components are generally 10.5×10^{-6}/°C for the electrolyte, 12.4×10^{-6}/°C for the cathode, 10-14.0×10^{-6}/°C for the anode, and 11.0-15.0×10^{-6}/°C for the interconnect [51-53]. Tensile stress often leads to cracks at the interface and in the glass. Compressive stress to some extent can be tolerated because the compressive strength of a seal glass is much higher than the tensile strength (as high as 15 times [54]) but a seal glass may delaminate from the interfacing components due to excessive compressive stress. In practice, a CTE of 9.5-12.0×10^{-6}/°C is required for a seal glass. Roles of different constituents on the CTE of a seal glass generally follow the opposite trend as on T_g and T_s. The specific effect can be analyzed based on the function of the glass constituents.

Regarding glass network formers, CTEs of 9.0-13.0×10^{-6}/°C, 9.5-10.5×10^{-6}/°C, and 9.0-13.0×10^{-6}/°C have been obtained for silicate, borate, and borosilicate glasses, respectively [29-35,37-42,55-57]. For borosilicate glasses, CTE increases by 1.0-2.0 $\times 10^{-6}$/°C with increase in B_2O_3/SiO_2 ratio.

Regardless of the modifier types, desired CTE has been obtained for seal glasses [29-35,37-42,56,57]. CTE increases with increasing modifier content and decreasing modifier field strength. For example, CTE increases from 8.5×10^{-6}/°C to 12.0×10^{-6}/°C in a BaO-MgO-silicate glass when BaO/MgO ratio increases from 0.67 to 4.0 because of the lower field strength of BaO [30]. CTE increases from ~ 8.0×10^{-6}/°C to 11.5×10^{-6}/°C in a BaO-borosilicate glass

with BaO content increase from 20 mol% to 40 mol% [42,58]. CTE increases from 8.08 × 10^{-6}/°C to 9.20 × 10^{-6}/°C in a SrO-borosilicate glass when SrO content increases from 35.31 mol% to 41.76 mol% [33].

Intermediate oxides play a dual role regarding CTE. For example, CTE decreases when Al_2O_3 is a network former and increases when it is a network modifier. 1-2 mol% Al_2O_3 addition decreases CTE by ~ 1.5 × 10^{-6}/°C for silicate and borosilicate seal glasses [46,47].

The effect of additives on CTE has no consistent trend. 2.0-3.0 mol% La_2O_3 increase in BaO-borosilicate and SrO-borosilicate seal glasses increases the CTE by ~ 1.0 ×10^{-6}/°C due to increased amount of non-bridging oxygen [33,37]. Addition of transitional metal oxides increases CTE if they are network modifiers and decreases CTE if they are network formers. 3 mol% NiO increases CTE by ~ 1.0 ×10^{-6}/°C for a BaO-borosilicate glass [37]. 2 mol% ZrO_2 decreases CTE by 0.5-0.7 ×10^{-6}/°C for a BaO-borosilicate glass [37] but has no impact for a MgO-borosilicate glass [36].

Thermal treatment affects the CTE due to two reasons: structural rearrangement [20] and formation of devitrified phases with different CTE values. The CTEs of different devitrified phases in alkaline earth oxide containing seal glasses are given in Table 1-2. Devitrified phases with CTE different from glass can generate thermal stress resulting in degradation of a seal glass. For example, the CTE of a BaO-borosilicate seal glass decreases from ~ 11.5× 10^{-6}/°C to ~ 7.5× 10^{-6}/°C due to formation of devitrified $BaAl_2Si_2O_8$ phases with low CTE [42]. CTE change of a seal glass with thermal treatment time and temperature is undesirable.

Table 1-2. CTE of devitrified phases in seal glasses.

Devitrified phases	**Formula**	**CTE ($\times 10^{-6}$/°C)**
Quartz	SiO_2	11.2-23.3
Enstatite	$MgSiO_3$	9.0-12.0
Clinoenstatite	$MgSiO_3$	7.8-13.5
Protoenstatite	$MgSiO_3$	9.8
Forsterite	Mg_2SiO_4	9.4
Wollastonite	$CaSiO_3$	9.4
Calcium orthosilicate	Ca_2SiO_4	10.8-14.4
Barium silicate	$BaSiO_3$	10.5-12.5
	$Ba_2Si_3O_8$	(12.6)
		α_a =4.0
Barium borate	BaB_2O_4	α_c=36.0
Barium zirconate	$BaZrO_3$	7.9
Hexacelsian	$BaAl_2Si_2O_8$	6.6-8.0
Monocelsian	$BaAl_2Si_2O_8$	2.3
Orthorhombic Celsian	$BaAl_2Si_2O_8$	4.5-7.1
Hexacelsian	$SrAl_2Si_2O_8$	7.5-11.1
Monocelsian	$SrAl_2Si_2O_8$	2.7
Orthorhombic Celsian	$SrAl_2Si_2O_8$	5.4-7.6
Cordierite	$Mg_2Al_4Si_5O_{18}$	2.0

1.4.2. Stability

1.4.2.1. Thermal stability

Thermal stability is defined as resistance to devitrification of a glass/glass-ceramic material at SOFC/SOEC operating conditions. Devitrification of a seal glass is undesirable because of the glass property change it incurs. Localized stresses due to the CTE difference between the devitrified phase(s) and the glass phase are of the most concern. These stresses and the lower flowability of the devitrified phases can create pores and cracks in the glass and at the interface. For example, pores and cracks form in a BaO-CaO-borosilicate glass after thermal treatment at 850°C for 1 hr followed by 4 hrs at 750°C because of the CTE difference between the devitrified phases and the glass phase [59]. Qualitatively, higher temperature and longer time required to devitrify a glass mean higher thermal stability.

The origins of devitrification are the very small nuclei formed during glass making, heterogeneity in glass network structure, surface flaws such as dust particles or other contaminant during glass preparation, and residual stress from mechanical polishing [15,22, 60,61]. Thermal stability depends on seal glass composition and thermal treatment conditions.

Glass formers can exist in different structural units. Silicate structural units (in silicate and borosilicate systems) and borate structural units (in borate and borosilicate systems) are common species. In silicate glass, the structural units are disilicate (Si_2O_5), metasilicate (Si_2O_6), pyrosilicate (Si_2O_7), and orthosilicate (SiO_4) with one, two, three, and four non-bridging oxygen atoms respectively. The silicate structural units can further form chains (such as Si_3O_4, Si_3O_{10}) or rings (such as Si_4O_{12}, Si_6O_{18}) [16,17,19,62]. In borate glass, the structural units are boroxyl (B_3O_6), diborate (B_4O_9), pentaborate (B_5O_{10}), dipentaborate (B_5O_{12}), tetraborate (B_8O_{16}),

metaborate (B_3O_6), pyroborate (B_2O_5), and orthoborate (BO_3) [63]. Coexistence of several different types of structural units induces heterogeneity in the network structure [64,65]. Devitrification of a lithium disilicate glass occurs due to the presence of pyrosilicate (Si_2O_7) and orthosilicate (SiO_4) structural units which cause glass structure heterogeneity [64,65]. Silicate glasses have a higher degree of devitrification resistance than borate and borosilicate glasses. For example, the devitrification temperature of a MgO-BaO-SiO_2 seal glass decreases from 918°C to 800°C with 5 mol% B_2O_3 addition [29].

Devitrification resistance of a seal glass also depends on glass modifiers. Fig. 1-4 shows the devitrification temperature of silicate and borosilicate glasses when alkaline earth oxides are used as glass network modifiers [30,36,57,66]. In these glasses, the overall composition is fixed but the type of modifier is varied. Devitrification temperature decreases in silicate glasses but increases in a borosilicate glass when the field strength of the modifier cation increases (Fig. 1-4). Generally, heterogeneity in glass structure increases with increasing modifier field strength [67]. As a result, the devitrification temperature in silicate glasses decreases (Fig. 1-4). For the specific silicate glass compositions in Fig. 1-4, the devitrifictaion temperature decreases in the order of $Ba^{2+}>Sr^{2+}>Ca^{2+}>Mg^{2+}$. In the borosilicate glasses, higher field strength modifiers improve the homogeneous mixing of the borate structural units and the silicate structural units. As a result, the devitrification temperature increases. For the specific borosilicate glass compositions in Fig. 1-4, the devitrification temperature increases in the order of $Ba^{2+}<Ca^{2+}<Mg^{2+}$.

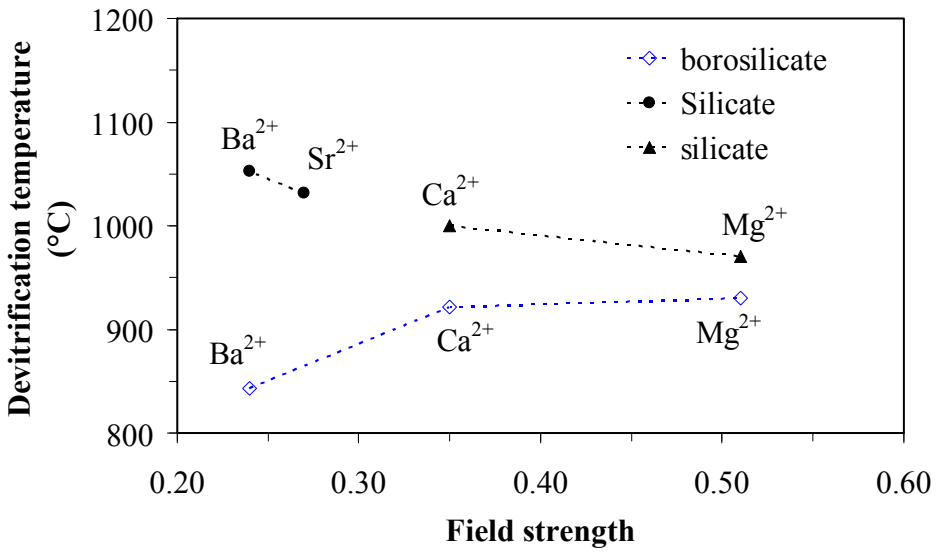

Fig. 1-4. Devitrification temperature vs field strength of modifier cations in silicate and borosilicate glasses.

A small amount (<10 mol%) of intermediates in a seal glass generally improves devitrification resistance [68]. In a borosilicate glass, 3-8 mol% Al_2O_3 improves the devitrification resistance by decreasing the amount of borate structural units, which are immiscible with silicate structural units [69,70]. If an excess amount of intermediate exists, it decreases the devitrification resistance. For example, 10 mol% Al_2O_3 degrades devitrification resistance by enhancing phase separation in a MgO-borosilicate glass [36].

Additives generally degrade devitrification resistance. In a BaO-borosilicate glass, 5 mol% La_2O_3 leads to formation of $Ba_4La_6O(SiO_4)_4$ at 800°C [37]. In SrO-borosilicate glasses, La_2O_3 (3-25 mol%) causes the formation of $LaBO_3$ and Sr-containing lanthanum borate [33]. Effect of transition metal oxides on devitrification is specific to the glass composition. Devitrification resistance can be improved if transition metal oxides participate in the glass network and degraded if otherwise. Initial addition of TiO_2 decreases devitrification temperature

of a MgO-borosilicate (2 mol% TiO_2) glass [36] and a borate glass (5 mol% TiO_2) [58] as shown in Fig. 1-5. Further addition of TiO_2 increases devitrification temperature in these glasses. In contrast, TiO_2 addition promotes devitrification in another MgO-containing glass due to glass composition difference [71]. Similar observations are made for ZrO_2 and ZnO additions in seal glasses [29,26,37].

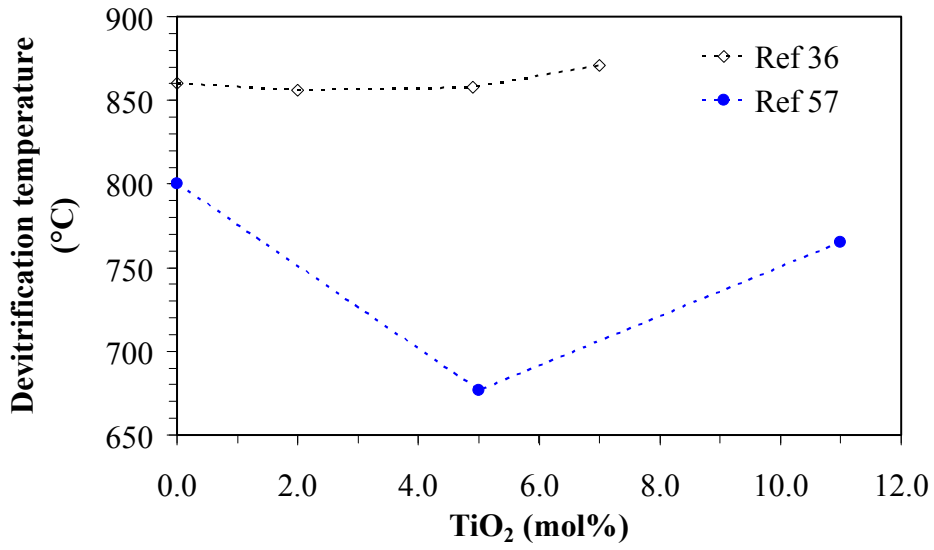

Fig. 1-5. Devitrifictaion temperature change with TiO_2 content in borate and borosilicate seal glasses.

Thermal stability of a seal glass also depends on the heating rate, thermal treatment time, and particle size, and SOFC/SOEC environment. Devitrification temperature increases with heating rate. For example, the devitrification temperature of a BaO-silicate glass increases from 994°C to 1062°C when the heating rate increases from 2.5°C/min to 40°C/min [28]. The extent of devitrification increases with thermal treatment time and becomes saturated after a certain time. For example, devitrification of a BaO-CaO-borosilicate glass increases from ~ 50% to ~ 70% after 120 hrs of thermal treatment in air at 750°C and stays constant afterwards [40].

Smaller particle size decreases the devitrification temperature. For example, devitrification temperature decreases from 910°C to 833°C when the particle size decreases from 500-850 μm to <20 μm for a MgO-BaO-silicate glass [27]. The effect of SOFC/SOEC environment will be discussed in section 1.4.2.2.

If a seal glass and its devitrified phases have similar CTEs and the new glass-ceramic system has high enough flowability, limited devitrification can be tolerated. However, such glass systems are very rare. Uncontrollable and/or progressive devitrification of a seal glass cause composition inhomogeneity and generate thermal stress due to CTE difference. This in turn leads to pores and cracks and thus gas leakage during sealing [38,60]. In addition, the poor flowability of the new glass-ceramic limits its use as a 'hermetic seal'.

1.4.2.2. Chemical Stability

A seal glass must possess high chemical stability since it is exposed to simultaneous oxidizing and reducing atmospheres and interfaces with ceramic and metallic materials of very different compositions at SOFC/SOEC operating temperatures. In general, seal glass chemical stability can be discussed from two aspects: stability of bulk seal glass and interfacial stability of seal glass with other SOFC/SOEC components.

Seal glasses are simultaneously exposed to oxidizing at cathode side and reducing atmospheres at anode side at high temperatures during SOFC operation. The reducing atmosphere also contains high water content (> 50%). In this context, atmospheres can adversely affect the properties of a seal glass by vaporizing glass constituents, changing glass microstructure, and accelerating glass devitrification.

Vaporization of glass constituents changes glass composition and can adversely affect the desired thermal, chemical, and electrical properties. Pure silica glass does not vaporize in dry air due to its high melting point but vaporizes in the form of $Si(OH)_4$ species by reacting with H_2O and in the form of SiO species by reacting with H_2 at 1000°C. Also, $Si(OH)_4$ species dominates in H_2O-containing reducing atmosphere at high temperatures [72]. B_2O_3 has a higher tendency to vaporize at SOFC operating temperatures due to its low melting point and high vapor pressure. Boron reacts with water and vaporizes in the form of HBO_2 gaseous species in alkaline oxide free glasses and in the form of RBO_2 (R = Na, K) and $B(OH)_3$ species in alkaline oxide containing glasses [73,74]. Weight loss a borosilicate seal glass increases from 0.16 to 0.98 mg/cm^2 due to gaseous $B_3H_3O_6$ vaporization when the atmosphere is changed from oxidizing atmosphere to 30% H_2O/H_2 atmosphere [75]. For this glass, the weight loss increases from 0.03 to 0.16 mg/cm^2 as the B_2O_3 content increases from 2 to 20 mol% [75].

To achieve 'gas-tightness', a seal glass should have high interfacial stability with other SOFC/SOEC components in order to avoid interfacial strength decrease and flaw formation [76]. Several factors such as compositions, wetting behaviors, and bonding conditions (temperature, pressure, and atmosphere) of the seal glass and the adjacent SOFC/SOEC components affect the interfacial stability. A seal glass should wet and bond with electrolyte, electrodes, and metallic interconnects uniformly to form good sealing without any pores or cracks at the interface. The interaction usually involves inter-diffusion and chemical reaction of the elements of the seal glass and interfacing components [77, 78]. Severe interaction between the seal glass and the adjacent components increases interfacial layer thickness, which in turn leads to pore and crack formation at the interface and delamination of the glass [51,78].

Interaction of a seal glass with metallic interconnect is more severe than with the other cell components. Subsequently, seal glass interaction with metallic interconnect has been the focus of most interfacial studies. Chromia forming ferritic stainless steel is the most preferred interconnect which contains more than 22.0 wt% Cr with different trade names such as Crofer 22 APU, AISI 446, AISI 430, and AL29-4C alloys [54]. Seal glass interaction with interconnect depends on the glass and interconnect compositions, exposed atmospheres, and sealing conditions. For example, a BaO-CaO-borosilicate glass forms a porous interface with cracks with the Crofer 22 APU alloy but pore- and crack- free interface has been observed for the same glass system with a slightly different composition [34,78].

B_2O_3 in a seal glass favors bonding with interconnect alloys because of its good wetting behavior but the extent of diffusion and chemical reaction may be high [29,79]. For example, more than 15 mol% B_2O_3 is required for BaO-MgO-silicate and BaO-ZnO-silicate glasses to bond with the Crofer 22 APU alloy [29].

An alkaline silicate glass can react with an interconnect and form alkaline chromates (such as Na_2CrO_4, K_2CrO_4), which vaporize and destabilize glass network [80,81]. Therefore, presence of alkaline oxide(s) in a seal glass is undesirable. Alkaline earth oxide containing glasses bond well with interconnect. BaO-CaO-silicate glasses bond well with the Crofer 22 APU alloy and form 1-3 μm thick interfaces which are stable for 500-1000 hrs at 800°C [82]. Alkaline earth borosilicate glasses bond well with the Crofer 22 APU alloy at 850°C and form 1-3 μm thick interface with extensive cracks followed by a 2-3 μm thick porous layer [35,79]. The origin of the porous layer and cracks at the interface is twofold. First, devitrification causes glass volume decrease, poor glass flow at the interface, and CTE mismatch between the glass phase and the devitrified phases. Second, the glasses react with the volatile chromium species such as

CrO_3 and $CrO_2(OH)_2$ from the interconnect and form $BaCrO_4$ and $SrCrO_4$ [78,84]. The CTEs of these chromate phases (21.0-23.0 × 10^{-6}/°C) are much higher than those of the seal glasses (10.0-12.0 × 10^{-6}/°C). These interfaces of borosilicate glasses are also not stable. For example, the interfacial layer thickness of a BaO-CaO-borosilicate glass with the Crofer 22 APU alloy increases from 10 μm to 76 μm after 200 hrs of thermal treatment at 750°C in air due to severe interaction [83].

Effect of additives on the seal glass bonding with metallic interconnect is not well understood. A BaO-CaO-borosilicate glass does not bond with the Crofer 22 APU alloy if minor amounts of La_2O_3 and ZnO are present in the glass [34]. However, other seal glasses bond with the Crofer 22 APU alloy well even if La_2O_3 is present. Transition metal oxides such as NiO and ZnO disrupt the network structure in alkaline earth borosilicate glasses and form interfaces with pores and cracks [29,84].

Interaction of seal glass with metallic interconnect and the interfacial stability are also affected by atmosphere. For example, a BaO-MgO-silicate glass does not bond with the Crofer 22 APU in an oxidizing atmosphere but bonds well with the same alloy in a H_2O/H_2 atmosphere [85].

Seal glasses generally wet ZrO_2 electrolyte well. Interfacial stability between a seal glass and ZrO_2 electrolyte is not a problem regardless of glass composition, sealing condition, and atmosphere [31,33,34,37,42,85]. There are a few cases that a seal glass interacts with the electrolyte. For example, a BaO-CaO-borosilicate glass reacts with yttria stabilized zirconia and forms $BaZrO_3$ after 1200 hrs of thermal treatment at 750°C [38]. Nonetheless, seal glass/ZrO_2 electrolyte interfacial stability is not a major concern.

Interaction between electrodes and seal glass can change the morphology of the electrodes [86-88]. One study shows that a silica layer of 0.4-0.6 μm thickness from a Na_2O-silicate seal glass segregates at the anode and electrolyte interface and covers the nickel particles in the anode. Distribution of nickel particles and pores in the anode may have changed due to the interaction with this seal glass [86]. Another report shows that a Na_2O-borosilicate glass reacts with the cathode and causes the cathode grains to coarsen from 0.69 to 1.13 μm [87]. Larger grain size and uneven distribution of grains and pores in the cathode degrade cell performances due to decreased number and length of triple phase boundaries. An electrically insulating layer can also form at the interface of electrode-electrolyte when a seal glass reacts with electrodes.

Interfacial stability can be improved by controlling sealing conditions such as heating rate, sealing temperature, preoxidation of the interconnect, and coating of an oxide layer on the interconnect. A slow heating rate during sealing is beneficial. For example, porosity and pore size at the interface decrease when the heating rate decreases from 25°C/min to 5°C/min for a Na_2O-CaO-silicate glass [31]. Increasing sealing temperature (>900°C) improves the interfacial stability for a SrO-CaO-borosilicate glass by hindering $SrCrO_4$ phase formation at the interface [84]. Preoxidation of interconnect at 800-1000°C introduces an oxide layer and enhances the bonding with seal glass. The possible reasons are twofold. First, the oxide layer acts as a transition layer with a CTE between those of the interconnect and the seal glass. The residual stress due to CTE mismatch is decreased. For example, 1-5 μm thick chromium–manganese-iron oxide layer in preoxidized AISI 430 alloy facilitates bonding with a Na_2O-CaO-silicate seal glass [79]. Second, the oxide layer decreases the contact angle between the seal glass and the interconnect and leads to better adhesion. For example, preoxidation of the AISI 430 alloy and the Crofer 22 APU alloy at 800-1000°C for 2 hrs decreases pores and cracks at the interface [89].

However, a thick oxide layer can cause spallation of seal glass [89]. Coating the interconnect with an oxide layer improves the interfacial stability by increasing adhesion and eliminating the direct contact of the interconnect with harsh environments. For example, NiO, Co_3O_4, Al_2O_3, and ZrO_2 coating on the Crofer 22 APU alloy improves the bonding and interface stability by improving adhesion and eliminating chromate and iron oxide formation at the interface [81,90].

1.4.3. Mechanical properties

A seal glass should withstand 14-35 kPa pressure due to gas flow, vibration, and thermal cycling during SOFC operation [11, 83]. It should also withstand more than 100 thermal cycles for stationary applications and more than 1000 thermal cycles for mobile applications [14]. Generally, higher strength is obtained in a glass with higher T_g. Elastic modulus of 30-100 GPa can be obtained in a seal glass [91]. Devitrification can either decrease or increase the elastic modulus of a seal glass depending on the specific composition. For a BaO-CaO-borosilicate seal glass, elastic modulus decreases from 78.0 to 60.8 GPa after 1000 hrs of thermal treatment at 750°C due to devitrification [92]. In contrast, the shear strength of a BaO-CaO-silicate seal glass with the Crofer 22 APU alloy increases from 0.3 MPa to 4 MPa due to glass devitrification [93,94].

Thermomechnical stress, σ, can be defined as

$$\sigma = \Delta E \Delta \alpha \Delta T \qquad (1\text{-}3)$$

where ΔE, Δα, and ΔT are the difference in elastic modulus, CTE, and temperature gradient, respectively, between the glass and the interfacing components [77]. Initiation and growth of cracks at the interface occur if the thermomechanical stress exceeds the tensile strength of seal glass or the interfacial bonding strength. Excessive compressive stress delaminates the seal glass

from the interface [51]. Thermal cycling induces thermomechanical stress due to temperature gradient and change in material properties with temperature. Thermal stress effect is more severe than mechanical stress effect for crack initiation and growth [95]. In this context, thermomechanical properties of the interface are also crucial. High interfacial bonding strength is desired to avoid failure at the interface but the desired value is unknown. Seal glass/interconnect interfacial strength of 2.0-8.5 MPa has been achieved [89,90]. The bonding strength depends on glass composition and sealing condition. Alkaline oxide containing seal glasses have lower interfacial strength than alkaline earth oxide containing seal glasses [89,93,96]. The interfacial bonding strength of Na_2O-silicate and SrO-CaO-borosilicate glasses with the Crofer 22 APU interconnect are ~ 2.0 MPa and 7 MPa, respectively. Higher field strength and charge of alkaline earth oxides hinder the rotational movement of glass structural units and result in higher elastic modulus. As a result, the mismatch in the elastic modulus between the seal glass and the interconnect deceases and the interfacial strength increases.

1.4.4. Electrical resistivity

The electrical resistivity of a seal glass depends on the composition and should be $>10^4$ Ω·cm in order to avoid shunting [97]. Effect of network former and modifier oxides are known but the effect of intermediates and additives are uncertain because of their different roles in a specific glass composition. The electrical resistivity of borate glasses is higher than that of silicate glasses due to 'boron anomaly' [16] Electrical resistivity of a Na_2O-silicate glass increases with initial addition but decreases with further addition of intermediate oxides probably due to the 'combined ion effect' [15]. Alkaline earth oxide containing glasses generally have electrical resistivity more than 10^4 Ω·cm. Electrical resistivity increases with ionic radius and

valence of the modifier ions [15,17]. For example, the electrical resistivity of a BaO-ZnO-silicate glass (~ 1.3×10^{9} Ω·cm) is ten times higher than that of a BaO-MgO-silicate glass (~ 5.8×10^{8} Ω·cm) due to the larger ionic radius of Zn^{2+} ions [97].

1.4.5. Sealing performance

Sealing performance is the ability to prevent mixing and leakage of gasses. Gas leakage less than 1% of the fuels used during the entire cell operation is needed [10]. However, currently there is no agreed procedure for sealing performance evaluation. Four different gas leakage units are reported in literature: sccm/cm (standard cubic centimeters per minute per centimeter), Pa·L/s, $Pa\cdot m^{2}\cdot s^{-1}$, and L/min [34,98,99]. Sealing performances are commonly evaluated by pressure-leakage test [10]. In this method, a seal glass is sandwiched between two SOFC components such as metallic interconnect and electrolyte to form a tri-layer assembly, which is subjected to a differential pressure of 14-35 kPa to simulate the gas flow in a typical SOFC [83].

Pores and cracks at the interface and in the seal glass are the gas leakage paths. Localized thermomechanical stress due to devitrification of the seal glass and severe interaction with the interfacing components can increase the numbers of pores and cracks and gas leakage rate. For example, the leakage rate increases from 10^{-3} -10^{-4} sccm/cm to 1-2 × 10^{-2} sccm/cm for a SrO-CaO-borosilicate seal glass due to the presence of pores and cracks. The leakage rate of a BaO-borosilicate glass increases by an order of magnitude during cooling from 700°C (10^{-3} sccm/cm) to 100°C (3 × 10^{-2} sccm/cm) because of extensive crack growth.

1.5. Objectives

The objectives of the present research are:

1. To develop a thermochemically stable seal glass for SOFC/SOEC operating at 800°C.
2. To understand the composition-structure-property relationships of a SrO-La_2O_3-Al_2O_3-B_2O_3-SiO_2-based seal glass.
3. To investigate the interfacial compatibility and stability of a SrO-La_2O_3-Al_2O_3-SiO_2 based seal glass with the Crofer 22 APU and AISI 441 interconnect alloys.
4. To understand the interconnect-seal glass reaction with respect to thermal treatment temperature, time, and atmosphere.

To evaluate the sealing performances of the SrO-La_2O_3-Al_2O_3-SiO_2-based seal glass.

1.6. Dissertation structure

This dissertation is divided into 8 chapters. The contents of each chapter are outlined below:

1. Chapter one is an introduction which covers a comprehensive literature review to provide background information for SOFC/SOEC seal glass. This chapter also includes the objectives of this research.
2. SrO-La_2O_3-Al_2O_3-B_2O_3-SiO_2-based seal glass is studied in chapter two to develop compositional design strategy in order to meet the demanding requirements.
3. In chapter three, composition-structure-property relationships of the SrO-La_2O_3-Al_2O_3-B_2O_3-SiO_2-based seal glass is investigated as a function of B_2O_3:SiO_2 ratio.

4. Chapter four deals with the role of nickel as an additive in the SrO-La_2O_3-Al_2O_3-B_2O_3-SiO_2-based seal glass structure and properties.
5. Interfacial studies between the SrO-La_2O_3-Al_2O_3-SiO_2 seal glass and the Crofer 22 APU alloy are documented in chapter five. The interfacial stability of this seal glass with the AISI 441 alloy is discussed in chapter six.
6. Sealing performances of the SrO-La_2O_3-Al_2O_3-SiO_2 seal glass has been evaluated in chapter seven.
7. Overall conclusions and the future research directions are given in chapter eight.

References

[1] M. Yokoo, Y. Tabata, Y. Yoshida, K. Hayashi, Y. Nozaki, K. Nozawa, and H. Arai, Highly efficient and durable anode-supported SOFC stack with internal manifold structure, Journal of Power Sources 178, 59-63, 2008.

[2] M. C. Williams, Solid oxide fuel cells: fundamentals to systems, Fuel Cells 7, 78-85, 2007.

[3] S. Elangovan, J. J. Hartvigsen, and L. J. Frost, Intermediate temperature reversible fuel cells, International Journal of Applied Ceramic Technology 4, 109-118, 2007.

[4] K. Kendall, Progress in solid oxide fuel cell materials, International Materials Reviews 50, 257-264, 2005.

[5] S. P. Jiang and S. H. Chan, A review of anode materials development in solid oxide fuel cells, Journal of Materials Science 39, 4405-4439, 2004.

[6] J. W. Fergus, Metallic interconnects for solid oxide fuel cells, Materials Science and Engineering A 397, 271-283, 2005.

[7] EG&G Technical Services, Fuel cell hand book, 7th edition, US Department of Energy, Office of Fossil energy, National Energy Technological Laboratory, Morgantown, West Virginia, 2004.

[8] F. P. Nagel, T. J. Schildhauer, S. M. A. Biollaz, and A. Wokaun, Performance comparison of planar, tubular and delta8 solid oxide fuel cells using a generalized finite volume model, Journal of Power Sources 184, 143-164, 2008.

[9] J. F. B. Rasmussen, P. V. Hendriksen, and A. Hagen, Study of internal and external leaks in tests of anode-supported SOFCs, Fuel Cells 8, 385-393, 2008.

[10] P. A. Lessing, J. Hartvigsen, and S. Elangovan, Sealants, Solid oxide fuel cells: materials properties and performance, ed. J. W. Fergus, R. Hui, X. Li, D. P. Wilkinson and J. Zhang, CRC Press Taylor & Francis Group, Boca Raton, Florida, 213-237, 2009.

[11] K. S. Weil, The state-of-the-art in sealing technology for solid oxide fuel cells, Journal of Materials (JOM) 58, 37-44, 2006.

[12] J. W. Fergus, Sealants for solid oxide fuel cells, Journal of Power Sources 147, 46-57, 2005.

[13] P. A. Lessing, A review of sealing technologies applicable to solid oxide electrolysis cells, Journal of Materials Science 42, 3465-3476, 2007.

[14] D. Stolten, L. G. J. B. d. Haart, and L. Blum, Design criteria for SOFC generatos, Ceramic Engineering and Science Proceedings 24, 263-272, 2003.

[15] J. E. Shelby, Introduction to glass science and technology, The Royal Society of Chemistry Cambridge, UK, 2005.

[16] H. Scholze, Glass nature, structure, and properties, Springer Verlag, New York, USA, 1991.

[17] W. D. Kingery, H. K. Bowen, and D. R. Uhlmann, Introduction to Ceramics, John Wiley and Sons, New York, 2nd edn., 1976, ch. 3 pp. 91-122, ch.17, pp. 873-888.

[18] G. Calas, L. Cormier, L. Galoisy, and P. Jollivet, Structure–property relationships in multicomponent oxide glasses, C R Chimie 5, 831-843, 2002.

[19] M. B. Volf, Chemical approach to glass, Glass Science and Technology, Elsevier, Amsterdam, vol. 7, ch. 1, pp. 22-35, 43-58, 88-113, ch. 2, pp. 141-205, 280-302, 1984.

[20] J. E. Shelby, Thermal expansion of mixed-alkai silicate glasses, Journal of Applied Physics 47, 4489-4496, 1976.

[21] G. N. Greaves, and S. Sen, Inorganic glasses, glass-forming liquids and amorphizing solids. Advances in Physics 56, 1-166, 2007.

[22] V. W. Vogel, Structure and crystallization of glass, Pergamon, New York, 1971.

[23] L. Galoisy, L. Cormier, S. Rossano, A. Ramos, G. Calas, P. Gaskell, and M. L. Grand, Cationic ordering in oxide glasses: the example of transition elements, Mineralogical Magazine 64, 409-424, 2000.

[24] Glass, Ceramic and Whiteware, ASTM international, 15.02, (C 162-05), 2006.

[25] P. Hrma, W. T. Han, and A. R. Cooper, Thermal healing of cracks in glass, Journal of Non-Crystalline Solids 102, 88-94, 1988.

[26] R. N. Singh, Sealing technology for solid oxide fuel cells (SOFC), International Journal of Applied Ceramic Technology 4, 134-144, 2007.

[27] M. J. Pascual, C. Lara, and A. Durán, Non-isothermal crystallization kinetics of devitrifying RO-BaO-SiO_2 (R=Mg,Zn) glasses, Physics and Chemistry of glasses, European Journal of Glass Science and Technology B 47, 572-581, 2006.

[28] N. P. Bansal, and M. J. Hyatt, Crystallization kinetics of BaO-Al_2O_3-SiO_2 glasses, Journal of Materials Research 4, 1257-1265, 1989.

[29] M. J. Pascual, A. Guillet, and A. Durán, Optimization of glass–ceramic sealant compositions in the system MgO–BaO–SiO_2 for solid oxide fuel cells (SOFC), Journal of Power Sources 169, 40-46, 2007.

[30] C. Lara, M. J. Pascual, and A. Durán, Glass-forming ability, sinterability and thermal properties in the systems RO–BaO–SiO_2 (R = Mg, Zn), Journal of Non-Crystalline Solids 348, 149-155, 2004.

[31] F. Smeacetto, M. Salvo, M. Ferraris, J. Cho, and A. R. Boccaccini, Glass-ceramic seal to join Crofer 22 APU alloy to YSZ ceramic in planar SOFCS, Journal of the European Ceamic Society 28, 61-68, 2008.

[32] T. J. Kohli, and R. Morena, Sealing frits, European Patent No. EP 0982274A2, 2000.

[33] K. L. Ley, M. Krumpelt, R. Kumar, J. H. Meiser, and I. Bloom, Glass-ceramic sealants for solid oxide fuel cells Part I. Physical properties, Journal of Materials Research 11, 1489-1493, 1996.

[34] S. Ghosh, A. D. Sharma, P. Kundu, and R. N. Basu, Glass-ceramic sealants for planar IT-SOFC: A bilayered approach for the joining electrolyte and metallic interconnect, Journal of the Electrochemical Society 155, B473-B478, 2008.

[35] Y. S. Chou, J. W. Stevenson, and P. Singh, Novel refractory alkaline earth silicate sealing glasses for planar solid oxide fuel cells, Journal of The Electrochemical Society 154, B644-B651, 2007.

[36] N. Lahl, K. Singh, L. Singheiser, K. Hilper, and D. Bahadur, Crystallisation kinetics in AO-Al_2O_3-SiO_2-B_2O_3 glasses (A = Ba, Ca, Mg), Journal of Materials Science 35, 3089-3096, 2000.

[37] S. B. Sohn, S. Y. Choi, G. H. Kim, H. S. Song, and G. D. Kim, Suitableglass-ceramic sealant for planar solid oxide fuel cells, Journal of the American Ceramic Society 87, 254-260, 2004.

[38] K. D. Meinhardt, D. S. Kim, Y. S. Chou, and K. S. Weil, Synthesis and properties of a barium aluminosilicate solid oxide fuel cell glass-ceramic sealant, Journal of Power Sources 182, 188-196, 2008.

[39] T. Yoshii, Sealing glass composition, dealing glass frit and sealing glass sheet, US Patent No. US 2006/0019813 A1, 2006.

[40] K. D. Meinhardt, J. D. Vienna, T. R. Armstrong, and L. R. Pederson, Glass-ceramic joint and method of joining, US Patent No. US 6532769 B1, 2003.

[41] I. D. Bloom and K. L. Ley, Compliant sealants for solid oxide fuel cells and other ceramics. US Patent No. 5453331, 1995.

[42] S. B. Sohn, S. Y. Choi, G. H. Kim, H. S. Song, and G. D. Kim, Stable sealing glass for solid oxide fuel cell, Journal of Non-Crystalline Solids 297, 103-112,2002.

[43] R. E. Loehman, H. P. Dumm, and H. Hofer, Evaluation of sealing glasses for solid oxide fuel cells, Ceramic Engineering and Science Proceedings 23, 699-705, 2002.

[44] J. E. Shelby and J. T. Kohli, Rare- earth aluminosilicate glasses, Journal of the American Ceramic Society 73, 39-42, 1990.

[45] Budd, M., Glass ceramic material and its use as means for joining different types of material and as support. European patent No EP 0975554B1 1998.

[46] Budd, M., Barium lanthanum silicate glass-ceramics. US Patent No. 7189668B2 2007.

[47] Y. S. Chou, J. W. Stevenson, and R. N. Gow, Novel alkaline earth silicate sealing glass for SOFC Part I The effect of nickel oxide on the thermal and mechanical properties, Journal of Power Sources 168, 426-433, 2007.

[48] S. T. Reis and R. K. Brow, Designing sealing glasses for solid oxide fuel cells, Journal of Materials Engineering and Performance 15, 410-413, 2006.

[49] R. Kirsch, Metals in glassmaking, Glass science and technology, vol. 13, Elsevier, Amsterdam, 1993.

[50] I. W. Donald, Preparation, properties and chemistry of glass and glass-ceramic-to-metal seals and coatings, Journal of Materials Science 28, 2841-2886, 1993.

[51] M. Radovic, E. Lara-Curzio, R. M. Trejo, H. Wang, and W. D. Porter, Thermophysical properties of YSZ and Ni-YSZ as a function of temperature and porosity, Ceramic Engineering and Science Proceedings 27, 79-85, 2006.

[52] M. Mori, Y. Hiei, N. M. Sammes, and G. A. Tompsett, Thermal-expansion behaviors and mechanisms for Ca- or Sr-doped lanthanum manganite perovskites under oxidizing atmospheres, Journal of the Electrochemical Society 147, 1295-1302, 2000.

[53] Z. Yang, Recent advances in metallic interconnects for solid oxide fuel cells, International Materials Reviews 53, 39-54, 2008.

[54] S. Linderoth, P. V. Hendriksen, and M. Mogensen, Investigations of metallic alloys for use as interconnects in solid oxide fuel cell stacks, Journal of Materials Science 31, 5077-5082, 1996.

[55] M. Brochu, B. D. Gauntt, R. Shah, G. Miyake, and R. E. Loehman, Comparison between barium and strontium -glass composites for sealing SOFCs, Journal of the European Ceamic Society 26, 3307-3313, 2006.

[56] C. Lara, M. J. Pascual, M. O. Prado, and A. Durán, Sintering of glasses in the system RO-Al_2O_3-BaO-SiO_2 (R=Ca,Mg,Zn) studied by hot-stage microscopy, Solid State Ionics 170, 201-208, 2004.

[57] R. K. Brow, H. L. McCollister, C. C. Phifer, and D. E. Day, Sealing glasses for titanium and titanium alloys, US Patent No. 5648302, 1997.

[58] E. S. Lim, B. S. Kim, J. H. Lee, J. J. Kim, Effect of BaO content on the sintering and physical properties of BaO–B_2O_3–SiO_2 glasses, Journal of Non-Crystalline Solids 352, 821-826, 2006.

[59] W. Liu, X. Sun, and M. A. Khaleel, Predicting Young's modulus of glass/ceramic sealant for solid oxide fuel cell considering the combined effects of aging, micro-voids and self-healing. Journal of Power Sources 185, 1193-1200, 2008.

[60] I. Avramov, The role of stress development and relaxation on crystal growth in glass. Journal of Non-Crystalline Solids 353, 2889–2892, 2007.

[61] T. Jin and K. Lu, Thermal Stability of a new solid oxide fuel/electrolyzer cell seal glass, Journal of Power Sources 195, 195-203, 2009.

[62] P. McMillan, Structural studies of silicate glasses and melts-applications and limitations of Raman Spectroscopy, American Mineralogist 69, 622-644, 1984.

[63] B. N. Meera and J. Ramakrishna, Raman spectral studies of borate glass, Journal of Non-Crystalline Solids 159, 1-21, 1993.

[64] B. H. W. S. D. Jong, C. M. Schramm, and V. E. Parziale, ^{29}Si magic angle spinning NMR study on local silicon environments in amorphous and crystalline lithium silicates, Journal of the American Chemical Society 106, 4396-4402, 1984.

[65] T. Maehara, T. Yano, S. Shibata, and M. Yamane, Structure and phase transformation of alkali silicate melts analyzed by Raman Spectroscopy, Philosophical Magazine 84, 3085-3099, 2004.

[66] M. J. Hyatt and N. P. Bansal, Crystal growth kinetics in $BaO-AI_2O_3-2SiO_2$ and $SrO-AI_2O_3-2SiO_2$ glasses, Journal of Materials Science 31, 172-184, 1996.

[67] P. Taylor, A. B. Campbell, and D. G. Owen, Liquid immiscibility in the systems X_2O-MO-B_2O_3-SiO_2 (X = Na, K; M = Mg, Ca, Ba) and Na_2O-MgO-BaO-B_2O_3-SiO_2, Journal of the American Ceramic Society 66, 347-351, 1983.

[68] J. H. Jean, T. H. Kuan, and T. K Gupta, Crystallization inhibitors during sintering of pyrex borosilicate glass, Journal of Materials Research 8, 356-363, 1993.

[69] W. F. Du, K. Kuraoka, T. Akai, and T. Yazawa, Study of Al_2O_3 effect on structural change and phase seperation in $Na_2O-B_2O_3-SiO_2$ glass by NMR, Journal of Materials Science 35, 4865-4871, 2000.

[70] L. S. Du and J. F. Stebbins, Network connectivity in aluminoborosilicate glasses: A high-resolution ^{11}B, ^{27}Al, and ^{17}O NMR study, Journal of Non-Crystalline Solids 351, 3508-3520, 2005.

[71] H. Shao, K. Liang, and F. Peng, Crystallization kinetics of $MgO–Al_2O_3–SiO_2$ glass-ceramics, Ceramics International 30, 927-930, 2004.

[72] P. Singh and S. D. Vora, Vapor phase silica transport during SOFC operation at 1000^0C, Ceramic Engineering and Science Proceedings 26, 99-100, 2005.

[73] M. J. Snyder, M. G. Mesko, and J. E. Shelby, Volatilization of boron from E-glass melts, Journal of Non-Crystalline Solids 352, 669-673, 2006.

[74] J. Simon, Boron chemistry in flue gases from borosilicate glass furnace, Ceramic Transactions 141, 389-395, 2004.

[75] T. Zhang, W. G. Fahrenholtz, S. T. Reis, and R. K. Brow, Borate volatility from SOFC sealing glasses, Journal of the American Ceramic Society 91, 2564-2569, 2008.

[76] J. M. Howe, Bonding, structure, and properties of metal/ceramic interfaces: Part 1 Chemical bonding, chemical reaction, and interfacial structure, International Materials Reviews 38, 233-256, 1993.

[77] J. M. Howe, Bonding, structure, and properties of metal/ceramic interfaces: Part 2 Interface fracture behavior and property measurement. International Material Reviews 38, 257-271, 1993.

[78] Z. Yang, G. Xia, K. D. Meinhardt, K. S. Weil, and J. W. Stevenson, Chemical stability of glass seal interface in intermediate temperature solid oxide fuel cells, Journal of Materials Engineering and Performance 13, 327-334, 2004.

[79] F. Smeacetto, M. Salvo, M. Ferraris, V. Casalegno, P. Asinari, and A. Chrysanthou, Characterization and performance of glass-ceramic sealant to join metallic interconnects to YSZ and anode-supported-electrolyte in planar SOFCs, Journal of the European Ceramic Society 28, 2521-2527, 2008.

[80] O K. Ogasawara, H. Kameda, Y. Matsuzaki, T. Sakurai, T. Uehara, A. Toji, N. Sakai, K. Yamaji, T. Horita, and H. Yokokawa, Chemical stability of ferritic alloy interconnect for SOFCs, Journal of the Electrochemical Society 154, B657-B663, 2007.

[81] K. A. Nielsen, M. Solvang, S. B. L. Nielsen, A. R. Dinesen, D. Beeaff, and P. H. Larsen, Glass composite seals for SOFC application, Journal of the European Ceamic Society 27, 1817-1822, 2007.

[82] N. H. Menzler, D. Sebold, M. Zahid, S. M. Gross, and T. Coppitz, Interaction of metallic SOFC interconnect materials with glass-ceramic sealant in various atmosphere, Journal of Power Sources 152, 156-167, 2005.

[83] K. S. Weil, J. E. Deibler, J. S. Hardy, D. S. Kim, G. G. Xia, L. A. Chick, and C. A. Coyle, Rupture testing as a tool for developing planar solid oxide fuel cell seals, Journal of Materials Engineering and Performance 13, 316-326, 2004.

[84] Y. S. Chou, J. W. Stevenson, and R. N. Gow, Novel alkaline earth silicate sealing glass for SOFC Part II. Sealing and interfacial microstructure. Journal of Power Sources 170, 395-400, 2007.

[85] C. Lara, M. J. Pascual, and A. Durán, Chemical compatibility of RO-BaO-SiO_2 (R=Mg, Zn) glass-ceramic seals with SOFC components, Physics Chemistry of glasses: European Journal of Glass Science and Technology, B 48, 218-224, 2007.

[86] A. Hauch, S. D. Ebbesen, S. H. Jensen, and M. Mogensen, Solid oxide electrolysis cells: microstructure and degradation of the Ni/Yttria-stabilized zirconia electrode, Journal of the Electrohemical Society 155, B1184-B1193, 2008.

[87] S. P. Jiang, L. Christiansen, B. Hughan, and K. Foger, Effect of glass sealant materials on microstructure and performance of Sr-doped LaMnO3 cathodes, Journal of Materials Science Letters 20, 695-697, 2001.

[88] J. H. Lee, T. Mori, J. G. Li, T. Ikegami, M. Komatsu, and H. Haneda, Improvement of grain-boundary conductivity of 8 mol% Yttria-stabilized zirconia by precursor scavenging of siliceous phase, Journal of the Electrochemical Society 147, 2822-2829,2000.

[89] Y. S. Chou, J. W. Stevenson, and P. Singh, Effect of pre-oxidation and environmental aging on the seal strength of a novel high-temperature solid oxide fuel cell (SOFC) sealing glass with metallic interconnect, Journal of Power Sources 184, 238-244, 2008.

[90] Y. S. Chou, J. W. Stevenson, and P. Singh, Effect of aluminizing of Cr-containing ferritic alloys on the seal strength of a novel high-temperature solid oxide fuel cell sealing glass, Journal of Power Sources 185, 1001-1008, 2008.

[91] T. Rouxel, Elastic properties and short to medium range order in glasses, Journal of the American Ceramic Society 90, 3019-3039, 2007.

[92] E. V. Stephens, J. S. Vetrano, B. J. Koeppel, Y. Chou, X. Sun, and M. A. Khaleel, Experimental characterization of glass–ceramic seal properties and their constitutive implementation in solid oxide fuel cell stack models, Journal of Power Sources 193, 625-631, 2009.

[93] J. Malzbender, R. W. Steinbrech, and L. Singheiser, Determination of the interfacial fracture energies of cathodes and glass ceramic sealants in a planar solid-oxide fuel cell design, Journal of Materials Research 18, 929-934, 2003.

[94] J. Malzbender, J. Mönch, R. W. Steinbrech, T. Koppitz, S. M. Gross, and J. Remmel, Symmetric shear test of glass-ceramic sealants at SOFC operation temperature, Journal of Materials Science 46, 6297-6301, 2007.

[95] C. K. Lin, T. T. Chen, Y. P. Chyou, and L. K. Chiang, Thermal stress analysis of a planar SOFC stack, Journal of Power Sources 164, 238-251, 2007.

[96] K. A. Nielsen, M. Solvang, S. B. L. Nielsen, and D. Beeaff, Mechanical behaviour of glassy composite seals for IT-SOFC Application, Ceramic Engineering and Science Proceedings 27, 315-323, 2007.

[97] C. Lara, M. J. Pascual, R. Keding, A. Durán, Electrical behavior of glass–ceramics in the systems RO–BaO–SiO_2 (R = Mg, Zn) for sealing SOFCs, Journal of Power Sources 157, 377-384, 2006.

[98] Y. S. Chou, J. W. Stevenson, and L. A. Chick, Ultra-low leak rate of hybrid compessive mica seals for solid oxide fuel cells, Journal of Power Sources 112, 130-136, 2002.

[99] N. Caron, L. Blanchi, and S. Methout, Development of a functional ealing layer for SOFC applications, Journal of Thermal Spray Technology 17, 598-602, 2008.

CHAPTER TWO

THERMAL PROPERTIES AND DEVITRIFICATION OF $SrO\text{-}La_2O_3\text{-}Al_2O_3\text{-}B_2O_3\text{-}SiO_2$ BASED SEAL GLASS

Abstract

Thermal behaviors of glass/glass-ceramic based sealant materials are critical issues for high temperature solid oxide fuel/electrolyzer cells. $SrO\text{-}La_2O_3\text{-}Al_2O_3\text{-}B_2O_3\text{-}SiO_2$ glass system has desired thermal properties but its devitrivifation behavior is unknown. Al_2O_3 can retard devitrication of a seal glass. To understand the effect of Al_2O_3 content on the thermal properties and devitrification behavior of $SrO\text{-}La_2O_3\text{-}Al_2O_3\text{-}B_2O_3\text{-}SiO_2$ system, glasses were prepared by quenching method of $(25-X)SrO\text{-}20La_2O_3\text{-}(7+X)Al_2O_3\text{-}40B_2O_3\text{-}8SiO_2$ compositions, where X was varied from 0.0-10.0 mol% at 2.5 mol% interval. Thermal properties were characterized by differential scanning calorimetry and dilatometry. Microstructural studies were performed by scanning electron microscopy (SEM), energy dispersive spectroscopy (EDS), and X-ray diffraction (XRD). All the compositions have a glass transition temperature greater than 620°C, a crystallization temperature greater than 826°C, and coefficient of thermal expansion between 9.0-14.5$\times 10^{-6}$/°C. La_2O_3 and B_2O_3 contribute to glass devitrification by forming crystalline $LaBO_3$ but Al_2O_3 suppresses the devitrification. Significant improvement in devitrification resistance is observed as X increases from 0.0 mol% to 10.0 mol%.

2.1. Introduction

Glass and glass-ceramic seals materials should meet the following criteria to be suitable

as SOFC/SOEC seal. Coefficient of thermal expansion (CTE) should be between 9.0-12.0 × 10^{-6}/°C in order to match with that of other cell components, such as zirconia, stainless steel, and lanthanum manganite. Glass transition temperature (T_g) should be less than the cell operating temperatures (800-900°C), and glass softening temperature (T_s) should be high enough to avoid excessive glass flow at cell operation temperatures. Also, continuous and/or excessive devitrification of glass or glass-ceramic sealant should not occur; this requires that glass crystallization temperature (T_c) be much higher than the cell operation temperatures. Chemical stability should be sufficient to sustain reducing and oxidizing atmospheres at high temperatures for long periods of time (40,000 hours) without failure. In addition to the above demands, sealant must be electrically insulating.

Several silicate, borate, and borosilicate glass systems have been studied as solid oxide cell seals [1,2]. Among them, borosilicate glass systems are preferred because a wide range of T_g (480-740°C), T_s (600-750°C), and CTE (9.0-13.0 × 10^{-6}/°C) have been obtained, which are suitable for SOFC/SOEC seal [3-11]. BaO containing borosilicate sealants are the mostly reported one. For BaO containing borosilicate sealants, the main disadvantages arise from the formation of monoclinic celsian ($BaAl_2Si_2O_8$) and its polymorph hexacelsian devitrified phases and deleterious interfacial reactions with metallic interconnects at 750-800°C [7,8]. Celsian and hexagonal phases have low CTE with different values, 2.29 × 10^{-6}/°C and 8.0 × 10^{-6}/°C, respectively [7]. The amount of low CTE celsian phase increases with thermal treatment time until complete devitrification. As a result, the CTE of BaO-containing seal glasses decreases from ~ 11.5 × 10^{-6}/°C to ~ 7.5 × 10^{-6}/°C as shown in Fig. 2-1 [7]. In a different study, an increase in CTE by ~ 24% is observed for a BaO-borosilicate seal glass after 8 hours of thermal treatment

at 800°C due to the formation of BaB_2O_4 and $Ba_2Si_3O_8$ phases with higher CTEs [8]. The CTE difference between the devitrified phases and also with the interfacing cell components develops thermal stress which degrades performance. Because of these shortcomings, there is a need to search new glass systems as sealant materials. In alkaline earth oxide containing glasses, the CTE decreases with the field strength of glass modifier ions [12]. For example, the CTE of a BaO-MgO-silicate glass increases from 8.5 × 10^{-6}/°C to 12.0 × 10^{-6}/°C as BaO/MgO ratio increases from 0.67-4.0 because of the lower field strength of BaO [13,14]. High field strength modifier ions promote devitrification by phase separation [15]. For example, a multi-component glass containing SrO, CaO, ZnO, and TiO_2 devitrifies into $Ca_2ZnSi_2O_7$, $CaSrAl_2SiO_7$, $CaSrSiO_4$, Sr_2SiO_4, Zn_2SiO_4, $CaSiO_3$, and $SrSiO_3$ at 750-800°C [16]. Lower flowabilty of devitrified phases also degrades the sealing performance. MgO-borosilicate glasses form cordierite ($Mg_2Al_4Si_5O_{18}$) phase of very low CTE (2.0× 10^{-6}/°C); which is the main disadvantage [6].

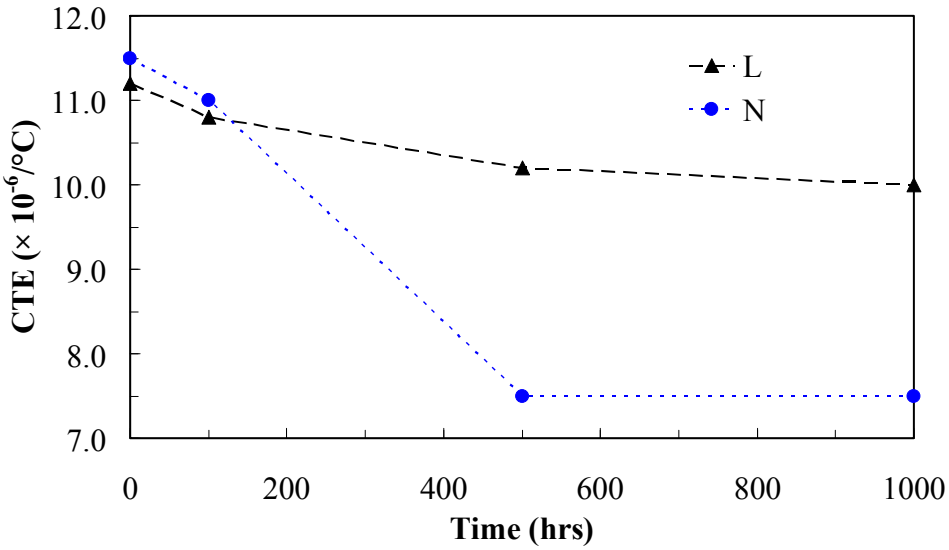

Fig. 2-1. CTE change due to devitrification of a BaO-Al_2O_3-B_2O_3-SiO_2 glass system with time at 800°C. L and N indicate 5 mol% La_2O_3 and 2 mol% Ni in the glass composition [7].

A SrO-La_2O_3-Al_2O_3-B_2O_3-SiO_2 glass system with desirable thermal properties has been reported [3] but the devitrification of this glass system has not been assessed. In this system, B_2O_3 and SiO_2 act as glass formers, La_2O_3 modifies viscosity [3], SrO modifies CTE [17], and Al_2O_3 retards devitrification [2,3].

In a silicate glass, Al_2O_3 participates in network formation when Al^{3+} ions exist as AlO_4^- tetrahedra if the concentration ratio of modifier oxides and Al_2O_3 is less than 0.5 for alkaline earth oxide [18]. Once the ratio is greater than 0.5, then Al^{3+} ions exist in AlO_6^- octahedra and Al_2O_3 acts as a glass network modifier [12]. Low field strength modifiers (such as Ba^{2+} and Sr^{2+}) favor the formation of AlO_4^- tetrahedra and high field strength modifier ions (such as Mg^{2+}) favor the formation of AlO_6^- octahedral for borate glass [19]. For borosilicate glass, modifier ions generally favor AlO_4^- tetrahedra formation [12]. In general, T_g and T_s increase if Al_2O_3 is a network former but decrease if Al_2O_3 is a network modifier. However, literature report is not available for the Al_2O_3 effect on T_g and T_s. CTE decreases when Al_2O_3 is a network former but increases when Al_2O_3 is a network modifier. For example, 1-2 mol% Al_2O_3 addition decreases CTE by ~ 1.5×10^{-6}/°C for silicate and borosilicate seal glasses [20,21].

To explore the potential of the SrO-La_2O_3-Al_2O_3-B_2O_3-SiO_2 glass system as a SOFC/SOEC sealant, the effect of Al_2O_3 contents on the thermal properties and the devitrification of the glass system is the focus of this chapter. Desired thermal properties for SOFC/SOEC seal such as T_g, T_s, and CTE have been obtained in 25SrO-20La_2O_3-7Al_2O_3-40B_2O_3-8SiO_2 composition and is chosen as base composition in this chapter. This study also suggests strategies for further optimization of the sealant glass composition.

2.2. Experimental procedure

2.2.1. Preparation of glass

Glass samples were prepared based on $(25-X)SrO\text{-}20La_2O_3\text{-}(7+X)Al_2O_3\text{-}40B_2O_3\text{-}8SiO_2$ compositions (SLABS), where X was varied from 0.0 mol% to 10.0 mol% at 2.5 mol% interval. The corresponding oxide powders were ball milled for overnight. The mixed powders were heated and melted in a platinum crucible at 1400°C for 4 hrs in a box furnace (Lindberg, Model No. 51314, Watertown, WI) at 10°C/min heating rate before being quenched into a graphite mold.

2.2.2. Differential scanning calorimetry

Differential scanning calorimetry (DSC) studies were conducted in a simultaneous TG-DTA/DSC apparatus (STA449C/3/G Jupiter, Netzsch Instruments Inc., Burlington, MA). The glass samples were thermally cycled three times at the same heating and cooling rates of 10°C /min up to 900°C and a dwell time of 2 hrs at 900°C for thermal behavior analysis. The T_g and T_c temperatures were determined from the DSC data.

2.2.3. Dilatometry

Softening temperature and CTEs of the glass samples from room temperature to 700°C were measured with a push-rod dilatometer (Model 1600R, The Edward Orton Jr. Ceramic Foundation, OH). This technique also provided another approach of measuring glass transition temperature. The samples were 27 mm in length and 5 mm in diameter. During the dilatometry study, the samples were heated to 700°C for 2 hrs and then cooled to room temperature at the

same heating and cooling rate of 3°C/ min. Each sample was thermally cycled three times under this condition.

2.2.4. Microstructural evolution

Microstructural studies were carried out in a field emission scanning electron microscope (SEM) (LEO 1550, Carl Zeiss MicroImaging, Inc, Thornwood, NY) for the as-quenched samples and the thermally cycled samples from the DSC experiments. Energy dispersive spectroscopy (EDS) (Helios 600 NanoLab, FEI, Hillsboro, OR) was used to analyze the compositions of the glass phase and the crystalline phase of the samples after the thermal cycling.

2.2.5. Phase analysis

X-ray diffraction (XRD) studies were carried out in an X'Pert PRO diffractometer (PANalytical B.V., EA Almelo, The Netherlands) to identify the devitrified phases in the thermally cycled samples. The scan rate was 0.0020° s^{-1} with CuK_{α} radiation (λ = 1.5406 Å) and a Ni filter.

2.3. Results and discussions

2.3.1. Glass transition and crystallization temperature

For the studied glass system, the DSC peak temperature was 900°C. Before 900°C, there are two heat flow changes on the DSC curves. One is endothermic and the other one is exothermic. The endothermic position indicates the glass transition temperature T_g and the exothermic position indicates the devitrification temperature T_c (Fig. 2-2).

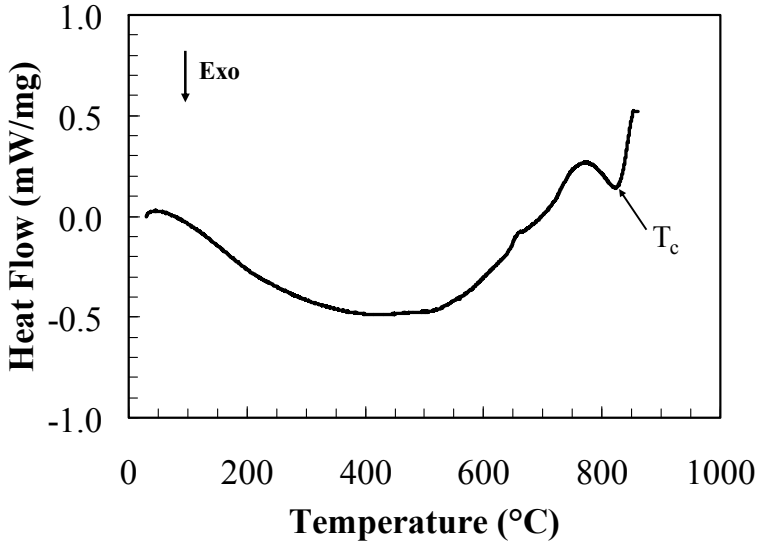

Fig. 2-2. DSC curve in the first heating cycle obtained for SLABS glass of X = 2.5 mol%

The T_g and T_c for all the glass compositions are extracted as given in Fig. 2-3. All the glasses have T_g greater than 620°C. T_g increases by 10°C as the Al_2O_3 content increases from 7.0 to 17.0 mol%. From Fig. 2-3, it can also be seen that T_c is 826 ± 1°C for X = 0.0-5.0 mol% and 850 ± 1°C for X = 7.5 -10.0 mol%.

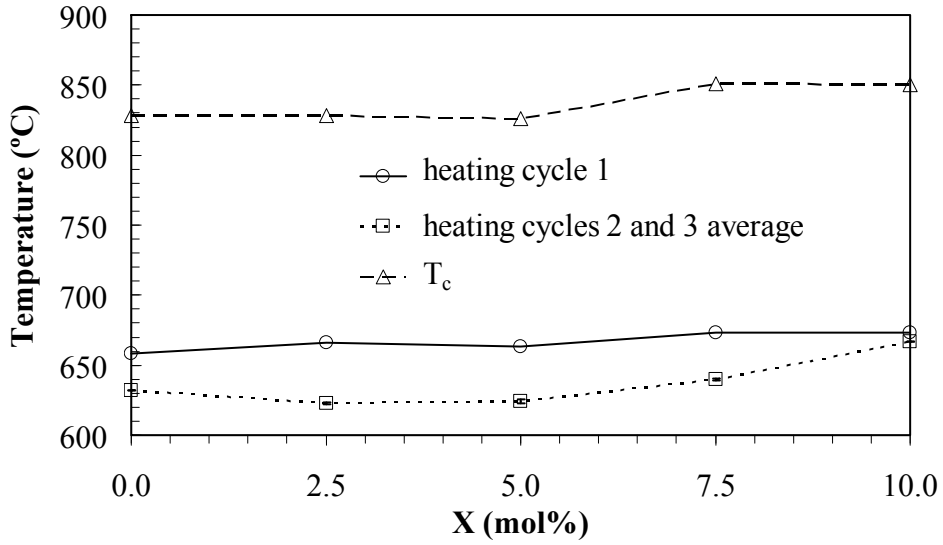

Fig. 2-3. T_g and T_c change vs Al_2O_3 content increase (X) from DSC experiments.

Al_2O_3 content has some effect on T_g and T_c but the impact is not significant. One important observation is that T_g decreases after the first heating cycle and remains the same for the remaining cycles. This T_g decrease after the first thermal cycle is most likely due to the devitrification of the glass matrix. It also indicates that the remaining glass phase after devitrification has a lower T_g. T_c reflects the temperature at which some of the glass transforms into one or more devitrified phases and is a direct representation of glass thermal stability. No T_c peaks are observed during the second and the third heating cycles in any of the studied compositions. This indicates that the glasses mainly devitrify during the first heating cycle.

2.3.2. Dilatometric softening temperature and thermal expansion coefficient

From the dilatometry study, the dilatometric softening point (T_d), glass transition temperature T_g' (in differentiation from the DSC glass transition temperature T_g), and CTE can be determined. The reading points for the T_d and T_g' are shown in Fig. 2-4. However, the $(25-X)SrO\text{-}20La_2O_3\text{-}(7+X)Al_2O_3\text{-}40B_2O_3\text{-}8SiO_2$ glass at X = 0.0 mol% has very limited glass forming ability. Transparent and crack free dilatometry sample could not be obtained even after six attempts of quenching. Consequently, no thermal expansion data are avialable for the X = 0.0 mol% composition. The dilatometry curve for the $(25-X)SrO\text{-}20La_2O_3\text{-}(7+X)Al_2O_3\text{-}40B_2O_3\text{-}8SiO_2$ glass at X = 2.5 mol% is shown in Fig. 2-4 and other compositions show similar trend.

In Fig. 2-4, it can be seen that the percent linear change curves shift downwards after each thermal cycle. This is due to a change in the sample length. Although no visual deformation is observed in the samples after the thermal cycles, the change in the sample dimension, however small it may be, may arise from the deformation of the glass under the compressive load applied

by the push rod. This artificially changes the absolute percent linear change value since the initial dimension was used in all the dilatometric calculation.

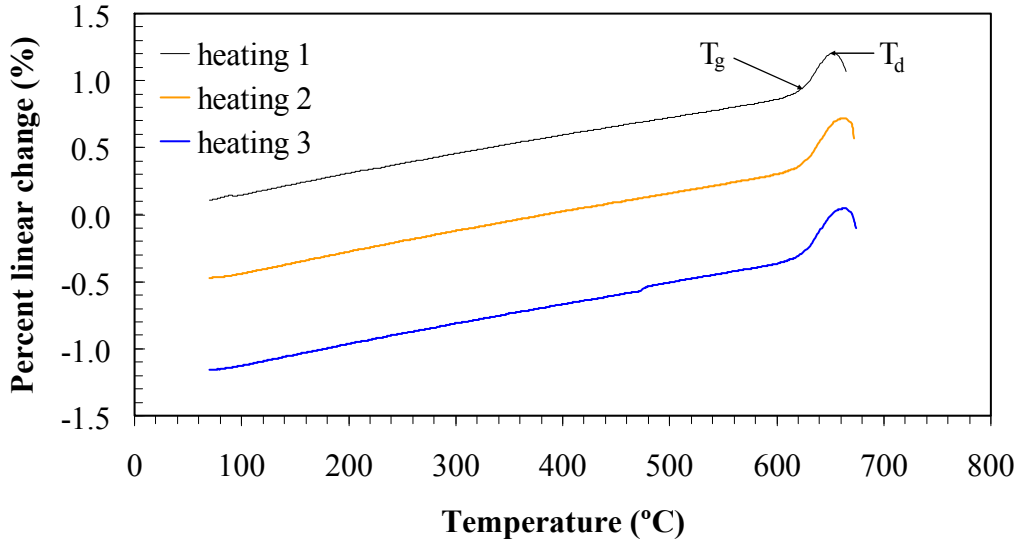

Fig. 2-4. Percent linear change (%) vs temperature for the (25−X)SrO-20La_2O_3-(7+X)Al_2O_3 40B_2O_3-8SiO_2 glass at X = 2.5 mol% from dilatometry.

T_d and T_g' changes vs. Al_2O_3 content are shown in Fig. 2-5. From Fig. 2-5, it can be observed that the softening temperature T_d is greater than 660°C for all the compositions. As X increases from 0.0 to 10.0 mol%, T_d increases from 661°C to 676°C. For all the thermal cycles, T_g' and T_d values and the differences between T_g' and T_d are very consistent. After the three thermal cycles, the physical appearance of the samples remains unchanged. This observation also indicates that the glass is stable up to at least 660°C. T_g' increases by 20°C with Al_2O_3 content increase from 2.5 to 10.0 mol%. This result is consistent with the DSC results (Fig. 2-3). However, the value of T_g' obtained from the dilatometry is about 30°C lower than that from the DSC experiments. The difference in T_g' and T_g from these different experimental methods has

been reported [7]. There are two possible reasons for this difference. First, the heating rates are different: 10°C/min in the DSC experiment and 3°C/min in the dilatometry. This may cause the difference in T_g' and T_g since glass transition temperature is thermal history dependent. Second, T_g' depends on the viscoelastic properties of the glass. In the dilatometry experiment, the samples were subjected to a compressive load by the push rod. This load may affect the viscoelasticity of the glass, shift the T_g' to lower temperatures, and thus cause difference in T_g' and T_g.

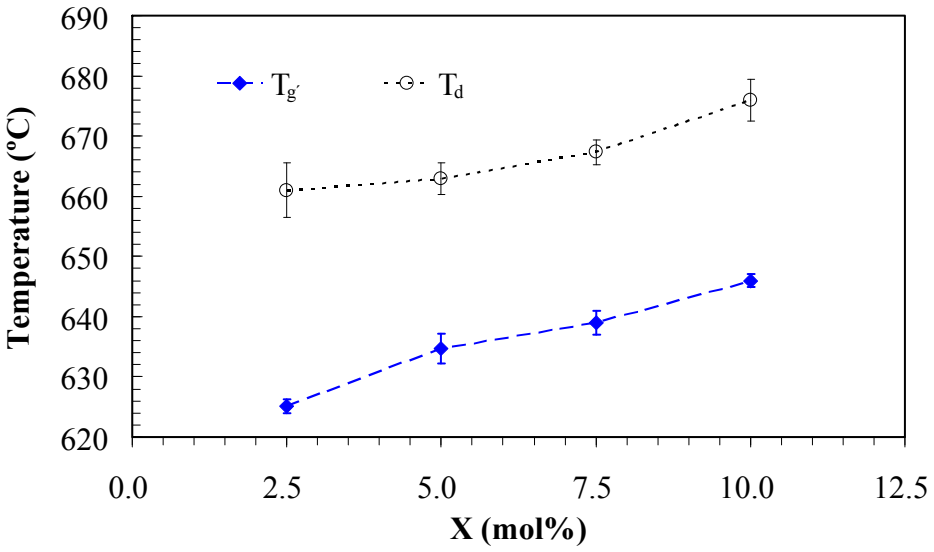

Fig. 2-5. T_g' and T_d change vs Al_2O_3 content increase (X) from dilatometry study.

CTE decreases with Al_2O_3 content increase X as shown in Fig. 2-6. Also, the CTE during the first thermal cycle is lower than those of the remaining thermal cycles at the temperatures below T_g'. After the first heating cycle, the CTEs remain consistent, demonstrated by the low CTE standard deviation. To illustrate the difference, Fig. 2-6 shows the CTE changes for the first thermal cycle and the remaining cycles. The CTE values obtained from the first heating cycle are

14.10 × 10^{-6}/°C at X = 2.5 mol%, 9.73 × 10^{-6}/°C at X = 5.0 mol%, 6.86 × 10^{-6}/°C at X = 7.5 mol% and 6.47 × 10^{-6}/°C at X = 10.0 mol%. Average CTE after the first heating cycle is 16.74 × 10^{-6}/°C for X = 2.5 mol%, 15.37 × 10^{-6}/°C for X = 5.0 mol%, 9.58 × 10^{-6}/°C for X = 7.5 mol%, and 9.30 × 10^{-6}/°C for 10.0 mol%. This difference in CTEs between the first and the remaining heating cycles may be explained as follows. The samples used in the dilatometry have been obtained by quenching. Structural rearrangement toward equilibrium glass state is incomplete as the glass melt quickly solidifies. Residual stress is likely to be created during the first thermal cycle. During the dilatometry measurements, the slower heating rate and the dwell time at the T_d remove the residual stress in the quenched glass. Since the cooling rate is also slower, no further thermal stress develops during cooling. Thus after the first heating cycle structural rearrangement of the glass is complete or nearly so. As a result, molar free volume of the sample decreases and CTE increases to a consistent value after the first heating cycle. This prediction is supported by the consistent CTEs in the annealed (25–X)SrO-20La_2O_3-(7+X)Al_2O_3-40B_2O_3-8SiO_2 sample at X = 7.5 mol% (Fig. 2-6).

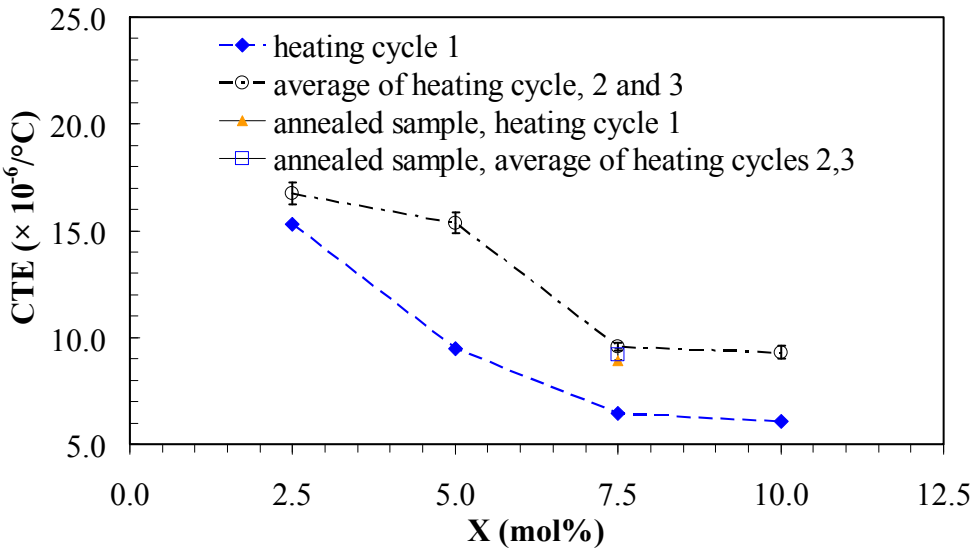

Fig. 2-6. CTE variation vs Al_2O_3 content increase (X) from dilatometry.

After the first thermal cycle, the CTEs of all the glass compositions are greater than 9.0 × 10^{-6}/°C and show good potential to match with the CTEs of other cell components [22]. Good thermal expansion match with other SOFC/SOEC components such as zirconia electrolyte and metallic interconnect [23], moderate T_g, and stability of these compositions are suitable as sealant materials below 800°C SOFC/SOEC operation temperatures.

2.3.3. Microstructural evolution

SEM images of the as-quenched glass samples are given in Fig. 2-7. No devitrified phase or phase separation is observed for any of the compositions, as supported by the XRD patterns to be shown in Fig. 2-10. The cracks observed in the SEM micrographs were created during SEM sample preparation. This means all the samples studied start with pure glass phase.

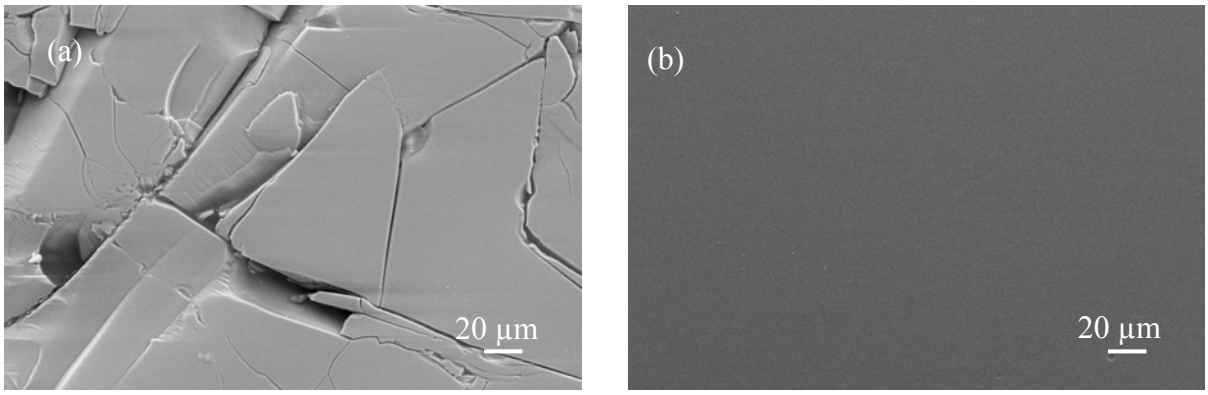

Fig. 2-7. SEM images of as-quenched glasses: (a) X = 0.0 mol%, and (e) X = 10.0 mol%.

The SEM micrographs of the samples after the DSC thermal cycling are given in Fig. 2-8. The dark phases are glass phase and the bright phases are crystalline phase. There are drastic microstructure differences among glass compositions ranging from X = 0.0 to 10 mol%. When the Al_2O_3 content is at X = 0.0 mol% (Fig. 2-8 (a)), irregular shaped, equiaxed devitrified appear

in the glass matrix. The sizes of the devitrified phases appear to be about 20 μm. When X increases to 2.5 mol% (Fig. 2-8(b)), elongated devitrified phases appear and have a dendritic morphology. Even though the short dimension of these elongated devitrified phases is less than 20 μm, the long dimension is mostly greater than 20 μm. When X increases to 5.0 mol% (Fig. 2-8(c)), the devitrified phases morphology becomes more needle-shaped. These needles form long strands that are separated by a small amount of glass phase. However, the size of individual devitrified phase is much smaller, mostly in the sub-micron to single micron range. When X is further increased to 7.5 mol% (Fig. 2-8(d)) and 10.0 mol% (Fig. 2-8(e)), the devitrified phases are only ~ 1 μm size, still with elongated shape. Sizes of the devitrified phases for X at 10.0 mol% are smaller than those for X at 7.5 mol%. More importantly, these devitrified phases uniformly distribute in the glass matrix. From the SEM observation, it demonstrates that Al_2O_3 is effective in suppressing glass devitrification. This means Al_2O_3 has the function of retaining the vitreous phase in the glass, preventing/delaying a glass matrix with large crystallites, and shifting the glass softening process to higher temperatures. Nevertheless, complete suppression of devitrified phases formation is not possible for the glass compositions studied. Also, Al_2O_3 content cannot be excessively increased for glass forming purpose.

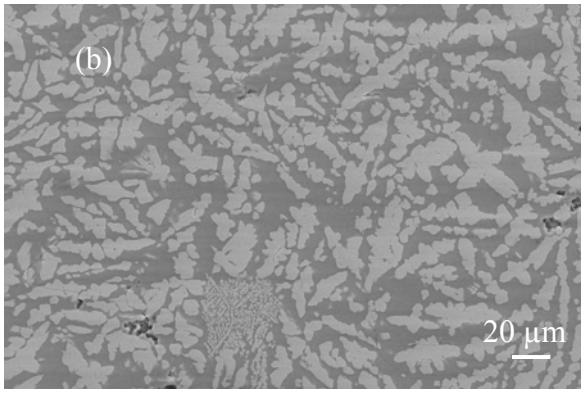

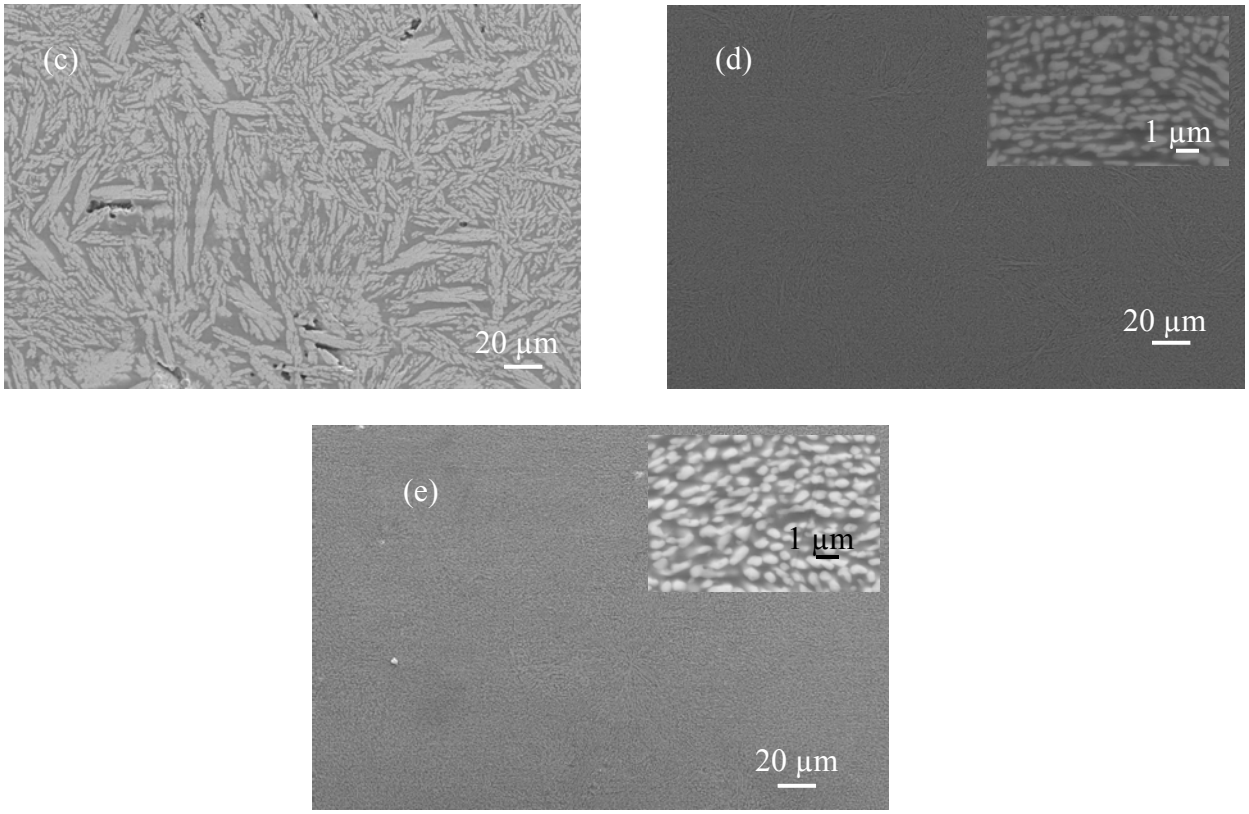

Fig. 2-8. SEM micrographs of thermally cycled glasses: (a) X = 0.0 mol%, (b) X = 2.5 mol%, (c) X = 5.0 mol%, (d) X = 7.5 mol%, and (e) X = 10.0 mol%.

2.3.4. Energy dispersive spectroscopy

The results of EDS are shown in Fig. 2-9 for the designed glass compositions, and the residual glass phase and the devitrified phase of the thermally cycled glasses. With the understanding that the EDS technique is not well suited for absolute quantification of sample compositions, the thermally cycled sample compositions are determined by using the as-quenched glass compositions as standard. The composition analysis obtained by this procedure is consistent as shown in Fig. 2-9. The larger standard deviation at high X values is a result of decreased size of the devitrified phases to the detection limit of the EDS technique.

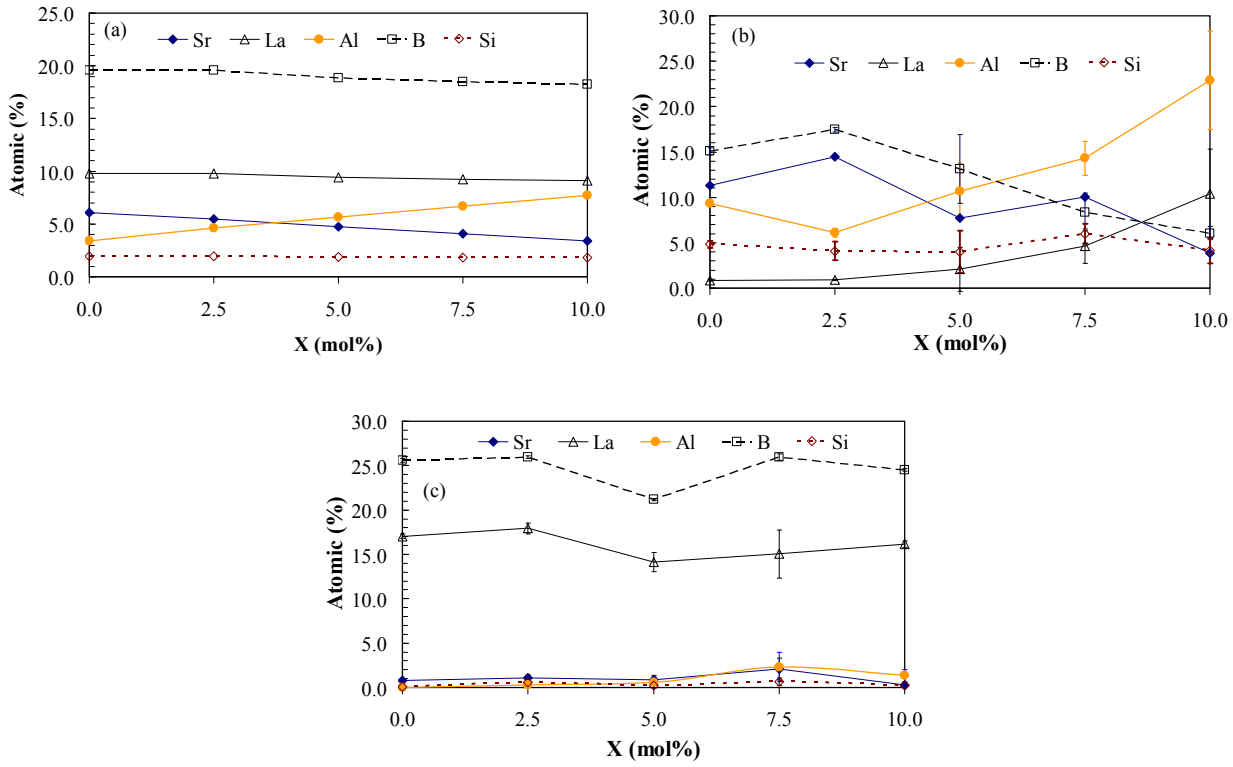

Fig. 2-9. Comparison of (a) the nominal compositions of the as-quenched glasses, (b) the glass phase compositions, and (c) the crystalline phase compositions of the DSC thermally cycled samples.

From Figs. 2-9(a) and (b), it can be seen that the composition of the glass matrix after thermal cycling is very different from that of the nominal composition of the as-quenched glass. The main difference is the substantially reduced La and B in the glass matrix after the thermal cycling. Significant increase in Sr, Al and Si contents is observed in the residual glass phase. The devitrified phase has the highest percent of B followed by La as shown in Fig. 2-9(c). Very small amount of Sr is also present. Small amounts of Al and Si concentrations in the crystalline phases are present except for X at 0.0 and 2.5 mol%. Since the crystalline phases are new compounds

that deviate from the simple mixture of original oxides, complete composition ratios in oxide format can not be obtained.

2.3.5. X-ray diffraction

The X-ray diffraction patterns of two as-quenched glass compositions (X = 0.0 mol% and 10.0 mol %) and the thermally cycled samples of all the glass compositions are shown in Fig. 2-10. For the as-quenched samples (Fig. 2-10(a)), no crystalline phase is detected. Since X = 0.0 mol% and X = 10.0 mol% covers the two limits of the glass compositions studied, this confirms the SEM observation (Fig. 2-7) that all the compositions start with pure glass phase. For the thermally cycled samples, devitrification is observed. From X = 0.0 mol% to 10.0 mol%, orthorhombic $LaBO_3$ is the main crystalline phase. At X = 0.0 mol%, small amount of orthorhombic SrB_2O_4 is identified. In other compositions, $Sr_2Al_2SiO_7$ is the minor phase. This observation also supports the EDS result about the presence of small amount of Sr, Al and Si. This means La_2O_3 and B_2O_3 devitrification into $LaBO_3$ is the main process during the thermal cycling. When the Al_2O_3 content is low (at X = 0 mol %), SrB_2O_4 crystallization cannot be effectively suppressed. SrO participates in devitrification at all conditions but the effect is small. Since Al and Si contents are higher in all other compositions except for X at 0.0 mol%, $Sr_2Al_2SiO_7$ is the minor phase in those compositions.

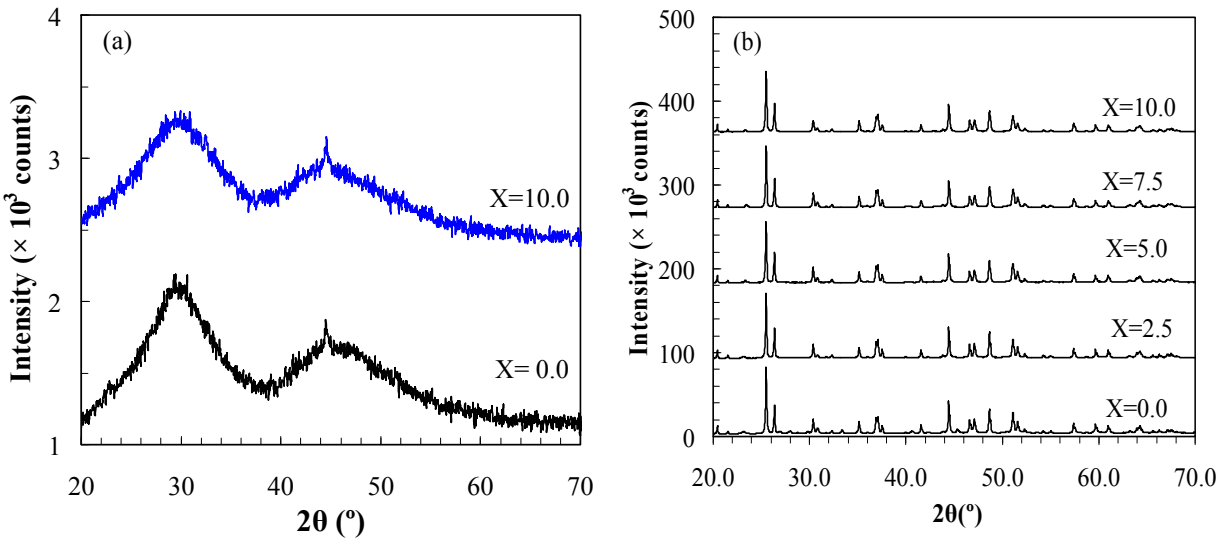

Fig. 2-10. X-ray diffraction patterns of (a) as-quenched and (b) thermally cycled samples.

The devitrification tendency of the studied glass system can be understood from the electrostatic bond strength point of view. The electrostatic bond strength of La^{3+} ion is 0.43 and Sr^{2+} ion is 0.27. La tends to separate from the parent glass phase due to its high electrostatic bond strength and bonds with trigonally-coordinated B to form $LaBO_3$ crystalline phase. Electrostatic bond strength of 0.27 for Sr^{2+} ion is a transition value for silicate glass. However, it can cause borate glass phase separation [26]. Since the glass compositions contain both B_2O_3 and SiO_2, Sr probably plays a minor role in phase separation. This assumption is supported by the presence of SrB_2O_4 crystal phase in minor amount for the composition of X = 0.0 mol% and very small amount of Sr in Fig. 2-9(c). Al^{3+} seems to display some unusual behavior. Inspite of the potential to have high electrostatic bond strength (0.5 in octahedral coordination and 0.75 in tetrahedral coordination), Al tends to be tetrahedrally-coordinated in the glass network [27]. This is supported by the enriched Al concentration in the residual glass phase and small concentration of Al in the crystalline phase in the thermally cycled samples (Fig. 2-9(b)). Absence of SrB_2O_4

phase and appearance of $Sr_2Al_2SiO_7$ phase in all the compositions except for X = 0.0 mol% indicate that there is a critical Al_2O_3 concentration to suppress the formation of SrB_2O_4. From XRD patterns it is also apparent that there is more minor phase in the composition of X = 0.0 mol% than in all other compositions. Based on these observations, La_2O_3 and B_2O_3 will be modified. B_2O_3 change should be made carefully because of its essential role in forming glass and increasing CTE. Although SrO participates in devitrification, reducing SrO will likely decrease CTE as seen from Fig. 2-6. From EDS and XRD analyses it indicates that Al_2O_3 should be lowered since it decreases CTE (Fig. 2-6) and forms minor phases at X = 10.0 mol%.

2.4. Conclusions

Seal glasses are synthesized based on $(25-X)SrO\text{-}20La_2O_3\text{-}(7+X)Al_2O_3\text{-}40B_2O_3\text{-}8SiO_2$ system and X has been varied from 0 to 10 mol%. All the compositions have glass transition temperatures T_g above 620°C and crystallization temperatures T_c above 826°C. Also, the glasses have thermal expansion coefficients CTE between 9.0 and 14.5×10^{-6}/°C after the first thermal cycle. Suitable increase of Al_2O_3 stabilizes the glass by suppressing devitrification. La_2O_3 and B_2O_3 contribute to devitrification by forming $LaBO_3$. The role of other oxides on the stability of this system is not significant.

References

[1] J. W. Fergus, Sealants for solid oxide fuel cells, Journal of Power Sources 147, 46-57, 2005.

[2] M. K. Mahapatra and K. Lu, Glass-based seals for solid oxide fuel/electrolyzer cells-A review, Materials Science and Engineering R, submitted, 2009.

[3] K. L. Ley, M, Krumpelt, R. Kumar, J. H. Meiser, and I. Bloom, Glass-ceramic sealants solid

for oxide fuel cells Part I. Physical properties, Journal of Materials Research 11, 1489-1493, 1996.

[4] S. Ghosh, A. D. Sharma, P. Kundu, and R. N, Basu, Glass-ceramic sealants for planar IT-SOFC: A bilayered approach for the joining electrolyte and metallic interconnect, Journal of the Electrochemical Society 155, B473-B478, 2008.

[5] Y. S. Chou, J. W. Stevenson, and P. Singh, Novel refractory alkaline earth silicate sealing glasses for planar solid oxide fuel cells, Journal of the Electrochemical Society 154, B644-B651, 2007.

[6] N. Lahl, K. Singh, L.Singheiser, K. Hilpert, and D. Bahadur, Crystallisation kinetics in AO Al_2O_3-SiO_2-B_2O_3 glasses (A = Ba, Ca, Mg), Journal of Materials Science 35, 3089-3096, 2000.

[7] S. B. Sohn, S. Y. Choi, G. H. Kim, H. S. Song, and G. D. Kim, Suitable Glass-ceramic sealant for planar solid oxide fuel cells, Journal of the American Ceramic Society 87, 254-260, 2004.

[8] K. D. Meinhardt, D. S. Kim, Y. S. Chou, and K. S. Weil, Synthesis and properties of a barium aluminosilicate solid oxide fuel cell glass-ceramic sealant, Journal of Power Sources 182,188-196, 2008.

[9] T. Yoshii, Sealing glass composition, sealing glass frit and sealing glass sheet, US Patent No. US 2006/0019813 A1 2006.

[10] K. D. Meinhardt, J. D. Vienna, T. R. Armstrong, and L. R. Pederson, , Glass-ceramic joint and method of joining, US Patent No. US 6532769 B1 2003.

[11] L. D. Bloom and K. L. Ley, Compliant sealants for solid oxide fuel cells and other ceramics, US Patent No. 5453331 1995.

[12] J. E. Shelby, Introduction to glass science and technology, 2nd edition, The Royal Society of

Chemistry, Cambridge, UK, 2005.

[13] C. Lara, M. J. Pascual and A. Durán, Glass-forming ability, sinterability and thermal properties in the systems RO–BaO–SiO_2 (R = Mg, Zn), Journal of Non-Crystalline Solids 348, 149-155, 2004.

[14] C. Lara, M. J. Pascual, M. O. Prado and A. Durán, Sintering of glasses in the system RO Al_2O_3-BaO-SiO_2 (R=Ca,Mg,Zn) studied by hot-stage microscopy, Solid State Ionics 170, 201-208, 2004.

[15] P. Taylor, A. B. Campbell, and D. G. Owen, Liquid immiscibility in the systems X_2O-MO B_2O_3-SiO_2 (X = Na, K; M = Mg, Ca, Ba) and Na_2O-MgO-BaO-B_2O_3-SiO_2, Journal of the American Ceramic Society 66, 347-351, 1983.

[16] S. T. Reis and R. K. Brow, Designing sealing glasses for solid oxide fuel cells, Journal of Materials Engineering and Performance 15, 410-413, 2006.

[17] M. B. Volf, Chemical approach to glass. Glass Science and Technology Elsevier, Amsterdam 1984.

[18] J. H. Jean, T.H. Kuan, and T. K. Gupta, Crystallization inhibitors during sintering of pyrex borosilicate glass, Journal of Materials Research 8, 356-363, 1993.

[19] J. H. Jean, S.C. Lin, and S. L. Yang, Effect of alumina on crystallization of low-dielectric lead borosilicate glass, Japanese Journal of Applied Physics 34, L422-L424, 1995.

[20] H. Scholze, Glass nature, structure, and properties, Springer Verlag, New York, USA, 1991.

[21] B. C. Bunker, R. J. Kirkpatrick, R. K. Brow, G. L. Turner, and C. Nelson, Local structure of alkaline-earth boroaluminate crystals and glasses: II, ^{11}B and ^{27}Al MAS NMR spectroscopy of alkaline-earth boroaluminate glasses, Journal of the American Ceramic Society 74, 1430-1438, 1991.

[22] M. Budd, Glass ceramic material and its use as means for joining different types of material and as support, European patent No. EP 0975554B1, 1998.

[23] M. Budd, Barium lanthanum silicate glass-ceramics. US Patent No. 7189668B2, 2007.

[24] R. N. Singh, Sealing technology for solid oxide fuel cells (SOFC), International Journal of Applied Ceramic Technology 4, 134-144, 2007.

[25] C. Story, K. Lu, W. T. Reynolds Jr., and D. Brown, Shape memory alloy/glass composite seal for solid oxide electrolyzer and fuel Cells, International Journal of Hydrogen Energy 33, 3970-3975, 2007.

[26] S. Block and E. M. Levin, Structural interpretation of immiscibility in oxide systems: II, coordination principles applied to immiscibility, Journal of the American Ceramic Society, 40 113-118, 1957.

[27] E. M. Levin and S. Block, Structural interpretation of immiscibility in oxide systems: III, effect of alkalis and alumina in ternary systems, Journal of the American Ceramic Society 41, 49-54, 1958.

CHAPTER THREE

NETWORK STRUCTURE AND THERMAL BEHAVIOR OF SrO-La_2O_3-Al_2O_3-B_2O_3 SiO_2 GLASS SYSTEM –EFFECT OF B_2O_3/SiO_2 RATIO

Abstract

Desirable thermal properties have been obtained in SrO-La_2O_3-Al_2O_3-B_2O_3-SiO_2 -based seal glasses. La_2O_3 and B_2O_3 in this system promote devitrification which degrades the thermal stability of a seal glass. A series of composition is designed with low La_2O_3 and B_2O_3 content with varying B_2O_3:SiO_2. The thermal properties and the devitrification behavior were investigated for all the compositions. The network structure evolution of the glasses with increasing B_2O_3:SiO_2 ratio was studied using Raman spectroscopy and nuclear magneto resonance spectroscopy to understand the role of B_2O_3 on the thermal properties and thermal stability. Glass network connectivity as well as silicon and boron glass former coordination was calculated for different B_2O_3:SiO_2 ratios. The study shows that high B_2O_3 content induces BO_4 and SiO_4 structural unit ordering, increases micro-heterogeneity and the amount of non-bridging oxygen; which decrease glass network connectivity. Correspondingly, the T_g of the SrO-La_2O_3-Al_2O_3-B_2O_3-SiO_2 glasses changes from 635°C to 775°C and the T_d changes from 670°C to 815°C with decreasing B_2O_3 content. Glass thermal stability decreases with B_2O_3:SiO_2 ratio increase. The glass without B_2O_3 is thermally stable and has the desired thermal properties.

3.1. Introduction

Desirable thermal properties such as glass transition temperature T_g, glass softening

temperature T_s, and thermal expansion coefficient CTE have been obtained in several seal glass systems as well as in SrO-La_2O_3-Al_2O_3-B_2O_3-SiO_2 (SABS) based seal glasses [1-6]. However, the thermal stability is a persistent problem for any seal glass. In chapter one, the advantages of the SABS based seal glasses than the other seal glass systems have been discussed. B_2O_3 is added in a seal glass to modify the thermal properties such as T_g, T_s, and CTE. T_g and T_s decreases 50-100°C with increasing B_2O_3:SiO_2 ratio in a BaO-MgO-borosilicate seal glass [3] as shown in Fig. 3-1 for example. The decrease in T_g and T_s can be understood by the low T_g of pure B_2O_3 glass and the presence of planar boroxyl groups in the network structure [7]. CTE increases 1.0-2.0 $\times$ 10^{-6}/°C with increase in B_2O_3/SiO_2 ratio [4,8]; which can be understood by the asymmetric structure of borate structural units [7]. However, opposite trend of the thermal properties with B_2O_3 addition have been also reported. For a MgO-BaO-silicate seal glass, T_s increases by 50-100°C when 0.2-0.5 wt% B_2O_3 is added [9]. For a BaO-silicate glasses, 10-30 mol% B_2O_3 addition decreases CTE by 1.0-3.0 $\times$ 10^{-6}/°C [3]. The reasons for the observed anomalies are related to the glass network structure but have not been investigated.

Thermal stability of a seal glass is defined as the resistance to devitrification. Devitrification of a seal glass is undesirable because of the glass property change it incurs, degrades thermal stability, and lowers the flowability. Localized stresses due to the CTE difference between the devitrified phase(s) and the glass phase are of most concern. For example, pores and cracks form in a BaO-CaO-borosilicate glass after thermal treatment at 850°C for 1 hr followed by 4 hrs at 750°C because of the CTE difference between the devitrified phases and the glass phase [10]. Subsequently, the performance of the seal glass degrades. Unfortunately, thermal stability is not well defined so far. Qualitatively, higher temperature and longer time required for a glass to devitrify mean higher thermal stability.

The thermal stability of a borosilicate seal glass degrades due to coexistence of several different types of structural units that induces heterogeneity in the network structure [11-14]. The thermal stability of a borosilicate glass decreases with increasing B_2O_3/SiO_2 ratio as can be seen in Fig. 3-1 for a MgO-BaO-borosilicate glass [3]. In this context, composition-structure-property relationships of a seal glass need to be understood to obtain desired thermal properties and stability. Moderate T_g, T_s, and CTE have been obtained in the SABS glasses studied in chapter two. However, La_2O_3 and B_2O_3 contribute to devitrification by forming $LaBO_3$ and degrade the thermal stability of the SABS glass system [15]. Also, B_2O_3 may evaporate in the form of volatile HBO_2 and $B(OH)_3$ species in the presence of water steam at cell operating temperature [16-18]. In this chapter, the effect of B_2O_3:SiO_2 in SABS glass system are studied at the network structure level in order to improve the thermal properties and stability of the glass system.

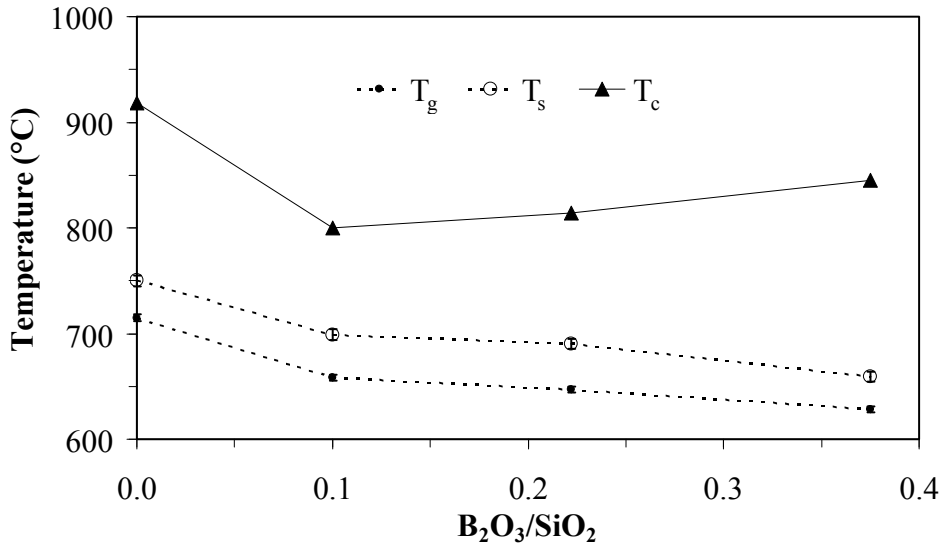

Fig. 3-1. T_g, T_s, and T_c change with B_2O_3/SiO_2 ratio in a BaO-MgO-borosilicate glass [3].

Raman spectroscopy is a technique that can identify the structural units present in a glass [19-21]. For chalcogenide glasses, Raman scattering played a pivotal role in elucidating the molecular structures and identifying domains of intermediate phases [22]. Raman spectra from Na_2O-CaO-MgO-$A1_2O_3$-SiO_2 system were interpreted in terms of structural alteration as the composition was altered from the binary end members to more complicated glasses [23]. Addition of CaO and MgO to Na_2O-SiO_2 glasses acted only to increase the disorder of the network slightly. Addition of $A1_2O_3$ greatly modified the network. In the $Na_2O{\cdot}R_2O_3{\cdot}SiO_2$ (R = A1, B) system, Raman spectroscopy showed that B_2O_3 induces destruction of the Q^3 species and creation of highly charged Q^2 and Q^1 species, as well as fully connected Q^4 silicate units [24].

Nuclear magnetic resonance (NMR) spectroscopy has been used to analyze glass structure differences. The temporal evolution of the coordination environments of boron atoms in borosilicate glasses was studied. The temperature dependence of boron speciation was found to be the most important source for the production of configurational entropy in these glasses, signifying a direct link between structure, configurational entropy, and viscous flow [25]. The structure of BeO-SiO_2 glasses with up to 20 mol% BeO was studied with ^{9}Be and ^{29}Si NMR spectroscopic techniques. The NMR results showed nano-clusters of corner-shared BeO_4 and highly strained corner-shared SiO_4 network [26]. Distributions of aluminum among the structural units in CaO-Al_2O_3-SiO_2 and MgO-Al_2O_3-SiO_2 glasses were investigated by ^{29}Si and ^{27}Al magic angle spinning (MAS) NMR. Taking the convention that the silicate units with four bridging oxygen atoms, three bridging oxygen atoms, two bridging oxygen atoms, one bridging oxygen atom, and zero bridging oxygen atom are denoted as Q^4, Q^3, Q^2, Q^1 and Q^0, respectively, the results indicated that aluminum is largely in Q^4 sites, except in Al-rich glasses where it is also in Q^3 sites [27]. ^{17}O enriched calcium and potassium aluminoborosilicate glasses were studied by

^{11}B, ^{27}Al, and ^{17}O NMR [11]. Dramatic differences in boron and oxygen speciation demonstrate a large effect of the modifier cations on glass former mixing behavior and stabilization of non-bridging oxygen atoms.

This chapter is focused on understanding the relations between the network structure and thermal properties and thermal stability of the SABS glass system. To examine the SABS glass structural evolution with B_2O_3:SiO_2 ratio change, Raman spectroscopy and MAS NMR studies have been carried out. Structural evolution data obtained from NMR and Raman spectroscopy, two complementary methods for giving detailed information about borosilicate glass structure, provide the best knowledge about the devitrification resistance of the studied SABS glass system. Raman spectroscopy gives information on glass structural unit types, ordering, and distribution whereas NMR gives access to the BO_3/BO_4 ratio and to the identification of different structural units' environment. Glass network connectivity and coordination have been calculated for different SABS glasses. Thermal properties of the glasses, including T_g, dilatometric softening temperature T_d, and CTE have been obtained from dilatometry. To understand the glass thermal stability, X-ray diffraction (XRD) analysis was used. The key aspects regarding glass structure are network connectivity and homogeneity, which directly affect the thermal properties and thermal stability of a glass. Connectivity in a glass structure is described by the number and arrangement of bridging and non-bridging oxygen atoms which link the structural units to their neighbors. Glass homogeneity is directly related to the distribution of different structural units and modifiers. If there is heterogeneity, such as structural unit ordering or distribution preference in a glass, even if in small localized regions, glass can devitrify easily [7]. The correlation between the glass network structure and the thermal properties and thermal stability is established.

3.2. Experimental procedure

3.2.1. Glass preparation

SABS glass samples were prepared with conventional quenching method. $SrCO_3$ (99.9%, Sigma Aldrich, St. Louis, MO), La_2O_3 (99.98%), Al_2O_3 (99.95%), B_2O_3 (99.98%), and SiO_2 (99.8%) (all oxides from Alfa Aesar, Ward Hill, MA) at designed ratios were mixed in a ball mill for overnight. The mixed powders were heated in a platinum crucible in a box furnace (Lindberg, Model No. 51314, Watertown, WI) to 1100°C and kept there for 1 hr for $SrCO_3$ to decompose. After that, the mixture was heated to 1400°C for 4 hrs. The heating rate was 10°C/min. The molten glass was quenched into a graphite mold.

All the glass compositions had 40 mol% of SrO, La_2O_3, and Al_2O_3 at fixed $SrO:La_2O_3:Al_2O_3$ ratios. The total amount of B_2O_3 and SiO_2 was 60 mol%. $B_2O_3:SiO_2$ ratio was varied from 0 to 1.4. The compositions were abbreviated as SABS-0, SABS-5, SABS-10, SABS-15, and SABS-35 in this study. The numbers represent the mol% of B_2O_3 in each composition.

3.2.2. Raman spectroscopy

For network structure analysis of the SABS glass compositions, quenched glass samples were polished to optical finish. Raman spectra of the polished samples were collected in 200-1600 cm^{-1} wave number range using a Raman spectrometer (JY Horbia LabRam HR 800, Horiba Ltd., Japan) with a CCD detector and a Labspec software package. The light source was a 514.57 nm argon laser at 50 mW power and 400 s exposure time. The spectra were later corrected for background noise and temperature effect [28]. For data analysis, the Raman spectra were fitted to Gaussian bands without any restrictions to deconvolute the superimposed Raman peaks [29,30].

Curve fitting was done with GRAMS/AI (7.02) software (Themo Fisher Scientific, Inc. Waltham, MA).

3.2.3. NMR spectroscopy

The ^{11}B, ^{29}Si, and ^{27}Al MAS NMR spectra of the SABS glass samples were collected with Bruker MAS probes and a Bruker Avance 500 spectrometer equipped with a widebore ultrashield magnet operating at a Larmor frequency of 160.4, 99.5, and 130.3 MHz for ^{11}B, ^{29}Si, and ^{27}Al, respectively. The applied magnetic field was 11.7 T. ^{11}B and ^{27}Al MAS NMR spectra were collected with a 4 mm-probe. Crushed SABS glass samples were spun in Si_3N_4 and ZrO_2 rotors at 15 kHz. All ^{11}B and ^{27}Al MAS spectra were collected using non-selective rf pulses with 15° tip angle and a recycle delay of 2 s. Approximately 500 to 1000 free induction decays were averaged to obtain each spectrum. The ^{11}B and ^{27}Al chemical shifts were externally referenced to 0.1 M $Na_2B_4O_7$ solution at 9.8 ppm and to 1 M $AlCl_3$ solution at 0 ppm, respectively. For ^{29}Si MAS NMR experiments the crushed glass samples were spun in a ZrO_2 rotor with a 7 mm Bruker MAS probe. The spectra were collected using rf pulses with 60º tip angle and a recycle delay of 30 s. Approximately 4000 free induction decays were averaged to obtain each spectrum. ^{29}Si chemical shifts were externally referenced to tetramethyl silane (TMS) at 0 ppm.

3.2.4. Thermal property measurement

Glass transition temperature T_g, dilatometric softening temperature T_d, and thermal expansion coefficient CTE were measured with a push-rod dilatometer (Model 1600R, The Edward Orton Jr. Ceramic Foundation, OH). Cylindrical samples of 27 mm long and 5 mm diameter were used. During the dilatometry study, the samples were heated at 3°C/min heating rate to 900°C for 2 hrs and then cooled to room temperature at the same rate. Each sample was

thermally cycled three times under this condition. Average T_g, T_d, and CTE values were obtained from both the heating and the cooling cycles [15].

3.2.5. Phase analysis

For thermal stability study, bulk SABS glass samples were put on a platinum foil and heated to 850°C at the same heating and cooling rate of 5°C/min. The samples were thermally treated at 850°C for 50-200 hrs. The bulk glass samples were crushed to fine powders for XRD study. XRD studies were carried out in an X'Pert PRO diffractometer (PANalytical B.V., EA Almelo, The Netherlands) to identify the crystalline phases in the thermally treated samples. The scan rate was 0.0020°/s with CuK_α radiation (λ = 1.5406 Å) and a nickel filter.

3.3. Results and Discussions

3.3.1. Glass network structure

3.3.1.1. Glass structural unit local ordering

Thermal properties of a glass depend on the presence of network level structural units, their relative arrangement, and the amounts of bridging and non-bridging oxygen atoms [31]. This is because these structural parameters determine the glass network connectivity. To understand the bonding structure of the SABS glasses, Raman spectroscopy results are shown in Fig. 3-2.

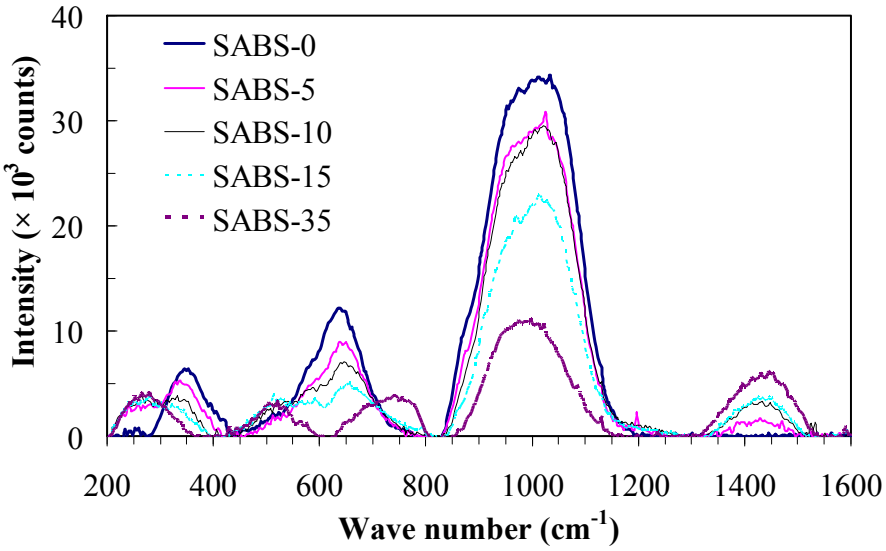

Fig. 3-2. As collected Raman spectra of different SABS glasses.

The Raman spectra of the SABS glasses can be first examined in a general term. In high wave number region (1300-1600 cm^{-1}), the structural units detected are only from B_2O_3 [29]. Both peak width and intensity increase with B_2O_3 content. The peak width increase means decreased local ordering of the B_2O_3-related structural units. The peak intensity increase means that the relative percent of the B_2O_3-related structural units increases. In 800-1200 cm^{-1} wave number region, the spectra contain both B_2O_3 and SiO_2 structural units; the intensity and width of the Raman peaks decrease as the B_2O_3 content increases. The decreased peak width indicates increased local ordering of the B_2O_3-related and the SiO_2-related structural units with B_2O_3 content. The decreased peak intensity means the relative percent of the B_2O_3-related structural units and the SiO_2-related structural units decreases. In 400-800 cm^{-1} wave number region, the spectra contain both B_2O_3 and SiO_2 structural units; the peak width increases but the peak intensity decreases with B_2O_3 content. This indicates that the B_2O_3 and SiO_2 structural units in this region have less local ordering and the relative percents of the B_2O_3-related structural units

and the SiO_2-related structural units decrease. In this region, a tendency of peak splitting is also seen with increasing B_2O_3 content. In lower than 400 cm^{-1} wave number range, the vibration modes are due to complicated twisting and torsion of the silicate networks and motion of the modifier cations. In vitreous silica, continuum is observed below 400 cm^{-1} wave number region [32]. In the SABS glass, distinct peaks are observed. This is believed to be caused by random distribution of tetrahedral structural units and Si-O-Si bond angles, as well as the structural units from the glass modifiers SrO and La_2O_3 [33]. The peaks shift to lower wave numbers as B_2O_3 content increases, indicating the increasing effect of the modifier species on the SABS glass network structure. However, detailed data on the bonding characteristics between the glass formers (SiO_2 and B_2O_3) and glass modifiers (SrO and La_2O_3) are beyond the scope of the current study.

To analyze the network structure of the SABS glasses, it is beneficial to examine silicate glass and borate glass structures first. In silicate glass, there are four major peaks representing the nature and contribution of different silicate structural units. The 1050-1100 cm^{-1} region describes the stretching motion of disilicate composition with three bridging oxygen atoms. The 950-1000 cm^{-1} peak describes the stretching motion of metasilicate composition with two bridging oxygen atoms. The 900 cm^{-1} peak reflects the pyrosilicate composition with one bridging oxygen atom. The 850 cm^{-1} peak represents orthosilicate composition with zero bridging oxygen atoms [20]. In this context, the silicate units with four bridging oxygen atoms, three bridging oxygen atoms, two bridging oxygen atoms, one bridging oxygen atom, and zero bridging oxygen atom can be denoted as Q^4, Q^3, Q^2, Q^1 and Q^0 respectively. The 400-700 cm^{-1} peak is due to the delocalized vibration of Si-O-Si bonding from mixed stretching and bending modes [24]. In borate glass, the 1300-1600 cm^{-1} peak describes the $B\text{-}O^-$ (O^- denotes the non-

bridging oxygen) stretching mode with chain and ring metaborates which also connect the network [21]. Based on the above understanding, peaks in different wave number ranges of the SABS glass spectra can be identified. However, individual peaks corresponding to different structural units have a tendency to overlap due to a high degree of disorder (peak widening). Also, wave number peak shift occurs for such complex glass systems [31,32]. To establish the correlation between the Raman peaks and specific glass structural units, the spectrum for each SABS glass sample needs to be deconvoluted. The deconvoluted spectra for different SABS glass compositions in the 400-1600 cm^{-1} range are given in Fig. 3-3. With the understanding that the composition difference between the conventional silicate glass and the SABS glasses can cause some peak shift, individual de-convoluted peaks can be identified. In this study, detailed Raman spectrum analysis can be separated into three wave number regions: 1200-1600 cm^{-1}, 800-1200 cm^{-1}, and 400-800 cm^{-1}, as outlined previously.

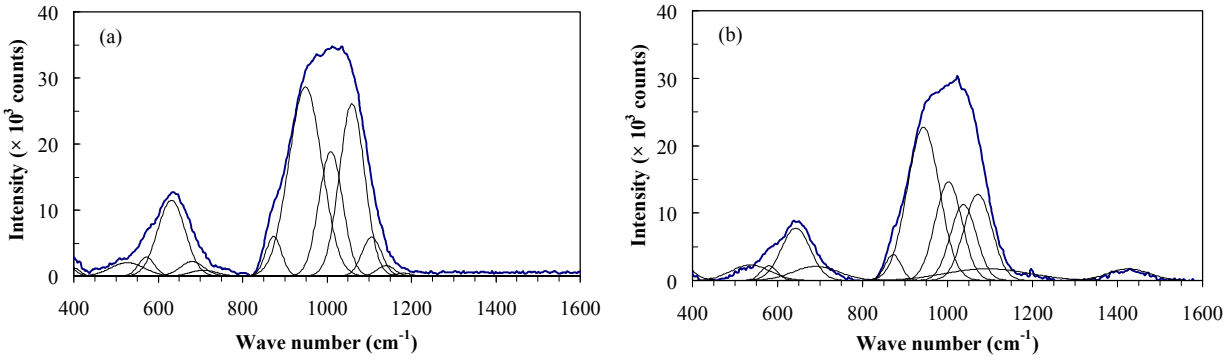

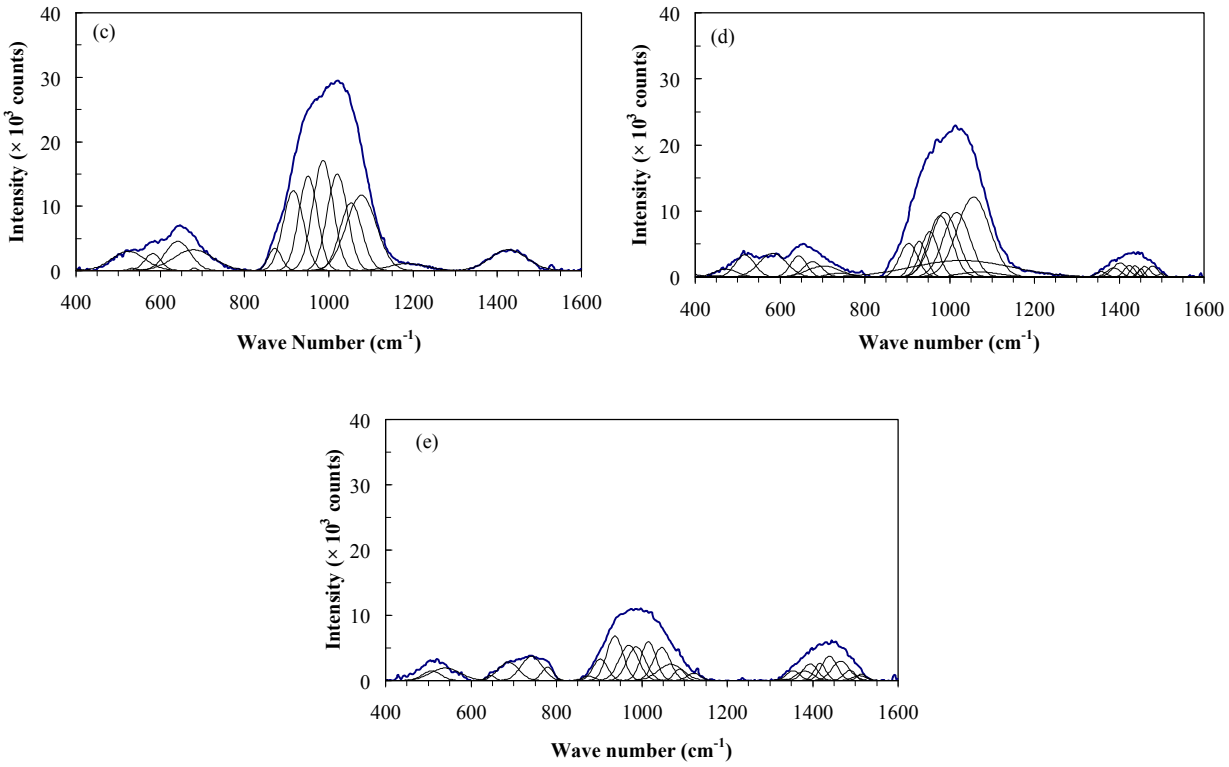

Fig. 3-3. Deconvoluted Raman spectra for: (a) SABS-0, (b) SABS-5, (c) SABS- 10, (d) SABS15, and (e) SABS-35 glasses.

For the SABS-0 glass, no peaks are detected in the 1300-1600 cm^{-1} wave number range, corresponding to the Raman peaks from B_2O_3. This is because the SABS-0 glass is B_2O_3 free. For the SABS-5 and SABS-10 glasses, the 1426 cm^{-1} peak is identified to be from the metaborate units [34]. For the SABS-15 glass, multiple peaks are identified after Raman peak deconvolution. The presence of 1387 cm^{-1} and 1357 cm^{-1} peaks indicate the $B\text{-}O^-$ vibrations in a large borate network [21]. The peaks at 1424 cm^{-1}, 1452 cm^{-1}, 1460 cm^{-1}, 1479 cm^{-1}, and 1501 cm^{-1} can be assigned to the metaborate units and localized stretching vibration modes of $B\text{-}O^-$ bonds as for the 1426 cm^{-1} peak in the SABS-5 and SABS-10 glasses. The two peaks at 1402 cm^{-1} and 1438 cm^{-1} cannot be identified. In the SABS-35 glass, the peaks at 1354, 1382, and 1394

cm^{-1} can be assigned to the splitted 1380 cm^{-1} peak identified for the $B\text{-}O^-$ vibrations [21]. The peaks at 1466 cm^{-1}, 1487 cm^{-1}, 1510 cm^{-1}, and 1514 cm^{-1} can be assigned to localized stretching vibration of the $B\text{-}O^-$ bonds which would be at 1468 cm^{-1}, 1475 cm^{-1}, and 1490 cm^{-1} wave numbers [24,28]. The 1330 cm^{-1}, 1417 cm^{-1}, and 1443 cm^{-1} peaks cannot be identified. Also, the high wave number Raman peak intensity increases with B_2O_3 content increase. From this analysis, it can be concluded that B_2O_3 progressively participates in the SABS network structure [24] the relative amount of non-bridging oxygen atoms increases and the glass network becomes less connected with B_2O_3 content increase.

For the de-convoluted peaks in the 800-1200 cm^{-1} wave number range, it can be understood as follows. For the SABS-0 glass, the weak 1180 cm^{-1} and 1143 cm^{-1} peaks correspond to the splitted 1060-1200 cm^{-1} peak in vitreous silica when peak shifting is considered [35]. These peaks describe the four bridging oxygen atom Q^4 units. The 1060 cm^{-1} and 1105 cm^{-1} peaks are from the three bridging oxygen atom Q^3 units. The 1010 cm^{-1} and 949 cm^{-1} peaks are from the two bridging oxygen atom Q^2 units. The 872 cm^{-1} peak is from the Q^0 units. For the SABS-5 glass, no Q^4 glass network units are detected. The 1037 cm^{-1}, 1072 cm^{-1}, and 1094 cm^{-1} peaks are from the Q^3 units. The 943 cm^{-1} and 1003 cm^{-1} peaks are from the Q^2 units. The 872 cm^{-1} peak is from the Q^0 units. In the SABS-10 glass, the peak at 1188 cm^{-1} is from the diborate or pyroborate units [21]. The peaks at 1053 cm^{-1} and 1077 cm^{-1} are from the Q^3 units. The peaks at 951 cm^{-1}, 986 cm^{-1}, and 1020 cm^{-1} are from the Q^2 units. The peak at 916 cm^{-1} is from the Q^1 units. The 872 cm^{-1} peak is from the Q^0 units. For the SABS-15 glass, the 1056 cm^{-1} peak is from the Q^3 units. The 953-1028 cm^{-1} peaks are from the Q^2 units. The 929 cm^{-1} peak is from the $Si(OAl)_3$ units with one bridging oxygen atom [36]. The 904 cm^{-1} peak is from the Q^1 units. For the SABS-35 glass, the 1122 cm^{-1} peak is attributed to the diborate units. The

1068 cm^{-1} and 1089 cm^{-1} peaks are attributed to the Q^3 units. The 970-1047 cm^{-1} peaks are attributed to the Q^2 units. The 937 cm^{-1} peak represents orthoborate or B-O-Si stretching mode [19]. The 875 cm^{-1} and 903 cm^{-1} peaks correspond to the Q^1 and Q^0 units respectively. This means some B-O-Si bonds exist in the SABS-35 glass. Again, the Raman peak analysis in the 800-1200 cm^{-1} region shows that B_2O_3 content increase causes boron-containing structural unit formation. Also, the amounts of silicon-containing structural units decrease. Both aspects indicate that the SABS glass network connectivity decreases.

For the SABS-0 glass, the 619 cm^{-1} and 641 cm^{-1} peaks are from the two bridging oxygen atom Q^2 units corresponding to the characteristic bands of metasilicate glasses between 620-640 cm^{-1}. The 606 cm^{-1} peak is from the broken Si-O bonds as in vitreous silica with the Q^3 units. For the SABS-5 glass, the 643 cm^{-1} peak is from the Q^2 units. The 690 cm^{-1} peak is from the Q^1 units [24]. The 537 cm^{-1} and 580 cm^{-1} peaks are from the $[BO_4]$ units in anionic rings. For the SABS-10 glass, the peaks at 679 cm^{-1} and 680 cm^{-1} peaks are from mixed Si-O-B linkage with the Q^1 units. Some metaborate units may also contribute to these peaks. The 642 cm^{-1} peak is from the Q^2 units. Some metaborate units also appear at the 642 cm^{-1} peak since the integral area increases with increasing B_2O_3 content. The peaks at 524 cm^{-1}, 534 cm^{-1}, and 582 cm^{-1} are from the BO_4^- anionic rings. For the SABS-15 glass, the 741-744 cm^{-1} peaks are attributed to the BO_4^- tetrahedral units. The 677 cm^{-1} and 704 cm^{-1} peaks are attributed to the Q^1 units along with some metaborate units. The peaks in the 400-644 cm^{-1} region are attributed to delocalized vibration of Si-O-Si bridging units. The 644 cm^{-1} peak is from the Q^2 units. The 517 cm^{-1} and 583 cm^{-1} peaks are from the BO_4^- units. The 471 cm^{-1} peak is due to the bending mode of B-O-B, B-O-Si, and Si-O-Si linkages associated with the Q^3 units [19]. The 446 cm^{-1} peak is from the Q^4 units. Simultaneous presence of 929 cm^{-1} and 471 cm^{-1} peaks indicate B-O-Si linkages. In alkaline

borate glass and alkaline earth borate glass, simultaneous presence of 930 cm^{-1}, 650 cm^{-1}, and 485 cm^{-1} peaks confirms the presence of pentaborate unit and the 755 cm^{-1} peak is from dipentaborate units. In the SABS-35 glass, simultaneous presence of 937 cm^{-1}, 779 cm^{-1}, 645 cm^{-1}, 508 cm^{-1} peaks confirms the presence of pentaborate and dipentaborate structural units. The 742 cm^{-1} peak is attributed to the BO_4^- tetrahedra. The 467 cm^{-1} and 688 cm^{-1} peaks are attributed to B-O-Si linkages. The 688 cm^{-1} peak may also be attributed to the metaborate units. The peak at 539 cm^{-1} is attributed to the BO_4^- units. As it shows, peak splitting increases with B_2O_3 content increase. From SABS-0 to SABS-35 glass, the boron-containing structure units change from metaborate to pentaborate and even to dipentaborate units with non-bridging oxygen atoms.

With the understanding that Raman spectroscopy can only provide a qualitative picture of the overall glass structure, the following observations can be made: a) The amount of non-bridging oxygen atoms increases along with the appearance of metaborate, orthoborate, and pentaborate units with increasing B_2O_3 content. B_2O_3 reduces the connectivity of the SABS glass. b) Peak splitting appears and then increases with increasing B_2O_3 content, suggesting increased localized ordering of the structural units in the SABS glasses. c) The peaks corresponding to B-O-Si linkages indicate that borate groups or boroxol rings mix with SiO_4 tetrahedral structural units.

3.3.1.2. Glass structural unit environment

The ^{11}B MAS NMR spectra of the SABS glasses are shown in Fig. 3-3. SABS-0 composition is not included since it is B_2O_3 free. The broad powder pattern on the left (12 ppm peak) and the narrow Gaussian curve on the right (0 ppm peak) can be readily assigned to BO_3 (trigonal boron species) and BO_4 (tetrahedral boron species), respectively. Direct simulation of

these spectra is difficult due to the heterogeneous broadening of the BO_3 line shape. Instead, these spectra are all normalized to the highest intensity of the BO_4 line shape. The relative intensity of the BO_3 peak maximum is used as a relative measure of BO_3:BO_4 ratio. As seen from Fig. 3-4, the BO_3:BO_4 ratio in the SABS glasses decreases significantly and systematically with B_2O_3 content increase. This means higher B_2O_3 content induces BO_4 glass structural unit formation. The fundamental cause is that the bonding between BO_3 and SiO_4 (trigonal and tetrahedral network units) is unfavorable because of their relatively high local charge concentrations. The degree of coordination with SiO_4 for BO_3 is less than that for BO_4 even though SiO_4 and BO_4 coordination needs to be further examined [37].

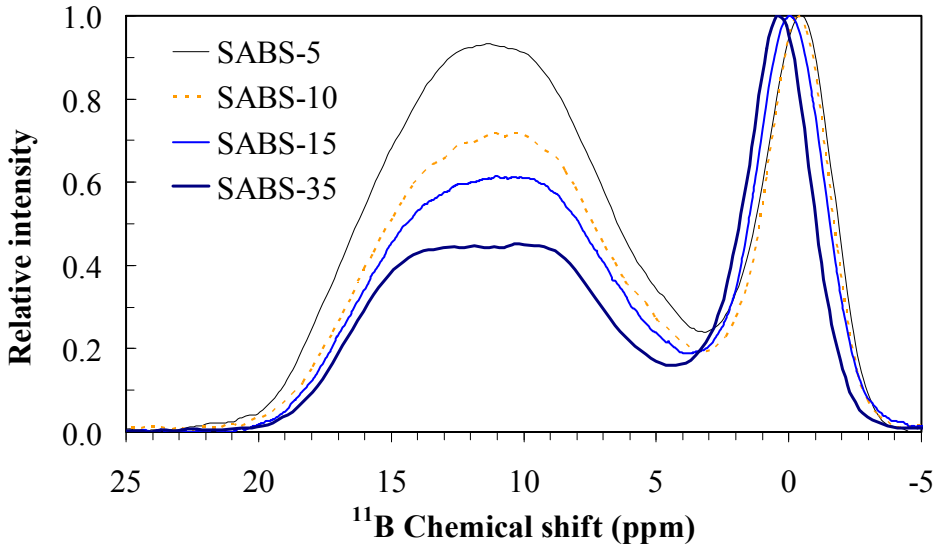

Fig. 3-4. ^{11}B MAS NMR spectra of SABS glasses.

Previous ^{11}B NMR studies of borosilicate glasses have shown that BO_3:BO_4 ratio is independent of B_2O_3:SiO_2 ratio at low modifier contents [38]. However, at high modifier concentrations that are characteristic of the SABS glasses studied here, the BO_3:BO_4 ratio is

expected to decrease at a rapid rate with B_2O_3 content increase [38]. This structural scenario is consistent with the compositional evolution of the ^{11}B MAS NMR spectra shown in Fig. 3-4. As it indicates, the BO_3:BO_4 ratio progressively decreases from SABS-5 to SABS-35. It is also interesting to note that the ^{11}B chemical shift for the BO_3 site is located around 11 ppm, indicating that these sites contain at least one non-bridging oxygen atom forming a T^2 boron site (where T stands for "ternary" by analogy to the Q^n nomenclature for quaternary silicon) [39]. In addition, the ^{11}B chemical shift for the BO_4 sites shows systematic increase from –0.50 ppm to 0.44 ppm with increasing B_2O_3 content from SABS-5 to SABS-35. This result means that increasing ^{11}B chemical shift for the BO_4 sites causes less sharing of oxygen between BO_4 and SiO_4 tetrahedra from SABS-5 to SABS-35 [40]. The bonding between BO_4 and SiO_4 is better than that between BO_3 and SiO_4 but keeps decreasing from SABS-5 to SABS-35.

The ^{29}Si MAS spectra of the SABS glasses are shown in Fig. 3-5. These spectra show a slightly asymmetric peak that centers from -85 to -87 ppm. The absence of B_2O_3 in the SABS-0 glass and the small amount of Al_2O_3 (in comparison to SiO_2) make the ^{29}Si peak assignment straightforward. The main structural unit is Q^3 (chemical shift of ~ -87 ppm) [41]. The shoulder near –100 ppm indicates the presence of a small amount of Q^4 species with one or two aluminum as next-nearest neighbors. The ^{29}Si MAS NMR spectra of SABS-5 to SABS-10 are very similar to that of SABS-0, in spite of the increase in the B_2O_3 content. This observation implies that SiO_4 tetrahedrals in these glasses share oxygen with BO_3 units to a certain extent. However, as mentioned above, the systematic change in the ^{11}B chemical shift of BO_4 units in these glasses indicates preferred linking of BO_4 and SiO_4 tetrahedra, which begins to influence the ^{29}Si chemical shift in SABS-15 and SABS-35 glasses. In SABS-35, characterized by the highest B_2O_3 content and the lowest BO_3:BO_4 ratio, the entire ^{29}Si MAS NMR spectrum shifts to higher

chemical shift values indicating either the formation of Q^2 species or Q^3 species linked with multiple B^{IV} next-nearest neighbors. SABS-15 glass reveals a chemical shift in-between those of SABS-10 and SABS-35. This means at low B_2O_3 content SiO_4 structural units may bond with BO_3 structural units. As B_2O_3 content increases, BO_4 content increases; SiO_4 structural units are more likely to bond with BO_4 structural units.

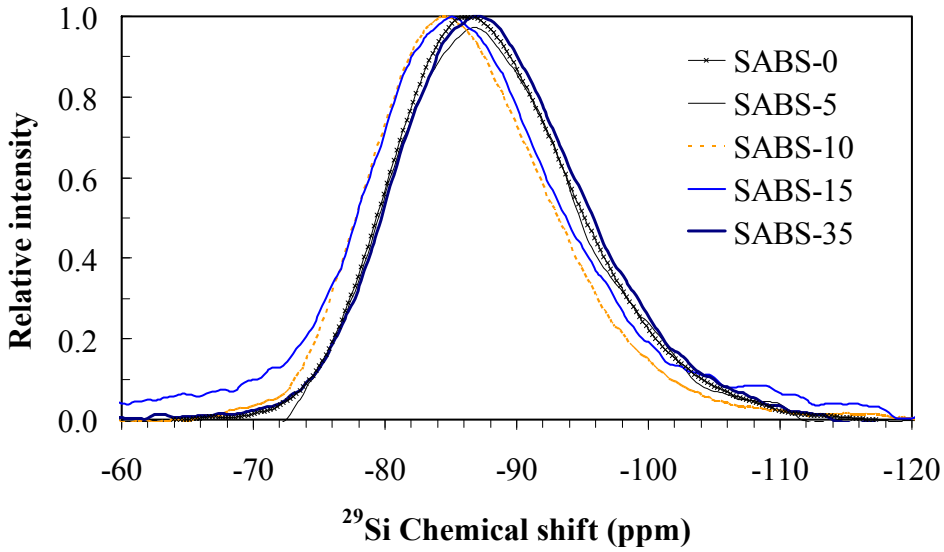

Fig. 3-5. ^{29}Si MAS NMR spectra of SABS glasses.

For clarity, only the ^{27}Al MAS NMR spectra of SABS-0, SABS-10, and SABS-35 glasses are shown in Fig. 3-6. These spectra are nearly identical and dominated by a strong, asymmetric peak positioned at 56 ppm that corresponds to tetrahedrally coordinated aluminum with a distribution of quadrupolar coupling coefficients, typical of oxide glasses. This means Al_2O_3 mainly acts as a glass former in the SABS glasses.

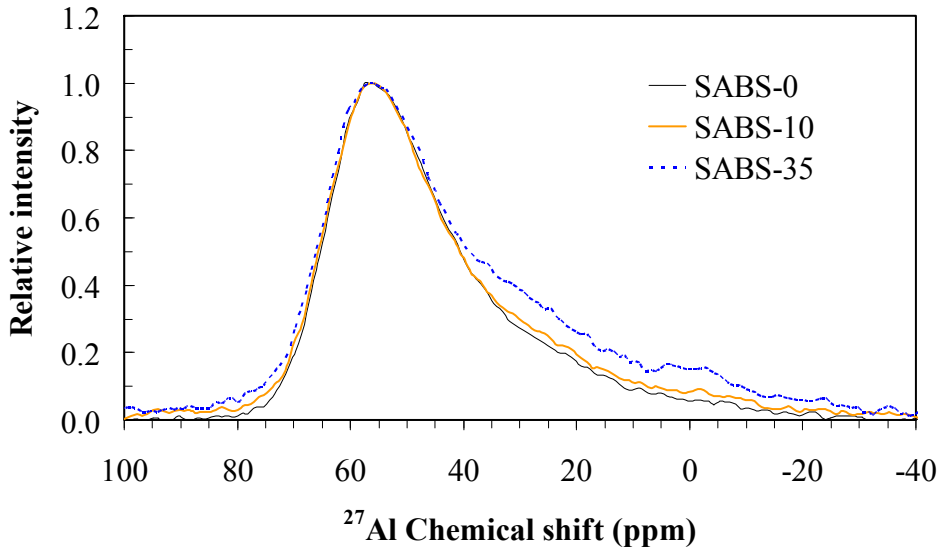

Fig. 3-6. ^{27}AlMAS NMR spectra of SABS-0, SABS-10, and SABS-35 glasses.

As reported before, the addition of Al_2O_3 can reduce the degree of phase separation in the SABS glasses; possibly by the formation of B-O-Al-O-Si linkages. These two observations are consistent. The ^{27}Al MAS NMR spectrum of SABS-35 displays clear but small shoulders near 28 and 0 ppm that correspond to small concentrations (a few %) of 5- and 6- coordinated aluminum [42]. This result is not surprising, as the structure of this glass with its low SiO_2 content would have a strong presence of boroaluminate network. Such networks are typically characterized by the presence of 5- and 6- coordinated aluminum atoms forming Al-O-B linkages [11]. This observation indicates that whether aluminum acts as a glass former or as a glass modifier depends on the B_2O_3 content in borosilicate glass. Even though Al_2O_3 mostly acts as a glass former, B_2O_3 content increase could change it to a glass modifier. The quantity of Al_2O_3 as a glass former in the SABS glasses requires ^{27}Al triple-quantum MAS NMR studies.

3.3.1.3. Connectivity

Thermal properties of a glass depend on the presence of atomic level structural units, their relative arrangement, and the amounts of bridging and non-bridging oxygen atoms [31]. This is because these structural parameters determine the glass network connectivity. If a glass has high connectivity, then it is likely to be stable and resistant to devitrification. If a glass has low connectivity, then it is likely to devitrify. Increasing non-bridging oxygen content decreases glass connectivity. In the SABS glass system, B_2O_3 becomes more dominant in the glass structure as its content increases. Along with the increase of the relative percent of BO_4 structural units, the absolute content of BO_3 structural units still increases. This leads to more chain and ring metaborate and even orthoborate (for SABS-35) contents and increasingly broken SiO_4 tetrahedral network. As a result, connectivity decreases.

Quantitatively, glass network connectivity ψ can be defined as follows based on prior knowledge of degree of network formation [7]:

$$\Psi = \frac{\left[\dfrac{\sum Z_i (F_i V_i)}{\sum Z_i V_i}\right]_{\text{Network Former}}}{\left[\dfrac{\sum F_i V_i}{\sum V_i}\right]_{\text{Network Former + Modifier}}} \times \frac{\sum O^+}{\sum O^- + \sum O^+} \qquad (3\text{-}1)$$

F_i is the field strength of oxide i in a glass system, V_i is the amount of oxide i in vol%, and Z_i is the atomic number of oxide i. The first term in Eq. (3-1) considers the bonding effect of cations that are present in a glass network. The second term represents the ratio of bridging oxygen atoms (O^+) vs. total oxygen atoms (O^- and O^+) in a glass network. ψ thus represents two aspects in a glass network: bonding effect of glass network cations and the ratio of bridging oxygen atoms vs. total oxygen atoms.

Based on the SABS glass compositions, the NMR spectra, and the Raman spectra, glass network connectivity for the SABS glasses has been calculated using Eq. (3-1) and the results are given in Table 3-1. The field strength of SiO_2, Al_2O_3, La_2O_3, and SrO are 1.56, 0.97, 0.43, and 0.27 respectively based on literature values and the cation function in the SABS glasses [43]. The field strength of B_2O_3 varies between 1.53 to 1.50 based on literature values and the BO_3:BO_4 ratios from SABS-0 to SABS-35 [43]. As it shows, the bonding ability of glass network cations, the relative percent of bridging oxygen atoms, and the SABS glass network connectivity all decrease with B_2O_3 content increase. This result is very consistent with the NMR and Raman spectra, as well as the SABS glass thermal stability to be discussed. Glass connectivity serves as an important parameter in evaluating the thermal stability of a glass system.

Table 3-1. Calculated glass network connectivity for SABS glasses.

Composition	$\frac{\left[\frac{\sum Z_i(F_iV_i)}{\sum Z_iV_i}\right]_{\text{Network Former}}}{\left[\frac{\sum F_iV_i}{\sum V_i}\right]_{\text{Network Former+ Modifier}}}$	$\frac{\sum O^+}{\sum O^- + \sum O^+}$	Glass Network Connectivity ψ (%)
SABS-0	1.40	0.53	74
SABS-5	1.38	0.52	72
SABS 10	1.37	0.48	66
SABS-15	1.36	0.49	66
SABS-35	1.31	0.37	48

While the connectivity calculation sheds new light on the glass network structure, it should be cautioned that the connectivity results in Table 3-1 involve two approximations. First, the amount of network forming cations contributed by Al^{3+} ions is unknown. Al_2O_3 participates in the glass network as a glass former but the relative amount decreases with B_2O_3 content increase. For the calculation in Table 3-1, Al_2O_3 is assumed to always act as a glass former throughout the SABS glass composition range. Second, there are two Raman peaks for SABS-15 (1402 cm^{-1} and 1438 cm^{-1}) and three Raman peaks for SABS-35 (1330 cm^{-1}, 1417 cm^{-1}, and 1443 cm^{-1}) that cannot be identified. In this calculation, they are assumed to come from borate structural units coordinated with glass modifiers.

Because of the configurational entropy difference between SiO_4 and BO_3 structural units, SiO_4 structural units preferentially link with BO_4 structural units, except for the linking among themselves. To understand the degree of bonding between SiO_4 and BO_4 units, two other related parameters can be calculated. One is probability of silicon coordinated to BO_4 and the other is mean number of silicon coordinated to BO_4. SiO_4 and BO_4 structural unit coordination has been discussed previously but is desired to be further quantified. For a given glass, the mean number of silicon coordinated to BO_4 species is approximately constant and can be averaged over compositions of SABS-0 to SABS-35. Taking X_{Si} as the molar ratio of silicon to total network formers (silicon and boron) and assuming no BO_4 units are linked with each other, the mean number of silicon coordinated to BO_4 can be expressed as [44]:

$$< l >= \frac{16 X_{Si}}{0.62 + 4.38 X_{Si} - X_{Si}^{\ 2}} \tag{3-2}$$

The probability of silicon coordinated to BO_4 becomes:

$$P(l) = \frac{4!}{l!(4-l)!} \left(\frac{4 X_{Si}}{0.62 + 4.38 X_{Si} - X_{Si}^{\ 2}}\right)^{l} \left(\frac{0.62 + 0.38 X_{Si} - X_{Si}^{\ 2}}{0.62 + 4.38 X_{Si} - X_{Si}^{\ 2}}\right)^{4-l} \tag{3-3}$$

Based on Eqs. (2) and (3), <*l*> and P(*l*) can be calculated for the SABS glasses as shown in Fig. 3-7. <*l*> and P(*l*) drastically decrease with B_2O_3 content increase. For SABS-5, the average mean number of silicon coordinated to BO_4 is 3.75; the probability P(*l*) of finding silicon coordinated to BO_4 is 0.77. For SABS-35, the average mean number of silicon coordinated to BO_4 is 2.47; the probability P(*l*) of finding silicon coordinated to BO_4 is 0.33. For SABS-10 and SABS-15, the values of <*l*> and P(*l*) are in-between the above ranges. This means as B_2O_3 content increases, there are not only fewer silicon atoms coordinated to BO_4 but the possibility of finding such coordination also drastically decreases. Put it differently, SiO_4 and BO_4 structural units are less and less likely to bond with each other with B_2O_3 content increase, even by assuming no BO_4 units are directly linked with themselves, an extreme assumption supported by the NMR results. This indicates that the glass network connectivity results in Table 3-1 should be considered jointly with the Q^n and T^n structural unit distribution and bonding when evaluating a glass system, such as thermal stability.

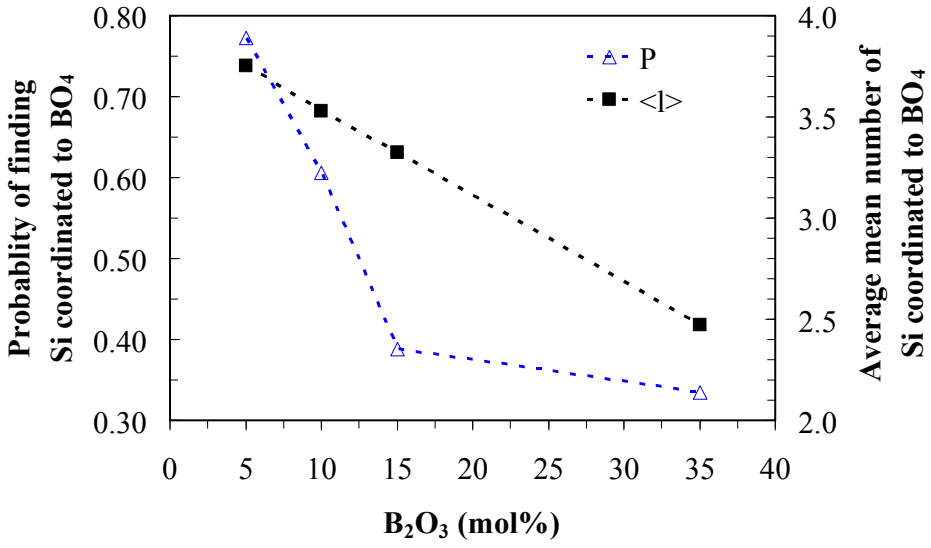

Fig. 3-7. Probability of silicon coordinated to BO_4 and average mean number of silicon

coordinated to BO_4 as a function of SABS glass composition.

3.3.2. Thermal properties

The T_g and T_d results obtained from the dilatometry experiments are shown in Fig. 3-8. From Fig. 3-8, it is observed that both T_g and T_d decrease as B_2O_3 content increases from 0 mol% to 35 mol%. The T_g values changes from 775°C to 635°C. The T_d value changes from 815°C to 670°C. This means the SABS glass network connectivity decrease directly affects the thermal properties [45].

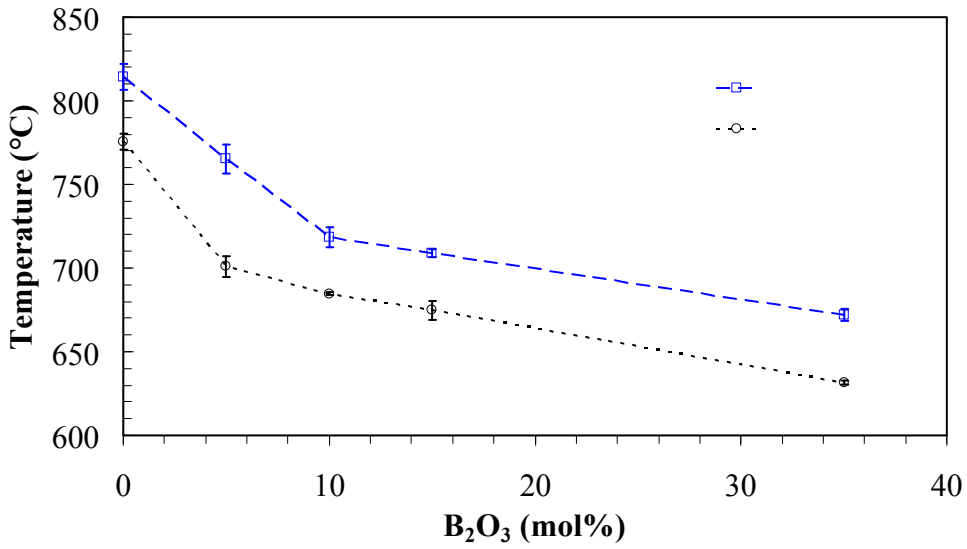

Fig. 3-8. Glass transition temperature (T_g) and glass softening temperature (T_d) variation with B_2O_3 content in SABS glasses.

The trend in decreased values of T_g and T_d with increasing B_2O_3 content is expected due to the low T_g and T_d of borate glass, contributed by the presence of $[BO_3]$ trigonal structures. The SABS-0 glass consists of stable $[SiO_4]$ tetrahedra in a connected network structure. A small

amount of the Q^4 units is present along with the Q^3, Q^2 and Q^0 units in the SABS-0 glass. The T_g and T_d are high since the glass network is more rigid and less mobile. As B_2O_3 is introduced into the SABS-5 glass, trigonal [BO_3] polyhedra cause the [SiO_4] glass network to re-arrange and result in a less connected 3D structure. In the SABS-5 glass, the amount of the Q^3 units increases and the amount of the Q^2 units decreases with the appearance of metaborate units and boroxol rings. Due to the presence of metaborate units and trigonal boroxol rings, the degree of connectivity decreases and consequently both T_g and T_d decrease sharply. With increasing B_2O_3 content, the content of the [SiO_4] structural units decreases and the content of the [BO_3] structural units increases. However, with increasing B_2O_3:SiO_2 ratio, the content of the borate structural units with both three and four-coordinated borons (metaborate, pentaborate, and orthoborate) increases. The bond energy of B-O-Si bond with four coordinated boron is 89 kcal/mol compare to 119 kcal/mole for B-O-Si bond with three coordinated boron [46]. The absence of the characteristic peak, 805 cm^{-1}, of boroxol rings with three coordinated boron in the SABS glasses indicates the dominance of the four coordinated borate structural units. The weaker bond energy of four coordinated B-O-Si bond also contributes to the lower T_g and T_d in the SABS glasses with increasing B_2O_3:SiO_2 ratio. In the SABS-15 glass, the amount of the Q^2 units decreases with the evolution of pentaborate units along with more metaborate and boroxol ring units. In the SABS-35 glass, decreased amount of the Q^3 units and increased amount of the pentaborate units further decrease the glass network connectivity, resulting in lower T_g and T_d. As a result, the decrease in T_g and T_d becomes more substantial.

The CTE obtained from dilatometry is shown in Fig. 3-9. The CTE of the SABS glasses increases with B_2O_3: SiO_2 ratio. The CTEs of the SABS-0 glass is $10.8 \pm 0.5 \times 10^{-6}$/°C and increases by ~ 1.0×10^{-6}/°C to $11.5 \pm 0.5 \times 10^{-6}$/°C for SABS-35 glass. Asymmetric structure of

boron structural units, increase in non-bridging oxygen, and decrease in network connectivity are corroborated to the CTE increase with B_2O_3:SiO_2 ratio. This observation is also consistent with decrease in T_g and T_d with increasing B_2O_3:SiO_2 ratio.

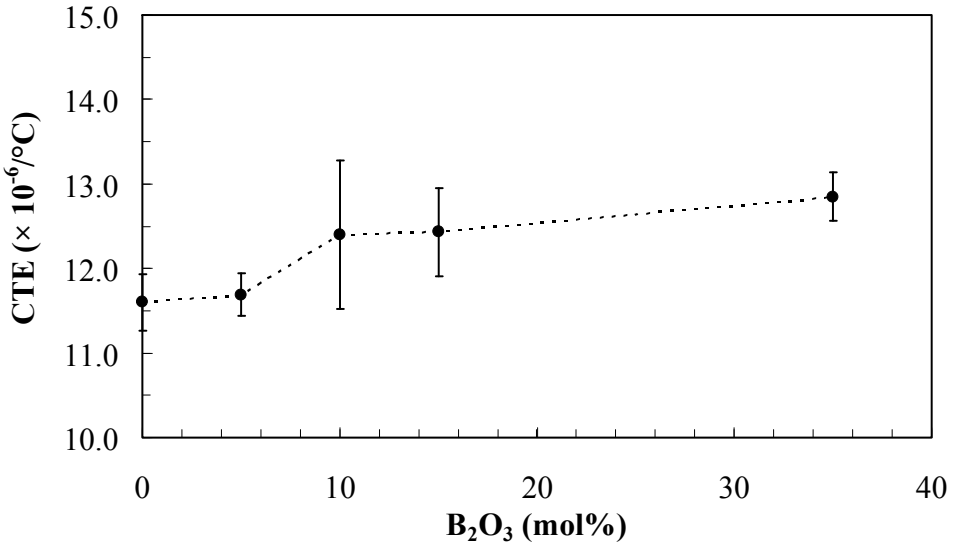

Fig. 3-9. CTE variation with B_2O_3 content in SABS glasses.

3.3.3. Thermal stability

Degree of glass network connectivity directly affects the devitrification tendency of a glass system. Decrease in connectivity increases the possibility for devitrification. If structural unit local ordering occurs in a glass, even if only in small localized areas, the glass will be prone to devitrification, likely caused by heterogeneous nucleation [47].

For the SABS-0 glass, the thermal treatment at 850°C is carried out up to 200 hrs. The XRD patterns at different thermal treatment times are given in Fig. 3-10. As can be seen from the halo shape of the XRD patterns, the glass does not devitrify after 200 hrs of thermal treatment. This result suggests that the SABS-0 glass is thermally stable.

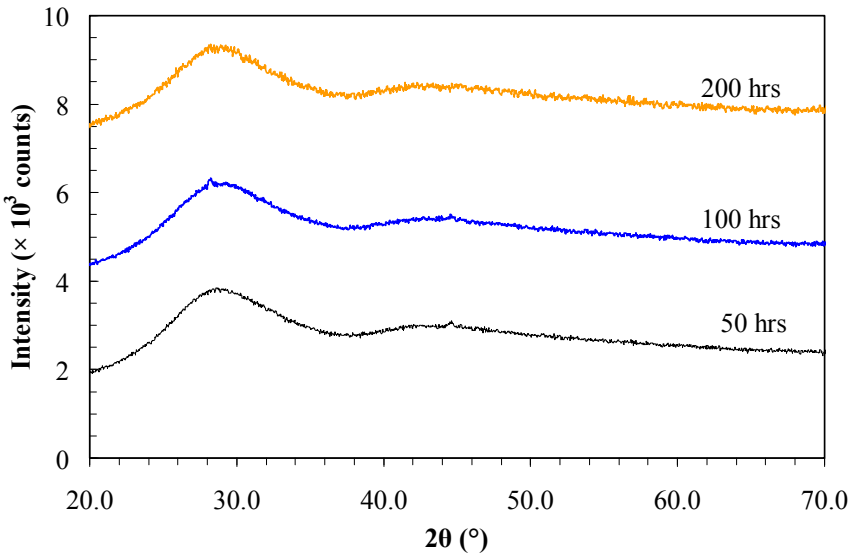

Fig. 3-10. XRD patterns of SABS-0 glass thermally treated at 850°C for different times.

For the SABS-5 glass, thermal treatment was conducted up to 100 hrs at 850°C. The glass devitrifies after 50 hrs thermal treatment as seen in Fig. 3-11. Small devitrification peaks are observed but the intensity and numbers of peaks are insufficient to determine the crystalline phases. After 100 hrs of thermal treatment at 850°C, monoclinic $La_2Si_2O_7$ is the main phase along with small amounts of α-$SrSiO_3$ and Sr_2SiO_4 phases. This means as the glass structure connectivity decreases, [SiO_4] becomes more likely to interact with glass modifier, such as SrO and La_2O_3, and form new species. This interaction away from the glass network leads to devitrification and crystalline phase formation.

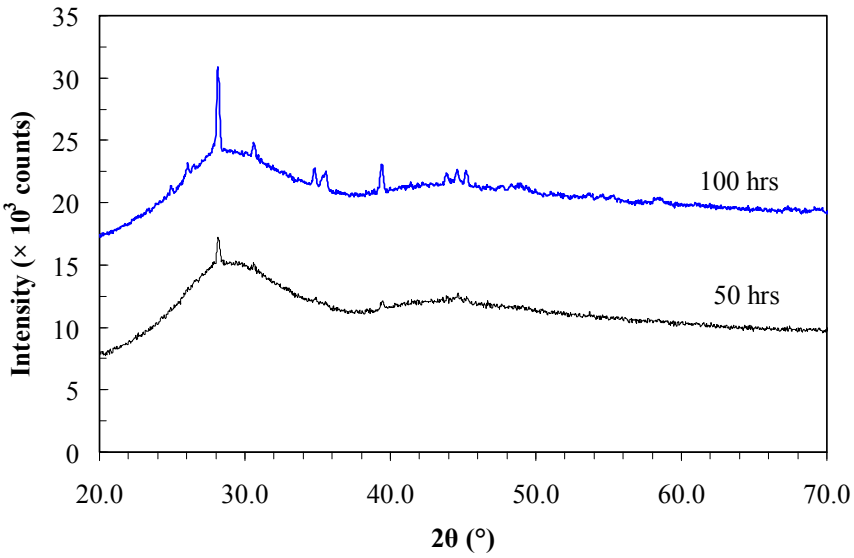

Fig. 3-11. XRD patterns of SABS-5 glass thermally treated at 850°C for different times.

The SABS-10, SABS-15 and SABS-35 glasses are thermally treated at 850°C for 50 hrs only since devitrification becomes apparent at this condition, as shown in Fig. 3-12. Monoclinic lanthanum silicate ($La_2Si_2O_7$) is the only phase in the SABS-10 glass. Three phases are identified in the SABS-15 glass. They are monoclinic lanthanum silicate ($La_2Si_2O_7$), rhombohedral aluminum borate ($AlBO_3$), and orthorhombic strontium boron aluminum oxide ($Sr_2B_2Al_2O_8$). In the SABS-35 glass, two phases, orthorhombic strontium borate (SrB_2O_4) and orthorhombic lanthanum borate ($LaBO_3$), are identified. $LaBO_3$ is the main phase. This appearance of totally different phases in the SABS-35 glass is also seen in the peak shifting in the XRD patterns whereas the major peaks are exactly overlapped for the SABS-10 and the SABS-15 glasses (Fig. 3-12).

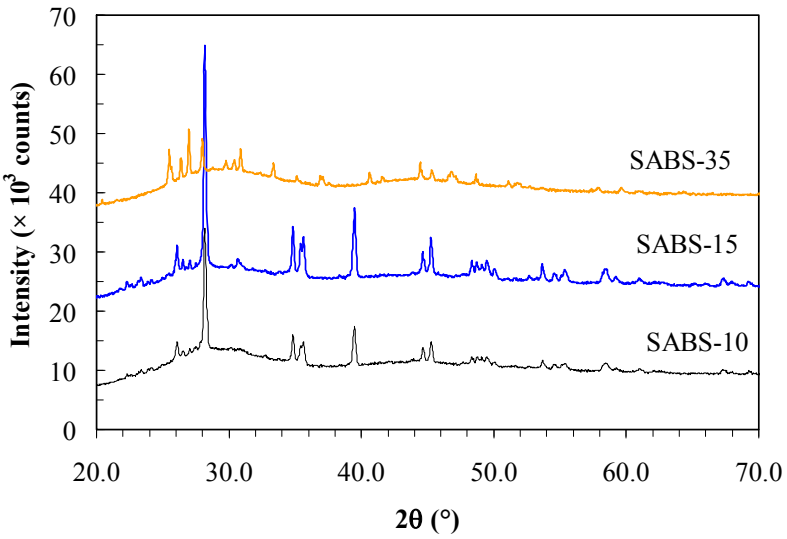

Fig. 3-12. XRD patterns of SABS-10, SABS-15, and SABS-35 glasses thermally treated at 850°C for 50 hrs.

In the studied SABS glass system, only B_2O_3:SiO_2 ratio changes. With increasing B_2O_3 content, different devitrified phases evolve. This indicates that the devitrification process is accompanied by the complex interaction between different glass structural units and glass modifiers. Gibbs free energy change during the devitrification process may be the most convincing approach to explain the devitrification tendency and the most likely devitrifying phases. However, thermodynamic data for the SABS glass system at high temperatures are not available, especially for the species involving the SrO and La_2O_3 modifiers. With the Raman spectra and NMR providing complementary data about BO_3:BO_4 ratios, environment of different structural units, as well as structural unit types, ordering, and distribution, XRD serves as an effective means to identifying the devitrified phases.

In borosilicate glasses, borate structural units and silicate structural units do not disperse well and tend to stay separated. This glass structural unit clustering is supported by the peak splitting in the deconvoluted Raman spectra in Fig. 3-3. The amount of non-bridging oxygen

atoms increases with B_2O_3 addition. Thus the amount of glass structural units with low connectivity increases. The presence of localized low connectivity structural unit promotes devitrification via nucleation in the glass [13,14]. Therefore, devitrification is more prominent with increasing B_2O_3:SiO_2 ratio.

Another important aspect to consider for the SABS glass system is the glass modifiers. The non-bridging oxygen atoms tend to coordinate with the glass modifiers and form new species. In K_2O-La_2O_3-SiO_2 system, the non-bridging oxygen atoms due to the Q^3 units at 1030 cm^{-1} and 1100 cm^{-1} peaks coordinate with La^{3+} ions [48]. In lanthanum containing glasses, lanthanum bonds either with silicate tetrahedra forming 'lanthanide Q^3' species (Si-O-La), La-O clusters, and linked La-O polyhedra by 'oxide-like' La-O-La [49, 50]. These structural units are energetically favorable [49,50] and forms small, isolated, phase-ordered domains which essentially also act as nucleation sites favoring devitrification of glass. In the SABS glasses, La^{3+} and Sr^{2+} ions act as modifiers. The intense peaks in the 1020-1030 cm^{-1} region in the SABS-5 (1037 cm^{-1}), SABS-10 (1020 cm^{-1}) and SABS-15 (1028 cm^{-1}) glasses suggest that the non-bridging oxygen atoms from the Q^3 units coordinate with La^{3+}. Consequently, $La_2Si_2O_7$ phase forms in the SABS-5, SABS-10, and SABS-15 glasses. For the SABS-35 glass, similar argument can be applied. Some non-bridging oxygen atoms are coordinated with Sr^{2+} ions and thus Sr-containing phases evolve. The isolated La-O clusters probably bond with borate structural units and form B-O-La instead of B-O-Si due to the higher concentration of borate structural units and higher electrostatic bond strength of boron (1.62) than silicon (1.54). Consequently, $LaBO_3$ phase forms as main phase in the SABS-35 glass. This interpretation is also supported by the appearance of several peaks above 1300 cm^{-1} wave number, similar to the crystalline phase $La(B_3O_6)$ peak in BaO-La_2O_3-B_2O_3 metaborate glass [51,52]. With addition of B_2O_3 in the SABS

glasses, the diborate, metaborate, orthoborate and pentaborate structural units evolve as seen from Raman spectroscopy. These borate structural units contain both four-coordinated and three-coordinated borons [53]. In Sr-containing boroaluminate glass, the devitification is favored by the formation of boroaluminate phase by the interaction of three coordinated boron and four coordinated aluminium [54,55]. With increasing B_2O_3 content, the tetraderal BO_4 structural units (four-coordinated boron) break the Al-O-Al bonds in glass network to form Al-O-B bonds and react with $SrAl_2O_4$ to form strontium aluminoborate and strontium borate phases [56]. Consequently, with increasing B_2O_3 content $AlBO_3$ and $Sr_2B_2Al_2O_8$ phases evolve along with $La_2Si_2O_7$ phase in SABS-15 glass and SrB_2O_4 evolves along with $LaBO_3$ phase in SABS-35 glass. As a result, analogous structural units of $LaBO_3$ and Sr-metaborate are present.

3.4. Conclusions

The effects of B_2O_3:SiO_2 ratio on the network structure and thermal properties of the SrO-La_2O_3-Al_2O_3-B_2O_3-SiO_2 glass system are studied. Increasing B_2O_3:SiO_2 ratio causes glass network connectivity decrease, non-bridging oxygen increase, glass structural unit local ordering, and glass former distribution inhomogeneity. Increased B_2O_3:SiO_2 ratio degrades the thermal properties. The micro-heterogeneity from different glass structural units also increases the tendency of devitrification and degrades thermal stability. Depending on the bonding affinity with glass modifiers, silicon-containing devitrified phases form for low B_2O_3 content SABS glasses and boron-containing devitrified phases form for high B_2O_3 content SABS glasses. Boron free SABS glass exhibits excellent combination of thermal properties and thermal stability.

References

[1] K. D. Meinhardt, D.S. Kim, Y. S. Chou, and K. S. Weil, Synthesis and properties of a barium

aluminosilicate solid oxide fuel cell glass-ceramic sealant, Journal of Power Sources 182, 188-196, 2008.

[2] N. Lahl, K. Singh, L. Singheiser, K. Hilper, and D. Bahadur, Crystallisation kinetics in AO -Al_2O_3-SiO_2-B_2O_3 glasses (A = Ba, Ca, Mg), Journal of Materials Science 35, 3089-3096, 2000.

[3] M. J. Pascual, A. Guillet, and Durán, Optimization of glass–ceramic sealant compositions in the system MgO–BaO–SiO_2 for solid oxide fuel cells (SOFC), Journal of Power Sources 169, 40-46, 2007.

[4] K. L. Ley, M. Krumpelt, R. Kumar, J. H. Meiser, and I. Bloom, Glass-ceramic sealants for solid oxide fuel cells Part I. Physical properties, Journal of Materials Research 11, 1489-1493, 1996.

[5] Y. S. Chou, J. W. Stevenson, and P. Singh, Novel refractory alkaline earth silicate sealing glasses for planar solid oxide fuel cells, Journal of the Electrochemical Society 154, B644-B651, 2007.

[6] J. W. Fergus, Sealants for solid oxide fuel cells, Journal of Power Sources, 147, 46-57, 2005.

[7] M. B. Volf, Chemical approach to glass, Glass Science and Technology, Elsevier, Amsterdam, 1984.

[8] S. B. Sohn, S. Y. Choi, G. H. Kim, H. S. Song, and G. D. Kim, Suitable glass-ceramic sealant for planar solid oxide fuel cells. Journal of the American Ceramic Society 87, 254-260, 2004.

[9] K.D. Meinhardt, J.D. Vienna, T.R. Armstrong, and L.R. Pederson, Glass-ceramic joint and method of joining, US Patent No. US 6532769 B1, 2003.

[10] W. Liu, X. Sun, and M. A. Khaleel, Predicting Young's modulus of glass/ceramic sealant

for solid oxide fuel cell considering the combined effects of aging, micro-voids and self-healing. Journal of Power Sources 185, 1193-1200, 2008.

[11] W. D. Kingery, H. K. Bowen, and D. R. Uhlmann, Introduction to Ceramics, John Wiley and Sons, New York, 2nd edn., 1976, ch. 3 pp. 91-122, ch.17, pp. 873-888.

[12] T. Maehara, T. Yano, S. Shibata, and M. Yamane, Structure and phase transformation of alkali silicate melts analyzed by Raman Spectroscopy, Philosophical Magazine 84, 3085-3099, 2004.

[13] B. H. W. S. D. Jong, K. D. Keefer Jr., and C. M. Taylor, Polymerization of silicate and aluminate tetrahedra in glasses, melts, and aqueous solutions-III. local silicon environments and internal nucleation in silicate glasses, Geochimia et Cosmochimia Acta 45, 1291-1308, 1981.

[14] J. Deubener, Structural aspects of volume nucleation in silicate glass, Journal of Non -Crystalline Solids 351, 1500-1511, 2005.

[15] M. K. Mahapatra, K. Lu, and W. T. Reynonds Jr., Thermophysical properties and devitrification of $SrO–La_2O_3–Al_2O_3–B_2O_3–SiO_2$-based glass sealant for solid oxide fuel/electrolyzer cells, Journal of Power Sources 179, 106-112, 2008.

[16] V. L. Stolyarova and E. N. Plotnikov, Vaporization processes and thermodynamic properties of oxide systems at high temperatures: experimental study and modeling, Glass Physics and Chemistry 31, 30-43, 2005.

[17] M. J. Snyder, M. G. Mesko, and J. E. Shelby, Volatilization of boron from E-glass melts, Journal of Non-Crystalline Solids 352, 669-673, 2006.

[18] T. Zhang, W. G. Fahrenholtz, S. T. Reis, and R. K. Brow, Borate volatility from SOFC sealing glasses, Journal of the American Ceramic Society 91, 2564-2569, 2008.

[19] B. N. Meera and J. Ramakrishna, Raman spectral studies of borate glasses, Journal of Non

Crystalline Solids 159, 1-21,1993.

[20] P. McMillan, Structual studies of silicate glasses and melts- applications and limitations of Raman Spectroscopy, American Mineralogist 69, 622-644, 1984.

[21] R. K. Brow and D. R. Tallant, Structural design of sealing glasses, Journal of Non -Crystalline Solids 222, 396-406, 1997.

[22] P. Boolchand, M. Jin, D. I. Novita, and S. Chakravarty, Raman scattering as a probe of intermediate phases in glassy networks, Journal of Raman Spectroscopy 38, 660–672, 2007.

[23] A. Steven, A. Brawer, and W. B. White, Raman Spectroscopic investigation silicate glasses (II). soda-alkaline and quaternary glasses, Journal of Non-Crystalline Solids 23, 261-278, 1977.

[24] E. I. Kamitoss, J. A. Kapoutsis, H. Jain, and C. H. Hsieh, Vibrational study of the role of trivalent ions in sodium trisilicate glass, Journal of Non-Crystalline Solids 171, 31-45, 1994.

[25] S. Sen, T. Topping, P. Yu, and R. E. Youngman, Atomic-scale understanding of structural relaxation in simple and complex borosilicate glasses, Physical Review B 75, 094203-094201-094207, 2007.

[26] S. Sen and P. Yu, Observation of a stuffed unmodified network in beryllium silicate glasses with multinuclear NMR spectroscopy, Physical Review B 72, 132203-132201-132204, 2005.

[27] C. I. Merzbacher, B. L. Sherriff, J. S. Hartman, and W. B. White, A High-Resolution ^{29}Si and ^{27}Al NMR-study of alkaline-earth aluminosilicate glasses, Journal Of Non-Crystalline Solids 124, 194-206, 1990.

[28] A. K. Hassan, L. M. Torell, L. Börjesson, and H. Doweidar, Structural changes of B_2O_3 through the liquid-glass transition ramnge: a Raman -scattering study, Physical Review B 45, 12797-12805, 1992.

[29] B. O. Mysen, L. W. Finger, D. Virgo, and F. A. Seifert, Curve-fitting of Raman

spectra in silicate glass, American Mineralogist 67, 686-695, 1982.

[30] H. Li, P. Hrma, J. D. Vienna, M. Qian, Y. Su, and D. E. Smith, Effects of Al_2O_3, B_2O_3, Na_2O, and SiO_2 on nepheline formation in borosilicate glasses: chemical and physical correlations, Journal of Non-Crystalline Solids 331, 202-216, 2003.

[31] J. E. Shelby, Introduction to glass science and technology, The Royal Society of Chemistry Cambridge, UK, 2005.

[32] S. K. Sharma, Raman investigation of ring configurations in vitreous silica, Nature 292, 140-141, 1981.

[33] T. Furukawa and W. B. White, Vibrational spectra and glass structure, Journal of Non -Crystalline Solids 38-39, 87-92, 1980.

[34] M. Środa and C. Paluszkiewicz, Spectroscopic study of the influence of LaF_3 admixture on the crystallization and structure of borosilicate glass, Journal of Molecular Structure 834-836, 302-307, 2007.

[35] F. Seifert, B. O. Mysen, and D. Virgo, Three-dimensional network structure of quenched melts (glass) in the systems SiO_2-$NaAlO_2$, SiO_2-$CaAl_2O_4$ and SiO_2-$MgAl_2O_4$, American Mineralogist 67, 696-717, 1982.

[36] B. O. Mysen, D. Virgo, and F. A. Seifert, Relationships between properties and structure of aluminosilicate melts, American Mineralogist 70, 88-105,1985.

[37] L.S. Du and J. F. Stebbins, Solid-state NMR study of metastable immiscibility in alkali borosilicate glasses, Journal of Non-Crystalline Solids 315, 239-255, 2003.

[38] W.J. Dell, P.J. Bray and S.Z. Xiao, ^{11}B NMR studies and structural modeling of Na_2O B_2O_3-SiO_2 glasses of high soda content, Journal of Non-Crystalline Solids 58, 1-16, 1983.

[39] S. Kroeker and J.F. Stebbins, Three-coordinated boron-11 chemical shifts in borates,

Inorganic Chemistry 40, 6239-6246, 2001.

[40] R. Martens, W. Müller-Warmuth, Structural groups and their mixing in borosilicate glasses for various compositions –an NMR study, Journal of Non-Crystalline Solids 265, 167-175, 2000.

[41] R. J. Kirkpatrick and R. K. Brow, Nuclear magnetic resonance investigation of the structures of phosphate and phosphate containing glasses: a review, Solid State Nuclear Magnetic Resonance 5, 9-21, 1995.

[42] L. S. Du and J. F. Stebbins, Network connectivity in aluminoborosilicate glasses: a high resolution ^{11}B, ^{27}Al, and ^{17}O NMR study," Journal of Non-Crystalline solids 351, 3508-3520, 2005.

[43] H. Scholze, Glass nature, structure, and properties, Springer Verlag, New York, USA, 1991.

[44] L. S. Du and J. F. Stebbins, Nature of silicon-boron mixing in sodium borosilicate glasses: a high-resolution ^{11}B and ^{17}O NMR Study, Journal of Physics and Chemistry B 107, 10063-10076, 2003.

[45] J. E. Shelby, Effect of morphology on the properties of alkaline earth silicate glass, Journa of Applied Physics 50, 8010-8015, 1979.

[46] W. F. Du, K. Kuraoka, T. Akai, and T. Yazawa, Study of Al_2O_3 effect on structural change and phase seperation in Na_2O-B_2O_3-SiO_2 glass by NMR, Journal of Materials Science 35, 4865-4871, 2000.

[47] V. W. Vogel, Structure and crystallization of glass, Pergamon, New York, 1971.

[48] A. J. G. Ellison and P. C. Hess, Vibrational spectra of high-silica glasses of the system K_2O SiO_2-La_2O_3, Journal of Non-Crystalline Solids 127, 247-258, 1991.

[49] M. Wilding, Y. Badyal, and A. Navrotsky, The local environment of trivalent lanthanide

ions in sodium silicate glasses: a neutron diffraction study using substitution, Journal of Non-Crystalline Solids 353, 4792-4800, 2007.

[50] T. Schaller, J. F. Stebbins, and M. C. Wilding, Cation clustering and formation of free oxide ions in sodium and potassium lanthanum silicate glasses: nuclear magnetic resonance and Raman spectroscopic findings, Journal of Non-Crystalline Solids 243, 146-157, 1999.

[51] R. K. Brow, D. R. Tallant, and G. L. Turner, Raman and ^{11}B nuclear magnetic resonance spectroscopic studies of alkaline-earth Llanthanoborate glasses, Journal of the American Ceramic Society 79, 2410-2416, 1996.

[52] I. N. Chakraborty, J. E. Shelby, S. Robert, and A. Condrate, Properties and structure of lanthanum borate glasses, Journal of the American Ceramic Society 67, 782-785, 1984.

[53] W. J. Dell, P. J. Bray, and S. Z. Xiao, ^{11}B NMR studies and structural modelling of Na_2O B_2O_3-SiO_2 glasses of high soda content, Journal of Non-Crystalline Solids 58, 1-16, 1983.

[54] B. C. Bunker, R. J. Kirkpatrick, and R. K. Brow, Local structure of alkaline-earth boroaluminate crystals and glasses: I, crystal chemical concepts-structural predictions and comparisons to known crystal structures, Journal of the American Ceramic Society 74, 1425-1429, 1991.

[55] B. C. Bunker, R. J. Kirkpatrick, R. K. Brow, G. L. Turner, and C. Nelson, Local structure and alkaline-earth boroaluminate crystals and glasses: II, ^{11}B and ^{27}Al MAS NMR spectroscopy of alkaline-earth boroaluminate glasses, Journal of the American Ceramic Society 74, 1430-1438, 1991.

[56] A. Nag and T. R. N. Kutty, Role of B_2O_3 on the phase stability and long phosphorescence of $SrAl_2O_4$:Eu,Dy, Journal of Alloys and Compounds 354, 221-231, 2003.

CHAPTER FOUR

EFFECT OF NICKEL ON THE STRUCTURE AND THERMAL BEHAVIOR OF SrO-La_2O_3-Al_2O_3-B_2O_3-SiO_2 GLASS

Abstract

Nickel is added in a seal glass composition to modify thermal properties depending on its role as network former or modifier. To understand the role of nickel in the network structure and thermal properties of SrO-La_2O_3-Al_2O_3-B_2O_3-SiO_2-based seal glass, 2 mol% SiO_2 and B_2O_3 glass formers and SrO glass modifier have been substituted with nickel. Glass network structure was studied by Raman spectroscopy and network connectivity was calculated. Nickel in the studied glasses does not significantly modify the thermal properties but degrades thermal stability by decreasing network connectivity, increasing micro-heterogeneity, and increasing non-bridging oxygen. Nickel behaves as a glass modifier in the studied glasses.

4.1. Introduction

Transition metal oxides such as TiO_2, ZrO_2, and NiO are added in a seal glass to modify the thermal properties. These oxides behave similarly as intermediate oxides depending on the glass composition [1,2]. Ni or NiO is commonly used additive in a seal glass due to its high thermal expansion coefficient CTE (14.0×10^{-6}/°C) [3]. Ni or NiO has been studied in several seal glasses as an additive, but the results are ambiguous, if not contradictory [4-6]. In BaO-borosilicate glasses, 2-5 mol% Ni addition decreases T_g by 5-10°C and increases CTE by ~1.0×10^{-6}/°C [7]. In a SrO-CaO-borosilicate glass, 5 mol% NiO addition decreases T_g by ~25°C, T_s by ~10°C, and CTE by ~ 0.5×10^{-6}/°C. Further increase in NiO (10-15 mol%) increases T_g and T_s

by ~ 10°C and ~ 5°C respectively [5]. 2 mol% Ni addition into a MgO-borosilicate glass increases T_c by 80°C but does not affect the CTE [6].

The field strength of nickel ion (0.55 when coordination number is 6 and 0.61 when coordination number is 4) and falls in-between the field strength of glass network former region (1.00-2.00) and modifier region (≈ 0.35) [7]. When Ni^{2+} ions are 4-coordinated, they participate in a glass network and act as a glass former. Subsequently, T_g and T_s increase and CTE decreases. When 6-coordinated, Ni^{2+} ions act as a modifier and decreases T_g and T_s and increases CTE. However, the role of Ni/NiO as network former or modifier in the studied seal glasses have not been reported and the contradictory results remain unexplained. In chapter three, desirable thermal properties and thermal stability have been obtained in SrO-La_2O_3-Al_2O_3-B_2O_3-SiO_2-based (SABS) glasses. The role of Ni to modify the network structure and thermal behavior of SABS glasses have been studied in this chapter.

This chapter is focused on understanding the effects of nickel replacement of glass former (SiO_2, B_2O_3) and glass modifier (SrO) on the SABS glass structure, thermal properties, and thermal stability. SABS glass with 0 mol% and 5 mol% B_2O_3 were studied. Nickel of 2 mol% was added to substitute either SiO_2, B_2O_3, or SrO in the same amount in order to understand the following: 1) How does nickel affect SABS glass structure and connectivity? Does nickel act as a glass modifier or glass network former? 2) How does nickel affect SABS glass thermal properties and thermal stability?

4.2. Experimental procedure

4.2.1. Glass preparation

SrO-La_2O_3-Al_2O_3-B_2O_3-SiO_2 based glass samples were prepared with conventional quenching method. $SrCO_3$ (99.9%, Sigma Aldrich, St. Louis, MO), La_2O_3 (99.98%), Al_2O_3 (99.95%), B_2O_3 (99.98%), SiO_2 (99.8%) (all oxides were from Alfa Aesar, Ward Hill, MA), and nickel metal powders (INCO powder type 110, Novamet, Wyckoft, NJ) at designed ratios were mixed in a ball mill for overnight. The mixed powders were heated in a platinum crucible in a box furnace (Lindberg, Model No. 51314, Watertown, WI) to 1100°C and kept there for 1 hr for $SrCO_3$ to decompose. After that, the mixture was heated to 1400°C for 4 hrs. The heating rate was 10°C·min^{-1}. The molten glass was quenched into a graphite mold. The glass compositions in this study were abbreviated as SABS-0 and SABS-5, in which the numbers 0 and 5 indicate 0 mol% and 5 mol% B_2O_3, respectively. All the glass compositions had 40 mol% of SrO, La_2O_3, and Al_2O_3 at fixed SrO:La_2O_3:Al_2O_3 ratios. The total amount of B_2O_3 and SiO_2 was 60 mol%. In the SABS-0 glass, 2.0 mol% nickel powder was used to replace the glass former SiO_2 or glass modifier SrO of the same amount. In the SABS-5 glass, 2 mol% nickel powder was added to replace glass former SiO_2 or B_2O_3.

4.2.2. Raman spectroscopy

For network structure analysis of the SABS glass compositions, quenched glass samples were polished to optical finish. Raman spectra of the polished samples were collected in 200-1600 cm^{-1} wave number range using a Raman spectrometer (JY Horbia LabRam HR 800, Horiba Ltd., Japan) with a CCD detector and a Labspec software package. The light source was a 514.57

nm argon laser at 50 mW power and 400 s exposure time. The spectra were later corrected for background noise and temperature effect [8]. For data analysis, the Raman spectra were fitted to Gaussian bands without any restrictions to deconvolute the superimposed Raman peaks [9,10]. Curve fitting was done with GRAMS/AI (7.02) software (Themo Fisher Scientific, Inc. Waltham, MA).

4.2.3 Thermal property measurement

Glass transition temperature T_g, dilatometric softening temperature T_d, and thermal expansion coefficient CTE were measured with a push-rod dilatometer (Model 1600R, The Edward Orton Jr. Ceramic Foundation, OH). Cylindrical samples of 27 mm long and 5 mm diameter were used. During the dilatometry study, the samples were heated at 3°C/min heating rate to 900°C for 2 hrs and then cooled to room temperature at the same rate. Each sample was thermally cycled three times under this condition. Average T_g, T_d, and CTE values were obtained from both the heating and the cooling cycles [11].

2.4 Phase analysis

For thermal stability study, bulk SABS glass samples were put on a platinum foil and heated to 850°C at the same heating and cooling rate of 5°C/min. The samples were thermally treated at 850°C for 50-200 hrs. XRD studies were carried out in an X'Pert PRO diffractometer (PANalytical B.V., EA Almelo, The Netherlands) to identify the crystalline phases in the thermally treated samples. The scan rate was 0.0020°/s with CuKα radiation (λ = 1.5406 Å).

4.3. Results and discussion

4.3.1. Overall glass structure

Thermal properties and thermal stability of a glass depends on the presence of structural units, their relative arrangement, and the amount of bridging oxygen [12]. These structural parameters in turn determine the glass network connectivity. To understand the network structure evolution of the SABS glasses, the Raman spectra of different SABS-0 glasses are shown in Fig. 4-1. Across 400-1200 cm^{-1} wave number range, peak intensity and peak width drastically decrease with nickel addition (Fig. 4-1(a)). Nickel replacement of SiO_2 has more dramatic effect on peak intensity and peak width than nickel replacement of SrO. Decreased peak width in Fig. 4-1(a) suggests that glass structural unit local ordering increases with nickel addition. Nickel replacement of SiO_2 has more effect on glass structure local ordering than nickel replacement of SrO. Absolute peak intensity decrease means decreased amount of structural units with nickel addition. However, relative change in peak intensity and peak width for a specific SABS glass is not directly comparable. Because of this, the Raman peaks of the three SABS-0 glasses were normalized. The normalized peaks do not show substantial peak intensity or peak width difference as shown in figure Fig. 4-1(b). This means the relative amount of different structural units in a SABS glass does not change significantly. Also, a strong peak shoulder appears around 885 cm^{-1} wave number, which will be discussed next.

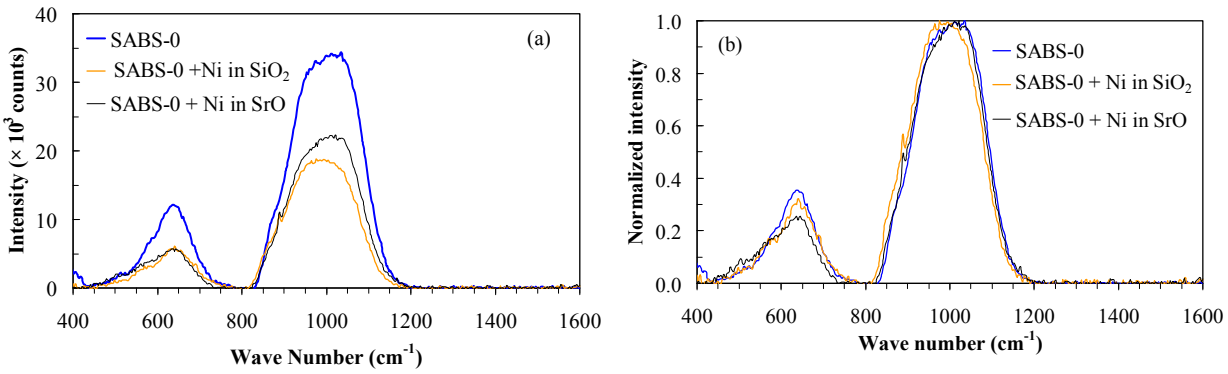

Fig. 4-1. Raman spectra of SABS-0 glasses: (a) as-collected, (b) normalized.

Raman spectra of different SABS-5 glasses are shown in Fig. 4-2. Peak intensity and peak width again drastically decrease with nickel replacement of SiO_2 or B_2O_3. The peak intensity decreases slightly more for the nickel replacement of B_2O_3 case. This again means the absolute amount of the glass structural units decreases but the local ordering increases for the SABS-5 glasses. Comparison of normalized peak intensity does not show any significant change for a specific SABS-5 glass, similar to Fig. 4-1(b). Also, nickel replacement of SiO_2 or B_2O_3 shows no change in the relative peak width. A strong peak again appears around 885 cm^{-1} wave number.

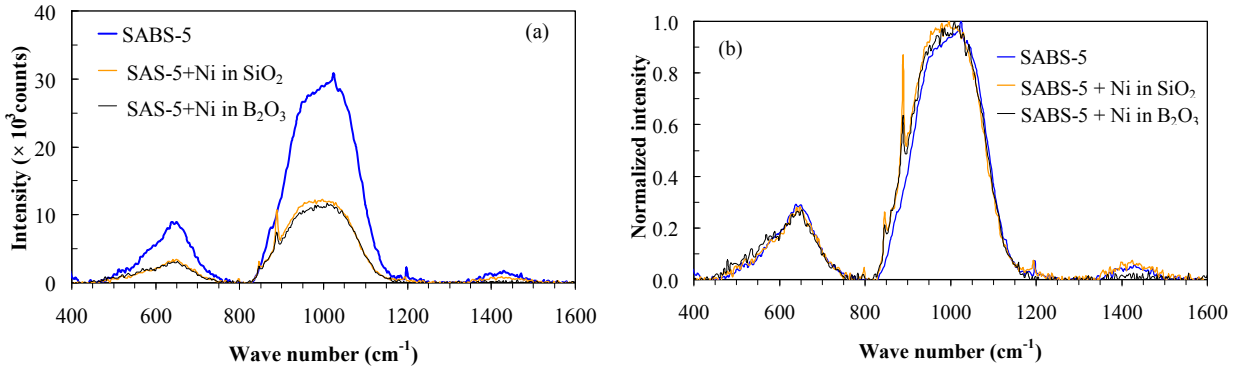

Fig. 4-2. Raman spectra of SABS-5 glasses: (a) as-collected, (b) normalized.

4.3.2. Glass structural unit local ordering

For discussion convenience, silicate glass and borate glass structures will be discussed again as in chapter three. In silicate glass, the 1060-1200 cm^{-1} wave number peak comes from vitreous SiO_2 with four bridging oxygen atoms. There are four major peaks representing the nature and contribution of different silicate structural units. The 1050-1100 cm^{-1} wave number peak describes the stretching motion of disilicate composition with three bridging oxygen atoms. The 950-1000 cm^{-1} wave number peak describes the stretching motion of metasilicate composition with two bridging oxygen atoms. The 900 cm^{-1} wave number peak reflects the pyrosilicate composition with one bridging oxygen atom. The 850 cm^{-1} wave number peak represents orthosilicate composition with zero bridging oxygen [13]. In this context the silicate units with four bridging oxygen atoms, three bridging oxygen atoms, two bridging oxygen atoms, one bridging oxygen atom, and zero bridging oxygen atom can be denoted as Q^4, Q^3, Q^2, Q^1, and Q^0 respectively. The numerals represent the number of bridging oxygen atoms that each structural unit has. The 400-700 cm^{-1} wave number peak is due to delocalized vibration of Si-O-Si bonding from mixed stretching and bending modes [13,14]. In borate glass, the 1300-1600 cm^{-1} wave number peak describes the $B\text{-}O^-$ (O^- denotes the non-bridging oxygen) stretching mode within chain and ring metaborates which also connect the network [15].

Based on the above understanding, the Raman peaks in different wave number ranges of the SABS glass spectra can be identified. However, peaks corresponding to different structural units have a tendency to overlap due to a high degree of disorder (peak widening). Also, peak frequency shift occurs for such complex glass systems [16]. To establish the correlation between the Raman peaks and specific glass structural units, the spectrum for each SABS glass sample needs to be deconvoluted. The deconvoluted spectra for the SABS-0 glass compositions are

given in Fig. 4-3 and for the SABS-5 glass compositions are given in Fig. 4-4. The thick line shows the as-collected Raman spectra. The thin lines show the deconvoluted peaks from the Gaussian fitting. With the understanding that the composition difference between the conventional silicate glass and the SABS glasses can cause some peak shift, deconvoluted Raman peaks can be identified. In this study, detailed Raman spectrum analysis can be separated into three regions: 1200-1600 cm^{-1}, 800-1200 cm^{-1}, and 400-800 cm^{-1}.

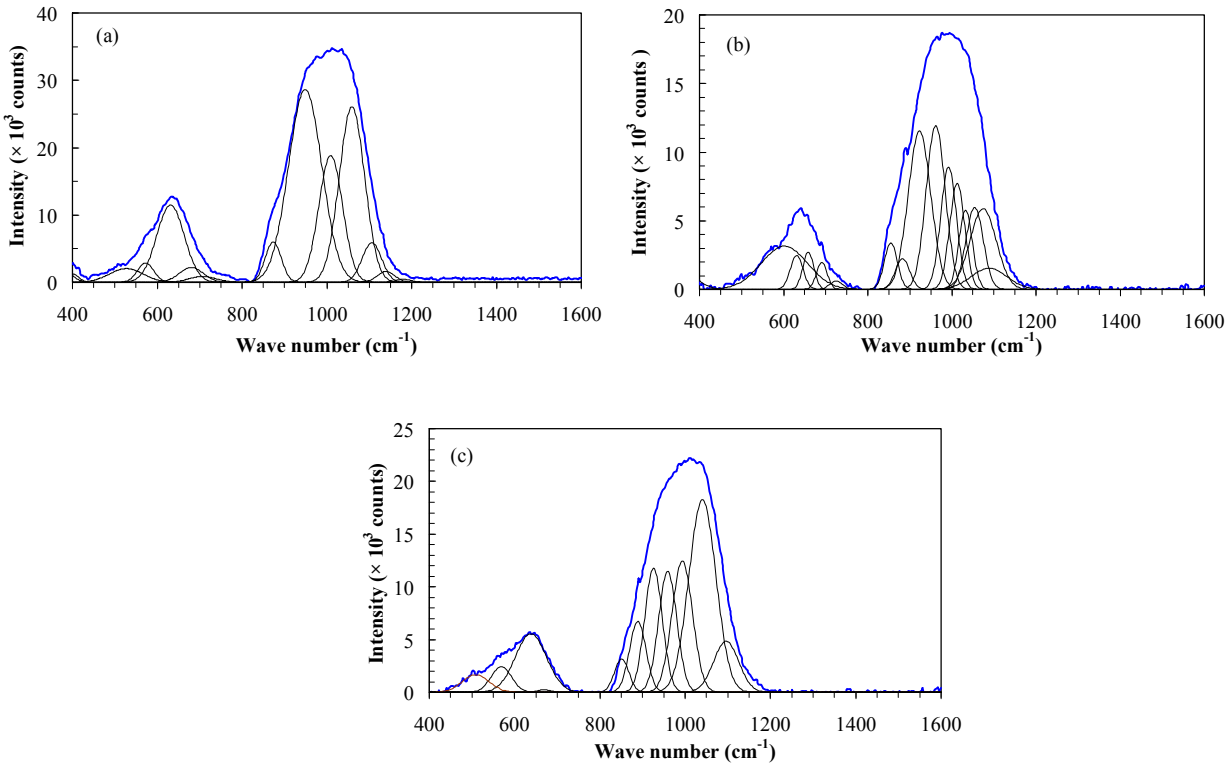

Fig. 4-3. Deconvoluted Raman peaks for: (a) SABS-0, (b) 2 mol% nickel replacement of SiO_2 in SABS-0, and (c) 2 mol% nickel replacement of SrO in SABS-0.

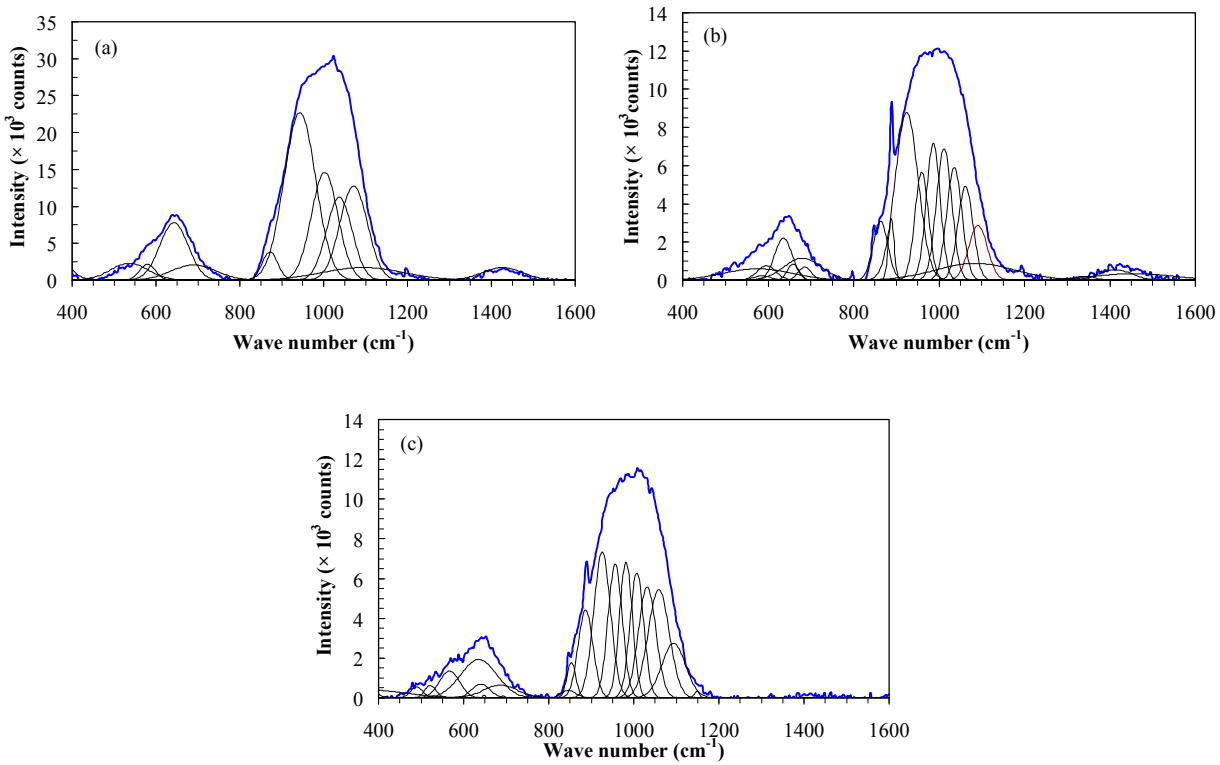

Fig. 4-4. Deconvoluted Raman peaks for: (a) SABS-5 glass, (b) 2 mol% nickel replacement of SiO_2 in SABS-5 glass, and (c) 2 mol% nickel replacement of B_2O_3 in SABS-5 glass.

For the SABS-0 glass, no peak is detected in the 1200-1600 cm^{-1} wave number range, corresponding to the Raman peaks from B_2O_3. For the SABS-5 glass, the 1426 cm^{-1} wave number peak is from metaborate units [17]. For the SABS-5 glass with 2.0 mol% nickel replacement of SiO_2, the peak at 1426 cm^{-1} splits into three peaks at 1340 cm^{-1}, 1413, and 1457 cm^{-1}. This peak splitting process is supported by comparing normalized areas of these peaks. The total area of the 1340 cm^{-1}, 1413 cm^{-1}, and 1457 cm^{-1} peaks match with the 1426 cm^{-1} peak area in the SABS-5 glass. The 1457 cm^{-1} peak can be assigned to localized stretching vibration of B-O^- bonds in BO_3 triangles [14] or di-triborate group [18]. The 1340 cm^{-1} peak can be assigned to di-triborate group or the stretching mode of metaborates associated with non-bridging oxygen

[15]. The peak splitting indicates local ordering of the metaborate structural units. For the SABS-5 glass with nickel replacement of B_2O_3, no peak is observed in the 1200-1600 cm^{-1} wave number region. This is consistent with the original spectrum in Fig. 2. Nickel replacement of B_2O_3 causes the disappearance of the $B\text{-}O^-$ stretching mode of ring and chain metaborates in the glass network. The effect of nickel addition on the SABS glass properties is similar to those of Fe^{2+} and Mn^{2+}, acting as a glass modifier [19]. In the nickel-containing SABS glasses, nickel likely forms short-range NiO_6 octahedra instead of tetrahedral arrangement.

For the de-convoluted peaks in the 800-1200 cm^{-1} wave number range, it can be understood as follows. For the SABS-0 glass, the weak 1180 cm^{-1} and 1143 cm^{-1} wave number peaks are from the Q^4 units [20]. The 1060 cm^{-1} and 1105 cm^{-1} wave number peaks are from the Q^3 units. The 1010 cm^{-1} and 949 cm^{-1} wave number peaks are from the Q^2 units. The 872 cm^{-1} wave number peak is from the Q^0 units [21]. This means for the SABS-0 glass, a small fraction of SiO_4 glass structure units are fully connected by bridging oxygen atoms, most of the SiO_4 glass structure units are partially connected with other SiO_4 structure units, and a small fraction of the SiO_4 glass structure units have zero bridging oxygen atoms and only coordinate with the glass modifier ions.

With 2.0 mol% nickel replacement of SiO_2 in the SABS-0 glass, the peaks corresponding to the Q^4 units are absent. The 1105 cm^{-1} wave number peak shifts to lower wave number of 1089 cm^{-1}. The 1060 cm^{-1} peak splits into four peaks: 1033 cm^{-1}, 1054 cm^{-1}, 1074 cm^{-1}, and 1089 cm^{-1} peak. The 1010 cm^{-1} peak splits into two peaks at 992 cm^{-1} and 1013 cm^{-1} wave numbers. The 948 cm^{-1} peak in the SABS-0 glass splits into two peaks at 962 cm^{-1} and 923 cm^{-1}. All these peak splitting processes can be confirmed by peak area integration. The 923 cm^{-1} peak is attributed to discrete $Si(OAl)_4$ units with one bridging oxygen [22]. A new peak at 882 cm^{-1}

appears, as pointed out before. This peak is associated with discrete $Si(OAl)_4$ units with zero bridging oxygen atom, which is analogous to the 850 cm^{-1} peak in silicate glass [22]. The 855 cm^{-1} wave number peak corresponds to the Q^0 units. This Raman peak analysis shows that for the SABS-0 glass with 2 mol% nickel replacement of SiO_2, no SiO_4 structure units are fully connected to its neighboring SiO_4 units. Most of SiO_4 glass structure units are partially connected to other SiO_4 units, and a small fraction of SiO_4 glass structure units stay separated from other SiO_4 units. The Q^0 unit content increases more obviously as evidenced by the 882 cm^{-1} and 855 cm^{-1} peak appearance.

For the SABS-0 glass with 2.0 mol% nickel replacement of SrO, similar observation can be made. The 949 cm^{-1} peak splits into 994 cm^{-1}, 959 cm^{-1}, and 926 cm^{-1} peaks. This peak splitting again means increased local ordering of glass structural units. The 889 cm^{-1} peak is attributed to discrete $Si(OAl)_4$ units with zero bridging oxygen atom.

For the SABS-5 glass, no Q^4 glass structural unit is detected. The 1094 cm^{-1}, 1072 cm^{-1}, and 1037 cm^{-1} wave number peaks are from the Q^3 units. The 943 cm^{-1} wave number peak is from the Q^2 units. The 872 cm^{-1} wave number peak is from the Q^0 units. This means for the SABS-5 glass, none of the SiO_4 glass units are fully connected to other SiO_4 units. Most of the SiO_4 units are partially connected to other SiO_4 units in the glass network. Some SiO_4 units stay separated from other SiO_4 units. For the SABS-5 glass with 2 mol% nickel replacement of SiO_2, the 1072 cm^{-1} peak splits into 1091 cm^{-1}, 1084 cm^{-1}, and 1062 cm^{-1} peaks. The 987 cm^{-1}, 1003 cm^{-1}, and 1012 cm^{-1} peaks can be assigned to Q^2 units. The 943 cm^{-1} peak splits into 924 cm^{-1} and 960 cm^{-1} peaks. The 872 cm^{-1} peak splits into 863 cm^{-1} and 888 cm^{-1} peaks. This extensive peak splitting again means increased local ordering of glass structural units. For the SABS-5 glass with 2 mol% nickel replacement of B_2O_3, similar observations can be made. A weak peak

appears at 1148 cm^{-1} wave number which can be assigned to the Q^4 units. The 1072 cm^{-1} peak splits into 1059 cm^{-1} and 1094 cm^{-1} peaks. The 1002 cm^{-1} peak splits into 982 cm^{-1} and 1008 cm^{-1} peaks. The 944 cm^{-1} peak splits into 926 cm^{-1} and 956 cm^{-1} peaks. The 874 cm^{-1} peak splits into 847 cm^{-1}, 857 cm^{-1}, and 887 cm^{-1} peaks. This again indicates that nickel replacement of SiO_2 and B_2O_3 in the SABS-5 glass increases glass local ordering and nickel ions act as a glass modifier.

For the SABS-0 glass, the 619 cm^{-1} and 641 cm^{-1} wave number peaks are from the Q^2 units corresponding to the characteristic bands of metasilicate glasses between 620-640 cm^{-1} [23]. The 606 cm^{-1} wave number peak is from the broken Si-O bonds as in vitreous silica with the Q^3 units [16,24]. With nickel replacement of SiO_2, peak shifting occurs in the SABS-0 glass along with the appearance of new peaks. The 606 cm^{-1} peak shifts to 602 cm^{-1} with significantly increased integrated area. The 619 and 641 cm^{-1} peaks shift to 631 cm^{-1} and 659 cm^{-1} respectively with decreased integrated area. The 690 cm^{-1} peak can be assigned to the Q^1 units [14,23]. A new, weak peak appears near 725 cm^{-1} wave number which can be assigned to the stretching vibrational mode of AlO_4 Q^4 units [14]. With nickel replacement of SrO, peak splitting is not clearly observed. However, new peaks appear. The 509 cm^{-1} peak is assigned to Si-O-Al linkages with four bridging oxygen [14]. The 569 cm^{-1} peak is attributed to Al-O-Al bonds originating from disordering of AlO_4 and SiO_4 structural units [25]. A very weak peak at 670 cm^{-1} wave number is attributed to the Q^1 units [13,14]. Increased amount of broken Si-O bonds in the SABS-0 glass with nickel replacement of SiO_2 and disordered Al-O-Al bonds in the SABS-0 glass with nickel replacement of SrO suggest that nickel addition weakens the overall glass structure.

For the SABS-5 glass, the 642 cm^{-1} and 692 cm^{-1} wave number peaks are from the Q^2 units, the Q^1 units, and Si-O-B bonds [14]. The 537 cm^{-1} and 580 cm^{-1} wave number peaks are

from BO_4 units in anionic rings [15]. With nickel replacement of SiO_2 in the SABS-5 glass, the 692 cm^{-1} peak splits into 686 cm^{-1} and 681 cm^{-1} peaks. The 642 cm^{-1} peak splits into 659 cm^{-1} and 636 cm^{-1} peaks. The 580 cm^{-1} peak splits into 596 cm^{-1}, 586 cm^{-1}, and 576 cm^{-1} peaks. The 537 cm^{-1} peak disappears. A very weak peak at 460 cm^{-1} wave number appears, which is assigned to BO_4 tetrahedra [17]. Also, the 692 cm^{-1} peak splits into 692 cm^{-1} and 687 cm^{-1} peaks. The 642 cm^{-1} peak splits into 636 cm^{-1}, 640 cm^{-1}, and 648 cm^{-1} peaks. A weak peak at 490 cm^{-1} wave number appears, which can be assigned to the broken Si-O bonds. Again, the splitting of peaks indicates the increased local ordering of the glass structural units.

Based on the Raman spectrum analysis of the nickel containing SABS-0 and SABS-5 glasses, two conclusions can be drawn for the effect of nickel addition on the SABS glass. First, nickel addition causes Q^4 unit disappearance in SABS-0 glass and increased amount of non-bridging oxygen atoms in both SABS-0 and SABS-5 glass. Second, the peaks correspond to the Q^2 and Q^3 units split and discrete $Si(OAl)_4$ and $Si(OAl)_4$ peaks appear, indicating increased local ordering of glass structural units and presence of microdomain region with heterogeneous composition. From these conclusions it can be inferred that nickel acts as a glass modifier.

4.3.3. Glass network connectivity

Glass network connectivity indicates glass forming and retaining ability. If a glass has high connectivity, it is likely to be stable and resistant to devitrification. If a glass has low connectivity, it is likely to devitrify. Connectivity in a glass structure is determined by the number and arrangement of bridging and non-bridging oxygen bonds which link each of the building blocks to its neighbors. High amount of non-bridging oxygen atoms decreases glass connectivity. To compare SABS glass connectivity, the relative percent of different SiO_4

structural units in the 800-1200 cm^{-1} region is given in Table 4-1. This particular region is chosen because in the 400-800 cm^{-1} wave number region, there are mixed stretching and bending vibration mode of silicate and borate structural units. In the 1200-1600 cm^{-1} wave number region, the characteristic peaks of SiO_4 structural units is absent. The 800-1200 cm^{-1} region provides a simpler view to understand the effect of nickel addition on the glass network structure without the presence of BO_3 and BO_4 structural units.

Table 4-1. Relative percent of different structural units in the 800-1200 cm^{-1} region

Composition	Q^4 (%)	Q^3 (%)	Q^2 (%)	Q^1 (%)	Q^0 (%)
SABS-0	1.36	33.18	61.97		3.49
SABS-0+Ni/SiO_2		32.24	39.88	21.58	6.31
SABS-0+Ni/SrO		42.57	32.21	14.43	10.80
SABS-5		39.99	56.93		3.07
SABS-5+Ni/SiO_2		34.44	33.65	24.17	7.74
SABS-5 +Ni/B_2O_3	0.23	36.62	35.53	16.27	11.36

As can be seen from Table 4-1, only the SABS-0 glass has significant amount of Q^4 units. SABS-5 glass with nickel replacement of B_2O_3 has only a negligible amount of Q^4 units. The most obvious trend is increased Q^1 and Q^0 structural units in the nickel containing SABS-0 and SABS-5 glasses. Qualitatively, this glass structural unit evolution leads to lower glass network connectivity. Network connectivity is calculated from equation 3-1 in chapter 3.

It should be pointed out that from the SABS glass Raman spectra, it is not possible to determine the amount of network forming cations contributed by intermediate ion Al^{3+}. From

Raman spectra, it can be seen that Al_2O_3 participates in the glass network. Since Al_2O_3 content is only 5 mol% in the SABS glass, all the Al^{3+} ions are assumed to participate in the glass network during glass network connectivity calculation. The bond strength of SiO_2, B_2O_3, Al_2O_3, La_2O_3, SrO, and NiO are 1.56, 1.62, 0.97, 0.43, 0.27, and 0.55 respectively [7]. The glass network connectivity of the SABS glasses is then calculated using equation (3-1) and the results are given in Table 4-2.

Table 4-2. Glass network connectivity of SABS glasses

Composition	$\frac{\left[\frac{\sum Z_i(F_iV_i)}{\sum Z_iV_i}\right]_{\text{Network Former}}}{\left[\frac{\sum F_iV_i}{\sum V_i}\right]_{\text{Network Former+Modifier}}}$	$\frac{\sum O^+}{\sum O^- + \sum O^+}$	Glass network connectivity ψ (%)
SABS-0	1.400	0.531	74.31
SABS-0 + Ni/SiO_2	1.415	0.518	73.23
SABS-0 + Ni/SrO	1.385	0.519	71.84
SABS-5	1.380	0.514	70.97
SABS-5 + Ni/SiO_2	1.394	0.487	67.95
SABS-5 + Ni/B_2O_3	1.402	0.474	66.42

From Table 4-2, it can be seen that glass network connectivity decreases with nickel addition for both SABS-0 and SABS-5 glasses. Also, nickel replacement of SrO induces more network connectivity decrease than nickel replacement of SiO_2 for SABS-0 glass; nickel replacement of B_2O_3 induces more network connectivity decrease than nickel replacement of

SiO_2 for SABS-5 glass. However, advanced techniques (e.g. ^{17}O NMR study) to quantify the amount of bridging and nonbriging oxygens in a glass system will give more precise quantification of network connectivity.

4.3.4. Thermal properties

Seal glass thermal properties (T_g, T_d, and CTE) have critical impact on glass sealing ability. T_g and T_d represent glass viscoelasticity and flowability at cell operation temperatures. From the dilatometry study, T_g, T_d, and CTE values for each SABS glass sample were obtained as given in Table 4-3. No devitrified phase appears in the SABS samples studied by dilatometry. This indicates that the SABS glasses do not devitrify at temperatures up to 820°C.

Table 4-3. Thermal properties of SABS glasses.

Composition	T_g (°C)	T_d (°C)	CTE ($\times 10^{-6}$/°C)
SABS-0	775	815	10.8 ± 0.5
SABS-0 +Ni/SiO_2	760	820	11.90 ± 0.44
SABS-0 +Ni/SrO	760	810	11.76 ± 0.35
SABS-5	710	765	11.80 ± 0.37
SABS-5 + Ni/SiO_2	705	755	12.31 ± 0.06
SABS-5 + Ni/B_2O_3	725	770	12.21 ± 0.22

For the SABS-0 glass with nickel replacement of SiO_2, decrease in T_g and insignificant change in T_d are observed. Nickel replacement of SrO decreases T_g but T_d remains unchanged. Decrease in T_g is consistent with the SABS glass network structure change with nickel addition. As seen from the glass structure analysis, nickel addition hinders Q^4 unit formation, weakens the network connectivity, and decreases T_g.

When 2 mol% nickel replaces SiO_2 in the SABS-5 glass, T_g and T_d decrease slightly by 5-10°C. However, when nickel replaces the same amount of B_2O_3 in the SABS-5 glass, T_g increases by 15°C and T_d increases by 5°C. For the SABS-5 glass, decrease in T_g and T_d with nickel replacement of SiO_2 is expected because of the decrease in glass network former SiO_2, which also has high T_g and T_d values. Nickel, as a glass modifier, creates non-bridging oxygen atoms in the SABS glass and causes lower glass network connectivity. For the SABS-5 glass, increases in T_g and T_d with nickel replacement of B_2O_3 can be from higher nickel bond strength effect and reduced amount of B_2O_3. Also, the SiO_4 tetrahedra Q^4 units (1148 cm^{-1} peak in Raman spectra) reappear and this could induce higher glass connectivity in very localized regions. From these observations, it may be concluded that nickel replacement of B_2O_3 shifts the glass T_g and T_d to higher temperatures while nickel replacement of SiO_2 shifts the glass T_g and T_d to lower temperatures.

2 mol% nickel replacement either for SiO_2 or SrO in SABS-0 glass does not significantly changes the CTE as can be seen from Table 4-3. All the nickel added SABS-0 glasses have the CTE within the error range of the SABS-0 glasses ($10.8 \pm 0.5 \times 10^{-6}$/°C). This observation is consistent with the insignificant decrease in T_g and T_d with nickel addition in SABS-0 glass. 2mol% nickel replacement in SABS-5 glass increases the CTE by ~ 5.0×10^{-6}/°C which is consistent with the decreased network connectivity in Table 4-2 and supports that nickel is a network modifier.

4.3.5. Thermal stability

Thermal stability of a seal glass is a must for solid oxide cells. The fundamental challenge is not the presence of devitrified phases, but the continuous evolution and instability of

the seal glass. Excessive devitrification causes the glass to undesirably change from being viscous to being rigid. Sealing ability deteriorates over time and thermal stress increases because of difference in CTEs of glassy phase and devitrified phase. The end result is cracking and degradation of sealing function. In this work, XRD is used to analyze the SABS glass phase evolution with different thermal treatment time at 850°C. Different phases are identified and given in Table 4-4.

Table 4-4. SABS glass phase evolution after different thermal treatment time at 850°C.

Sample	20 hr	50 hr	100 hr	200 hr
SABS-0	×	×	×	×
SABS-0 +Ni/SiO_2	×	×	×	t-$La_2Si_2O_7$
SABS-0 +Ni/SrO	×	×	$La_{10}Al_4O_{21}$, $La_4Sr_3O_9$	$La_{10}Al_4O_{21}$, La_2SiO_5, $SrSiO_3$, $Sr_5Al_2O_8$
SABS-5	×	×	m-$La_2Si_2O_7$, α-$SrSiO_3$, Sr_2SiO_4	Not studied
SABS-5 + Ni/SiO_2	m-$La_2Si_2O_7$, α-$SrSiO_3$	m-$La_2Si_2O_7$, $SrSiO_3$, Sr_2SiO_4	Not studied	Not studied
SABS-5 + Ni/B_2O_3	$Sr_7Al_2O_{10}$	m-$La_2Si_2O_7$, α-$SrSiO_3$, Sr_2SiO_4	Not studied	Not studied

As shown in Table 4-4, multiple phases evolve simultaneously for the same glass composition at different thermal treatment times or for different glass compositions at the same thermal treatment time. Devitrified phases that form at shorter thermal treatment time can disappear at longer thermal treatment time. One example is the $La_4Sr_3O_9$ phase for the SABS-0 glass with nickel replacement of SrO and the other is the $Sr_7Al_2O_{10}$ phase for the SABS-5 glass with nickel replacement of B_2O_3. These phase changes suggest that the devitrified phase nucleation and growth are accompanied by decomposition reactions. Simultaneous evolution of several devitrified phases indicates that eutectic crystallization occurs in these glasses [26].

In the SABS-0 glass, no devitrified phase is detected up to 200 hrs of thermal treatment (Fig. 4-5(a)). When nickel is added to replace SiO_2, the SABS-0 glass devitrifies after 200 hrs of thermal treatment with the appearance of tetragonal $La_2Si_2O_7$ phase (Fig. 4-5(b)). The SABS-0 glass with nickel replacement of SrO devitrifies at 100 hrs with the appearance of $La_4Sr_3O_9$ and $La_{10}Al_4O_{21}$ phases. $La_4Sr_3O_9$ phase is metastable and disappears after 200 hrs of thermal treatment with the appearance of new phases La_2SiO_5, $SrSiO_3$, and $Sr_5Al_2O_8$. La, Si, Sr, and Al ions separate from the glass network and participate in devitrification. Nickel addition degrades the SABS-0 glass thermal stability by facilitating devitrification. This can be explained from the change in glass structure. Appearance of less connected structural units such as Q^1 and Q^0 enhances devitrification [27]. With nickel addition, Q^0 and Q^1 units increase in the SABS glass structure and Si-O bond breaks. Thus network connectivity of the SABS glass decreases. This is further supported by the evolution of aluminum containing phases in the SABS-0 glass with nickel replacement of SrO, in which the Q^0 unit content is higher than that of the SABS-0 glass with nickel replacement of SiO_2. Also, portions of Q^1 and Q^0 units are composed of $Si(OAl)_4$.

Microdomains with heterogeneous composition then act as nucleation sites and induce devitrification.

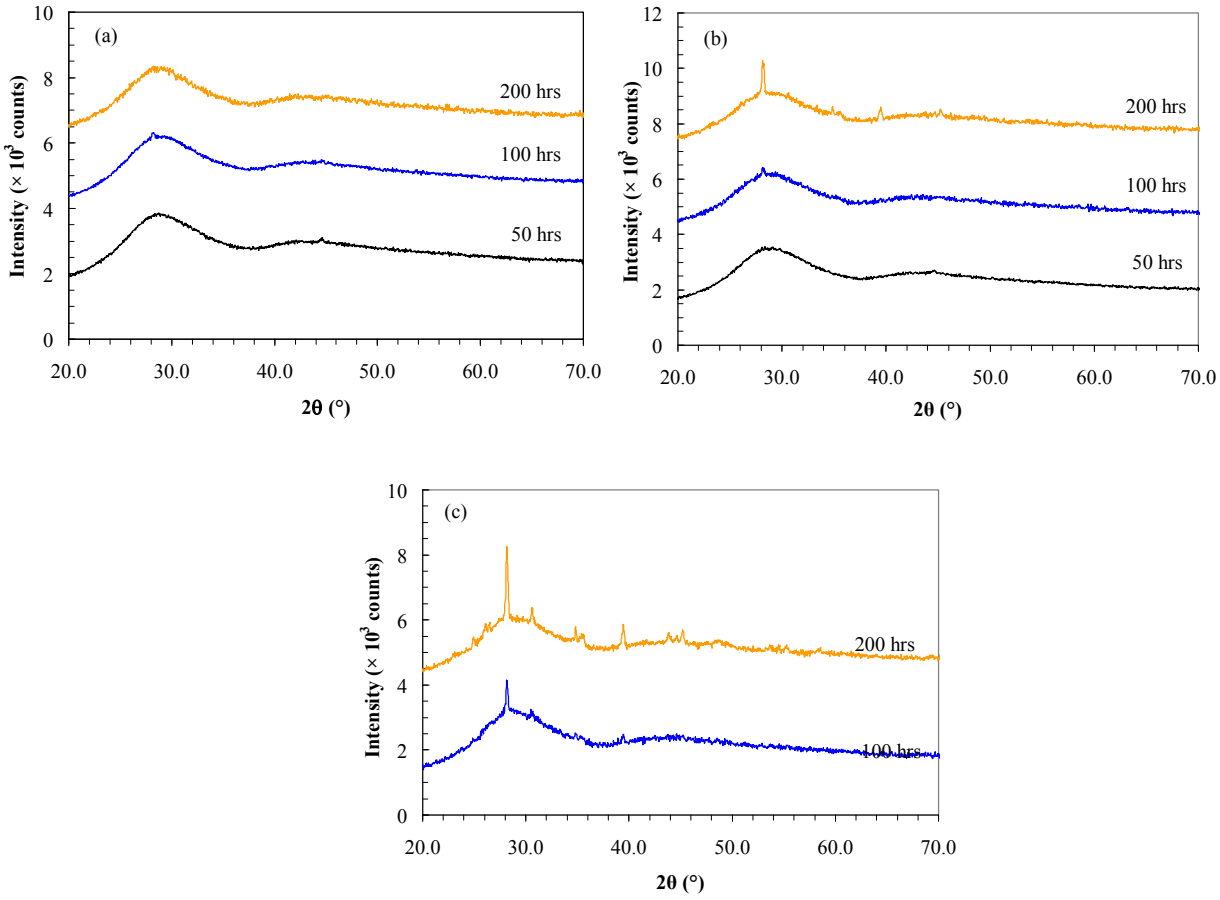

Fig. 4-5. XRD patterns of SABS-0 glass after thermal treatment at 850°C for different times: (a) no nickel addition, (b) 2 mol% nickel replacement of SiO_2, and (c) 2 mol% nickel replacement of SrO.

The SABS-5 glass devitrifies after 50 hr thermal treatment as shown in Fig. 4-6. Small devitrified peaks are observed but the intensity and number of peaks is insufficient to determine the devitrified phases. After 100 hr thermal treatment at 850°C, monoclinic $La_2Si_2O_7$ phase along with small amounts of α-$SrSiO_3$ and Sr_2SiO_4 phases appears. When 2 mol% nickel is added to

replace SiO_2 (Fig. 4-6(b)) or B_2O_3 (Fig. 4-6(c)), devitrification occurs much earlier, only after 20 hrs of thermal treatment.

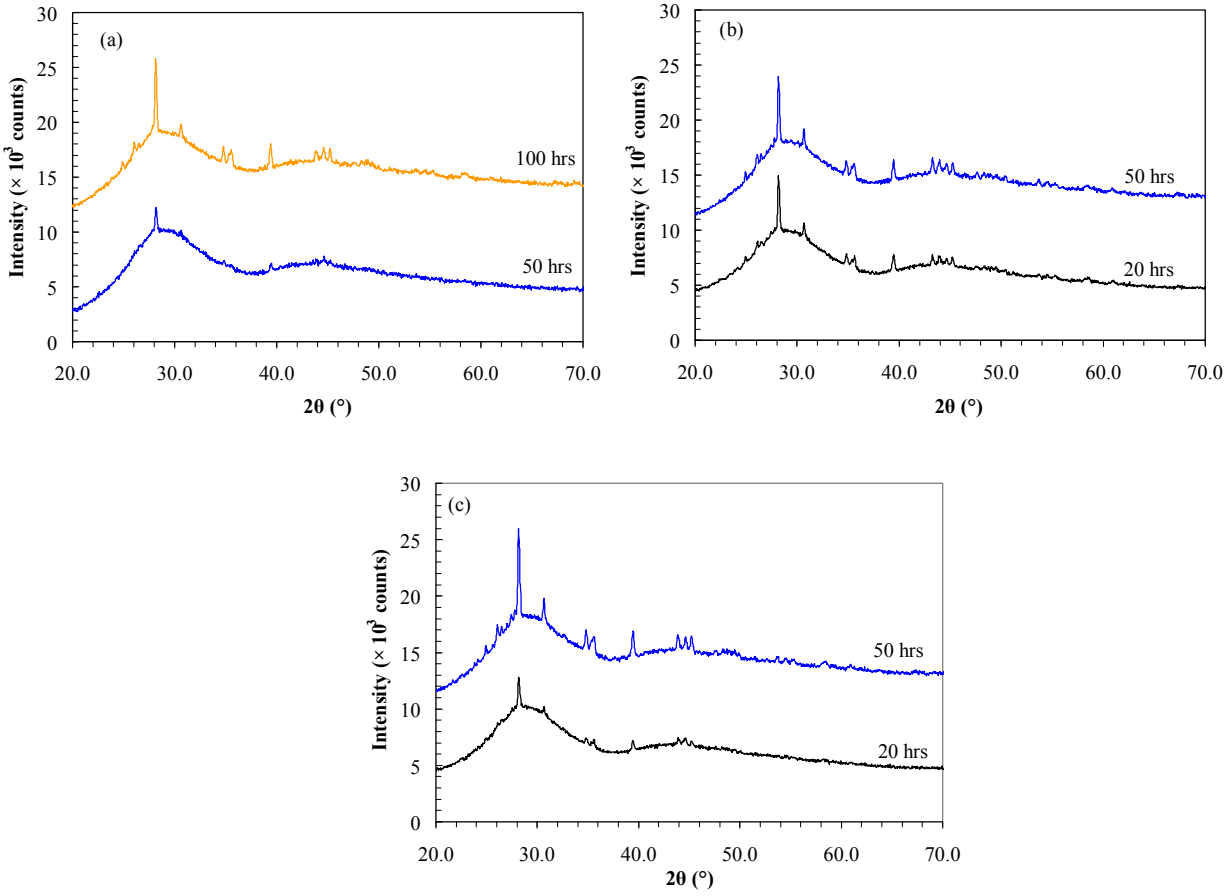

Fig. 4-6. XRD patterns of SABS-5 glass after thermal treatment at 850°C for different times: (a) no nickel addition, (b) 2 mol% nickel replacement of SiO_2, and (c) 2 mol% nickel replacement of B_2O_3.

For the nickel replacement of SiO_2 glass sample, the devitrified phases are monoclinic $La_2Si_2O_7$ and α-$SrSiO_3$ in contrast to the tetragonal $La_2Si_2O_7$ phase for the SABS-0 glass. For nickel replacement of B_2O_3 in the SABS-5 glass, the devitrified phase is $Sr_7Al_2O_{10}$. However, as the thermal treatment time increases to 50 hr, the devitrified phases evolve into the same species as in the SABS-5 glass: $La_2Si_2O_7$, SrSiO3, and Sr_2SiO_4. $La_2Si_2O_7$ is the main phase among the

three. This means nickel replacement of either SiO_2 or B_2O_3 in the SABS-5 glass exacerbates devitrification. The species that separate from the glass network are lanthanum, silicon, and strontium ions. Boron species is not involved in the devitrified phase formation. Also, $Sr_7Al_2O_{10}$ phase is thermodynamically metastable for the SABS-5 glass with 2 mol% nickel replacement of B_2O_3. Absence of Al_2O_3 containing phases in the 50 hr thermally treated sample supports the observation that devitrification occurs through decomposition reactions. The devitrified phases after 50 hr thermal treatment of the SABS-5 glass with 2 mol% nickel replacement of SiO_2 are also the same phases as those in the SABS-5 glass after 100 hr thermal treatment. The reason for earlier devitrification with nickel addition is the same as in the SABS-0 glass. The absence of nickel in the devitrified phases suggests that nickel mainly acts as a nucleating agent during the devitrification process.

4.4. Conclusions

This study is focused on the effects of 2 mol% nickel replacement of glass formers SiO_2 and B_2O_3 and glass modifier SrO on SrO-La_2O_3-Al_2O_3-B_2O_3-SiO_2 (SABS) glass structure and thermal properties. Glass structural unit local ordering has been systematically studied. Nickel decreases SABS glass network connectivity and acts as a modifier in the glass system. Nickel replacement of SrO and SiO_2 in SABS-0 glass decreases T_g. Nickel replacement of B_2O_3 and SiO_2 in SABS-5 decreases T_g and T_d. Nickel replacement in SABS-5 glass increase CTE by ~ 0.5×10^{-6}/°C. Nickel addition in both SABS-0 and SABS-5 glasses degrades thermal stability by inducing microheterogeneity. Fundamental glass structure evolution with nickel addition has been elucidated by comparing glass network connectivity of different compositions.

References

[1] G. Calas, L. Cormier, L.Galoisy, and P. Jollivet, Structure–property relationships in multicomponent oxide glasses, C R Chimie 5, 831-843, 2002.

[2] L. Galoisy, L. Cormier, S. Rossano, A. Ramos, G. Calas, P. Gaskell, M. L. Grand, Cationic ordering in oxide glasses: the example of transition elements, Mineralogical Magazine 64, 409-424, 2000.

[3] E. A. Brandes, G. B. Brook, Smithells Metals Reference Book, 7th edition, Butterworth Heinemann, Oxford, UK, 14-4, 1992.

[4] S. B. Sohn, S. Y. Choi, G. H. Kim, H. S. Song, and G. D. Kim, Suitable glass-ceramic sealant for planar solid oxide fuel cells, Journal of the American Ceramic Society 87, 254-260, 2004.

[5] Y. S. Chou, J. W. Stevenson, and R. N. Gow, Novel alkaline earth silicate sealing glass for SOFC Part I The effect of nickel oxide on the thermal and mechanical properties, Journal of Power Sources 168, 426-433, 2007.

[6] N. Lahl, K. Singh, L. Singheiser, K. Hilper, and D. Bahadur, Crystallisation kinetics in AO -Al_2O_3-SiO_2-B_2O_3 glasses (A = Ba, Ca, Mg), Journal of Materials Science 35, 3089-3096, 2000.

[7] H. Scholze, Glass nature, structure, and properties, Springer Verlag, New York, USA, 1991.

[8] A. K. Hassan, L. M. Torell, L. Börjesson, and H. Doweidar, Structural changes of B_2O_3 through the liquid-glass transition ramnge: A Raman-scattering study, Physical Review B 45, 12797-12805, 1992.

[9] B. O. Mysen, L. W. Finger, D. Virgo, and F. A. Seifert, Curve-fitting of Raman spectra in silicate glass, American Mineralogist 67, 686-695, 1982.

[10] H. Li, P. Hrma, J. D. Vienna, M. Qian, Y. Su, and D. E. Smith, Effects of Al_2O_3, B_2O_3,

Na_2O, and SiO_2 on nepheline formation in borosilicate glasses: chemical and physical correlations, Journal of Non-Crystalline Solids 331, 202-216, 2003.

[11] M. K. Mahapatra, K. Lu, and W. T. Reynolds. Jr., Thermophysical properties and devitrification of $SrO–La_2O_3–Al_2O_3–B_2O_3–SiO_2$-based glass sealant for solid oxide fuel/electrolyzer cells, Journal of power sources 179, 106-112, 2008.

[12] J. E. Shelby, Introduction to glass science and technology, The Royal Society of Chemistry Cambridge, UK, 2005.

[13] P. McMillan, Structual studies of silicate glasses and melts- applications and limitations of Raman Spectroscopy, American Mineralogist 69, 622-644, 1984.

[14] E. I. Kamitoss, J. A. Kapoutsis, H. Jain, and C. H. Hsieh, "Vibrational study of the role of trivalent ions in sodium trisilicate glass, Journal of Non-Crystalline Solids 171, 31-45, 1994.

[15] R. K. Brow, D. R. Tallant, and G. L. Turner, Raman and ^{11}B nuclear magnetic resonance spectroscopic studies of alkaline-earth lanthanoborate glasses, Journal of the American Ceramic Society 79, 2410-2416, 1996.

[16] S. K. Sharma, Raman investigation of ring configurations in vitreous silica, Nature 292, 140-141, 1981.

[17] M. Środa, and C. Paluszkiewicz, Spectroscopic study of the influence of LaF_3 admixture on the crystallization and structure of borosilicate glass, Journal of Molecular Structure 834-836, 302-307, 2007.

[18] W. L. Konijnendijk, and J. M. Stevels, The structure of borate glasses studied by Raman Scattering, Journal of Non-Crystalline Solids 18, 307-331, 1975.

[19] G. Calas, and J. Petiau, The structure of non-Crystalline Materials: Proc. Second

International Conference (Cambridge, UK,12-15 July, 1982) (Society of Glass Technology) ed P.H. Gaskel, J.M. Parker, E.A. Davis, Taylor and Francis Ltd., London, New York, 18-28, 1982.

[20] F. Seifert, B. O. Mysen, and D. Virgo, Three-dimensional network structure of quenched melts (glass) in the systems SiO_2-$NaAlO_2$, SiO_2-$CaAl_2O_4$ and SiO_2-$MgAl_2O_4$, American Mineralogist 67, 696-717, 1982.

[21] M. K. Mahapatra, K. Lu, and R. J. Bodnar, Network structure and thermal property of a novel high temperature seal glass, Applied Physics A 95, 493-500, 2009.

[22] P. McMillan, B. Piriou, and A. Navrotsky, A Raman spectroscopic study of glasses along the joins silica-calcium aluminate, silica-sodium aluminate, and silica-potassium aluminate, Geochimica et Cosmochimica Acta 46, 2021-2037, 1982.

[23] B. O. Mysen, D. Virgo, and F. A. Seifert, Relationships between properties and structure of aluminosilicate melts. American Mineraogist 1985, 70, 88-105.

[24] N. F. Mott, The viscosity of vitreous silicon oxide, Philosophical Magazine B 56, 257-262, 1987.

[25] C. I. Merzbacher, and W. B. White, The structure of alkaline earth aluminosilicate glasses as determined by vibrational spectroscopy, Journal of Non-Crystalline Solids 130, 18-34, 1991.

[26] D. Shi, M. Tang, M. S. Boley, M. Hash, K. Vandervoort, H. Claus, and Y. N. Lwin, Crystallization of metal-oxide glasses in Bi-Sr-Ca-Cu-O systems, Physical Review B 40, 2247-2253, 1989.

[27] J. Deubener, Structural aspects of volume nucleation in silicate glass, Journal of Non -Crystalline Solids 351, 1500-1511, 2005.

CHAPTER FIVE

INTERFACE OF $SrO\text{-}La_2O_3\text{-}Al_2O_3\text{-}SiO_2$ SEAL GLASS WITH CROFER 22 APU ALLOY INTERCONNECT

Abstract

In planar solid oxide fuel/electrolyzer cells, compatibility and thermochemical stability of interconnect-seal glass interface is essential in order to avoid mixing and leakage of different gases and degradation of cell performances. Crofer 22 APU alloy is the commonly used metallic interconnect. In this chapter, the interfacial compatibility and thermochemical stability are studied for $SrO\text{-}La_2O_3\text{-}Al_2O_3\text{-}SiO_2$ (SABS-0) seal glass with the Crofer 22 APU alloy with respect to thermal treatment temperature (700-850°C), atmosphere, and time (0-1000 hrs). The seal glass is compatible with the Crofer 22 APU alloy and pore and crack-free interface is maintained for all the thermal treatment conditions. The interfaces were investigated by scanning electron microscopy (SEM), energy dispersive spectroscopy (EDS), and X-ray diffraction (XRD). Other complementary techniques such as wave length dispersive spectroscopy (WDS) and SEM of thin (~ 200 nm) samples were used to analyze selected samples. Chemical reaction and inter-diffusion between the seal glass and the Crofer 22 APU alloy occur simultaneously with the devitrification of the seal glass. Same crystalline compounds are found across the interface regardless of the thermal treatment conditions, which suggests thermochemical stability of the interface although the interface morphology differs with the thermal treatment conditions.

5.1. Introduction

A seal glass should bond well with other solid oxide fuel/electrolyzer cell (SOFC/SOEC) components which include electrolyte (stabilized cubic zirconia), interconnect (high chromium ferritic stainless steel), and electrodes (lanthanum strontium manganite and Ni-ZrO_2 cermet) without severe reactions. Among all these cell components, interaction of a seal glass with the metallic interconnect is the most crucial. Oxidation resistant alloys, ferritic stainless steel, are the top choice as interconnect in SOFCs/SOECs. Crofer 22 APU alloy is the most preferred interconnect alloy because of the good electrical conductivity of its Cr_2O_3 surface layer (7.69×10^{-4} $S \cdot cm^{-1}$at 25°C and 1×10^{-2} $S \cdot cm^{-1}$ at 800°C), high oxidation resistance, and the thermal expansion coefficient (CTE: 11.4-12.5 $\times 10^{-6}$/°C) which matches with that of the other cell components [1,2].

To achieve 'gas-tightness', the interface of a seal glass with the metallic interconnect must be pore and crack free, and stable for the entire period (≥ 40,000 hrs) of cell operation at 800°C in oxidizing and wet (≥ 50% H_2O) reducing atmospheres. The interface formation between a seal glass and metallic interconnect usually involves inter-diffusion of elements and chemical reaction between them [3,4]. Severe interaction between the seal glass and metallic interconnect increases interfacial layer thickness, which in turn leads to pore and crack formation at the interface and delamination of the glass [4,5]. At the interconnect-seal interface, chromium diffusion into the seal glass should be minimal in order to prevent electrical resistivity decrease and 'chromium poisoning'. Iron from the interconnect side should not diffuse extensively into the glass since formation and growth of conductive Fe-containing phases may create a short circuit in the cell stacks [6]. Diffusion of seal glass elements into the interconnect is undesirable in order to retain stable glass network structure.

BaO-CaO-borosilicate seal glasses have been extensively studied. However, this family of glass reacts with chromium in the Crofer 22 APU alloy and forms detrimental $BaCrO_4$ of very high CTE (21.0-23.0 $\times$ 10^{-6}/°C). Due to the thermal expansion mismatch between $BaCrO_4$ and the seal glass, thermal stress arises resulting in pores and cracks at the interface [7,8]. Other BaO-CaO –silicate seal glasses also react severely with the Crofer 22 APU alloy and induce cracks at the interface when exposed to either oxidizing or reducing atmosphere [6,9,10]. SrO-CaO-borosilicate seal glasses react with the Crofer 22 APU alloy and form $SrCrO_4$ of high CTE (~ 21.0-23.0 $\times$ 10^{-6}/°C) and pores at the interfaces [11]. It has also been demonstrated that undesirable chromate formation is severe at the interconnect-glass seal-air phase boundary.

Interfacial stability of seal glass with the Crofer 22 APU alloy strongly depends on the exposed atmosphere. For example, A BaO-MgO-silicate glass does not bond with the Crofer 22 APU alloy in an oxidizing atmosphere but bonds well with the same alloy in a wet reducing atmosphere [12].

For most of the interconnect-seal glass interfacial studies, the experiments have been conducted in an oxidizing atmosphere. The detrimental chromate ($BaCrO_4$, $SrCrO_4$) formation may be eliminated by avoiding direct exposure of the interconnect-seal glass boundary to air. Seal glass can be bonded with the interconnect in an inert atmosphere, such as argon. To achieve strong bonding with the metal interconnect, the seal glass and the metal must have certain extent of inter-diffusion, which is dependent on the bonding temperature and time for a given atmosphere. Stability of the interconnect- seal glass interface has been studied as a function of thermal treatment time but no literature report is available regarding the impact of the thermal treatment temperature. In addition, SOFC/SOEC reducing atmosphere usually contains $\geq$ 50% H_2O but most of the studies have been conducted in 3% H_2O containing reducing atmosphere.

In this dissertation, several seal glasses have been investigated based on SrO-La_2O_3-Al_2O_3-B_2O_3-SiO_2 system (SABS) among which B_2O_3 free SABS-0 has almost all the desired thermal properties along with the thermal stability (chapter 2, 3, and 4). This chapter is focused on the interfacial compatibility and thermochemical stability of the SABS-0 glass with the Crofer 22 APU alloy. The effects of thermal treatment temperature, atmosphere, and time on the Crofer 22 APU alloy-SABS-0 interface were investigated.

5.2. Experimental procedure

5.2.1. Glass preparation

SABS-0 glass was prepared with conventional method. $SrCO_3$ (99.9%, Sigma Aldrich, St. Louis, MO), La_2O_3 (99.98%), Al_2O_3 (99.95%), and SiO_2 (99.8%) (all oxides were from Alfa Aesar, Ward Hill, MA) at designed ratios were mixed in a ball mill for overnight. The mixed powders were heated in a platinum crucible in a box furnace (Lindberg, Model No. 51314, Watertown, WI) to 1100°C and kept there for 1 hr for $SrCO_3$ to decompose. After that, the mixture was heated to 1400°C for 4 hrs. The heating rate was 10°C/min. The molten glass was quenched into a graphite mold.

5.2.2. Sample preparation for interfacial study

Crofer 22 APU samples (ThyssenKrupp VDM, Germany) were polished to remove oxidized layer, if any, and to obtain scratch-free flat surface. The nominal composition of the Crofer 22 APU is given in Table 5-1. The polished samples were cleaned by ultrasound in water and then in acetone before being dried and wiped with acetone. A clean and flat SABS-0 glass

piece was put on the polished Crofer 22 APU surface and thermally treated at 960°C for 30 minutes in argon in order to bond the SABS-0 glass with the Crofer 22 APU. No external load was applied during the bonding process.

Table 5-1. Crofer 22 APU alloy composition (wt %) (ThyssenKrupp VDM, Germany) [7]

Cr	Fe	Mn	Ti	Si	Al	C	S	P	La
22.8	Balance	0.45	0.08	…	…	0.005	0.002	0.016	0.06

To study the effect of thermal treatment temperature and time, the bonded Crofer 22 APU/SABS-0 couple was thermally treated at 700°C, 750°C, 800°C, and 850°C for 100 hrs in argon atmosphere. The thermal treatment at 800°C was carried out for different times (0-100 hrs). First, the bonded Crofer 22 APU/SABS-0 couple was thermally treated for 10 hrs. Then a portion of the Crofer 22 APU/SABS-0 couple was removed. The remaining part of the Crofer 22 APU/SABS-0 sample was thermally treated for 20 hrs, 50 hrs, and 100 hrs respectively. The dwell times at 800°C were accumulative with interruptions for sample removal.

To study the effect of atmospheres, the bonded Crofer 22 APU/SABS-0 couple was thermally treated at 800°C for 100 hrs in argon, air, and H_2O/H_2 atmospheres. The H_2O/H_2 atmosphere was created by passing hydrogen gas through a water bath. The temperature of the water bath was maintained at 83 ± 2°C to obtain approximately 50% water vapor [13]. The bonded Crofer 22 APU/SABS-0 couple was also thermally treated at 800°C in air and H_2O/H_2 atmospheres for 500 and 1000 hrs to study the long-term interfacial stability. The same heating and cooling rates of 3°C/min were used for all the thermal treatment experiments.

5.2.3. Characterization

The cross sections of all the thermally treated Crofer 22 APU/SABS-0 couples were finely polished to optical finish. Field emission SEM (Quanta 600 FEG, FEI Company, Hillsboro) was used to examine the interfacial morphology between the SABS-0 glass and the Crofer 22 APU interconnect. The EDS module (Bruker AXS, MiKroanalysis, Gmbh, Berlin, Germany) attached to the SEM was used for composition analysis in order to understand the elemental distribution in the Crofer 22 APU metal and the SABS-0 glass. The analyses followed standardless method. The elemental distribution along the interface was determined by EDS spot and line scan and area mapping. For all the studied samples the EDS spot and line scan were done in at least three randomly selected regions. The results given here are the averages of these scan data. To investigate the devitrified phases at the interface of the Crofer 22 APU/SABS-0 couple, high resolution X-ray diffraction (XRD) studies were carried out in an X'Pert PRO diffractometer (PANalytical B.V., EA Almelo, The Netherlands). SABS-0 glass coated Crofer 22 APU surface was polished until the glass layer was 15 - 20 μm thick. Such SABS-0 glass layer thickness was deemed suitable since X-ray detects 95% of the phase information from 25 μm penetration depth [14]. The scan time per step was 3000 s with CuK_{α} radiation (λ = 1.5406 Å).

5.3. Results and discussion

5.3.1.Crofer 22 APU/SABS-0 couple thermally treated in argon for different times and temperatures

5.3.1.1. Interfacial microstructure

The microstructures of the Crofer 22 APU/SABS-0 couple thermally treated at 700°C, 750°C, 800°C, and 850°C in argon for 100 hrs are given in Fig. 5-1. The microstructures at different temperatures show distinct, intimate, and pore free interfaces. The interfacial zone thickness fluctuates but is generally less than 3 μm. Elongated phases with different orientations can be seen in the SABS-0 glass matrix close to the interface. The elongated phases are only present in the regions very close to the interface for the thermally treated sample at 700°C. For the 750°C thermally treated sample, the elongated phases are locally distributed in the SABS-0 glass matrix. However, for the 800°C and 850°C thermal treatment conditions, the elongated phases extend well into the SABS-0 glass matrix. This means the amount of the elongated phases increases with thermal treatment temperature. Based on the chapter two for similar glass system, the elongated phases are the newly devitrified phases. This is also consistent with the knowledge that localized devitrification occurs when a glass is bonded to metal [15]. However, the elongated phases in the SABS-0 glass do not exist beyond 10 μm on the SABS-0 glass side (lower magnification images are not shown). For all the Crofer 22 APU/SABS-0 samples treated at different temperatures, small black spots (<<1 μm) can be seen on the interconnect side near the interface. These may be closed pores which form as a result of chromium evaporation from the interconnect [7]. At the studied temperatures the pore sizes are <<1 μm.

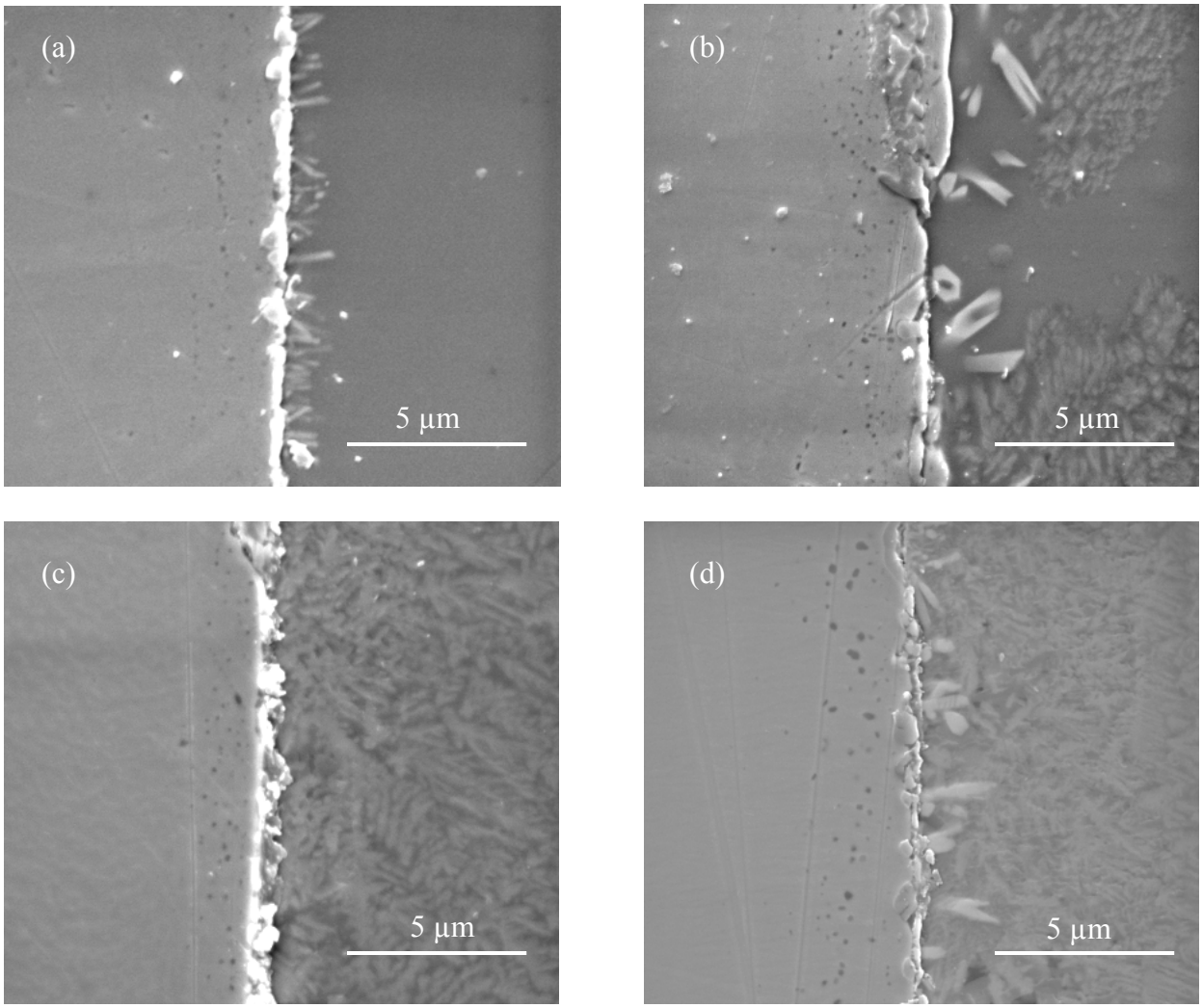

Fig. 5-1. SEM images of the Crofer 22 APU/SABS-0 samples thermally treated for 100 hrs : a) 700°C, b) 750°C, c) 800°C, and d) 850°C.

The microstructures of the Crofer 22 APU/SABS-0 samples thermally treated at 800°C for different dwell times are given in Fig. 5-2. The SABS-0 glass bonds well with the Crofer 22 APU alloy as seen in Fig. 5-2(a). In the as-bonded sample (Fig. 5-2(a)), elongated, needle-shaped bright phase on the SABS-0 glass side is observed. For all the thermally treated samples, such elongated phases become more widespread on the SABS-0 glass side. The samples show a distinct, thin interfacial layer. Evolution of the interfacial layer with thermal treatment time

suggests that the diffusion of the Crofer 22 APU and the SABS-0 glass elements plays an important role in the interfacial new phase formation. Again, small pores (<<1 μm) near the interface on the Crofer 22 APU side are observed, similar to the samples thermally treated for 100 hrs at different temperatures.

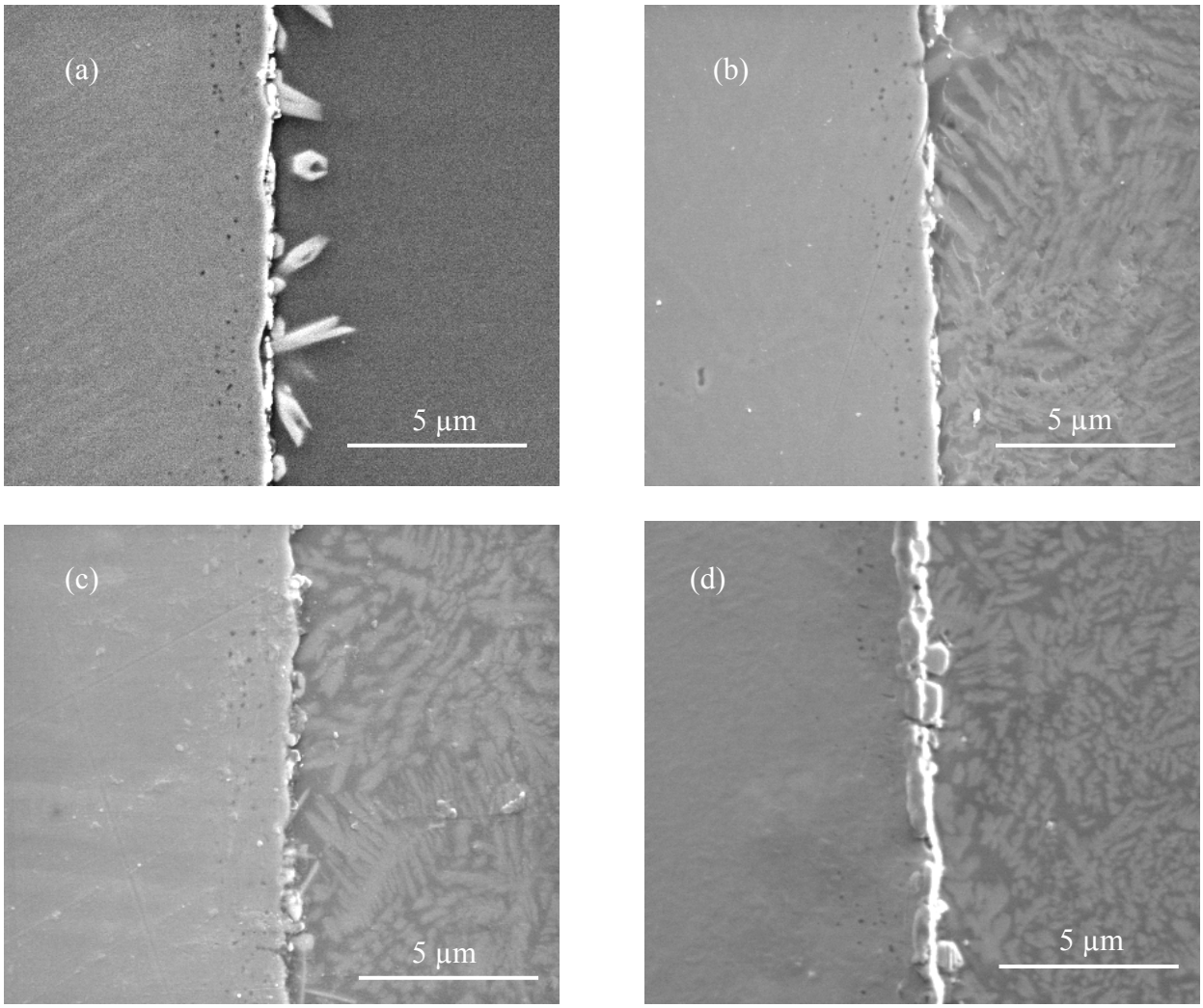

Fig. 5-2. SEM images of Crofer 22 APU/SABS-0 couples thermally treated at 800°C for different times: (a) as-bonded, b) 10 hrs, c) 20 hrs, and d) 50 hrs.

5.3.1.2. Elemental distribution across the interface

Elemental distribution across the interface of the Crofer 22 APU/SABS-0 samples thermally treated at different temperatures for 100 hrs is given in Fig. 5-3. On the x-axis, '0' indicates the center of the interface. The left (negative) side is the Crofer 22 APU alloy and the right (positive) side is the SABS-0 glass. The atomic concentration of each element has been normalized based on its maximum concentration. From the microstructures in Figs. 5-1 and 5-2, it can be seen that diffusion and chemical reaction occur between the SABS-0 glass and the Crofer 22 APU alloy. Devitrification of the SABS-0 glass is also observed. Chemical reaction between the Crofer 22 APU alloy and the SABS-0 glass and devitrification of the SABS-0 glass itself make quantitative diffusion analysis ambiguous. The elemental distribution profile across the interface is not the classical 'S' shape. Still, approximate diffusion distance can be determined by identifying the inflection point and diffusion tail at the interface.

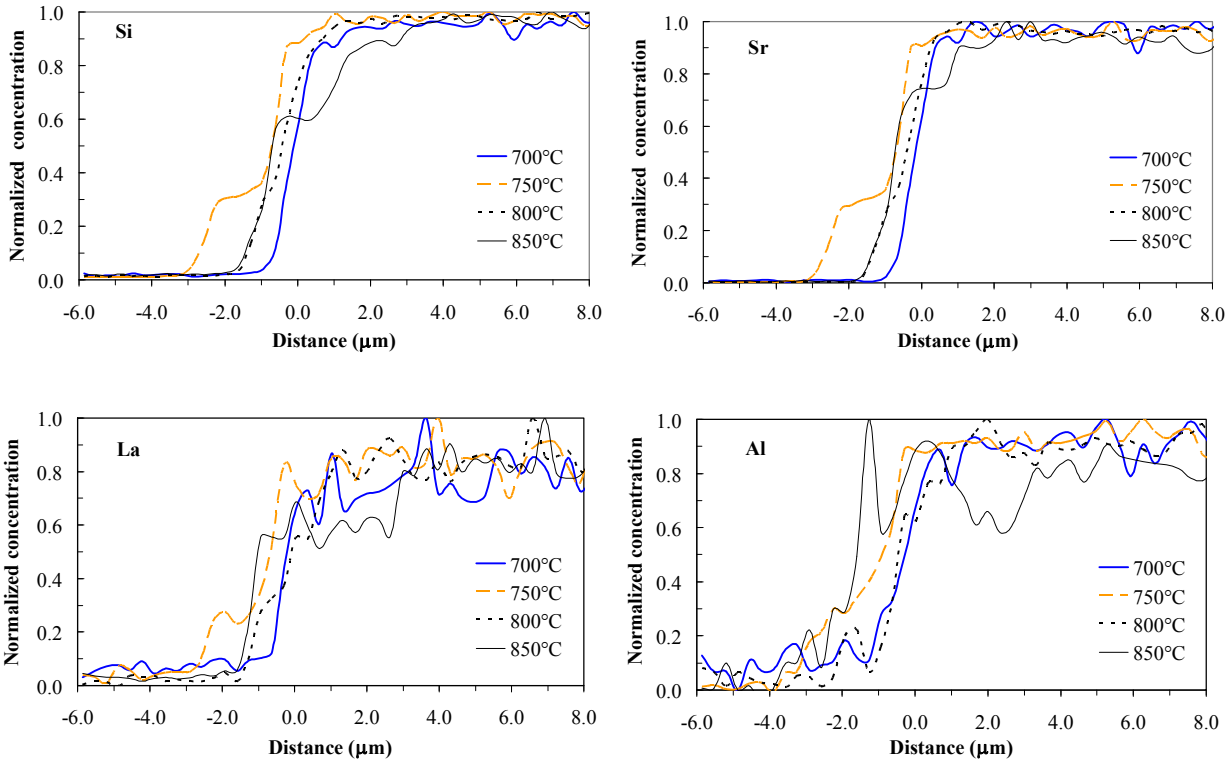

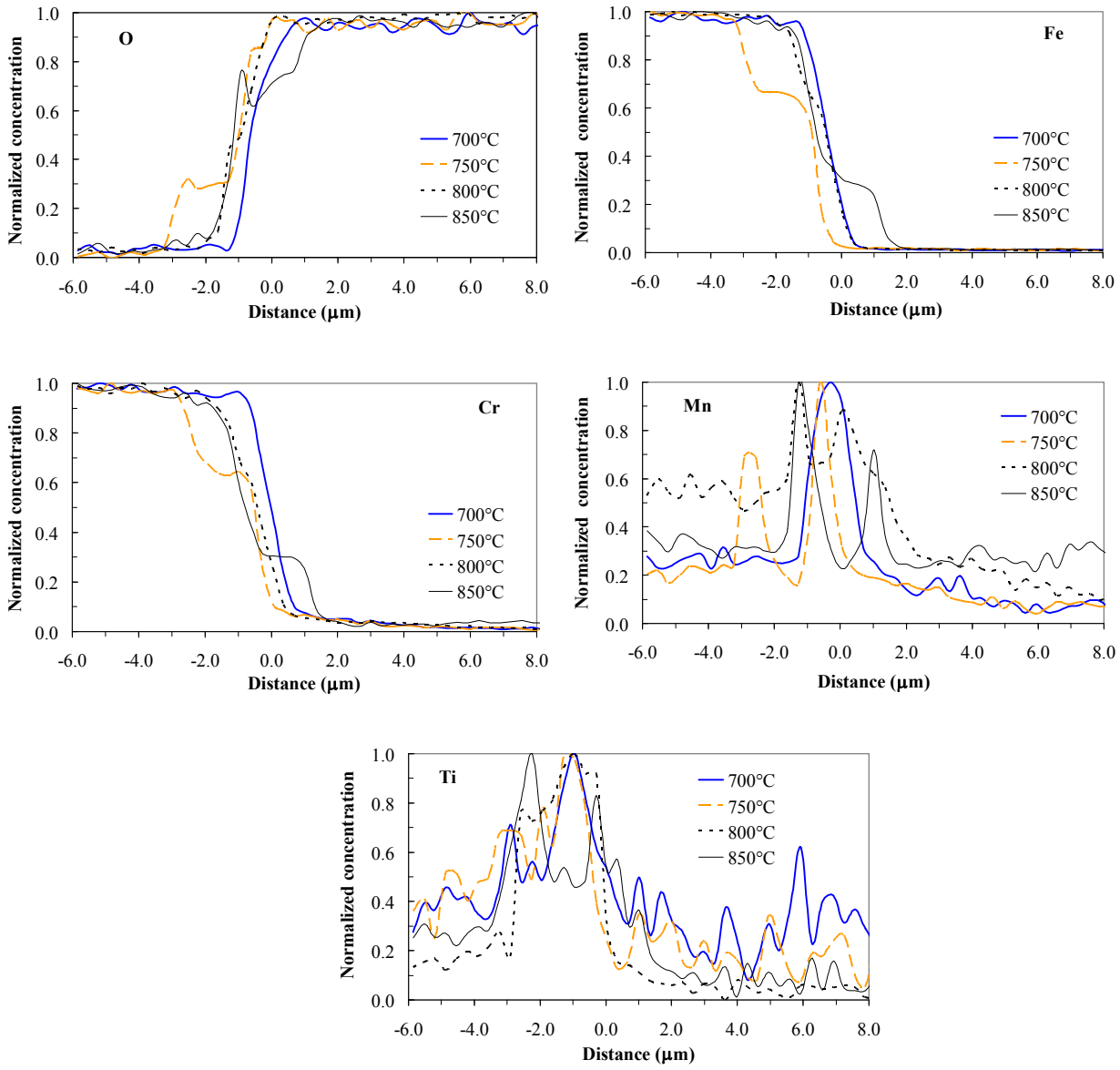

Fig. 5-3. Elemental distribution of thermally treated Crofer 22 APU/SABS-0 couples thermally treated at different temperatures for 100 hrs.

Oscillations in the concentration profiles are observed for the SABS-0 glass elements and can be explained as follows. First, the step size of the EDS line scan was 0.06 µm for this study. The spatial resolution of the secondary X-rays is ≥ 1 µm. Interaction between the X-ray of the different elements can be expected for the experimental step size resulting in oscillations in the

concentration profiles. Second, low concentration of La and Al, compositional difference between the devitrified and glass phases, and low density of the SABS-0 glass are also the likely reasons for the oscillations in the concentration profiles [16].

All the elements in the SABS-0 glass, silicon, strontium, lanthanum, aluminium, and oxygen, diffuse 2-3 μm into the Crofer 22 APU alloy side. Iron in the Crofer 22 APU alloy diffuses 2-3 μm into the SABS-0 glass. Chromium diffuses ~ 5 μm into the SABS-0 glass for the samples thermally treated at 700°C and 750°C and ~ 7 μm into the SABS-0 glass for the samples thermally treated at 800°C and 850°C. The concentrations of manganese and titanium are at maximum at the interface as revealed from the sharp peaks at the interface. Also, titanium concentration peaks shift to the left in comparison to the manganese peaks. Manganese (0.4-0.8 wt %) and titanium (0.2 wt %) are the minor elements in the Crofer 22 APU alloy. Manganese is added in the Crofer 22 APU alloy to suppress chromium evaporation and diffusion. Titanium is added to improve the electrical conductivity of the alloy [17]. Since manganese and titanium have higher affinity with oxygen than chromium [18,19], they are more likely to react with oxygen and form oxides to prevent further Crofer 22 APU alloy degradation. Because of their higher oxygen affinity and diffusivity, manganese and titanium accumulate at the interface and hinder the diffusion of the SABS-0 glass elements and the Crofer 22 APU elements into each other.

Elemental distribution of the Crofer 22 APU/SABS-0 sample thermally treated at 800°C for different thermal treatment times is shown in Fig. 5-4. The elements in the SABS-0 glass and iron in the Crofer 22 APU alloy diffuse a similar distance of ~ 2 μm. This implies that the diffusion of the SABS-0 glass elements is not significantly affected by the thermal treatment time for up to 100 hrs. Chromium in the Crofer 22 APU alloy diffuses into the SABS-0 glass at ~

5 μm in the as-bonded sample. The diffusion distance of chromium increases to ~ 7 μm in the 50 hr thermally treated sample and remains almost unchanged for the 100 hr thermally treated sample. This suggests that chromium diffusion increases with the thermal treatment time. Manganese and titanium concentrations are highest at the interface. Again, titanium peaks reside beneath the manganese-rich layer on the Crofer 22 APU side.

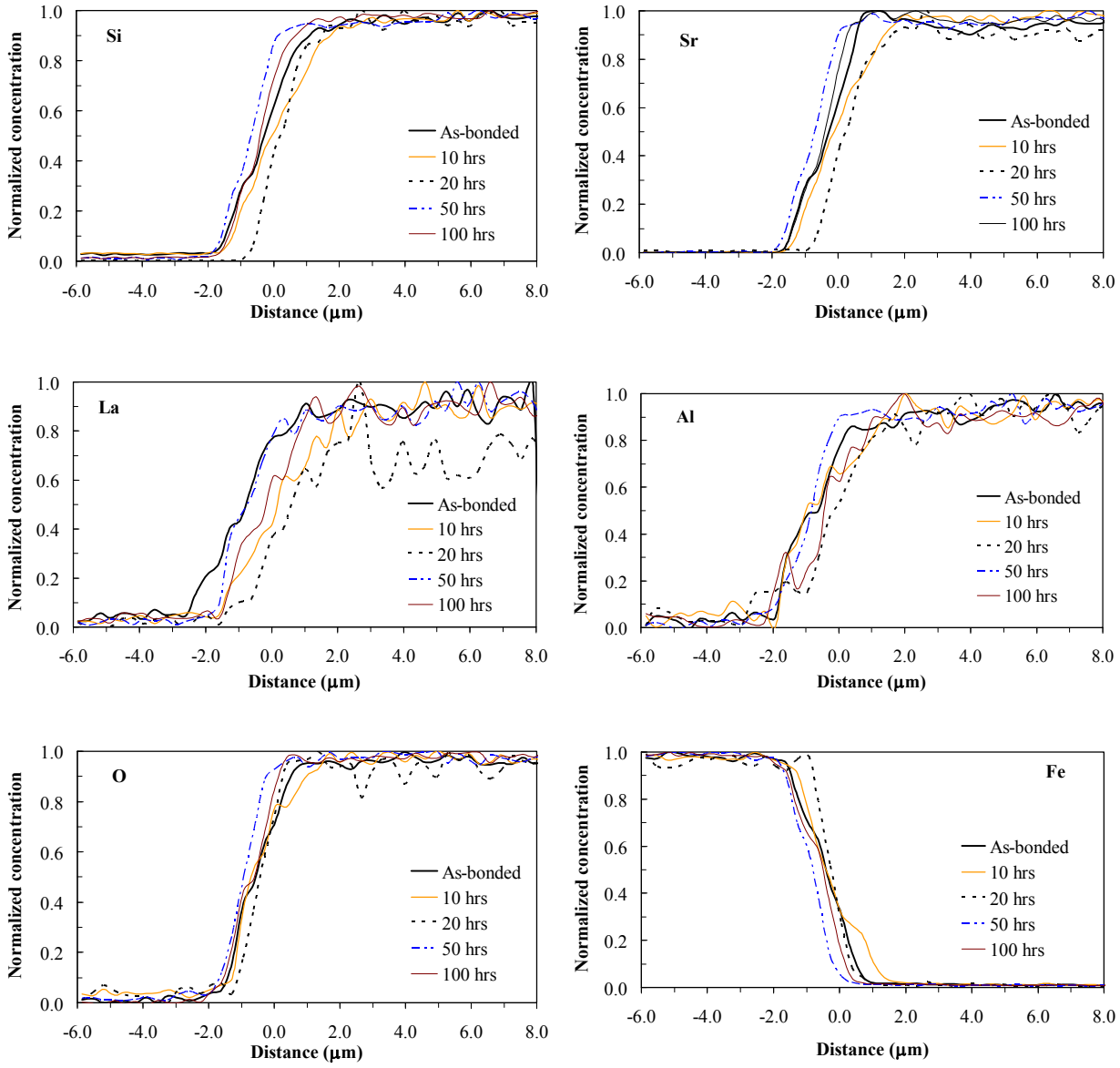

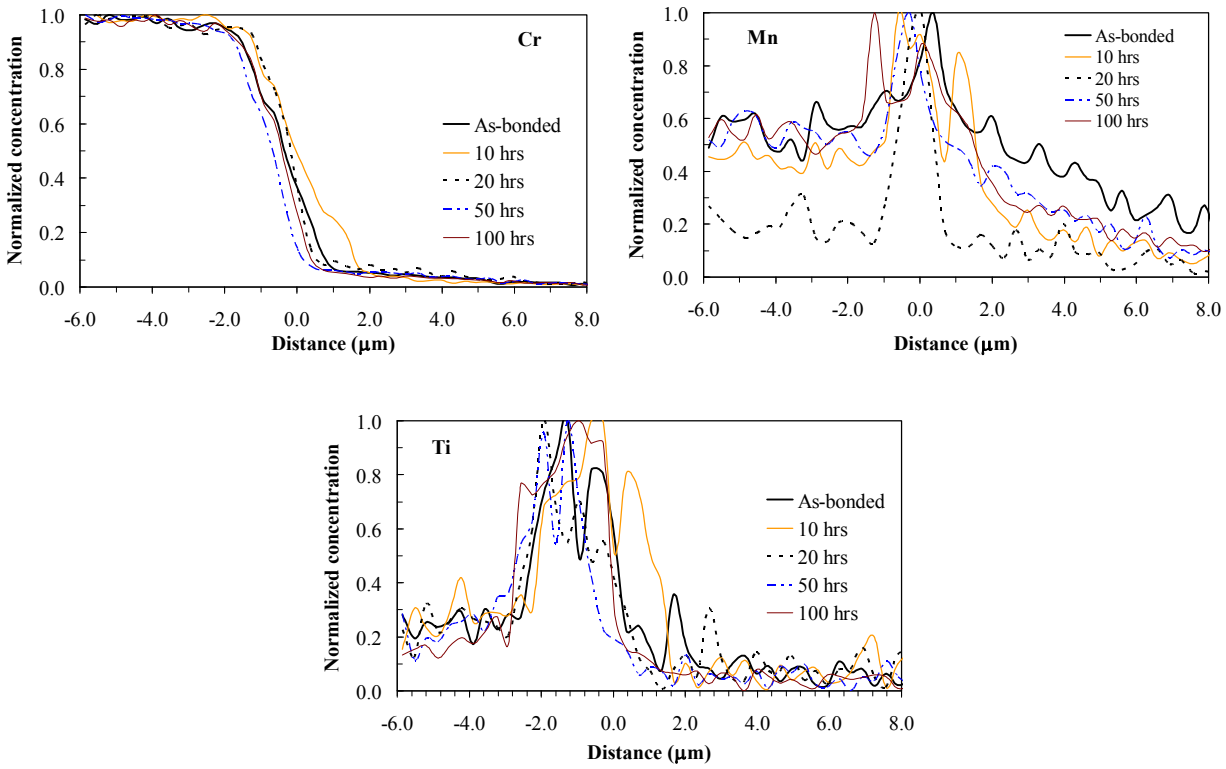

Fig. 5-4. Elemental distribution of Crofer 22 APU/SABS-0 couples thermally treated at different thermal treatment times at 800°C.

The diffusion distances of the SABS-0 glass elements and the Crofer 22 APU elements except for chromium remain unchanged at ~ 2 μm with different thermal treatment time. Such diffusion distances are close to the interfacial zone thickness (<3 μm) shown in Figs. 5-1 and 5-2. This indicates that the interface is formed by the diffusion-controlled chemical reaction. The fluctuations in lanthanum and aluminium distributions may be due to the compositional difference between the elongated crystalline phases and the glass matrix. Diffusion distance of chromium also remains unchanged at ~ 7 μm after 50 hrs of thermal treatment time. Longer diffusion distance of chromium than that of other elements in the Crofer 22 APU alloy suggests that volatile chromium species might have diffused into the SABS-0 glass.

To further understand the interaction between the Crofer 22 APU alloy and the SABS-0 glass at the interface, elemental mapping results are shown in Fig. 5-5 for the sample thermally treated at 850°C for 100 hrs. This thermal treatment condition should provide the most severe interfacial interaction scenario. As shown, the interfacial layer has higher concentrations of manganese and titanium from the Crofer 22 APU alloy and lanthanum and oxygen from the SABS-0 glass. Consistent with the EDS plot (Figs. 5-3), titanium-enriched layer is present beneath the manganese-enriched layer. Chromium is also rich at localized interfacial spots. Aluminium and lanthanum have also diffused to the Crofer 22 APU side. Other than the above observations, the distributions of both the Crofer 22 APU and the SABS-0 glass elements are homogeneous after thermal treatment at 850°C for 100 hrs. This means the elongated phases on the SABS-0 glass side observed in Figs. 5-1 and 5-2 are due to the devitrification of the SABS-0 glass.

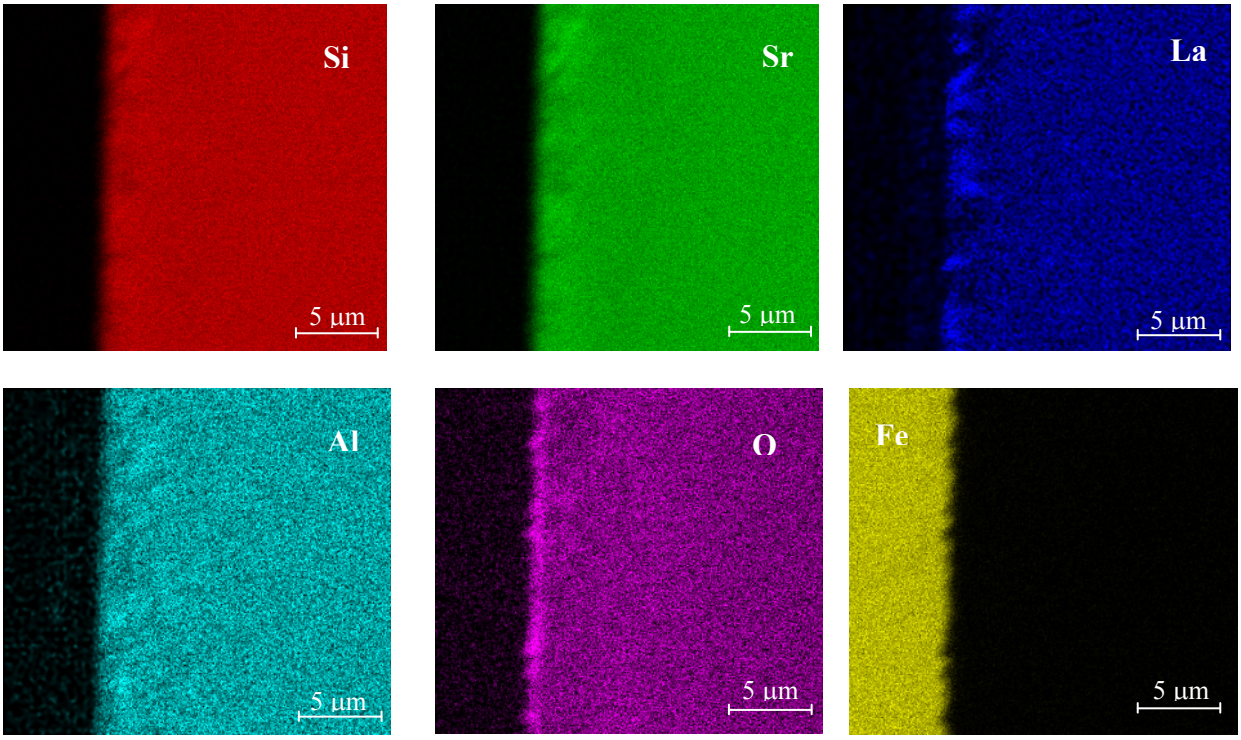

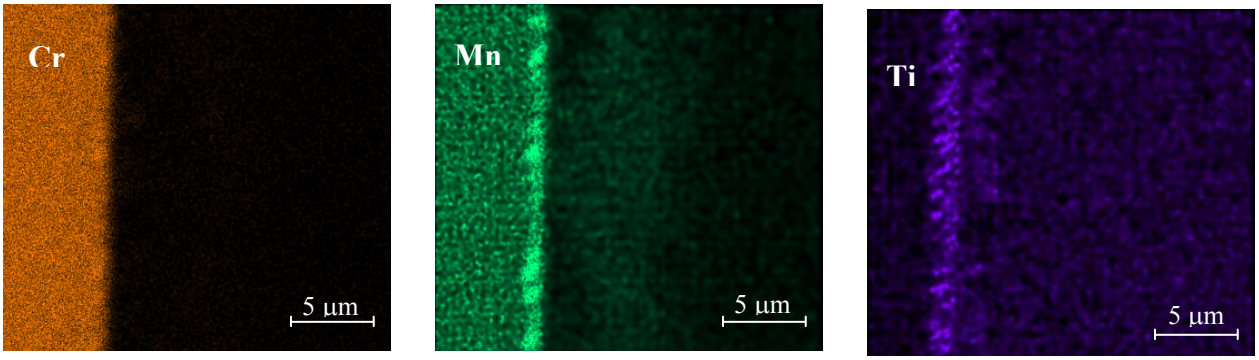

Fig. 5-5. Elemental distribution maps of the SABS-0/Crofer 22 APU couples thermally treated at 850°C for 100 hrs.

5.3.1.3. X-ray diffraction analysis

In addition to the microstructure and the elemental distribution results obtained, the Crofer 22 APU/SABS-0 glass interfacial phase changes need to be understood. In this study, the SABS-0 glass layer is thin enough that all the phases at the interface can be detected by passing X-ray from the top of the SABS-0 glass layer into the Crofer 22 APU alloy.

The XRD pattern for the Crofer 22 APU alloy is shown in Fig. 5-6(a). The characteristic (110) plane of iron can be seen. The XRD patterns for the as-bonded Crofer 22 APU/SABS-0 sample and the thermally treated Crofer 22 APU/SABS-0 at different temperatures for 100 hrs are given in Fig. 5-6(b). The presence of the characteristic (110) plane of iron at 44.67° in all the samples confirms that the XRD patterns include all the crystal phases across the interface. For the bonded samples, the indexing of X-ray patterns was done using standard method for polycrystalline materials [20]. As Fig. 5-6(b) shows, new crystalline phases are present at the Crofer 22 APU/SABS-0 interfaces for all the samples. The crystal phases can be identified as monoclinic $La_2Cr_2O_9$ and hexagonal $Sr_7Al_{12}O_{25}$. It should be noticed that the peaks of these two

phases overlap. The same number and location of peaks in the XRD patterns mean that the crystal phases are the same for all the studied thermal treatment times and temperatures. However, the XRD peak intensities vary. This is likely due to the thermal treatment effect and the slightly different thickness of the SABS-0 glass layer on the Crofer 22 APU alloy.

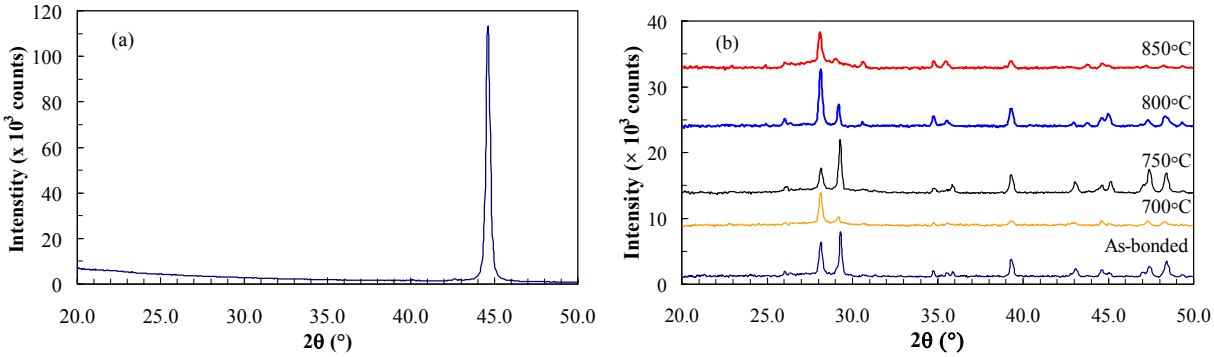

Fig. 5-6. XRD patterns of a) Crofer 22 APU alloy and b) of the Crofer 22 APU/SABS-0 interfaces. The samples include the as-bonded condition and thermally treated conditions at different temperatures for 100 hrs.

It can be understood that devitrification of the SABS-0 glass causes formation of $Sr_7Al_{12}O_{25}$. In the SABS-0 glass, Al^{3+} is a glass former [21]; Sr^{2+} is a charge compensator for the nearest localized $(AlO_4)^-$ tetrahedral structural units [22]. Microheterogeneity in the SABS-0 glass structure, such as localized $(AlO_4)^-$ tetrahedral units, induces the devitrification of the SABS-0 glass. Accordingly, $Sr_7Al_{12}O_{25}$ crystalline phase forms.

Formation of $La_2Cr_2O_9$ can be explained as follows. La_2O_3 containing glass tends to form energetically favorable, isolated, small, and phase ordered clusters. These clusters generally contain La-O-La structural units. These La-O-La structural units are overlapped in 1105 cm^{-1} and 1010 cm^{-1} wave numbers in the Raman spectra of the SABS-0 glass (chapter three). These

isolated La-O-La clusters act as nucleation sites for devitrification of the SABS-0 glass. Accumulation of lanthanum and oxygen at the interface can be seen in Fig. 5-5. At the same time, chromium diffuses to the SABS-0 glass side as observed from the EDS analysis (Figs. 5-3 and 5-4). This leads to the breakdown of the SABS-0 glass network structure [23]. According to Sanderson, acidobasicity value, a glass property related to the chemical environment, is 3.50 for chromium and 1.95 for lanthanum [24]. This means chromium is acidic and lanthanum is basic in nature. Therefore, reaction among lanthanum, chromium, and oxygen favors $La_2Cr_2O_9$ formation. $La_2Cr_2O_9$ phase, likely a result of diffusion-controlled reaction, should be the interfacial crystalline phase

Almost similar morphologies of the interfaces and same crystalline phases for all the thermally treated samples suggest that the SABS-0 glass is compatible and the interface is stable regardless of the thermal treatment times (0-100 hrs) and temperatures (700-850°C).

5.3.2.Crofer 22 APU/SABS-0 couple thermally treated at 800°C in argon, air, and H_2O/H_2 atmospheres

5.3.2.1. Interfacial microstructure

Microstructures of the as-bonded and the thermally treated Crofer 22 APU/SABS-0 couples in agon, air, and H_2O/H_2 atmospheres are shown in Fig. 5-7. The as-bonded sample is included in Fig. 5-7 for ease of discussion. In the images, the left side is the Crofer 22 APU alloy and the right side is the SABS-0 glass. The microstructures at all the studied conditions show distinct bonding interfaces. The microstructures can be divided into three regions near the

interface: tiny (<<1 μm) black spots on the Crofer 22 APU alloy side, interfaces with some scattered and elongated secondary phases, and partially devitrified SABS-0 glass side.

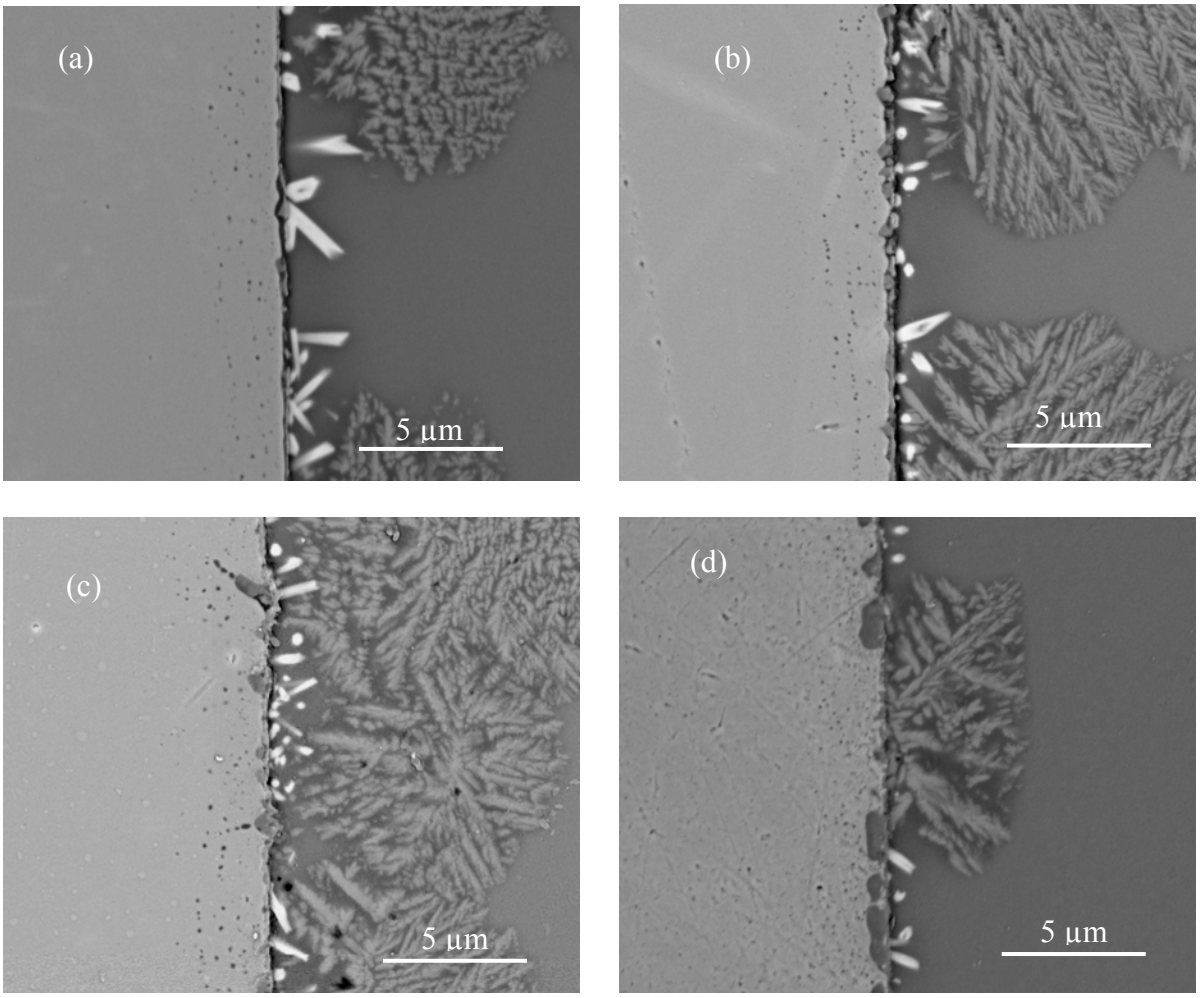

Fig. 5-7. SEM images of Crofer 22 APU/SABS-0 couples: a) as-bonded, b) argon, c) air, and d) H_2O/H_2 atmosphere. The samples were thermally treated for 100 hrs at 800°C in different atmospheres.

The interface morphologies differ for the as-bonded and the thermally treated samples. The interface for the as-bonded condition is smoother (no granular phase on the Crofer 22 APU

alloy side at the interface) than the thermal treatment conditions. Rough interfaces with granular phases are observed for the thermally treated samples. The morphologies of the interfaces again differ with the thermal treatment atmospheres. The distribution of granular phases at the interface is uniform for argon but non-uniform for air and H_2O/H_2 treated samples. The granular and rough interface can be understood from the chemical interaction between the Crofer 22 APU alloy and the SABS-0 glass. For the H_2O/H_2 treated sample, two types of granular phases, small and large, are observed. The interface morphology is also the roughest for the H_2O/H_2 treated sample than the other samples. This can be explained as follows. In H_2O/H_2 atmosphere, both oxygen and hydrogen are present. Subsequently, simultaneous oxidation and reduction of the Crofer 22 APU alloy elements occur which in turn may slightly increase the size of the granular phases in expense of some granular phases by the reduction process and change the composition. Subsequently, the interface becomes the roughest in H_2O/H_2 atmosphere among all the studied conditions. These observations agree with the rough surface due to oxidation of a Fe-Cr alloy in H_2O/H_2 atmosphere [25]. The black spots at the interface similar to the as-bonded sample are distinct for the argon and air treated samples but almost invisible for the H_2O/H_2 treated samples. A distinct black layer on the glass side near the interface is observed for all the thermally treated samples and the composition is similar to that of the as-bonded sample.

On the SABS-0 glass side, two types of secondary phases are observed for all the samples: bright phase close to the interface and dendritic phase in the SABS-0 glass. The orientations of both the phases are random for all the samples. Equiaxed and platelet like bright phases are observed. This means the morphology of the bright phases depend on the interaction between the Crofer 22 APU alloy and the SABS-0 glass elements. The bright phases form due to the redox reaction between the the Crofer 22 APU alloy and the SABS-0 glass [15, 26]. The

dendritic phases form due to the SABS-0 glass devitrification. The devitrified phases are not uniformly distributed. The localized devitrication of the SABS-0 glass is also consistant with the glass/metal interfacial study reported in literatures [15, 26]. The amount of dendritic phases increase from the as-bonded condition to the thermally treated conditions in argon and air atmospheres and the highest for the air treated sample. For the H_2O/H_2 treated sample, the dendritic phases are the lowest and also spread to the lowest extent. Nonetheless, the devitrified phases do not extend beyond 10 μm from the interface. However, the redox reaction, the localized devitrifictaion, and effect of thermal treatment conditions on the devitrication are not understood. The thermal treatment atmospheres significantly affect the overall oxidation of the Crofer 22 APU alloy, its interaction with the SABS-0 glass, and the interface formation.

5.3.2.2. Elemental distribution across the interface

Energy dispersive spectroscopy (EDS) analysis was carried out to explore the compositional difference among the different types of phases observed in the microstructures in Fig. 5-7. For spot analysis, higher magnification (>30,000 X) images (not shown here) and electron beam of 6 nm diameter was used. However, the spatial resolution is > 1μm and the analysis can not give absolute composition. The analysis can only provide qualititative information to understand the trend in compositional difference between the different phases. To maintain consistency, a constant collection time (60 s) was used for all the spot analysis. Average compositions of the different phases are reported in atomic%.

The compositions of the tiny black spots on the Crofer 22 APU alloy near the interface are approximately same (Fe 65.13, Cr 20.81, Mn 0.53, Ti 2.96, O 10.57) and different from the Crofer 22 APU alloy composition (Fe 75.58, Cr 23.99, Mn 0.43) for all the thermally treated

samples. Titanium concentration in the bulk Crofer 22 APU alloy is too low for the EDS detection limit. High content of titanium with oxygen indicates that the black spots are titanium oxide. In the Crofer 22 APU alloy, titanium concentration is the lowest between the minor alloying elements, titanium and manganese (Table 5-1). Low concentration and low diffusivity (mobility) of the alloying elements, and high solubility of oxygen in the alloying elements favor the internal oxidation [27]. The diffusivity of titanium is lower than manganese in a Fe-Cr alloy [28, 29]. Subsequently, titanium oxide is formed by internal oxidation in which oxygen diffuses inwardly into the alloy rather than the outward cationic diffusion of the alloying elements. Similar orientation and composition regardless of the thermal treatment atmosphere suggest that the thermal treatment atmosphere do not affect the internal oxidation of titanium in the Crofer 22 APU alloy. It can be mentioned that the tiny black spots are not closed pores as mentioned in section 5.3.1.

The compositions of the granular phases are similar for argon and air treated sample (Fe 16.03, Cr 18.64, Mn 3.35, Ti 0.37, Si 3.76, Sr 3.39, La 0.49, Al 1.64, and O 52.31) suggesting the chemical interaction between the Crofer 22 APU alloy and the SABS-0 glass. For the H_2O/H_2 treated sample, the large granular phases have less iron and the SABS-0 glass elements and more chromium and manganese than the small granular phases. This means thermal treatment atmosphere affects the chemical reaction which is consistent with the different interface morphologies in Fig. 5-7.

Bright and black spots are observed at the interfaces in Fig. 5-7. The bright spots are higher in iron and chromium content (Fe 37.36, Cr 16.17, Mn 1.30, Ti 0.25, Si 5.33, Sr 4.27, La 0.85, O 34.47) and the black spots are higher in silicon and strontium content (Fe 24.02, Cr 12.54, Mn 1.37, Ti 0.21, Si 8.84, Sr 6.73, La 1.76, Al 1.95, O 42.59). This means the interface

composition is not homogeneous. The black layer on the SABS-0 glass side is enriched in glass compositions (Fe 9.93, Cr 9.24, Mn 1.48, Ti .21, Si 16.17, Sr 7.69, La 2.10, Al 3.14, and O 50.05). These observations again indicate the chemical interaction between the Crofer 22 APU alloy and the SABS-0 glass.

On the SABS-0 glass side in Fig. 5-7, the equiaxed bright phases have more Crofer 22 APU alloy contents (Fe 7.67, Cr 10.10, Mn 2.02, Ti 0.21, Si 13.62, Sr 7.99, La 4.45, Al 2.99, and O 50.95) than the platelet like phases (Fe 1.33, Cr 2.14, Mn 0.64, Ti 0.37, Si 15.74, Sr 8.95, La 5.22, Al 3.00, and O 62.63). The devitrified phases have slightly higher strontium and lanthanum and lower aluminium than glass. It can be mentioned that the glass and devitrified phases near the interface (within ~ 5 μm) also consist of little amount of Crofer 22 APU alloy elements among which chromium content increases with the increasing order of H_2O/H_2 > air > argon. This can be explained by the higher rate of chromium vaporization from the Crofer 22 APU alloy in the same order with the studied atmospheres [30]. From EDS spot analysis, it can be understood that the internal oxidation of titanium and chemical reaction between the Crofer 22 APU alloy and the SABS-0 glass occur simultaneously.

Elemental distribution across the Crofer 22 APU alloy/SABS-0 glass interface has also been carried out by EDS line scan. The diffusion behavior of the elements is analyzed by the concentration profiles obtained from EDS. The concentration profiles of the Crofer 22 APU/SABS-0 samples are shown in Fig. 5-8. The concentration profiles of iron and chromium in the Crofer 22 APU and the SABS-0 glass elements (Si, Sr, La, Al, and O) are ‘S’ shaped with two diffusion tails: one at the higher concentration and other at the lower concentration. This means the elemental inter-diffusion of the Crofer 22 APU alloy and SABS-0 glass occurs during interface formation [31]. However, oscillations in the concentration profiles are observed for the

SABS-0 glass elements and the possible reasons are discussed in section 5.3.1.2. The oscillations are more distinct for the air treated sample and aluminium and lanthanum. However, approximate diffusion distance can be determined by identifying the inflection point and diffusion tail at the interface. In Fig. 5-8, '0' on the 'x' axis indicates the boundary between the alloys and the interface. The left (negative) side is the alloy and the right (positive) side is the SABS-0 glass. 'y' axis shows the normalized concentration of the elements.

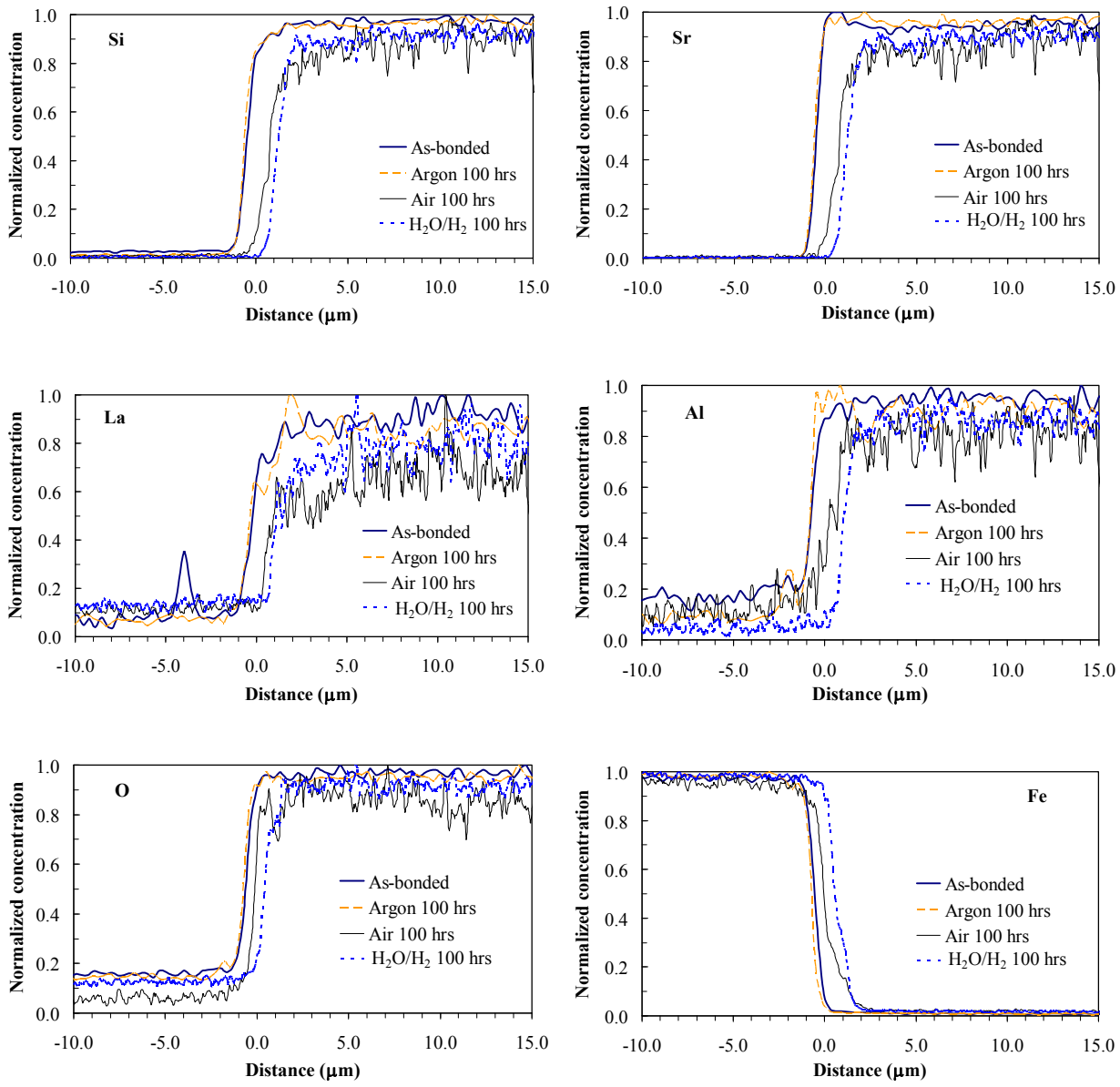

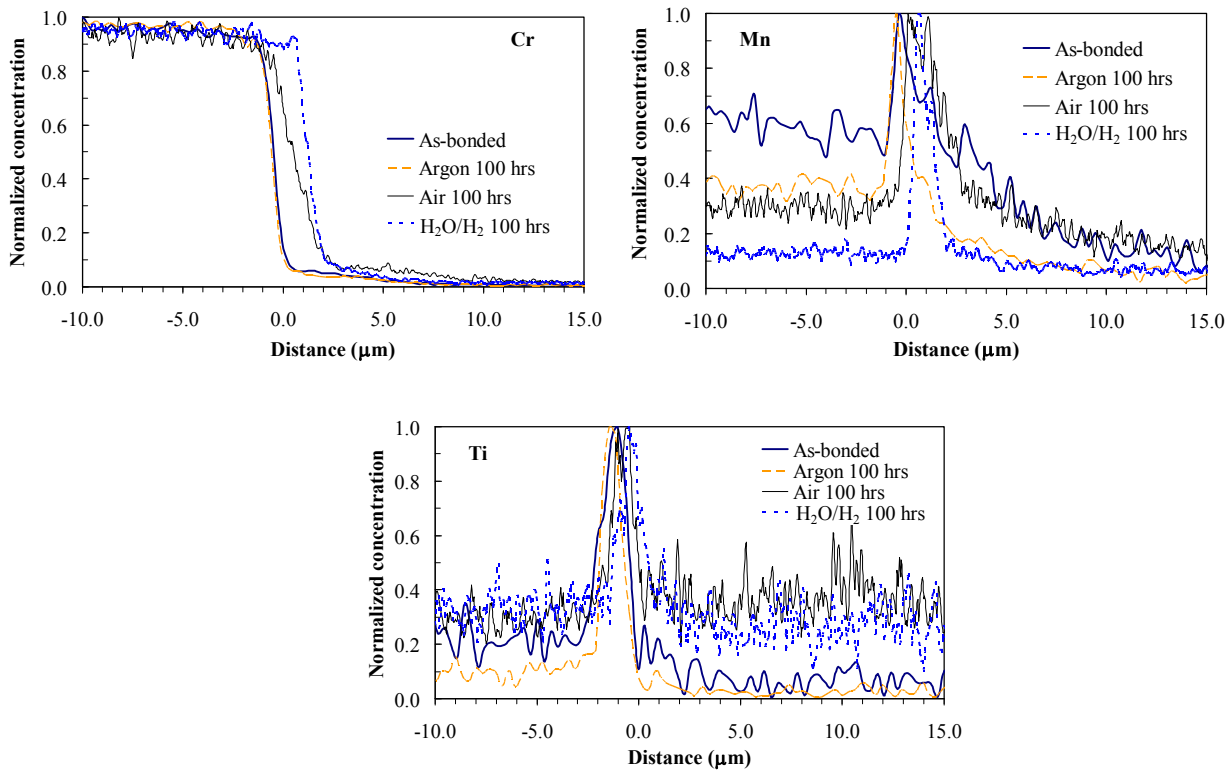

Fig. 5-8. Elemental concentration profiles of the Crofer 22 APU/SABS-0 couples thermally treated in argon, air, and H_2O/H_2 atmosphere.

The SABS-0 glass elements (Si, Sr, La, Al, and O) diffuse 2-3 μm into the Crofer 22 APU alloy side for all the samples. However, in comparison with the as-boned sample, diffusion distances slightly increase in the samples thermally treated in argon and air although the diffusion distances remain 2-3 μm. The diffusion distances are maximum for the samples thermally treated in air. The diffusion distances of these elements, except oxygen, decrease in the H_2O/H_2 treated sample and remain at ≤ 2 μm. Oxygen diffusion distance remains almost unchanged. Iron in the Crofer 22 APU alloy diffuses 2-3 μm into the SABS-0 glass for the as-bonded samples and the thermally treated samples. Chromium diffuses ~ 5 μm into the SABS-0 glass for the as-bonded sample, increases to ~ 7 μm and 10-11μm, respectively, for the argon and

air treated samples, but decreases to ~ 6 μm for the H_2O/H_2 treated sample. Increased diffusion distances of these elements in air mean that the interaction between the Crofer 22 APU alloy and the SABS-0 glass due to elemental inter-diffusion depends on the thermal treatment atmosphere. Chromium vaporizes in the form of CrO_3 species in air and $CrO_2(OH)_2$ in H_2O containing atmosphere [30]. The rate of chromium vaporization from the Crofer 22 APU alloy is more in the H_2O containing atmosphere. So, the diffusion length of chromium into the SABS-0 glass should be more for the H_2O/H_2 treated sample. But the $CrO_2(OH)_2$ is thermodynamically more stable than CrO_3 [30]. Accordingly, chromium diffuses more into the SABS-0 glass side in the air treated sample than that of H_2O/H_2 but its concentration on the SABS-0 glass side near the interface is more for H_2O/H_2 treated sample as discussed in the composition analysis by EDS spot analysis. This means both thermodynamics and kinetics simultaneously affect the interfacial kinetics. Manganese and titanium concentration is maximum at/near the interface as can be seen from the sharp humps in the concentration profiles rather than 'S' shape. Also, titanium concentration humps shift to the left in comparison to that of manganese. This is consistent with the presence of titanium oxide (tiny black spots) on the Crofer 22 APU alloy side near the interface as shown in the microstructures of the Crofer 22 APU/SASB-0 glass (Fig. 5-7).

The elemental distribution can be better understood from the EDS maps. The elemental maps of the Crofer 22 APU/SABS-0 samples are shown in Fig. 5-9. It can be observed that silicon, strontium, and aluminium in the SABS-0 glass are uniformly distributed and do not diffuse into the Crofer 22 APU alloy. The bright spots on the SABS-0 glass side near the interface in the microstructures (Fig. 5-7) are enriched in lanthanum. Oxygen is accumulated at the interface. These observations mean that the SABS-0 glass structure is perturbed to form the interface which is in agreement with the presence of the SABS-0 glass elements at the interface

in the microstructures and diffusion of these elements into the Crofer 22 APU alloy. However, the overall distribution of the SABS-0 glass elements are uniform as can be understood by a little compositional difference among the dendritic phases, black spots between the dendritic phases, and the bulk glass. Chromium, manganese, and oxygen enriched and iron depleted regions are observed and superimposed with the granular phase positions on the Crofer 22 APU alloy side in the microstructures (Fig. 5-7). This means the interface consists of chromium and manganese rich oxide phases. Chromium enrichment at the interface is not clearly observed for the as-boned and the air treated samples which is consistent with the absence of the granular phase for the as-bonded sample (Fig. 5-7(a)) and little amount of the granular phases for the air treated sample (Fig. 5-7 (c)). However, very small second phases are also observed in the microstructures of the as-bonded and air treated samples. Titanium accumulation can be observed beneath the manganese-enriched layer for the air and H_2O/H_2 treated samples which is also consistent with the titanium enrichment on the Crofer 22 APU alloy side near the interface in the microstructures (Fig.5-7) and titanium concentration profiles (Fig. 5-8). Titanium accumulation is not observed for the as-bonded and the argon treated samples although titanium enrichment on the Crofer 22 APU alloy side is observed in the microstructures and the concentration profiles. This may be attributed to the low concentration of titanium.

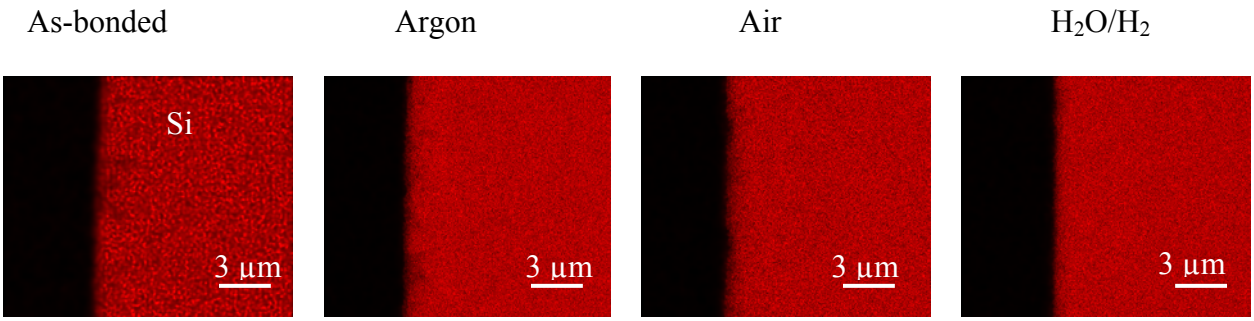

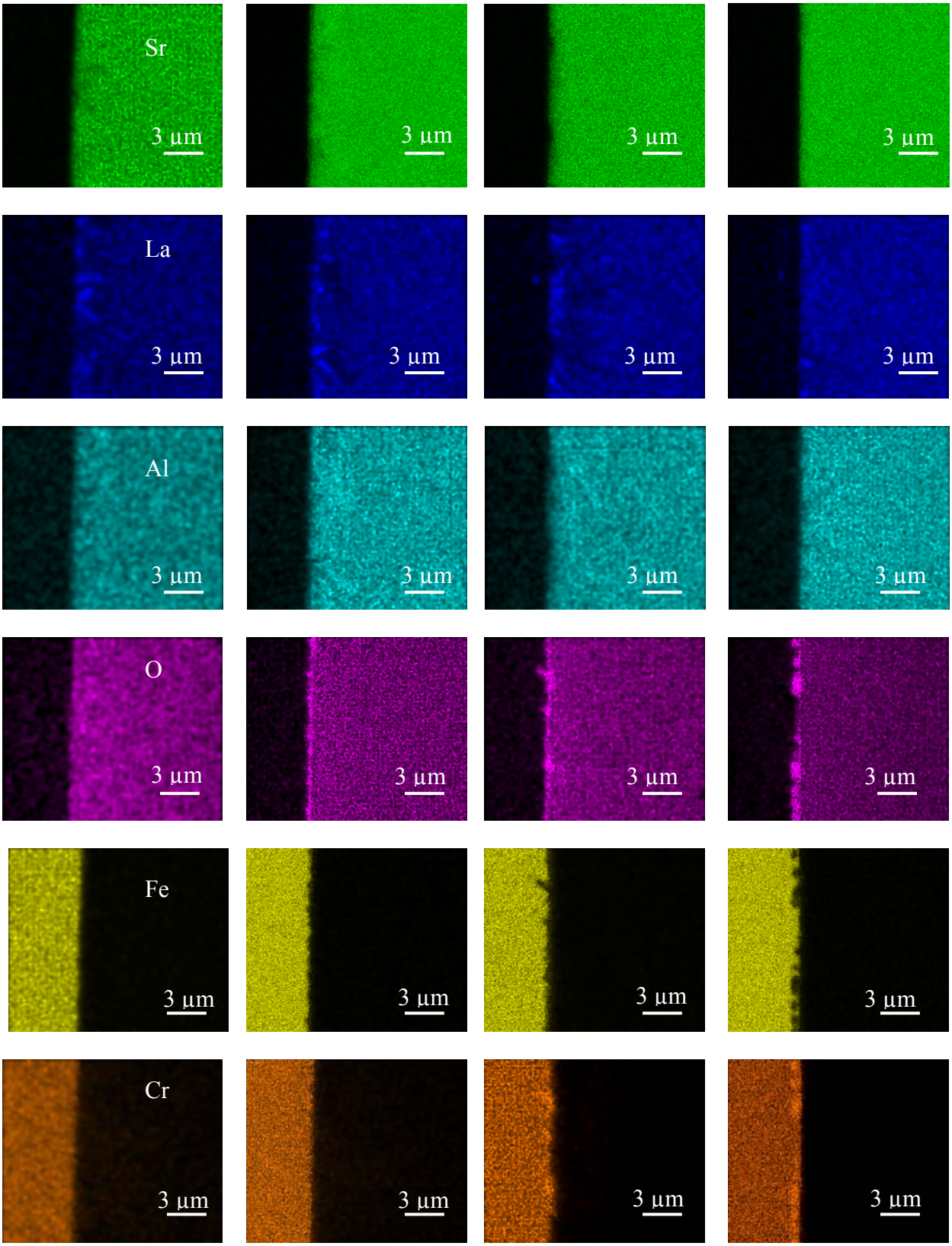
Sr
La
Al
O
Fe
Cr
3 µm

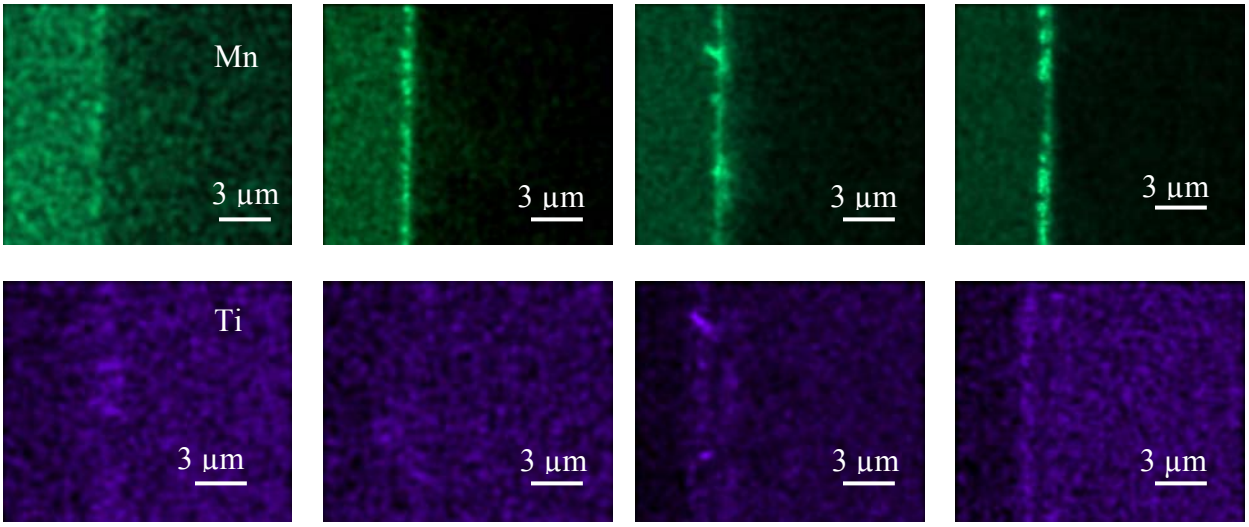

Fig. 5-9. EDS maps for the as-bonded the argon, air, and H_2O/H_2 treated Crofer 22 APU/SABS-0 glass couples.

Overall, the compositional analysis by EDS spot and line scans is consistent with the elemental maps. From the elemental maps, it can be concluded that the interface consists of mainly chromium, manganese, and oxygen. The SABS-0 glass composition remains almost homogeneous although being devitrified.

5.3.2.3. X-ray diffraction analysis

The XRD patterns of the Crofer 22 APU alloy and the studied Crofer 22 APU/SABS-0 samples are shown in Fig. 5-10. The presence of the Crofer 22 APU alloy peaks in all the samples confirms that the XRD patterns include all the crystal phases across the interface. The crystal phases can be identified as $Sr_7Al_{12}O_{25}$, α-$SrSiO_3$, $Mn(CrMn)O_4$, Ti_8O_{15}, and $LaMn_2O_5$. The same number and location of peaks in the XRD patterns mean that the crystal phases are the same for all the studied samples. However, the XRD peak intensities vary. This is likely due to the thermal treatment effect and the slightly different thickness of the SABS-0 glass layer on the

Crofer 22 APU alloy. It can be mentioned that in section 5.3.1.3, only $Sr_7Al_{12}O_{25}$ and $La_2Cr_2O_9$ phases were found. This may be explained as follows. The planes of several crystalline phases overlap in a multicomponent system. The indexing is done by comparing the intensity ratios and most likely matched crystal planes of the crystalline phases. The XRD patterns in section 5.3.1.3 were collected for only 20-50° 2θ range which was unable to distinguish other phases. In the present study, the XRD patterns were collected for wide 2θ range (20-90°). So, more planes were detected from the corresponding crystalline phases and the indexing was more certain. Subsequently, different crystalline phases than $La_2Cr_2O_9$ are identified.

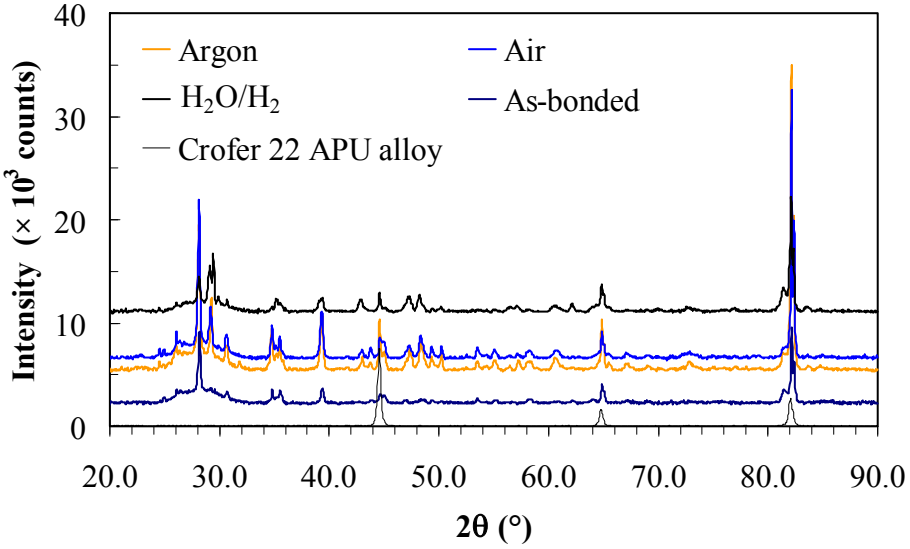

Fig. 5-10. XRD patterns of the Crofer 22 APU alloy, the as-bonded, and the thermally treated Crofer 22 APU/SABS-0 couples.

Based on the identification of the crystalline phases, it can be understood that $Sr_7Al_{12}O_{25}$ and α-$SrSiO_3$ phases form due to devitrification of SABS-0 glass itself. The process can be understood as follows. In the SABS-0 glass, Al^{3+} is a glass former; Sr^{2+} is a charge compensator

for the nearest localized $(AlO_4)^-$ tetrahedral structural units. Microheterogeneity in the SABS-0 glass structure, such as localized $(AlO_4)^-$ tetrahedral units, induces the devitrification of the SABS-0 glass. Accordingly, $Sr_7Al_{12}O_{25}$ crystalline phase forms. In analogy, Si^{4+} is a glass former. Sr^{2+} is a charge compensator for the nearest silicate structural units. Q^0, Q^1, Q^2, and Q^3 silicate structural units with non-bridging oxygen have been observed in the SABS-0 glass in chapter 3. These structural units can induce devitrification and subsequently α-$SrSiO_3$ phase forms. The formation of these phases is also consistent with the higher strontium content in the devitrified phases. Formation of the $Mn(CrMn)O_4$ phase can be understood from the oxidation of the Crofer 22 APU alloy. Manganese is added in the Crofer 22 APU alloy to form protective manganese-chromium spinel at the surface. This is supported by the superimposed manganese and chromium-enriched layer at the interface (Fig 5-9). Formation of Ti_8O_{15} phase can be understood by the internal oxidation of titanium which is supported by the tiny black spots enriched in titanium on the Crofer 22 APU alloy side. However, other forms of titanium oxide such as TiO_2 might be present since these peaks overlap with the Ti_8O_{15} phases. $LaMn_2O_5$ phase forms due to the interaction between La_2O_3 in the SABS-0 glass and the Mn enriched interface on the Crofer 22 APU alloy side. This is supported by the observed La accumulation at the interface in the EDS maps (Fig. 5-9).

The XRD results are consistent with the EDS results. Microstructure and the EDS spot analysis show that the interaction between the Crofer 22 APU alloy and the SABS-0 glass depends on the thermal treatment atmospheres and changes the interface morphology. However, the same crystalline phases for all the thermally treated samples and the as-bonded sample show that the interface is stable regardless of the thermal treatment atmospheres.

5.3.3. Long-term thermal treatment of Crofer 22APU/SABS-0 couple in air and H_2O/H_2 atmospheres

5.3.3.1. Interfacial microstructure

Microstructures of the Crofer 22 APU/SABS-0 glass samples thermally treated in air, and H_2O/H_2 atmospheres for 500 and 1000 hrs are shown in Fig. 5-11. In the images, the left side is the Crofer 22 APU alloy and the right side is the SABS-0 glass. The microstructures at all the studied conditions show distinct bonding interfaces. The microstructures again can be divided into three regions near the interface: tiny (<<1 μm) black spots on the Crofer 22 APU alloy side, crack-free interface, and partially devitrified SABS-0 glass side. The tiny black spots distribute in the Crofer 22 APU alloy within 3 μm region from the interfaces for all the thermally treated samples.

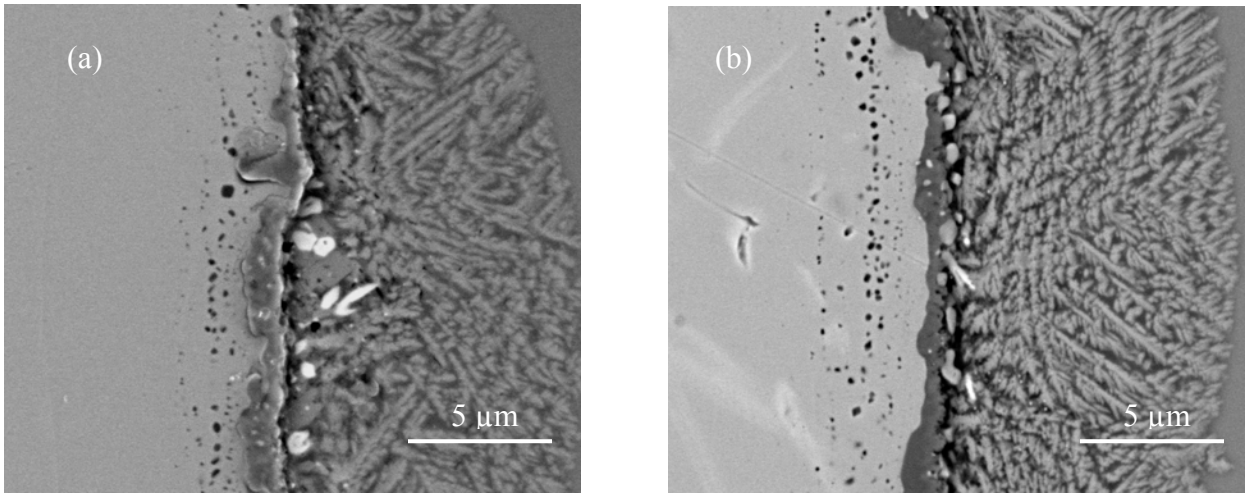

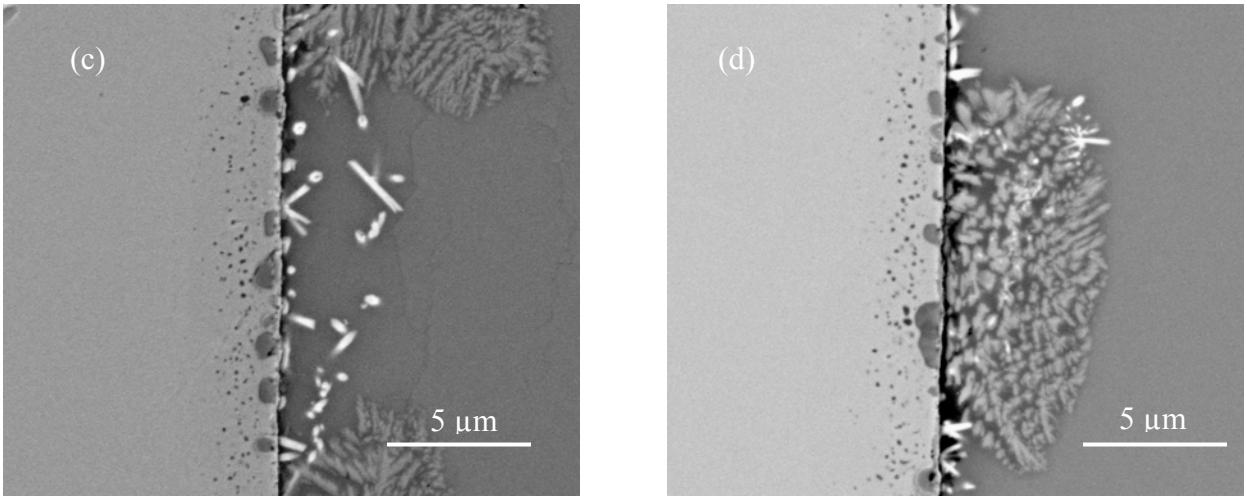

Fig. 5-11. SEM images of thermally treated Crofer 22 APU/SABS-0 couples for: a) 500 hrs in air, b) 1000 hrs in air, c) 500 hrs in H_2O/H_2 atmosphere, and d) 1000 hrs in H_2O/H_2 atmosphere.

The interface morphologies differ for the air treated and the H_2O/H_2 treated samples. The interfaces are uniform, smooth, and 1-2 μm thick with randomly distributed tiny bright spots (<< 1 μm) for the air treated samples. For the H_2O/H_2 treated samples, the interface is thinner (<<1 μm) with granular phases on the Crofer 22 APU alloy side. This suggests that the thermal treatment atmosphere affects the interface morphology. It can be noticed that the granular phases are completely disappeared when thermal treatment time increases from 100 hrs (Fig. 5-7 (c)) to 500 and 1000 hrs (Figs. 5-11 (a) and (b)) for the air treated samples. The granular phases are also reduced with thermal treatment time for the H_2O/H_2 treated samples. This means the chemical reactions between the Crofer 22 APU alloy and the SABS-0 glass change the interface morphology with thermal treatment time. However, the interface morphologies are same for 500 and 1000 hrs thermally treated samples. This means the interface may become in equilibrium after 500 hrs thermal treatment.

On the SABS-0 glass side, different types of secondary phases are observed for the air treated samples: small grayish secondary phases attached to the interface, and equiaxed and platelet bright spots at/near the interface. For the H_2O/H_2 treated sample, only the equiaxed and platelet bright spots are observed. The bright spots are due to the redox reaction between the Crofer 22 APU alloy and the SABS-0 glass. It can be noticed that the bright spots are more in the H_2O/H_2 treated samples than the air treated samples; an opposite trend to that of the samples thermally treated for 100 hrs in air and H_2O/H_2 atmospheres (Figs. 5-7 (c) and (d)). Apparently, this may mean that the H_2O/H_2 atmosphere significantly affect the redox reaction for the long-term thermal treatment. However, the SEM images shown here contain all the observed features and are limited to a very small region compared to the bulk sample. So, the difference in the quantity of bright spots can not be considered as real feature. Partial devitrification of the SABS-0 glass is observed for all the samples as seen by the dendritic phases in the microstructures (Fig. 5-7). However, the extent of devitrification is less in the H_2O/H_2 treated samples and consistent with the microstructures in Figs. 5-7 (c) and (d).

5.3.3.2. Elemental distribution across the interface

The compositional analysis of the different phases in the microstructures across the Crofer 22 APU/SABS-0 interfaces have been carried out by the EDS spot and line scan.

The compositions of the tiny black spots on the Crofer 22 APU alloy near the interface are approximately same (Fe 51.59, Cr 17.44, Mn 0.39, Ti 10.55, Al 1.61, O 18.42) for the air and the H_2O/H_2 treated samples. Again, the tiny black spots are the titanium oxide.

The interface of the air treated sample is enriched in chromium and manganese (Fe7.47, Cr 26.82, Mn 0.91, Si 1.19, Al 0.45, O 59.56). For the H_2O/H_2 treated sample, the composition

of the interface is almost similar but contains all the SABS-0 glass elements (Fe 26.20, Cr 16.50, Mn 1.85, Ti 2.10, Si 3.53, Sr 4.31, La 0.77, Al 2.27, and O 42.46). For the H_2O/H_2 treated sample, the granular phases on the Crofer 22 APU alloy side near the interface has the composition of Fe 22.49, Cr 22.98, Mn 3.10, Ti 2.12, Si 0.67, Sr 1.72, Al 0.58, and O 46.34 (Fig. 5-11 (d)).

On the SABS-0 glass side, the granular bright spots attached to the interface for the air treated sample consists of Fe 58.67, Cr 12.53, Mn 1.46, Si 3.59, Sr 1.74, La 0.73, Al 1.61, and O 19.68. The bright spots due to redox reactions have the similar compositions for the air and the H_2O/H_2 treated samples (Fe 3.26-8.97, Cr 3.30-3.70, Mn 0.49-0.74, Si 18.71-19.43, Sr 9.75-11.12, La 6.89-6.99, Al 3.41-3.84, and O 34.47-47.77). The devitrified phases of the SABS-0 glass can not be distinguished from the glass phases for the air treated sample. For the H_2O/H_2 treated sample, the devitrified phases have higher Sr and La and lower Al content than the glass phase. Again, the devitrified phases and the black spots between them near the interface also contain small amount of iron and chromium.

The concentration profiles of the air and the H_2O/H_2 treated Crofer 22 APU/SABS-0 are shown in Fig. 5-12. In Fig. 5-12, '0' on the 'x' axis indicates the boundary between the alloys and the interface. The left (negative) side is the alloy and the right (positive) side is the SABS-0 glass. 'y' axis shows the normalized concentration of the elements.

The SABS-0 glass elements (Si, Sr, La, Al, and O) diffuse 2-4 μm into the Crofer 22 APU alloy side for the air and the H_2O/H_2 treated samples regardless of thermal treatment time. Iron in the Crofer 22 APU alloy diffuses ~ 6 μm and 3-5 μm, respectively, into the SABS-0 glass for the air and the H_2O/H_2 treated samples. Chromium diffuses 5-7 μm and 8-9 μm, respectively, into the SABS-0 glass for the air and the H_2O/H_2 treated samples. Manganese and titanium

concentration is maximum at/near the interface. Also, the highest titanium concentration is observed beneath the highest manganese concentration.

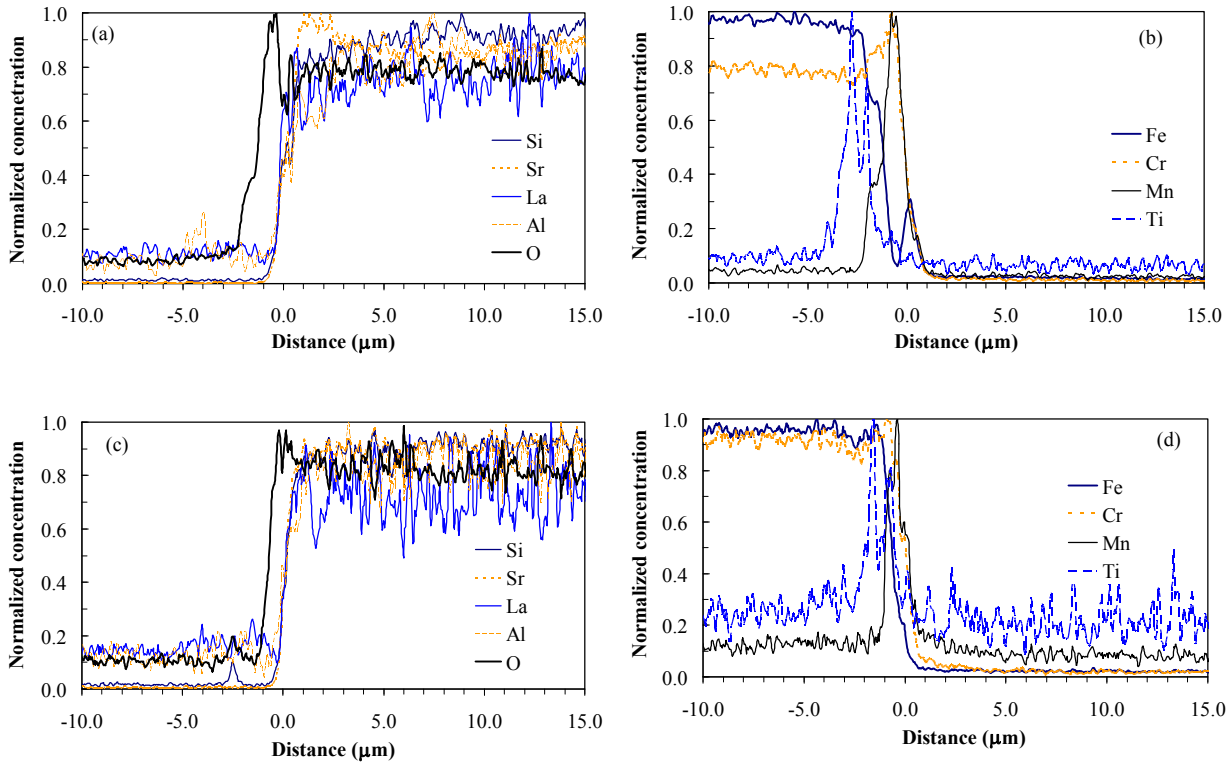

Fig. 5-12. Elemental concentration profiles of the thermally treated Crofer 22 APU/SABS-0 couples for 1000 hrs: a) SABS-0 glass elements and b) Crofer 22 APU elements for air treated sample; and c) SABS-0 glass elements and d) Crofer 22 APU elements for H_2O/H_2 treated samples.

For better understanding about the elemental distribution across the interface, the EDS maps are shown for 1000 hrs thermally treated couples in Fig. 5-13 for the air treated sample and in Fig. 5-14 for the H_2O/H_2 atmosphere. It can be observed that silicon and strontium in the SABS-0 glass are uniformly distributed and do not diffuse into the Crofer 22 APU alloy.

Aluminium in the SABS-0 glass diffuses slightly to the Crofer 22 APU alloy as seen by the localized aluminium enriched region superimposed with the tiny black spots on the Crofer 22 APU alloy. This is also consistent with the presence of aluminium in the composition of the tiny black spots. Lanthanum is slightly enriched at the interface. By comparing the lanthanum enriched spots with the microstructures (Figs. 5-11(b) and (d)), it can be understood that the platelet bright spots have lanthanum. This observation is consistent with the EDS spot analysis. Oxygen is accumulated at the interface. Iron is depleted at the interface where chromium and manganese are enriched. For the air treated sample, Fe-rich localized region is observed on the SABS-0 glass side near the interface; which superimposes with the granular bright spots in the microstructure (Fig. 5-11 (b)). Chromium- and manganese –enriched regions superimpose with the interface for the air treated sample and the granular phases on the Crofer 22 APU alloy side along with the interface for the H_2O/H_2 treated sample. Titanium-enriched region is again observed beneath the manganese-enriched region. However, the overall distribution of the SABS-0 glass elements are uniform as can be understood by a little compositional difference among the dendritic phases, black spots between the dendritic phases, and the bulk glass. Chromium, manganese, and oxygen-enriched and iron depleted regions are observed and superimposed with the granular phase positions on the Crofer 22 APU alloy side in the microstructures (Fig. 5-11).

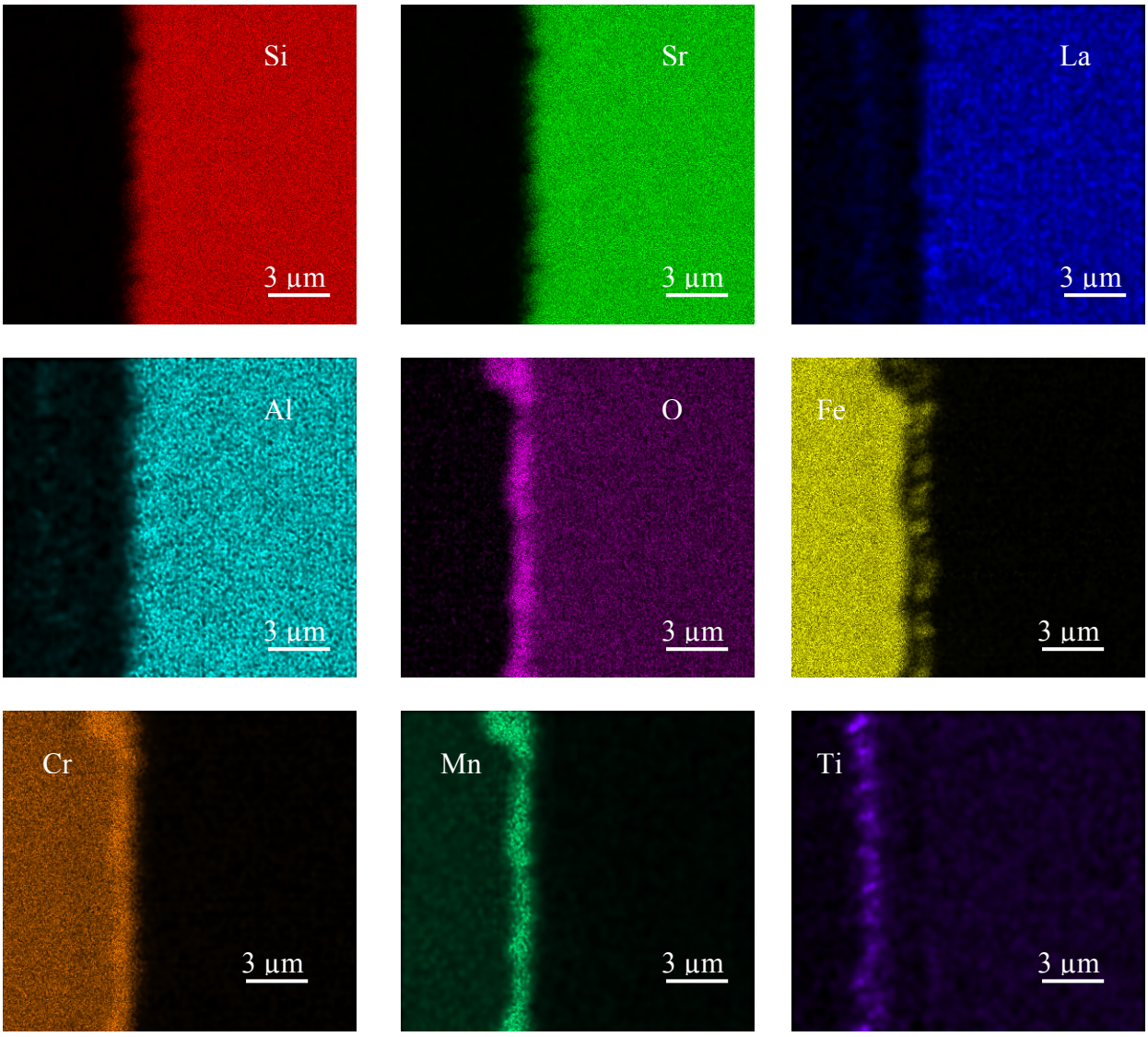

Fig. 5-13. Elemental maps for the Crofer 22 APU/SABS-0 couple thermally treated at 800°C for 1000 hrs in air.

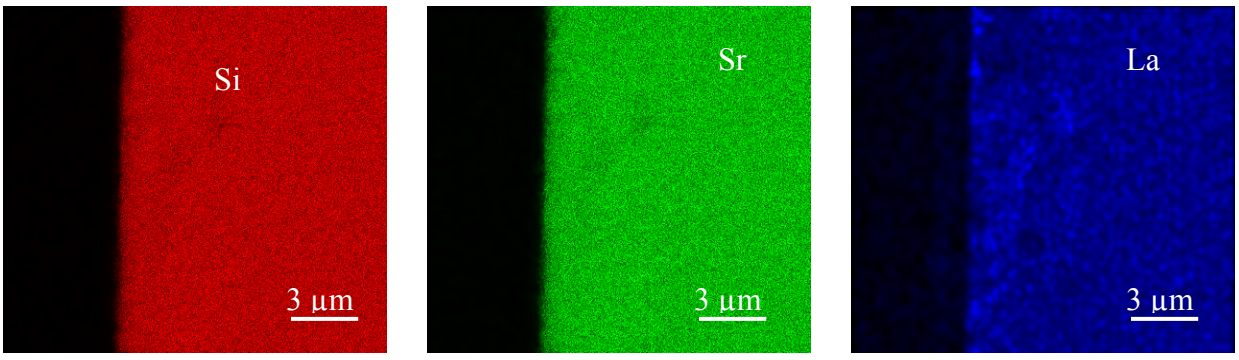

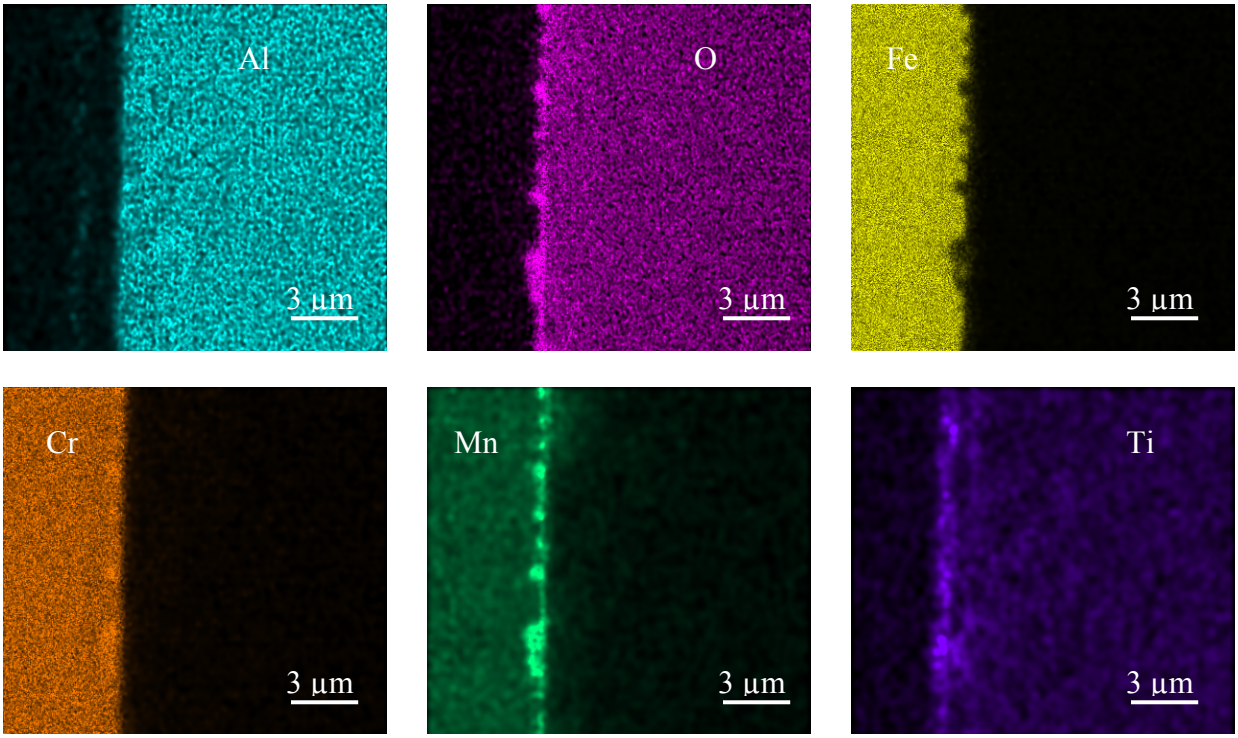

Fig. 5-14. Elemental maps for the Crofer 22 APU/SABS-0 couple thermally treated at 800°C for 1000 hrs in H_2O/H_2 atmosphere.

5.3.3.3. X-ray diffraction

The XRD patterns of the Crofer 22 APU alloy and the Crofer 22 APU/SABS-0 samples are shown in Fig. 5-15. The presence of the Crofer 22 APU alloy peaks in all the samples confirms that the XRD patterns include all the crystal phases across the interface. The crystal phases can be identified as $Sr_7Al_{12}O_{25}$, α-$SrSiO_3$, $Mn(CrMn)O_4$, Ti_8O_{15}, and $LaMn_2O_5$. The same locations of peaks in the XRD patterns mean that the crystal phases are the same for all the studied samples. However, the XRD peak intensities vary. This is likely due to the thermal treatment effect and the slightly different thickness of the SABS-0 glass layer on the Crofer 22 APU alloy. Same crystalline phases regardless of thermal treatment times and the atmospheres again indicate the interface stability.

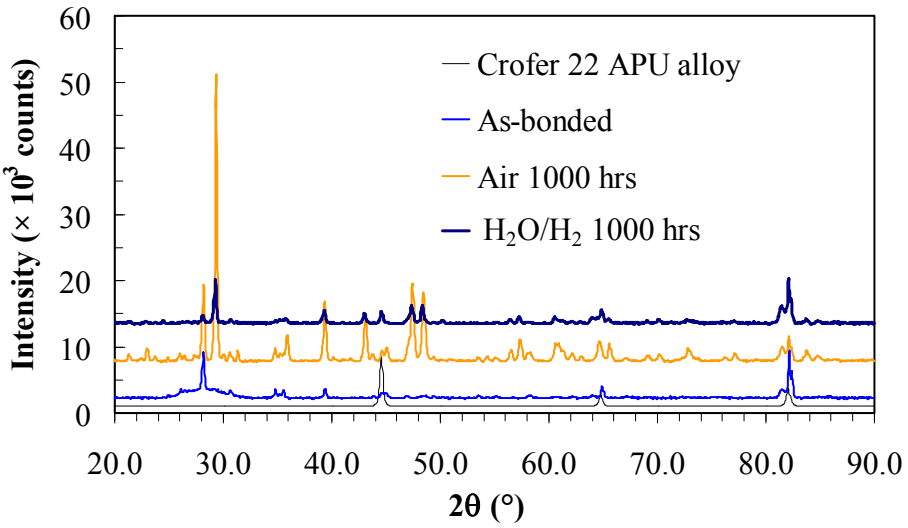

Fig. 5-15. XRD patterns of the Crofer 22 APU alloy and the as-bonded and the thermally treated Crofer 22 APU /SABS-0 couples.

5.3.4. Interfacial study by complementary methods

The spatial resolution of EDS is ≥ 1 μm. The elemental peaks in the EDS spectra can overlap. To check the reliability of the compositional analysis by EDS, two complementary techniques were carried out for selected samples: wave length dispersive spectroscopy (WDS) and EDS analysis of thin (~ 200 nm) Crofer 22 APU/SABS-0 samples.

5.3.4.1. Wave length dispersive spectroscopy (WDS)

In WDS analysis, the signal processing is based on the characteristic wavelength of the backscattered electrons by Bragg's law of diffraction. The count rate is proportional to the energy corresponding to the characteristic wavelength of the backscattered X-rays of the elements. The resolution of WDS is better (10-30 times) than that of EDS because of the absence of peak overlaps [16]. However, the spatial resolution is similar to the EDS. Crofer 22

APU/SABS-0 couple thermally treated in air for 1000 hrs has the thickest interface and the highest quantity of the devitrified phases. So, this sample is the most suitable to study the composition across the interface and the compositional difference between the devitrified phases and the glass. Subsequently, WDS was carried out only for this sample.

'Standard' method was used for the WDS analysis. Line scans were taken across the interface with 2 μm step size in order to eliminate fluorescence effect and can be compared directly with the elemental distribution obtained by EDS. Similar to EDS analysis, three line scans were taken from randomly selected regions across the interface.

The concentration profiles obtained from WDS line scan are shown in Fig. 5-16. The oscillations in the concentration profiles of the SABS-0 glass elements (Fig. 5-16 (a)) are again observed instead of the larger step size. In addition the oscillations are also extended beyond the devitrified region on the SABS-0 glass side (≥ 10 μm from the interface). Again, oscillations are also observed for silicon and strontium. This confirms that the lower density of the SABS-0 glass contributes to the oscillations [16]. From Fig. 5-16(a) it can be seen that the SABS-0 glass elements do not diffuse more than 2 μm into the Crofer 22 APU alloy. Fig. 5-16 (b) shows the humps near the interface for chromium, manganese, and titanium. The hump for oxygen is not distinguishable because of larger step size compared to EDS analysis. Similar concentration profiles from EDS and WDS analysis complement each other. This means the compositional analysis obtained from EDS is reliable.

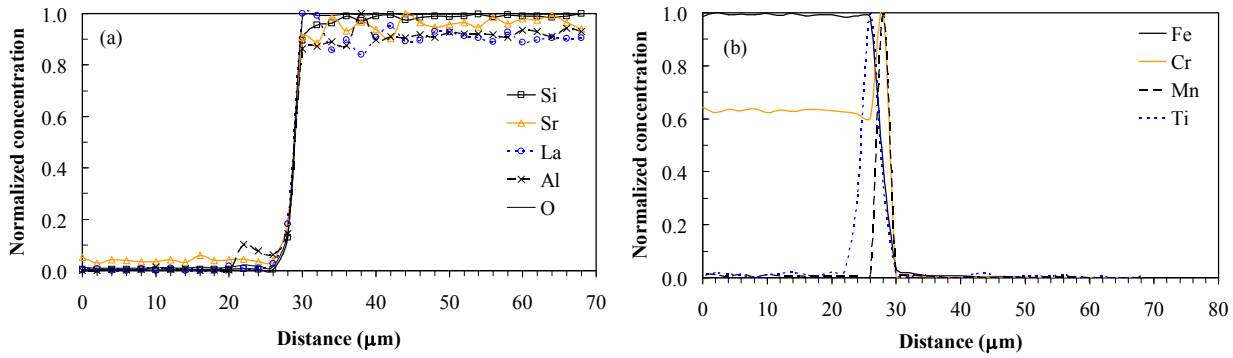

Fig. 5-16. WDS line scan across the Crofer 22 APU/SABS-0 interface: a) concentration profile of SABS-0 glass elements and b) concentration profile of Crofer 22 APU elements.

5.3.4.2. Interfacial study of thin Crofer 22 APU/SABS-0

The spatial resolution of EDS is ≥ 1μm. The secondary X-rays of the elements interact more in the transverse direction than the lateral direction. Therefore, thin sample can eliminate the interactions of different elements to a certain extent. Crofer 22 APU/SABS-0 couples thermally treated for 1000 hrs at 800°C in air and H_2O/H_2 were analyzed by using this approach. The samples were thinned to ~ 200 nm using focused ion beam (FEI Helios 600 NanoLab, USA).

Microstructures of the thin Crofer 22 APU/SABS-0 couples shown in Fig. 5-17. In the images, the left side is the Crofer 22 APU alloy and the right side is the SABS-0 glass. Simialr to the bulk samples, the microstructures again can be divided into three regions near the interface: tiny (<<1 μm) black spots on the Crofer 22 APU alloy side, crack-free interface, and partially devitrified SABS-0 glass side. The tiny black spots distribute in the Crofer 22 APU alloy within 3 μm region from the interfaces for both the air and H_2O/H_2 treated samples similar to the bulk samples (Figs. 5-11(b) and (d)).

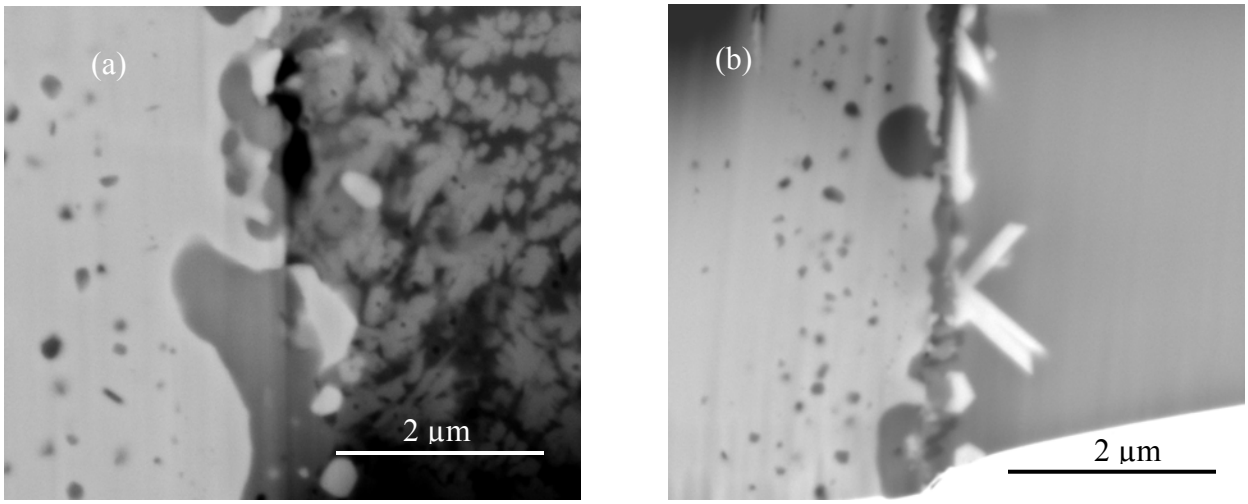

Fig. 5-17. SEM images of thin Crofer 22 APU/SABS-0 couple thermally treated for 1000 hrs at 800°C in: a) air and b) H_2O/H_2 atmospheres.

The interface morphologies differ for the air and the H_2O/H_2 treated samples. The interface is thinner for the H_2O/H_2 treated sample than that of air and consistent with the microstructures of the bulk sample (Figs. 5-11 (b) and (c)). On the Crofer 22 APU alloy side near the interface, secondary phases are observed for both the air and H_2O/H_2 treated samples but the interface is relatively rough for the H_2O/H_2 treated sample. The interface morphologies are also similar to the bulk samples (Figs. 5-11(b) and (d)).

On the SABS-0 glass side, bright secondary phases are observed near the interface. The bright phases are observed for both the samples. However, the platelet bright spots are observed only for the H_2O/H_2 treated sample. This may be attributed to the small scan area of the samples. Devitrified phases of the SABS-0 glass and the black spots between them are distinguishable for the air treated sample (Fig. 5-17(a)). The devitrified phases are absent for the H_2O/H_2 treated sample (Fig. 5-17(b)). This observation is consistent with the microstructures of the bulk samples (Figs. 5-11(b) and (d)); where the devitrified phases are present in localized region for the

H_2O/H_2 treated sample. Since the scan area is very small for the thin samples, the devitrified phases are not covered.

The compositional analysis of the different phases in the microstructures across the Crofer 22 APU/SABS-0 interfaces has been carried out by the EDS spot and line scans with the same conditions as for the bulk samples.

The compositions of the tiny black spots on the Crofer 22 APU alloy near the interface are approximately same (Fe 60.11, Cr 21.17, Mn 0.49, Ti 12.98, O 0.5-1.0) but 4.67 at% aluminium is present for the air treated and 1.19 at% silicon is present for the H_2O/H_2 treated samples. However, presence of aluminium is also observed for the bulk samples but silicon is not present in the tiny spots of the bulk samples (Figs. 5-11(b) and (d)). In addition, the oxygen is very less compared to the bulk sample. These discrepancies may be attributed to the damage of sample during sample preparation using ion beam. Nonetheless, the compositions of the tiny black spots are almost consistent with the composition obtained from the bulk samples.

For the air treated sample, the secondary phases on the Crofer 22 APU alloy side near the interface consists of Fe 1.17, Cr 37.09, Mn 6.37, Ti 2.55, Si 6.85, Sr 3.55, Al 5.10, O 32.31. For the H_2O/H_2 treated sample, the composition of the granular secondary phases on the Crofer 22 APU alloy side near the interface is Fe 23.65, Cr 57.90, Mn 8.80, Ti 2.23, Si 0.88, Sr 1.86, Al 1.16, O 3.54. The composition is consistent with the composition of the granular phases in the bulk H_2O/H_2 sample (Figs. 5-11(d)) and also similar with that of the secondary phases for the air treated sample. The composition shows that these secondary phases form due to the reaction between the Crofer 22 APU alloy and the SABS-0 glass. The interface of the air treated samples consists of Fe 7.69, Cr 44.32, Mn 6.89, Si 21.87, Al 7.67, O 11.45 and similar to the secondary phases on the Crofer 22 APU alloy side. The quantity of the Crofer 22 APU alloy elements at the

interface is consistent with the bulk sample but the quantity of the SABS-0 elements is inconsistent with the bulk sample composition. The quantity of silicon and aluminium is very high and oxygen is very low for the thin samples than the bulk samples. This may again be attributed to the sample damage during thin sample preparation. For the H_2O/H_2 treated sample, the composition of the interface is almost similar and consistent with the bulk samples (Fe 18.03, Cr 37.57, Mn 5.17, Ti 2.04, Si 8.45, Sr 3.97, La 2.32, Al 3.06, and O 19.40). The composition of the interface is similar to the granular secondary phases on the Crofer 22 APU alloy side.

On the SABS-0 glass side, the bright spots for the air treated sample consist of Fe 60.50, Cr 23.26, Mn 1.01, Sr 8.62, La 0.90, Al 6.05, and O 0.25. Again, discrepancies of the silicon and oxygen content are observed with the composition of the bright spots in the bulk sample. The platelet bright spots in the H_2O/H_2 treated sample consist of Fe 2.68, Cr 2.98, Mn 0.71, Si 11.04, Sr 7.35, Al 1.78, O 67.83 and consistent with bulk sample (Figs. 5-11(d)). For the air treated sample, the compositional difference between the devitrified phases and the black spots between the devitrified phases is distinct. The devitrified phases are enriched in strontium and have slightly higher lanthanum and silicon and slightly lower aluminium than the black spots. This observation is consistent with the bulk sample and with the identified crystalline phases. Similar to the bulk sample, the devitrified phases and the black spots between them near the interface contain small amount of iron and chromium. For H_2O/H_2 treated sample, iron and chromium are also found in the SABS-0 glass composition near the interface.

The concentration profiles of the air and the H_2O/H_2 treated thin Crofer 22 APU/SABS-0 are shown in Fig. 5-18. Oscillation in the concentration profiles of the SABS-0 glass elements are also observed for both air and H_2O/H_2 treated samples. The extent of the oscillations in the concentration profiles is more for the air treated sample. This supports the previous explanation

that the oscillations are due to the compositional difference between the devitrified phases of the SABS-0 glass and the black spots between them. This observation is also consistent with the absence of devitrified phases for the H_2O/H_2 treated sample (Fig. 5-18 (b)). The oscillations in the concentration profiles of the SABS-0 glass elements for the H_2O/H_2 treated sample can be understood for lanthanum and aluminium due to their low concentration. However, Si and Sr content in the SABS-0 glass are sufficient for the detection limit of the EDS but oscillations are observed. In the thin samples, the spatial resolution is improved in the transverse direction but the lateral resolution remains same as in the bulk sample. It has been argued in previous sections that the oscillations may be due to the small step size used for the line scan. In the thin samples the given concentration profile is the line scan from one region. The SABS-0 glass is homogeneous in the H_2O/H_2 treated sample due to the absence of devitrified phases and also confirmed by spot and areal compositional analysis in randomly selected regions. Therefore, the spatial resolution limit in the EDS can not be the sole reason oscillations in EDS profiles. In Fig. 5-18, '0' on the 'x' axis indicates the boundary between the alloys and the interface. The left (negative) side is the Crofer 22 APU alloy and the right (positive) side is the SABS-0 glass. 'y' axis shows the normalized concentration of the elements.

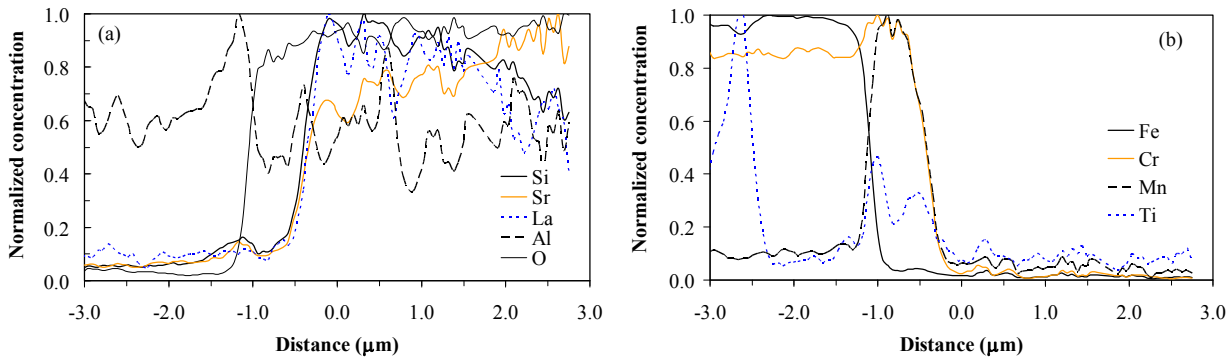

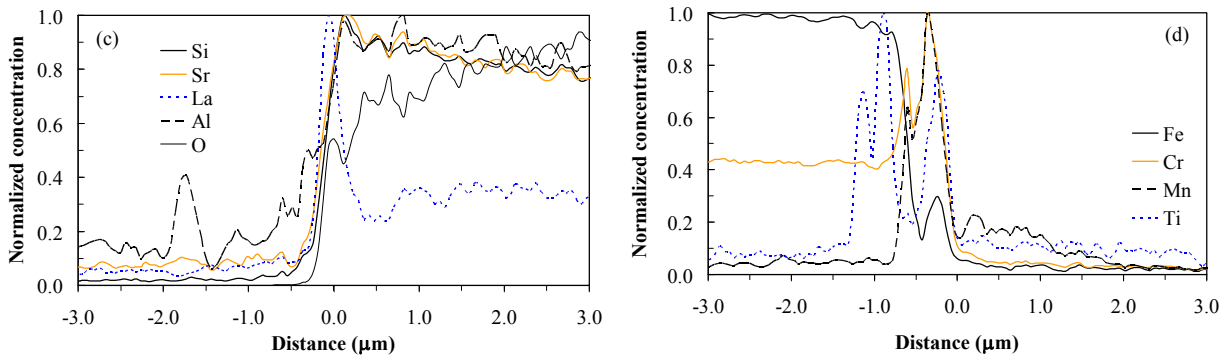

Fig. 5-18. Elemental concentration profiles of thin Crofer 22 APU/SABS-0 couples thermally treated for 1000 hrs: a) SABS-0 glass elements and b) Crofer 22 APU elements for air treated sample; and c) SABS-0 glass elements and d) Crofer 22 APU elements for H_2O/H_2 treated samples.

The SABS-0 glass elements (Si, Sr, La, Al, and O) diffuse 2-4 µm into the Crofer 22 APU alloy side for the air and the H_2O/H_2 treated samples. Hump in aluminium concentration profile is observed on the Crofer 22 APU alloy side and consistent with the presence of aluminium in the tiny black spots. The concentration of aluminium is also higher than other SABS-0 glass elements on the Crofer 22 APU side. This can be understood by the fact that the tiny black spots extend ~ 3 µm from the interface. Iron in the Crofer 22 APU alloy diffuses 1-3 µm into the SABS-0 glass for the air and the H_2O/H_2 treated samples. Chromium diffuses 2-3 µm into the SABS-0 glass for the air and the H_2O/H_2 treated samples. Iron and chromium diffusion distances are not consistent with the bulk sample. The inconsistency may have two origins. First, the concentration profiles of the bulk samples are the average of three line scans form randomly selected regions. The interface thickness is not uniform throughout the sample. So, the average can include more error. Second, interaction between the X-rays of different elements due to relatively poor spatial resolution in the bulk sample can also contribute to

apparently longer diffusion distance. Manganese and titanium concentration is maximum at/near the interface similar to the bulk samples. Also, the highest titanium concentration is beneath the highest manganese concentration. However, the hump in titanium concentration profile is far from the interface and is not consistent with the bulk samples. The reason is not understood.

The elemental maps for the thin Crofer 22 APU/SABS-0 couples are shown in Figs. 5-19 and 5-20 for the air and H_2O/H_2 treated samples, respectively. It can be observed that silicon and strontium in the SABS-0 glass are uniformly distributed and do not diffuse into the Crofer 22 APU alloy. Lanthanum, aluminium, and oxygen diffuse into the SABS-0 glass for the air treated sample but these elements do not diffuse into the Crofer 22 APU alloy for the H_2O/H_2 treated sample. Lanthanum is enriched at the interface for the H_2O/H_2 treated sample. By comparing the lanthanum enriched spots with the microstructure (Figs. 5-17(b)), it can be understood that the platelet bright spots have lanthanum. This observation is consistent with the EDS spot analysis as well as with the bulk sample. Iron is depleted near the interface for both the samples and the depleted regions superimpose with the secondary phases on the Crofer 22 APU alloy side (Figs. 5-17(a) and (b)). Unlike bulk samples, chromium enriched region at the interface is not observed. For the air treated sample, iron and chromium enriched localized spots are observed on the SABS-0 glass side; which superimpose with the bright spots and consistent with their composition and the bulk sample. Manganese enriched region at the interface is also consistent with the bulk sample. Titanium-enriched region is again observed beneath the manganese-enriched region and consistent with the observations in the bulk samples.

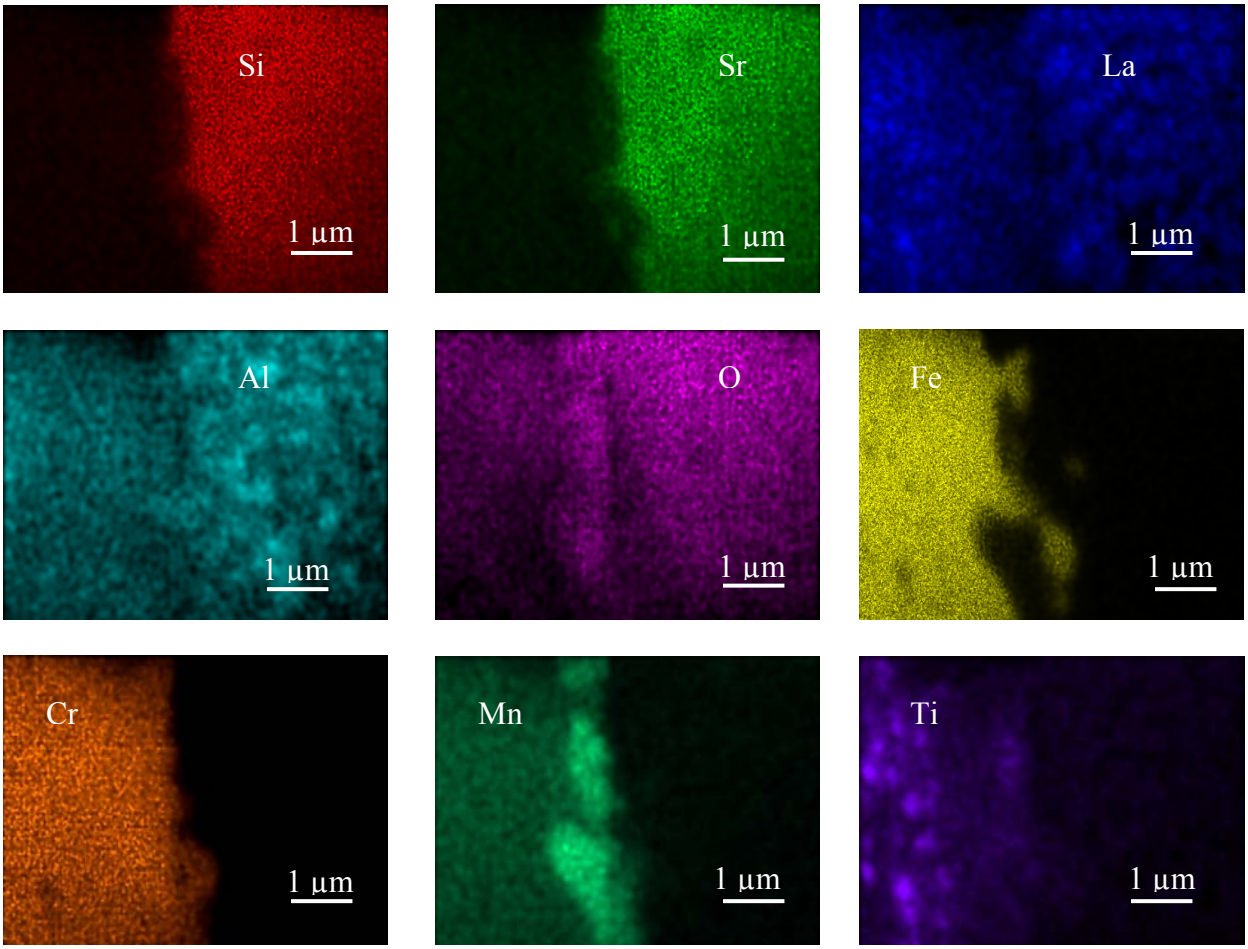

Fig. 5-19. Elemental maps for the Crofer 22 APU/SABS-0 couple thermally treated at 800°C for 1000 hrs in air.

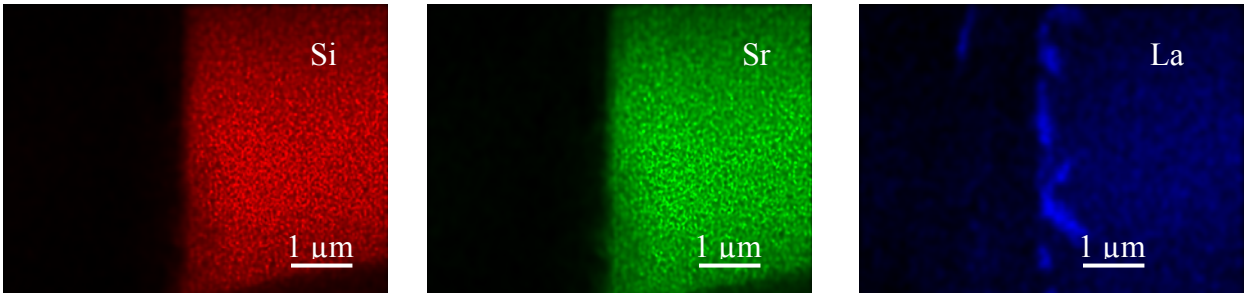

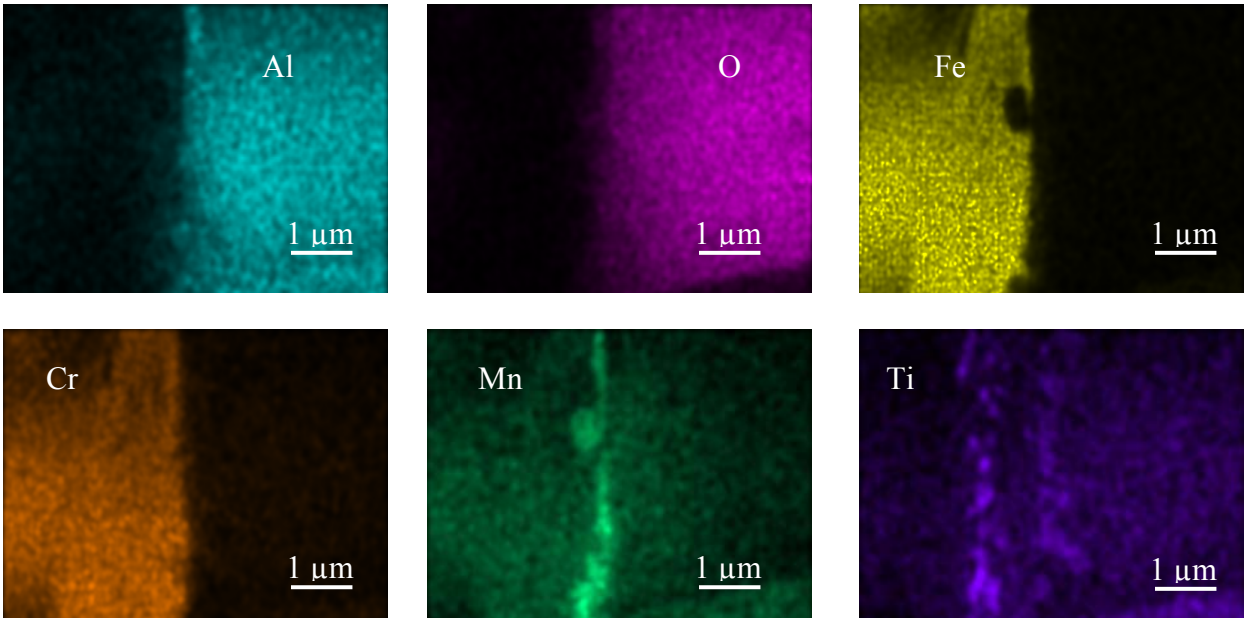

Fig. 5-20. Elemental maps for the Crofer 22 APU/SABS-0 couple thermally treated at 800°C for 1000 hrs in H_2O/H_2 atmosphere.

The interface morphologies and the compositional analysis of the thin Crofer 22 APU/SABS-0 couples are consistent with the bulk samples. This means the compositional trend across the interfaces obtained from EDS are reliable. However, the elemental maps for chromium and oxygen for the thin couples are inconsistent with the bulk sample. The reasons are not understood. Overall, compositional analysis of the thin Crofer 22 APU/SABS-0 couples complement with the bulk sample analysis.

5.4. Conclusions

Interfacial compatibility and stability of Crofer 22 APU/SABS-0 couple has been studied with respect to thermal treatment time, temperature, and atmosphere. The SABS-0 glass (SrO-La_2O_3-Al_2O_3-SiO_2) is compatible with the Crofer 22 APU alloy. The Crofer 22 APU/SABS-0 interface is thermochemically stable at 800°C for 1000 hrs in both oxidizing and reducing

(H_2O/H_2) atmospheres. Chemical reactions and inter-diffusion between the Crofer 22 APU alloy and the SABS-0 glass along with the SABS-0 glass devitrification occur simultaneously during sealing and the thermal treatments. $Sr_7Al_{12}O_{25}$ and α-$SrSiO_3$ phases form due to the SABS-0 glass devitrification. $Mn(CrMn)O_4$ and Ti_8O_{15} phases form at the interface due to oxidation of the Crofer 22 APU alloy. $LaMn_2O_5$ phases form at the interface due to the inter-diffusion and chemical reactions between the Crofer 22 APU alloy and the SABS-0 glass. The long-term (1000 hrs) interfacial stability Crofer 22 APU/SABS-0 couple demonstrates the suitability of the SABS-0 seal glass for SOFC/SOEC application.

The compositional trend across the interface obtained from EDS was verified by WDS and EDS analysis for the selected Crofer 22 APU/SABS-0 couples. Similar compositional trends across the interface obtained from all of these complementary methods prove the reliability of bulk sample analysis. However, some deviation in the compositional trends are observed for the thin Crofer 22 APU/SABS-0 couples, which can be attributed to the sample damage during sample thinning by ion beam.

References

[1] W. Z. Zhu and S. C. Deevi, Development of inteconnect materials for solid oxide fuel cell,. Materials Science and Engineering A 348, 227-243, 2003.

[2] Z. Yang, Recent advances in metallic interconnects for solid oxide fuel cells, International Materials Reviews 53, 39-54, 2008.

[3] J. M. Howe, Bonding, structure, and properties of metal/ceramic interfaces: Part 1 Chemical bonding, chemical reaction, and interfacial structure, International Materials Reviews 38, 233-256, 1993.

[4] J. M. Howe, Bonding, structure, and properties of metal/ceramic interfaces: Part 2 Interface fracture behavior and property measurement, International Material Reviews 38, 257-271, 1993.

[5] I. W. Donald, Preparation, properties and chemistry of glass and glass-ceramic-to-metal seals and coatings, Journal of Materials Science 28, 2841-2886, 1993.

[6] P. Batfalsky, V. A. C. Haanappel, J. Malzbender, N. H. Menzler, V. Shemet, I. C. Vinke, and R. W. Steinbrech, R. W., Chemical interaction between glass-ceramic sealants and interconnects in SOFC stack, Journal of Power Sources 155, 128-137, 2006.

[7] Z. Yang, G. Xia, K. D. Meinhardt, K. S. Weil, and J. W. Stevenson, Chemical Stability of glass seal interface in intermediate temperature solid oxide fuel cells, Journal of Materials Engineering and Performance 13, 327-334, 2004.

[8] Z. Yang, K. D. Meinhardt, and J. W. Stevenson, Chemical compatibility of barium-calcium aluminosilicate -based sealing glasses with the ferritic stainless steel interconnect in SOFCs, Journal of the Electrochemical Society 150, A1095-A1101. 2003.

[9] V. A. C. Haanappel, V. Shemet, I. C. Vinke, S. M. Gross, T. H. Koppitz, N. H. Menzler, M. Zahid, and W. J. Quadakkers, Evaluation of the suitability of various glass sealant-alloy combinations under SOFC stack conditions, Journal of Materials Science 40, 1583-1592, 2005.

[10] V. A. C. Haanappel, V. Shemet, S. M. Gross, T. Koppitz, N. H. Menzler, M. Zahid, and W. J. Quadakkers, Behavior of various glass-ceramic sealants with ferritic steels under simulated SOFC stack conditions, Journal of Power Sources 150, 86-100, 2005.

[11] Y. S. Chou, J. W. Stevenson, and P. Singh, Novel refractory alkaline earth silicate sealing glasses for planar solid oxide fuel cells, Journal of the Electrochemical Society 154, B644-B651, 2007.

[12] C. Lara, M. J. Pascual, and A. Durán, Chemical compatibility of RO-BaO-SiO_2 (R = Mg,

Zn) glass-ceramic seals with SOFC components, Physics Chemistry of glasses: European Journal of Glass Science and Technology B 48, 218-224, 2007.

[13] N. H. Menzler, D. Sebold, M. Zahid, S. M. Gross, and T. Koppitz, Interaction of metallic SOFC interconnect materials with glass-ceramic sealant in various atmosphere, Journal of Power Sources 152, 156-167, 2005.

[14] B. D. Cullity, Elements of X-ray diffraction, 2nd ed., Addision-Wesley Publishing Company Inc., Philippines, 292-294, 1978.

[15] P. Kumar and V. A. Greenhut, Metal-ceramic Joining, TMS Minerals, Metals, Materials, Warrendaley, Pennsylvania, 3-11, 1990.

[16] J. Goldstein, D. Newbury, D. Joy, C. Lyman, P. Echlim, E. Lifshin, L. Sawyer, and J. Michael, Scanning electron microscopy and X-Ray microanalysis. 3rd ed. Springer, New York, USA, 2007.

[17] W.J. Quadadakkers, V. Shemet and L. Singheiser, US Patent No. 0,059,335, 2003.

[18] G. Beranger, F. Armanet, and M. Lambertin, Active elements in oxidation and their properties pp. 33-51 in The Role of Active Elements In the Oxidation Behaviour of High Temperature Metals and Alloys, Edited by E. Lang, Elsevier Applied Science, London, 1989.

[19] M.J. Bennet and D.P. Moon, Effect of active elements on the oxidation behavior of Cr_2O_3 formers, pp. 111-129 in The Role of Active Elements In the Oxidation Behaviour of High Temperature Metals and Alloys, Edited by E. Lang, Elsevier Applied Science, London, 1989.

[20] H.P. Klug and L.E. Alexander, X-ray diffraction procedures for polycrystalline and amorphous materials, 2nd ed., John Wiley and Sons, New York, 1974.

[21] K. LU, and M. K. Mahapatra, Network structure and thermal stability study of high temperature seal glass, Journal of Applied Physics 104, 074910, 2008.

[22] L. Cromier, G. Calas, S. Creux, P.H. Gaskell, B. Bouchet-Fabre, and A.C. Hannon, Environment around strontium in silicate and aluminosilicate glasses, Physical Review B 59, 13517-13520, 1999.

[23] N. Jiang, J. Silox, Observations of reaction zones at the chromium/oxide glass interfaces, Journal of Applied Physics 87, 3768-3776, 2000.

[24] M.B. Volf, Chemical approaches to glass: glass science and technology, vol. 7, Elsevier, Amsterdam, 83-88, 1984.

[25] E. Essuman, G. H. Meier, J. Żurek, M. Hänsel, and W. J. Quadakkers, The effcet of water vapor on selective oxidation of Fe-Cr alloys, Oxidation of Metals 69, 143-162, 2008,.

[26] J.A. Pask, The American Society of Mechanical Engineers, New York, 1-7, 1987.

[27] P. Kofstad, High temperarture corrosion. Elsevier Applied Science Publishers Ltd, England, 1988.

[28] R. E. Lobbing, H. P. Schmidt, K. Hennesen, and H. J. Grabke, Diffusion of cations in chromia layers grown on iron-base alloys, Oxidation of Metals 37, 81-93, 1992.

[29] M. G. C. Cox, B. McEnaney, and V. D. Scott, A chemical diffusion model for partitioning of transition elements in oxide scales of alloys, Philosophical Magazine 2, 839-851, 1972.

[30] B. B. Ebbinghaus, Thermodynamics of gas phase chromium species: The chromium oxides, the chromium oxyhydroxides, and volatility calculations in waste incineration processes, Combustion and Flame 93, 119-137, 1993.

[31] W. D. Kingery, H. K. Bowen, and D. R. Uhlmann, Introduction to Ceramics, John Wiley and Sons, New York, 2nd ed., 1976.

CHAPTER SIX

INTERFACIAL STUDY OF SEAL GLASS WITH AISI 441 ALLOY METALLIC INTERCONNECT

Abstract

AISI 441 alloy is a metallic interconnect for planar solid oxide fuel and electrolyzer cells. The interfacial compatibility and thermochemical stability are studied for SrO-La_2O_3-Al_2O_3-SiO_2 (SABS-0) seal glass with the AISI 441 alloy with respect to thermal treatment atmospheres such as argon, air, and H_2O/H_2, and time (0-1000 hrs). The interfaces were investigated by scanning electron microscopy (SEM), energy dispersive spectroscopy (EDS), and X-ray diffraction (XRD). Chemical reaction and inter-diffusion between the seal glass and the AISI 441 alloy occur simultaneously with the devitrification of the seal glass. Interface morphology differs with the thermal treatment conditions but same crystalline compounds are found across the interface regardless of the thermal treatment conditions.

6.1. Introduction

AISI 441 alloy is a ferritic chromia forming alloy which is under intensive study for solid oxide fuel/electrolyzer cell (SOFC/SOEC) interconnect. AISI 441 alloy has some advantages than the Crofer 22 APU alloy. AISI 441 alloy has comparable oxidation resistance (rate constant 5.0×10^{-4} g^2 cm^{-4} s^{-1}) but superior yield strength (83 MPa at 760°C) than the Crofer 22 APU alloy (rate constant 7.96×10^{-4} g^2 cm^{-4} s^{-1} and yield strength 31 MPa at 760°C) [1,2]. AISI 441 alloy has lower chromium content (~ 18 wt%) and subsequently chromium vaporization rate can

be reduced [3]. The cost of AISI 441 alloy is less than the Crofer 22 APU alloy, which is the driving force for intensive study. The importance of the interconnect-seal interfacial study has been discussed in chapter five. However, the interconnect-glass seal interfacial studies for the AISI 441 alloy has not been reported in literature.

In this chapter, interfacial study of a SrO-La_2O_3-Al_2O_3-SiO_2 –based seal glass (SABS-0) with the AISI 441 alloy is studied. The effects of thermal treatment atmospheres and time on the AISI alloy-SABS-0 interface were investigated by detailed microstructural analysis using scanning electron microscopy (SEM), energy dispersive spectroscopy (EDS), and X-ray diffraction.

6.2. Experimental procedure

6.2.1. Glass preparation

SABS-0 glass was prepared by conventional quenching method. $SrCO_3$ (99.9%, Sigma Aldrich, St. Louis, MO), La_2O_3 (99.98%), Al_2O_3 (99.95%), and SiO_2 (99.8%) (all oxides were from Alfa Aesar, Ward Hill, MA) at designed ratios were mixed in a ball mill for overnight. The mixed powders were heated in a platinum crucible in a box furnace (Lindberg, Model No. 51314, Watertown, WI) to 1100°C and kept there for 1 hr for $SrCO_3$ to decompose. After that, the mixture was heated to 1400°C for 4 hrs. The heating rate was 10°C/min. The molten glass was quenched into a graphite mold.

6.2.2. Sample preparation for interfacial study

AISI 441 samples (ThyssenKrupp VDM, Germany) were polished to remove oxidized

layer, if any, and to obtain scratch-free flat surface. The nominal composition of the AISI 441 alloy is given in Table 6-1. The polished samples were cleaned by ultrasound in water and then in acetone before being dried and wiped with acetone. A clean and flat SABS-0 glass piece was put on the polished the AISI 441 alloy surface and thermally treated at 960°C for 30 minutes in argon in order to bond the SABS-0 glass with the AISI 441 alloys. No external load was applied during the bonding process.

Table 6-1. AISI 441 alloy composition (wt %) [1]

Interconnect	**Cr**	**Fe**	**Mn**	**Ti**	**Si**	**Al**	**C**	**S**	**P**	**Ni**	**Nb**
AISI441	17.6	80.68	0.33	0.18	0.47	0.045	0.01	0.001	0.024	0.20	0.46

The bonded AISI 441/SABS-0 sample was thermally treated at 800°C for 100 hrs in argon, air, and H_2O/H_2 atmospheres. H_2O/H_2 atmosphere was created by passing hydrogen gas through a water bath. The temperature of the water bath was maintained at 83 ± 2°C to obtain approximately 50% water vapor [4]. The bonded AISI 441/SABS-0 sample was also thermally treated at 800°C in air and H_2O/H_2 atmospheres for 500 and 1000 hrs to study the long-term interfacial stability. The same heating and cooling rates of $3°C \cdot min^{-1}$ were used for all the thermal treatment experiments.

6.2.3. Characterization

The cross sections of all the thermally treated diffusion couples were finely polished to optical finish. Field emission SEM (Quanta 600 FEG, FEI Company, Hillsboro) was used to examine the interfacial morphology between the SABS-0 glass and the AISI 441 alloy. The EDS

module (Bruker AXS, MiKroanalysis, Gmbh, Berlin, Germany) attached to the SEM was used for composition analysis in order to understand the elemental distribution across the AISI 441/SABS-0 interfaces. The analyses followed standardless method. The elemental distribution along the interface was determined by EDS spot and line scan and area mapping. For all the studied samples, the EDS spot and line scans were taken in at least three randomly selected regions. The results given here are the averages of these scan data. To investigate the devitrified phases at the interface of the AISI 441/SABS-0 couple, high resolution X-ray diffraction (XRD) studies were carried out in an X'Pert PRO diffractometer (PANalytical B.V., EA Almelo, The Netherlands). SABS-0 glass coated AISI 441 surface was polished until the glass layer was 15 - 20 μm thick. Such SABS-0 glass layer thickness was deemed suitable since X-ray detects 95% of the phase information from 25 μm penetration depth [5]. The scan time per step was 3000 s with CuK_α radiation (λ = 1.5406 Å).

6.3. Results and discussion

6.3.1. AISI 441/SABS-0 couple thermally treated at 800°C in argon, air, and H_2O/H_2 atmospheres

6.3.1.1. Interfacial microstructure

Microstructures of the as-bonded and the thermally treated AISI 441/SABS-0 couples in argon, air, and H_2O/H_2 atmospheres are shown in Fig. 6-1. In the images, the left side is the AISI 441 alloy and the right side is the SABS-0 glass. The microstructures at all the studied conditions show distinct bonding interfaces. This means the SABS-0 glass has good adhesion with the AISI

441 alloy. The microstructures can be divided into three regions: tiny (<<1 μm) black spots on the AISI 441 alloy side, crack-free interface, and the SABS-0 glass side.

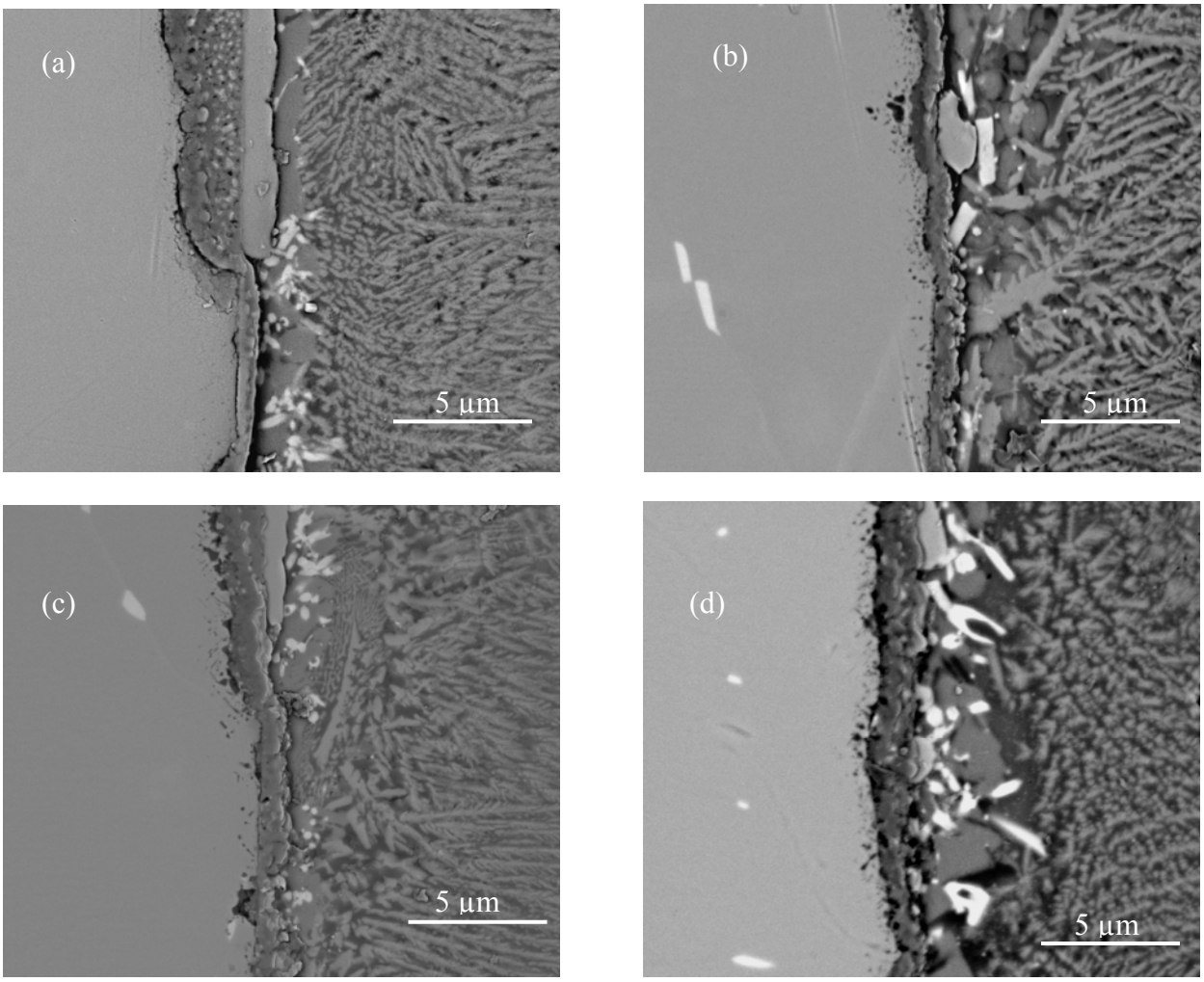

Fig. 6-1. SEM images of AISI 441/SABS-0 couples: a) as-bonded, b) argon, c) air, and d) H_2O/H_2 atmosphere. The samples were thermally treated for 100 hrs at 800°C in different atmospheres.

Tiny black spots are observed on the AISI 441 alloy side for the as-bonded and the thermally treated samples regardless of thermal treatment atmospheres. A layer consisting of

uniformly distributed black spots attached to the interface on the AISI 441 alloy side is observed for all the samples except for the air treated sample where the layer is not uniform.

The interface morphology of the as-bonded AISI 441/SABS-0 couple is different from the thermally treated samples. The interface of the as-bonded AISI 441/SABS-0 couple (Fig. 6-1(a)) has two types of morphologies: thick interface at the upper part followed by a long, bright secondary phases and thin interface at the lower part followed by a black layer on the SABS-0 glass side. The thermally treated AISI 441/SABS-0 couples have similar interface morphologies with uniform thickness. However, the interface thickness seems to increase with the thermal treatment atmospheres in the order argon < air < H_2O/H_2. The bright secondary phase is also observed on the SABS-0 glass side in localized area.

On the SABS-0 glass side, equiaxed and platelet like bright spots are observed for all the samples. Equiaxed bright spots are not distinct for the argon treated sample and platelet like bright spots are not distinct for the air treated samples. The equiaxed and platelet like bright spots indicate the redox reaction between the AISI 441 alloy and the SABS-0 glass [6,7]. For the argon and air treated samples, granular shaped secondary phases are observed between the interface and the dentritic phases. For the H_2O/H_2 treated sample, distinct angular phases are observed surrounded by distinguishable black spots. This means thermal treatment atmosphere affects the interfacial morphology of the AISI 441 alloy/SABS-0 couple. The dendritic phases are the devitrified phases of the SABS-0 glass as discussed in chapter five and extend 10-15 μm from the interface.

6.3.1.2. Elemental distribution across the interface

Energy dispersive spectroscopy (EDS) analysis was carried out to explore the

compositional difference among the different types of phases observed in the microstructures in Fig. 6-1. Spot analysis was carried out using 6 nm diameter electron beam and higher magnification (>30,000 X) images (not shown here). However, the spatial resolution of the secondary X-ray in EDS is > 1μm and the analysis can not give absolute composition. The analysis only provides qualititative information to understand the trend in compositional difference between different observed phases. To maintain consistency, a constant collection time (60 s) was used for all the spot analysis. The compositions are given in atomic%.

Tiny black spots on the AISI 441 alloy side near the interface in the microstructures (Fig. 6-1) are of similar compositions (Fe 65.02, Cr 15.35, Mn 0.75, Ti 4.41, Nb 1.81, Si 0.70, Al 2.71, O 9.63) for the as-bonded and the thermally treated AISI 441/SABS-0 couples. High content of Ti with oxygen indicates that the black spots may be titanium oxide. The compositions of the black spots on the AISI 441 alloy side in a layer form are different for different thermal treatment atmospheres but follows similar trend. This means the black layer also consists of oxides of the minor alloying elements of the AISI 441 alloy. These black spots have less Fe and more Cr than the tiny black spots and also contain 2-5 at% Mn and Ti, 2-3 at% Si and 1-2 at% Al. Mn, Ti, Al, and Si are the minor alloying elements in the AISI 441 alloy with the concentration order Si > Mn > Ti > Al (Table 6-1). Low concentration and low diffusivity (mobility) of the alloying elements, and high solubility of oxygen in the alloying elements favor the internal oxidation [8]. The stability of the corresponding oxides are Al_2O_3>TiO_2>SiO_2>MnO_2. Al and Ti may be oxidized by internal oxidation because of their lower concentration comparing to Si and Mn. Si and Mn are also oxidized but it is not clear that whether the internal or external oxidation predominates. The diffusivity of Mn is probably higher than Si due to the lower mobility of Si^{4+} attributed to higher valency. So, it can be interpreted

that Mn is oxidized by external oxidation and Si is oxidized by internal oxidation. However, the diffusivity of Si is not available for Fe-Cr alloy. Thermal treatment atmosphere may affect the oxidation of AISI 441 alloy as observed from the lower tiny black spots for the as-bonded sample and non-uniform distribution of the black layer for the air treated sample. However, the effect is not understood.

The overall compositions of the AISI 441/SABS-0 interfaces vary with thermal treatment atmospheres but follows similar trend. The AISI 441/SABS-0 interface mainly consists of the AISI 441 alloy elements (Fe 7-15, Cr 25-30, Mn 2-5, Ti 1-2, O 34-52) and less than 3 at% SABS-0 glass elements (Si, Sr, La, and Al) among which chromium concentration is the highest. This means the interface consists of mainly the AISI 441 alloy elements. It can be noticed that the interface for the AISI 441/SABS-0 samples have very small concentration of the SABS-0 glass elements.

There are several distinct features on the SABS-0 glass side. Localized, gray-colored spots ($\geq$ 1 μm) near the interface mainly consist of Fe, Cr, and O with little (<5 at%) amount of Si, Sr, and Al among which Fe concentration is the highest. Fe and Cr in the AISI 441 alloy can be oxidized by external oxidation due to their high concentration. The diffusivity of Fe is higher than Cr and the stability of Fe_3O_4 and Fe_2O_3 are also higher than chromium oxide [9,10]. Accordingly, these spots have the highest Fe. However, the reason for the localized oxidation is not understood. The smaller bright spots (< 1μm) on the SABS-0 glass side, which are due to the redox reaction, consist mainly the glass elements with little amount of Fe and Nb from the AISI 441 alloy (Fe 5-7, Nb 2-3, Si 15-22, Sr 16-18, La 5-7, Al 3-6, O 38-50) and the compositions are same for both the equiaxed and the platelet types. The granular phases on the SABS-0 glass side (mainly consist of the SABS-0 glass elements with 1-2 at% Fe and 2 at% Nb.

The composition of angular phases on the SABS-0 glass side for H_2O/H_2 treated samples (Fig. 6-1(d)) are different from the granular phases. The angular phases contain higher Fe, Nb, Sr, and lower Si, Al content than the granular phases. From these observations it can be understood that the AISI 441 alloy oxidation and the chemical reaction between the AISI 441 alloy and the SABS-0 glass contribute to the interface formation depending on the thermal treatment atmospheres.

Dendritic phases and the black spots between them have almost similar composition of the SABS-0 glass. Dendritic phases of the devitrified SABS-0 glass have slightly higher Sr and La content and slightly lower Al content than the black spots between them. However, the devitrified phases and the black spots near the interface contain small amount of Fe and Cr.

The concentration profiles of the AISI 441/SABS-0 glass elements across the interface has been studied by EDS line scan and are shown in Fig. 6-2. The concentration profiles of Fe and Cr in the AISI 441 alloy and Si, Sr, La, Al, and O in SABS-0 glass are 'S' shaped with two diffusion tails: one at the higher concentration and other at the lower concentration. This means the elemental inter-diffusion of the AISI 441 alloy and SABS-0 glass occurs during interface formation [11]. However, oscillations in the concentration profiles are observed for the SABS-0 glass elements and can be explained as follows. First, the step size of the EDS line scan was 0.06 μm for this study to obtain smooth concentration profile. The spatial resolution of the secondary X-rays is ≥ 1 μm. Interaction between the X-ray of the different elements can be expected for the experimental step size resulting in oscillations in the concentration profiles. Second, low concentration of La and Al, compositional difference between the devitrified and glass phases, and low density of the SABS-0 glass are also the likely reasons for the oscillations in the concentration profiles [12]. However, approximate diffusion distance can be determined by

identifying the inflection point and diffusion tail at the interface. In Fig. 6-2, '0' on the 'x' axis indicates the boundary between the alloys and the interface. The left (negative) side is the alloy and the right (positive) side is the SABS-0 glass. 'y' axis shows the normalized concentration of the elements.

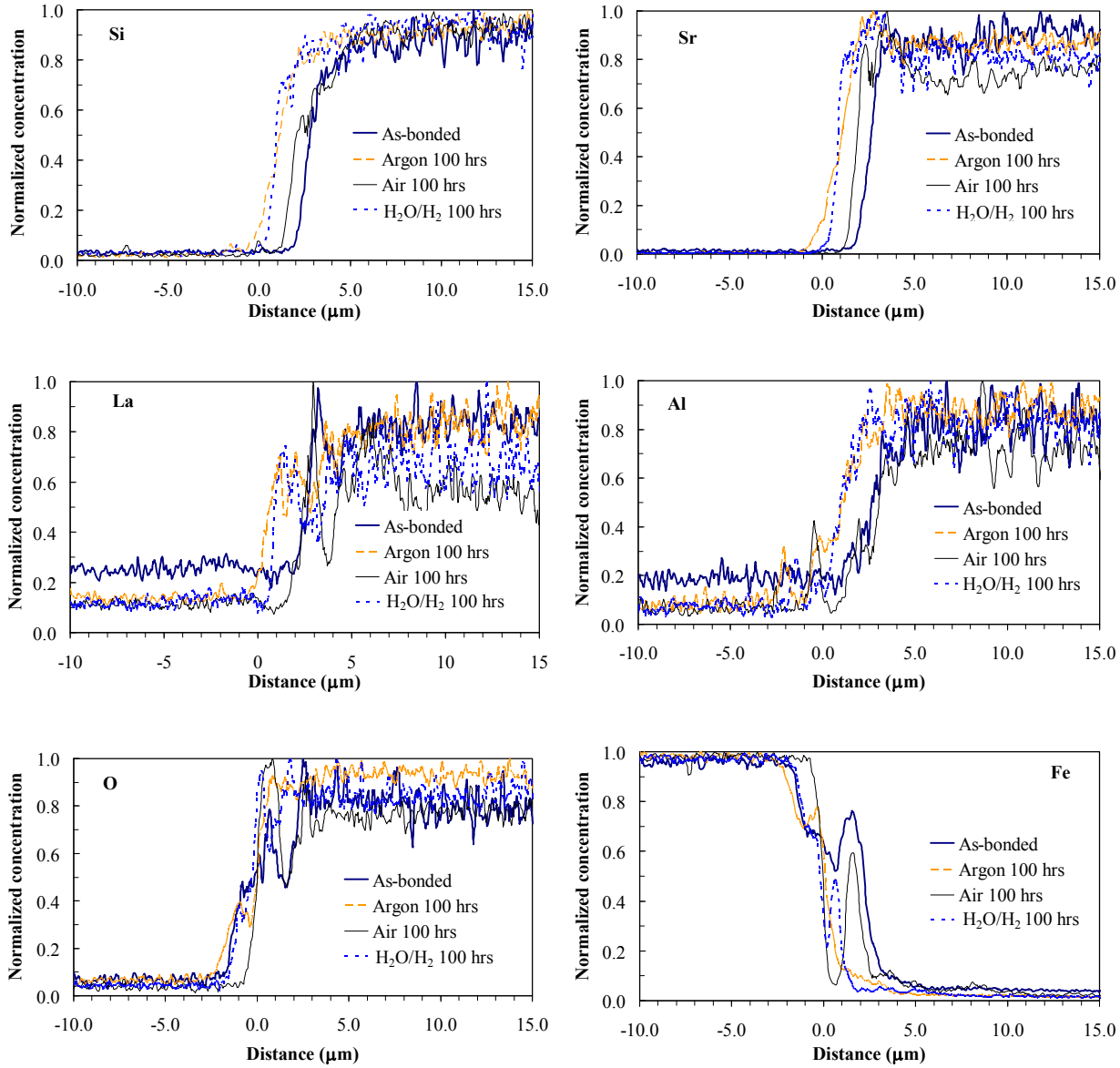

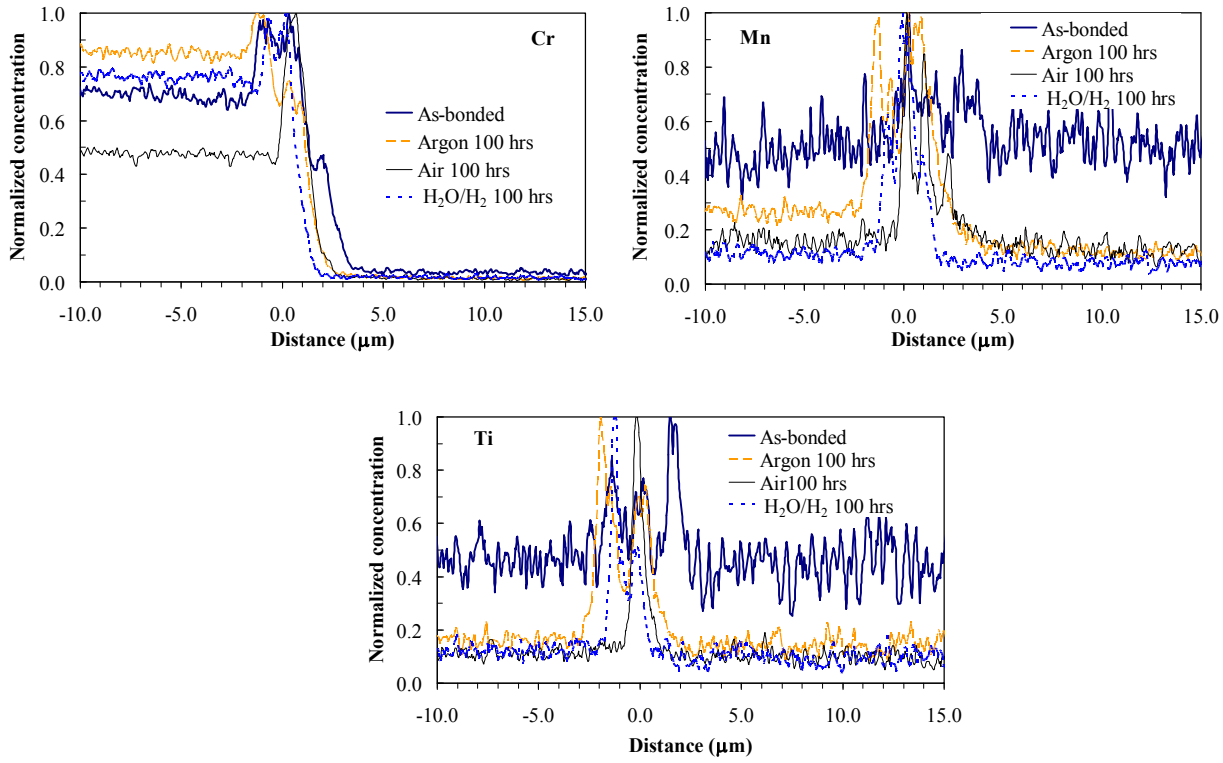

Fig. 6-2. Elemental concentration profiles of the as-bonded and the argon, air, and H_2O/H_2 treated AISI441/SABS-0 couples.

All the SABS-0 glass elements (Si, Sr, La, Al, and O) diffuse 2-3 µm into the AISI 441 alloy for all the AISI 441/SABS-0 couples. Humps at the AISI 441 alloy side near the interface are observed for Si and Al for all the samples. This suggests that Al and Si concentrations are more near the interface on the AISI 441 alloy than the bulk. This observation is supported by the presence of black layers consisting Al_2O_3 and SiO_2 on the AISI 441 alloy side near the interface as seen in the microstructures of the AISI 441/SABS-0 couples (Fig. 6-1). Humps are also observed for Sr on the SABS-0 glass side near the interface. This indicates that the SABS-0 glass near the interface is enriched in Sr. Fe in the AISI 441 alloy diffuses 5-7 µm into the SABS-0 glass for all the samples. Hump in the Fe concentration profile is consistent with the Fe-rich

bright phases (≥ 1μm) on the SABS-0 glass side near the interface (Fig. 6-1). Cr in the AISI 441 alloy diffuses ~ 5 μm, ~ 4 μm, ~ 3 μm, and ~ 3 μm into the SABS-0 glass for the as-bonded, argon, air, and H_2O/H_2 treated AISI 441/SABS-0 couples. Hump in Cr distribution at the AISI 441 alloy side near the interface is observed for all the samples. Cr rich layer at the interface and the oxide layers of Al, Si, and Ti probably hinder further diffusion of Cr from the AISI 441 alloy into the SABS-0 glass and consequently the diffusion distances remain almost unchanged for the thermally treated samples. The atmospheric effect on the AISI 441/SABS-0 interface is not significant as can be understood by the comparable diffusion distances for all the SABS-0 glass and the AISI 441 alloy elements for all the thermal treatment conditions. Mn and Ti concentration are maximum at/near the interface as can be seen from the peaks in the concentration profiles rather than 'S' shape. Mn and Ti are the alloying elements in the AISI 441 alloy. Since Mn and Ti have higher affinity with oxygen than Cr, they are more likely to react with oxygen and form oxides and may also hinder the diffusion of the SABS-0 glass elements and the AISI 441 elements into each other [13,14].

For better understanding of the elemental distribution across the AISI 441/SABS-0 interfaces, elemental maps were obtained from secondary X-ray mapping by EDS. The elemental maps of the AISI 441/SABS-0 couples are shown in Fig. 6-3.

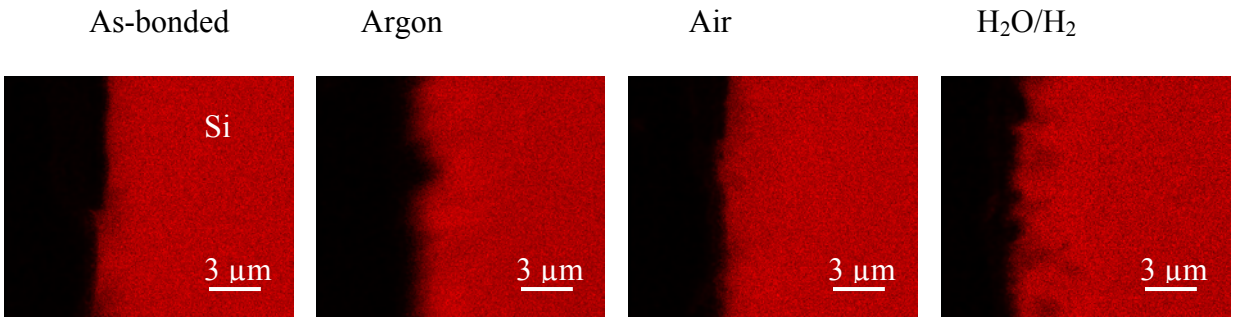

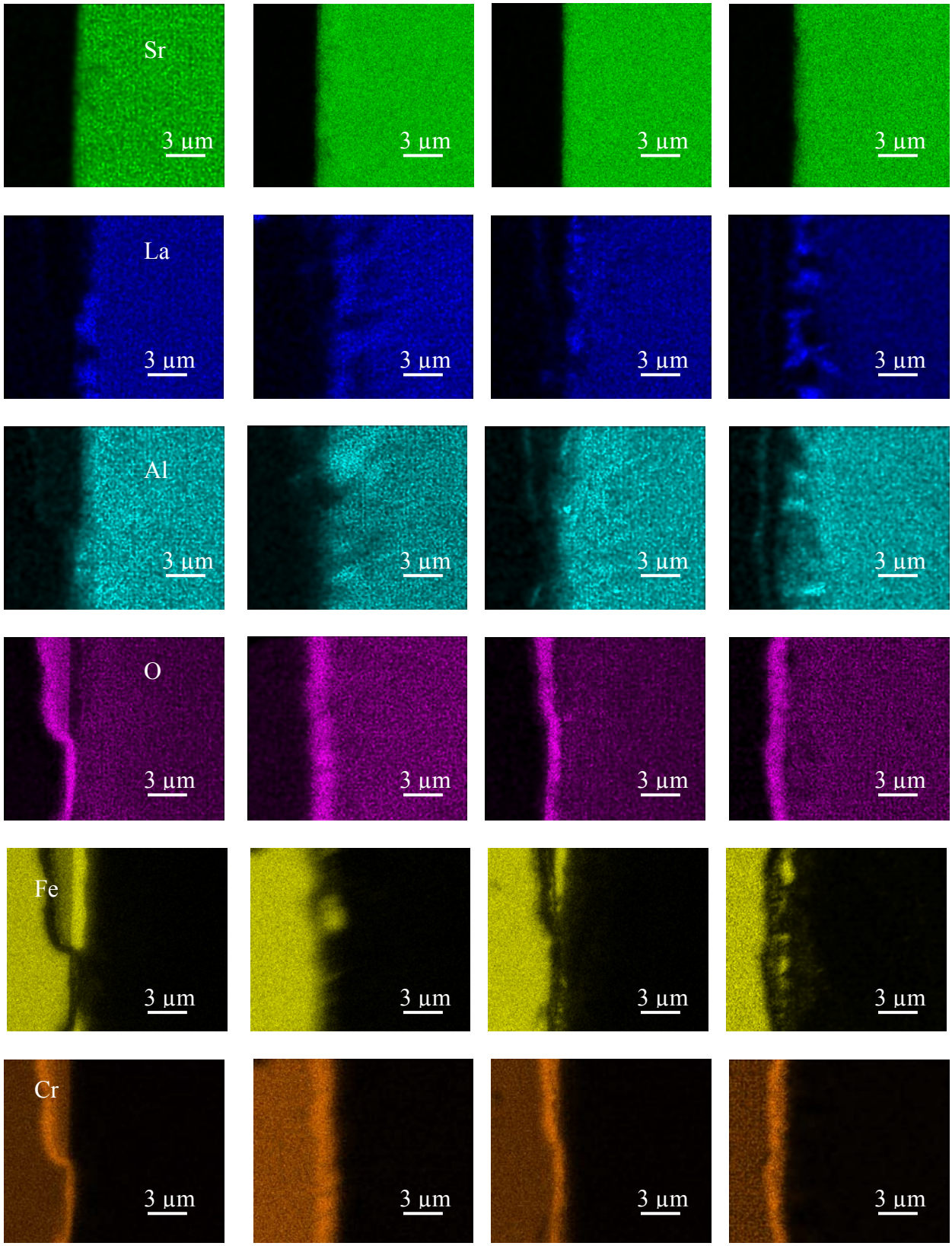
Sr
La
Al
O
Fe
Cr
3 µm

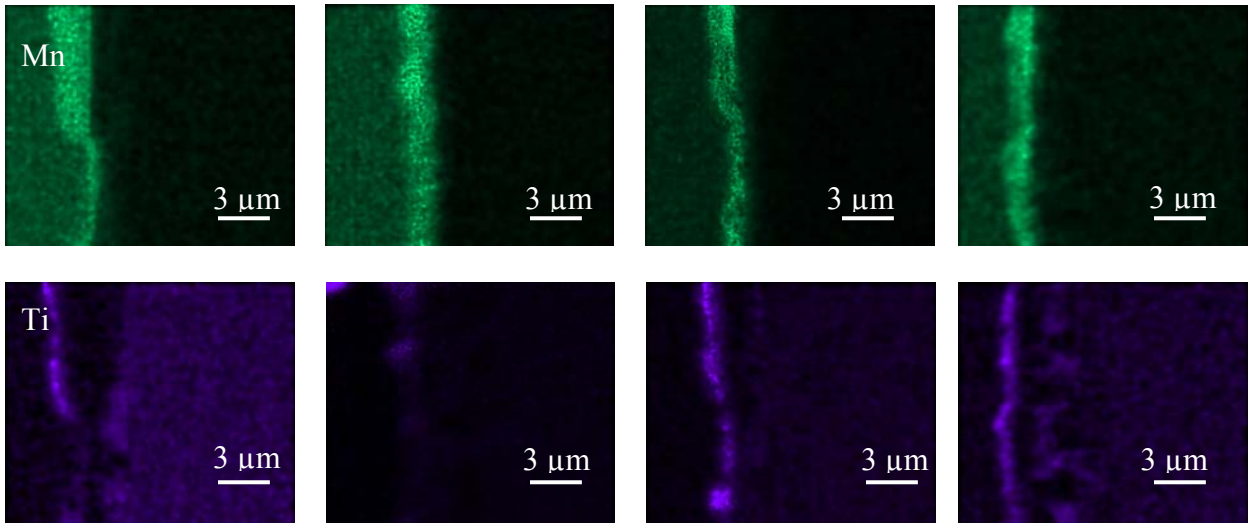

Fig. 6-3. Elemental maps for the as-bonded and the argon, air, and H_2O/H_2 treated AISI 441/SABS-0 couples.

It can be seen from Fig. 6-3 that Si and Sr in the SABS-0 glass are homogeneously distributed and does not diffused into the AISI 441 alloy. La and Al accumulate at the interface. O, Cr, and Mn are accumulated at the interface. Fe-accumulation on the SABS-0 glass side near the interface and at the localized region coincides with the localized Fe-rich phases in the microstructures (Fig. 6-1) and also consistent with the spot analysis. Ti is also accumulated beneath the Mn-layer but the accumulation is not seen for the argon treated sample. Ti enriched layer on the AISI 441 alloy side near the interface can be understood by the presence of titanium oxide as revealed by spot analysis.

6.3.1.3. X-ray diffraction analysis

The XRD patterns of the AISI 441 alloy and the AISI 441/SABS-0 samples are shown in Fig. 6-4. The presence of the AISI 441 alloy peaks in all the samples confirms that the XRD patterns include all the crystal phases across the interface. The same number and location of

peaks in the XRD patterns mean that the crystal phases are the same for all the studied samples. The crystal phases can be identified as $Sr_4(Si_4O_{12})$, $La_2Si_2O_7$, $Sr_7Al_{12}O_{25}$, $FeSiO_3$, La_2CrO_6, Ti_6O_{11}, and TiO_2.

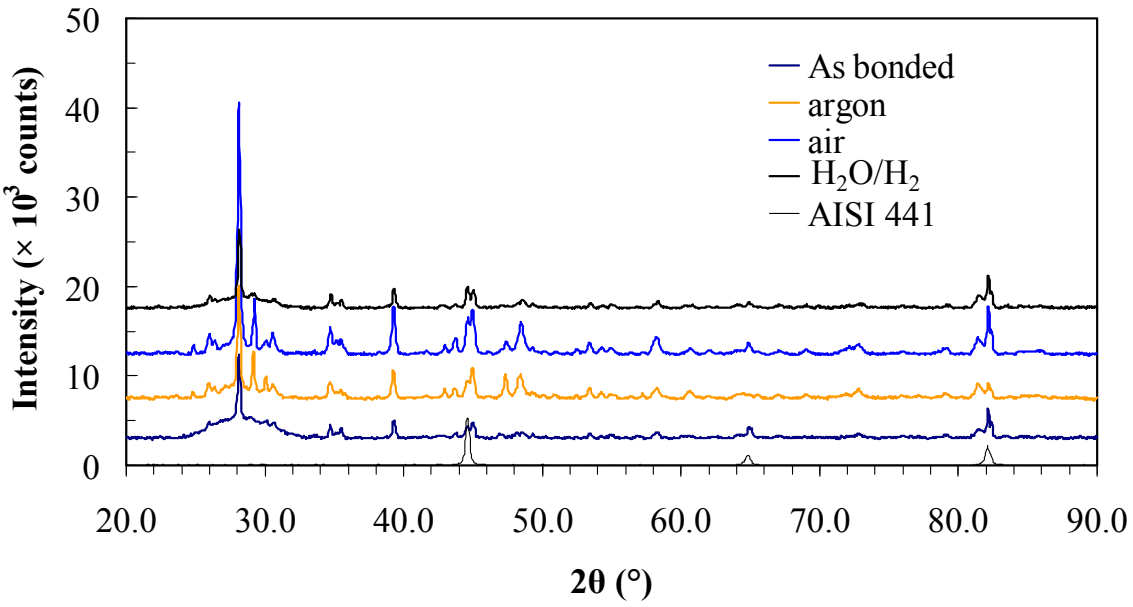

Fig. 6-4. XRD patterns of the AISI 441 alloy and the as-bonded and the thermally treated AISI 441/SABS-0 couples.

It can be understood that $Sr_4(Si_4O_{12})$, $La_2Si_2O_7$, and $Sr_7Al_{12}O_{25}$ phases form due to devitrification of SABS-0 glass itself. Formation of these phases can be understood as follows. Q^0, Q^1, Q^2, and Q^3 silicate structural units with non-bridging oxygen have been observed in the SABS-0 glass in chapter 3. The non-bridging oxygens tend to coordinate with the glass modifiers and form new species. In the SABS-0 glasses, La^{3+} and Sr^{2+} ions act as modifiers. Consequently, $Sr_4(Si_4O_{12})$ and $La_2Si_2O_7$ phases form. Regarding the $Sr_7Al_{12}O_{25}$ phase formation, Al^{3+} is a glass former in the SABS-0 glass [15] and Sr^{2+} is a charge compensator for the nearest localized

$(AlO_4)^-$ tetrahedral structural units [16]. Microheterogeneity in the SABS-0 glass structure, such as localized $(AlO_4)^-$ tetrahedral units, induces the devitrification of the SABS-0 glass. Accordingly, $Sr_7Al_{12}O_{25}$ crystalline phase forms.

$FeSiO_3$ and La_2CrO_6 phases form due to the interaction of the AISI 441 alloy and the SABS-0 glass. Formation of $FeSiO_3$ and La_2CrO_6 can be explained as follows. The microstructures and the EDS analysis show that Fe from the AISI 441 alloy diffuses to the SABS-0 glass and consistent with the elemental maps (Fig. 6-3). It is also analyzed that the bright spots (Fig. 6-1) due to redox reactions contain certain amount of Fe along with the SABS-0 glass elements. So, the SABS-0 glass network structure has been broken prior to the redox reaction. Subsequently, $FeSiO_3$ phase forms. Formation of La_2CrO_6 phase can be explained as follows. La_2O_3 containing glass tends to form energetically favorable, isolated, small, and phase ordered clusters. These clusters generally contain La-O-La structural units. Indeed, these La-O-La structural units are overlapped in 1105 cm^{-1} and 1010 cm^{-1} wave numbers in the Raman spectra of the SABS-0 glass (chapter three). The elemental mapping results in Fig. 6-3 show accumulation of La and O at the interface. At the same time, Cr diffuses to the SABS-0 glass side as observed from the EDS analysis across the interface. This leads to the breakdown of the SABS-0 glass network structure. According to Sanderson, acidobasicity value, a glass property related to the chemical environment, is 3.50 for Cr and 1.95 for La [17]. This means Cr is acidic and La is basic in nature. Therefore, reaction among lanthanum, chromium, and oxygen favors La_2CrO_6 formation.

Formation of Ti_6O_{11} and TiO_2 phases can be understood by the internal oxidation of titanium which is supported by the tiny black spots and the black layer enriched in titanium on the AISI 441 alloy side.

Same crystalline phases for all the AISI 441/SABS-0 couples for all the AISI 441/SABS-0 couples suggest that the SABS-0 glass is compatible with the AISI 441 alloy and the interface between them are stable regardless of thermal treatment atmospheres.

6.3.2. Long-term thermal treatment of AISI 441/SABS-0 glass in air and H_2O/H_2 atmosphere

6.3.2.1. Interfacial microstructure

Microstructures of the AISI 441/SABS-0 glass samples thermally treated at 800°C for 500 hrs and 1000 hrs in air and H_2O/H_2 atmospheres are shown in Fig. 6-5. In the images, the left side is the AISI 441 alloy and the right side is the SABS-0 glass. The microstructures at all the studied conditions show distinct bonding interfaces. The microstructures again can be divided into three regions: tiny (<<1 μm) black spots on the AISI 441 alloy side, crack-free interface, and the SABS-0 glass side.

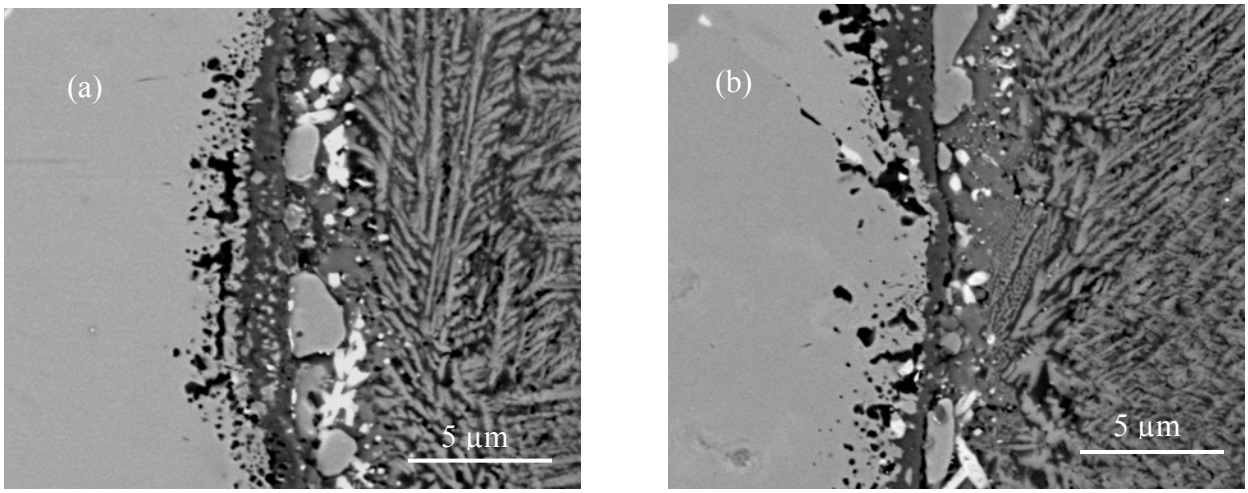

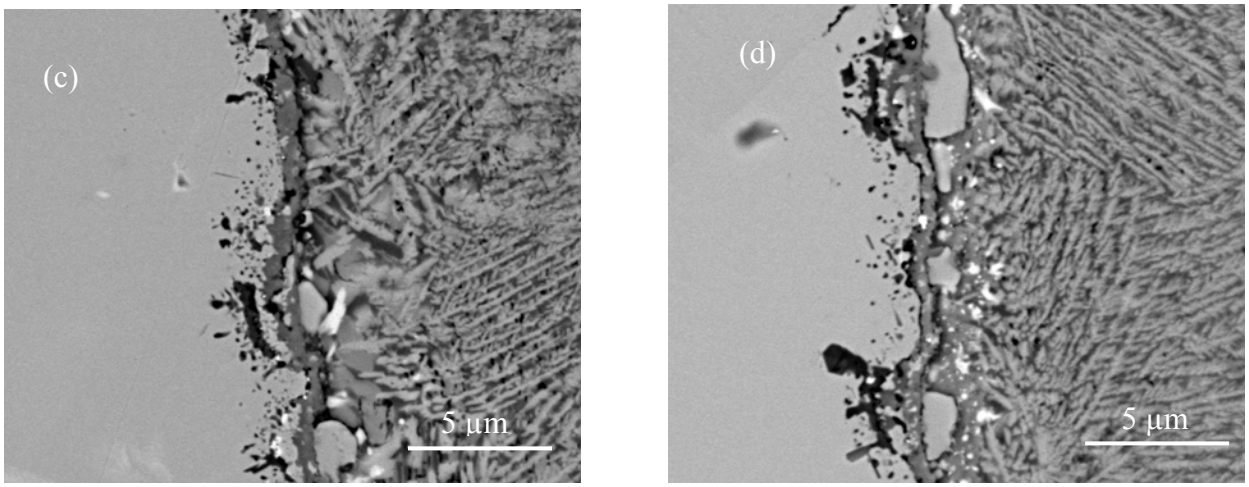

Fig. 6-5. SEM images of thermally treated AISI 441/SABS-0 couples at 800°C: a) 500 hrs in air, b)1000 hrs in air, c) 500 hrs in air H_2O/H_2, and d) 1000 hrs in H_2O/H_2 atmosphere.

Tiny black spots are observed on the AISI 441 alloy side for all the thermally treated samples regardless of thermal treatment time and atmosphere. The tiny black spots tend to form a black layer as seen in Fig. 6-1. The black layer is more distinct compared to the samples thermally treated for 100 hrs in Fig. 6-1. However, the black layer is less uniform for the H_2O/H_2 treated samples (Figs. 6-5(c) and (d)).

The interface thickness of the air treated sample for 1000 hrs is apparently smaller than the 500 hrs but remains at 1-3 μm similar to the 100 hrs thermally treated samples (Figs. 6-1(a) and (c)). This can be explained as follows. First, the interface thickness may not uniform as can observed in slight variation of thickness in the microstructures (Fig. 6-5(a) and (b)). So, the change in interface thickness may not be real. Second, Cr in the AISI 441 alloy evaporates at 800°C as CrO_3 species. With increased thermal treatment time, the extent of evaporation may have been increased resulting in smaller thickness for the 1000 hrs thermally treated sample. Subsequently, the interface thickness decreases. The interface thicknesses of the H_2O/H_2 treated

samples are uniform and same (~ 1 μm) for 500 hrs and 1000 hrs thermal treatment times (Figs. 6-5(c) and (d)) but smaller than the 100 hrs thermally treated sample (~ 3μm, Fig. 6-1(d)). The reduction in thickness may be due to the increased rate of vaporization of Cr in the AISI 441 alloy in the form of $CrO_2(OH)_2$ species. The interface morphologies of 500 hrs and 1000 hrs thermally treated samples are almost similar containing scattered bright spots on the AISI 441 alloy side. It can be mentioned that these bright spots are not distinguished for the 100 hrs thermally treated sample (Fig. 6-1 (c)). The interface morphologies of the H_2O/H_2 treated samples are also same for 500 hrs and 1000 hrs thermal treatment time and contain bright spots on the AISI 441 alloy side; which is not distinguishable for the 100 hrs thermally treated sample (Fig. 6-1(d)). These observations suggest that the thermal treatment time changes the interface morphology.

On the SABS-0 glass side, equiaxed and platelet like bright spots are observed for all the thermally treated samples regardless of thermal treatment time and atmosphere. Apparently, the bright spots are more distinct for the air treated samples, an opposite trend as is observed for the 100 hrs thermally treated samples (Fig. 6-1(c) and (d). Since these bright spots are randomly distributed on the SABS-0 glass side near the interface and the SEM images are taken from few microns region, the atmosphere effect can not be interpreted. The equiaxed and platelet like bright spots are due to the redox reaction between the AISI 441 alloy and the SABS-0 glass. Localized and distinct grayish secondary phases (≥ 1μm) on the SABS-0 glass side near the interface are observed. The granular phases between the interface and the dentritic phases on the SABS-0 glass side are likely to be present for the air treated samples but less distinguishable than the 100 hrs thermal treatment time (Fig. 6-1(c)). For the H_2O/H_2 treated sample, small granular secondary phases are observed for 500 hrs thermal treatment time but not distinguishable for

1000 hrs thermal treatment time. It can be noticed that the distinct angular phases observed for 100 hrs thermal treatment time disappear for longer thermal treatment times. This again means that the interface morphologies change with the thermal treatment time. The dendritic phases due to SABS-0 glass devitrificattion are observed for all the samples and extend 10-15 μm from the interface.

6.3.2.2. Elemental distribution across the interface

The compositions of the different types of observed features in the microstructures (Fig. 6-5) have been identified by energy dispersive spectroscopy (EDS) analysis. EDS spot analysis was carried out for the air and H_2O/H_2 treated samples for 1000 hrs because this is the longest thermal treatment time in the present study. The trend can be compared with the short-term thermal treatment samples.

Tiny black spots on the AISI 441 alloy side near the interface in the microstructures have similar compositions for the air treated sample (Fe 53.84, Cr 14.33, Mn 0.45, Ti 4.49, Nb 0.20, Si 0.81, Al 3.54, O 22.35). The compositions are also similar for the H_2O/H_2 treated sample with higher Ti and lower Fe content than the air treated sample. It can be noticed that the tiny black spots and the black layer have almost similar compositions for all the samples, as-bonded and thermally treated regardless of the thermal treatment time and atmospheres (Figs. 6-1 and 6-5). These black spots are the oxides of the alloying elements, Ti, Al, Si, and Mn as discussed in the previous section (6.3.1.2).

The AISI 441/SABS-0 interfaces have similar compositions for the air and the H_2O/H_2 treated samples (Fe 12.30-16.70, Cr 16.50-20.20, Mn-1.94-3.08, Ti 1.56-2.37, Nb 0.25, Si 1.51-3.23, Sr 1.00-2.33, Al 0.4-0.6, O 56.92-58.92). The composition shows that the interface mainly

consists of the AISI 441 alloy. It is also noticed that the compositions of the AISI 441/SABS-0 interfaces are similar for the as-bonded and argon, air, and H_2O/H_2 treated samples for 100 hrs thermal treatment time (Fig 6-1 and section 6.3.1.2). The bright spots at the interface contain higher Fe and slightly higher Nb and Si than the interfaces. The bright spots were not observed for the as-bonded and the thermally treated samples for 100 hrs (Fig. 6-1). This suggests that the thermal treatment time affects the AISI 441/SABS-0 interfaces but atmospheres do not.

On the SABS-0 glass side, the equiaxed and the platelet bright spots (< 1 μm) have similar compositions for the air and H_2O/H_2 treated AISI 441/SABS-0 sampels and consists of mainly SABS-0 glass compositions and Fe (Fe 4.83-8.38, Cr 0.90-1.07, Mn 0.7-0.9, Nb 0.0-0.3, Si 18.55-19.50, Sr 12.10-12.35, La 3.27-5.15, Al 3.28-3.49, O 50.33-55.66). The composition is also similar with the bright spots observed for the as-bonded and thermally treated samples for 100 hrs in different atmospheres. These bright spots are due to redox reaction between the AISI 441 alloy and the SABS-0 glass. From the composition it can be understood that the redox reaction oxidizes mainly Fe in the AISI 441 alloy. Localized, gray colored spots (≥ 1 μm) near the interface mainly consist of Fe, Cr, and O with little (<5 at%) amount of Si, Sr, and Al among which Fe concentration is the highest (Fe 63.42-84.41,Cr 7.52-15.72, Mn 0.55, Si 2.83-4.26, Sr 1.55-3.10, La 0.70, Al 1.34-1.61, O 1.03-10.65). Fe content is the highest for both the samples but higher for the air treated sample and the Cr content is higher for the H_2O/H_2 treated sample. Highest Fe content for the air treated sample is consistent with the 100 hrs sample and has been discussed. However, very low oxygen content suggests that some Fe and Cr may be present in the metallic form. These localized spots also have similar compositions with those of the as-bonded and the thermally treated samples for 100 hrs in different atmospheres (Fig. 6-1and section 6.3.1.2).

Dendritic phases of the devitrified SABS-0 glass have higher Sr (~ 3 at%), Al (1-2 at%) and lower La (1-2 at%) content than the black spots between the dendritic phases for both the air and H_2O/H_2 treated samples (Fig. 6-5). However, the dendritic phases near the interface also contain higher Fe, Cr, and Mn than the black spots. Fe, Cr, and Mn content are at 4-5 at% and 1-2 at%, and 0.7-1.0 at%, respectively; which are higher than the as-bonded and the thermally treated samples for 100 hrs. This means the interaction between the AISI 441 and the SABS-0 glass increases with thermal treatment time. Far from the interface on the SABS-0 glass side (≥ 10 μm), no AISI 441 alloy elements are found in the devitrified phases and the black spots between them.

From the microstructures and the compositional analysis, it is understood that the interface morphology changes with thermal treatment time but the composition of the different phases are almost same. This means the interfaces of the AISI 441/SABS-0 couples are stable for long-term thermal treatment.

The concentration profiles of the AISI 441/SABS-0 glass elements across the interface has been studied by EDS line scan and are shown in Fig. 6-6. The concentration profiles of the samples thermally treated for 500 hrs are not given for brevity. 'S' shaped with two diffusion tails and oscillations in the concentration profiles are observed for the SABS-0 glass elements are observed as discussed in section 6.3.1.2. However, the oscillations in the concentration profiles of the SABS-0 elements are relatively lower in the air treated couples than the H_2O/H_2 treated couples (Figs. 6-6 (a) and (c)). The possible reasons for the oscillations are discussed in section 6.3.1.2. In Fig. 6-6, '0' on the 'x' axis indicates the boundary between the alloys and the interface. The left (negative) side is the alloy and the right (positive) side is the SABS-0 glass. 'y' axis shows the normalized concentration of the elements.

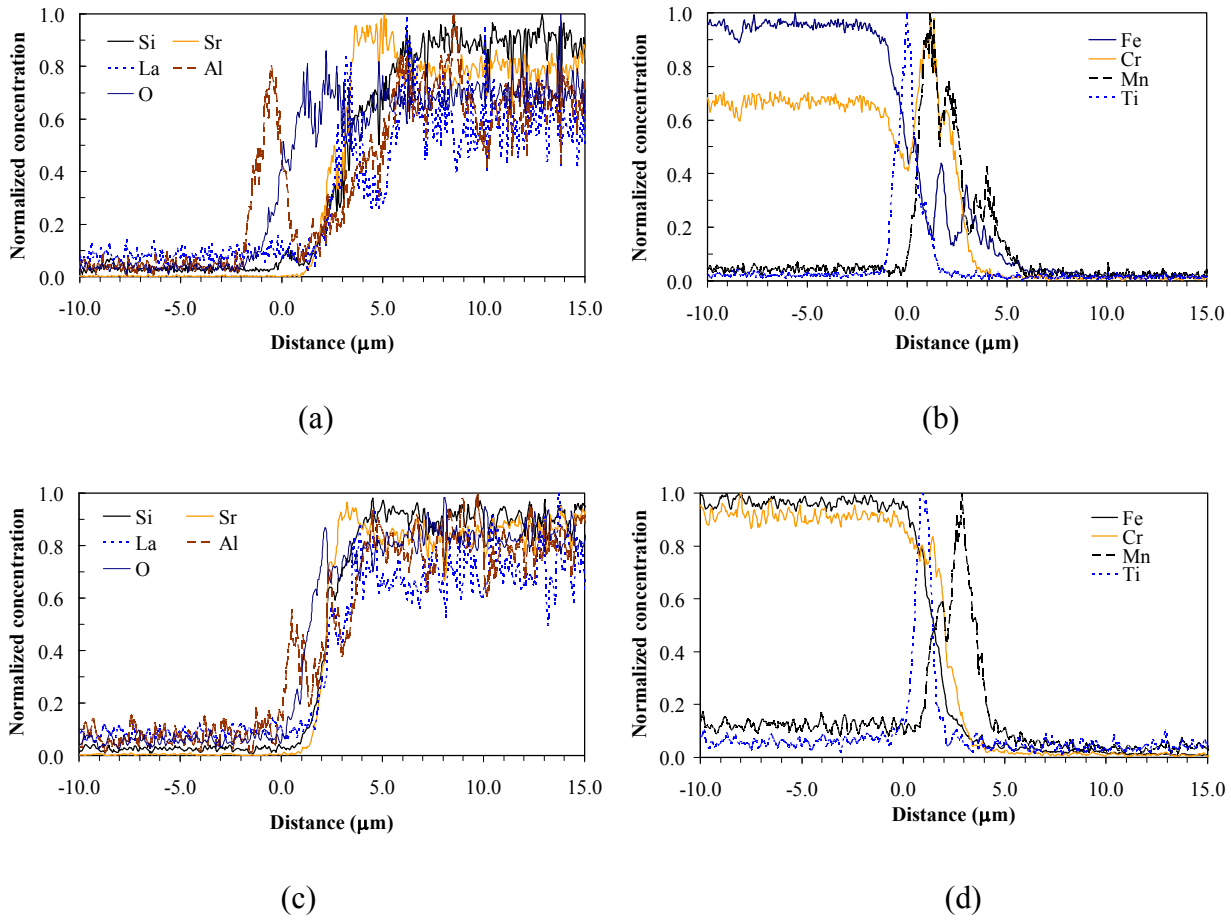

Fig. 6-6. Elemental concentration profiles of the AISI441/SABS-0 couples thermally treated at 800°C for 1000 hrs: a) SABS-0 glass elements and b) AISI 441 elements for air treated couple; and c) SABS-0 glass elements and d) AISI 441 elements for H_2O/H_2 treated couple.

The approximate diffusion distances of the elements are determined as described in section 6.3.1.2. Si and Sr diffuse 3-5 μm and ~ 2 μm, respectively, into the AISI 441 alloy for all the samples thermally treated in air and H_2O/H_2 for 500 and 1000 hrs. The diffusion distances for La, Al, and O can not be determined due to severe oscillations in their concentration profiles. A hump is observed in the Sr and Al concentration profiles on the SASB-0 glass side and the AISI 441 alloy side, respectively, near the interface. This means Sr is enriched on the SABS-0 glass

side near the interface but no distinguishable compositional difference has been found from the EDS spot analysis to support this observation. Higher concentration of Al on the AISI 441 alloy side near the interface is consistent with the EDS spot analysis. This can be understood from the Al-containing (~ 3 at%) black spots and layer on the AISI 441 alloy side near the interface (Fig. 6-5). Fe in the AISI 441 alloy diffuses 7-9 μm into the SABS-0 glass for the thermally treated samples for 500 and 1000 hrs in air and H_2O/H_2 atmosphere. However, the diffusion distance slightly decreases in the H_2O/H_2 treated samples than in air. This diffusion distance is also consistent with the observation that the devitrified SABS-0 glass and the black spots between them near the interfaces contain Fe. Hump in the Fe concentration profile is due to the Fe-enriched secondary phases on the SABS-0 glass side near the interface (Fig. 6-5). However, the hump is less distinct for the H_2O/H_2 treated sample (Fig. 6-6(d)) which can be explained as follows. The Fe-enriched secondary phases on the SABS-0 glass sides are localized. The given concentration profiles are the average of three EDS line scan collected from randomly selected regions. So, all the line scans may not be taken from the localized Fe-rich regions. Subsequently, the hump is not distinct for the H_2O/H_2 treated sample. Cr in the AISI 441 alloy diffuses 3-5 μm into the SABS-0 glass for all the samples. Hump in Cr distribution at the AISI 441 alloy side near the interface is distinct for the air treated sample (Fig. 6-6 (b)) but not for the H_2O/H_2 treated sample. Cr-content at the interface is higher for the air treated (20.20 at%) and lower for the H_2O/H_2 treated samples (16.50 at%) than the bulk AISI 441 alloy as revealed from the EDS spot analysis. Subsequently, hump is observed for the air treated sample. Mn and Ti concentration is maximum at/near the interface as can be seen from the peaks in the concentration profiles rather than 'S' shape. Ti peak is beneath the Mn peak which is consistent with the microstructures (Figs. 6-5 (b) and (d)) and also with the as-bonded and the thermally

treated samples for 100 hrs in Fig. 6-2. This again can be understood by the Ti-enriched black spots and layer on the AISI 441 alloy near the interface.

Elemental distribution across the AISI 441/SABS-0 interfaces were obtained from secondary X-ray mapping by EDS. The elemental maps of the thermally treated samples in air and H_2O/H_2 atmosphere for 1000 hrs are shown in Fig. 6-7 and 6-8, respectively. Si and Sr are homogeneously distributed on the SABS-0 glass although hump in the Sr concentration profile is observed in Figs. 6-6 (a) and (c). La-enriched region is near the interfaces both on the SABS-0 glass side and the AISI 441 alloy side. On the SABS-0 glass side, the La-enriched regions coincide with the small (< 1μm) equiaxed and platelet bright spots in the microstructures (Figs. 6-5 (b) and (d)) and also consistent with the EDS spot analysis. The La-enriched regions coincide with the black layer on the AISI 441 alloy in the microstructures but inconsistent with the EDS spot analysis. The reason is not understood. Al-enriched regions are observed on the AISI 441 alloy side superimposed with the black spots and the black layer in the microstructures (Fig. 6-5 (b) and (d)) and also consistent with the compositional analysis from EDS and the hump in the Al concentration profiles (Figs. 6-6 (a) and (c)). This further confirms that the black spots contain Al. O is enriched at the interfaces. Localized Fe-enriched regions are observed on the SABS-0 glass side. The Fe-enriched regions are superimposed with the localized grayish Fe rich secondary phases in the microstructures (Figs. 6-5 (a) and (c)). It should be noticed that O is depleted at the Fe-rich localized regions; which is consistent with the EDS spot analysis of these secondary phases. Cr and Mn are accumulated at the interface and superimposes with each other. Cr and Mn accumulation at the interface is consistent with the observed humps in their concentration profiles for the air treated sample in Fig. 6-6 but Cr hump is not observed for the H_2O/H_2 treated sample. However, the thickness of the Cr- and Mn-enriched region at the

interface is comparable with the interface thicknesses for both the air and the H_2O/H_2 treated samples. This means the interface mainly consists of Cr, Mn, and O. Ti is also accumulated beneath the Mn-layer and coincides with the black spots on the AISI 441 alloy near the interface.

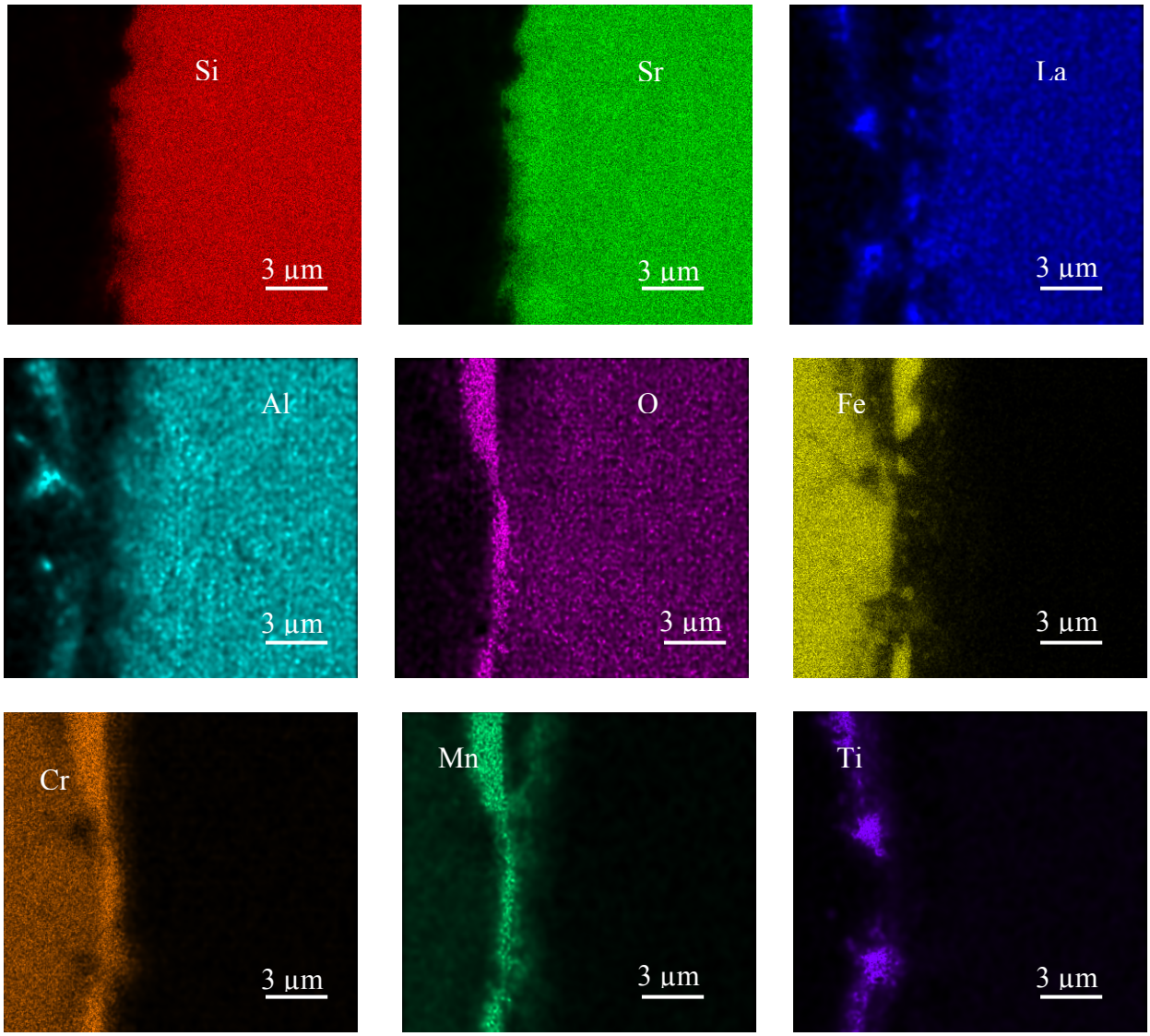

Fig. 6-7. Elemental maps for the AISI 441/SABS-0 couple thermally treated at 800°C for 1000 hrs in air.

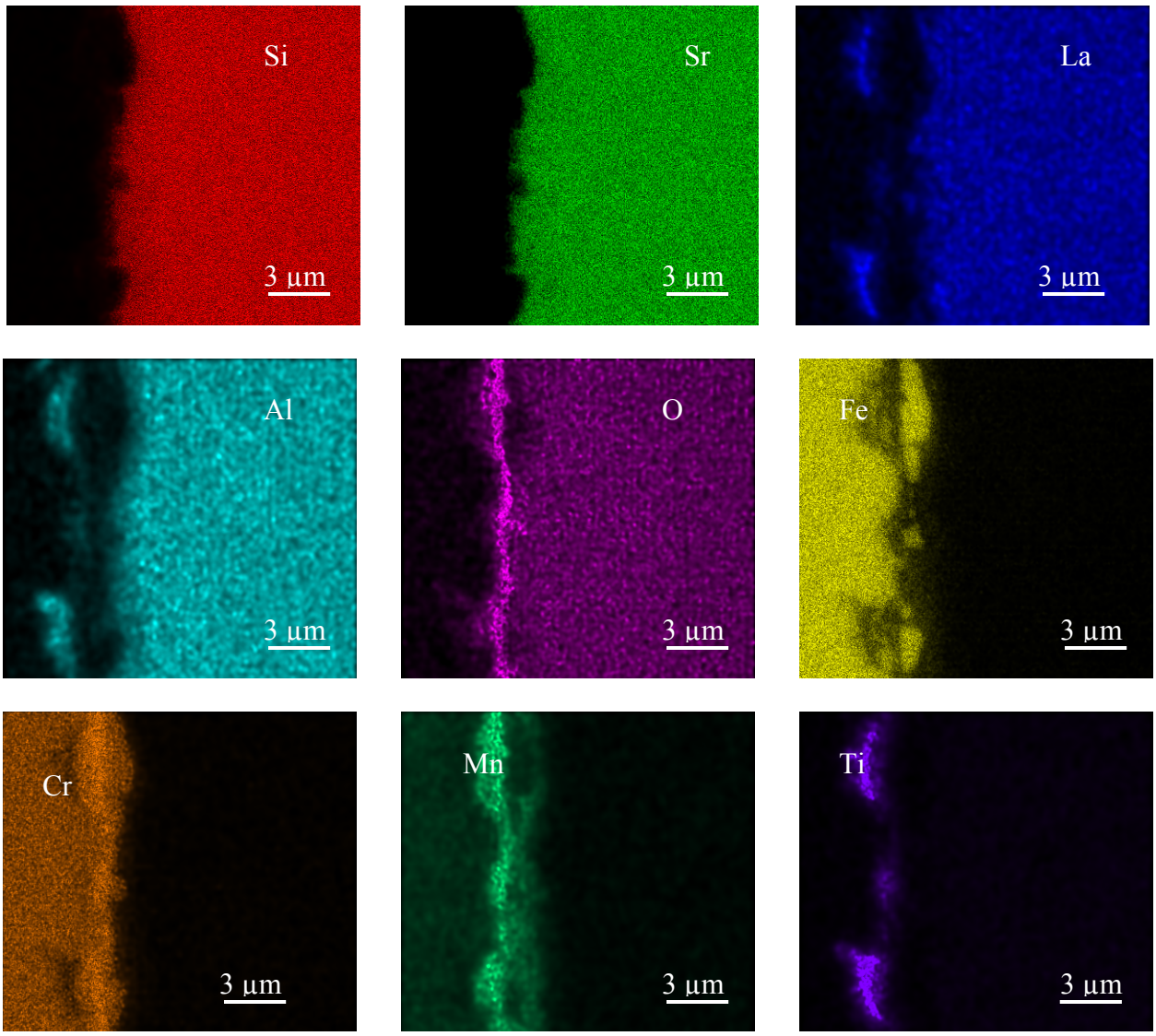

Fig. 6-8. Elemental maps for the AISI 441/SABS-0 couple thermally treated at 800°C for 1000 hrs in H_2O/H_2 atmosphere.

6.3.2.3. X-ray diffraction analysis

The XRD patterns of the AISI 441/SABS-0 samples thermally treated in air and H_2O/H_2 atmosphere for 1000 hrs are shown in Fig. 6-9. The XRD patterns of the AISI 441 alloy and the as-bonded samples are also included for the ease of discussion. The presence of the AISI 441 alloy peaks in all the samples confirms that the XRD patterns include all the crystal phases

across the interface. The positions of the peaks are same for the as-bonded, air, and H_2O/H_2 treated samples. This means same phases are present for all the samples. However, the peak intensity varies which may be due to the effect of thermal treatment condition. Apparently, the intensity is less for the H_2O/H_2 treated and the highest for the air treated sample. This means the amount of the crystal phases are less for the H_2O/H_2 treated sample. This observation is also consistent with the low extent of oscillations in the concentration profiles of the SABS-0 glass elements for the H_2O/H_2 treated sample (Fig. 6-6 (c)). The crystal phases also contain the devitrified SABS-0 glass. This means the devitrification rate of the SABS-0 glass is lower in H_2O/H_2 atmosphere than air. However, the intensity can also vary due to the variation in thickness of the SABS-0 glass layer during sample preparation. The numbers of crystal planes are apparently higher for the air treated samples but there are same number of peaks as revealed by close observation and the X-Pert software. The same number and location of peaks in the XRD patterns mean that the crystal phases are the same for all the studied samples.

The crystal phases are identified as $Sr_4(Si_4O_{12})$, $La_2Si_2O_7$, $Sr_7Al_{12}O_{25}$, $FeSiO_3$, La_2CrO_6, Ti_6O_{11}, and TiO_2; which are similar to those of the as-bonded, air, argon, and H_2O/H_2 treated samples thermally treated for 100 hrs (Fig. 6-4).

Formation of the crystal phases have been discussed in the section 6.3.1.3. Same crystalline phases for the as-bonded and the thermally treated samples regardless of thermal treatment time and atmosphere again indicate the long-term interfacial stability of the AISI 441/SABS-0 couple.

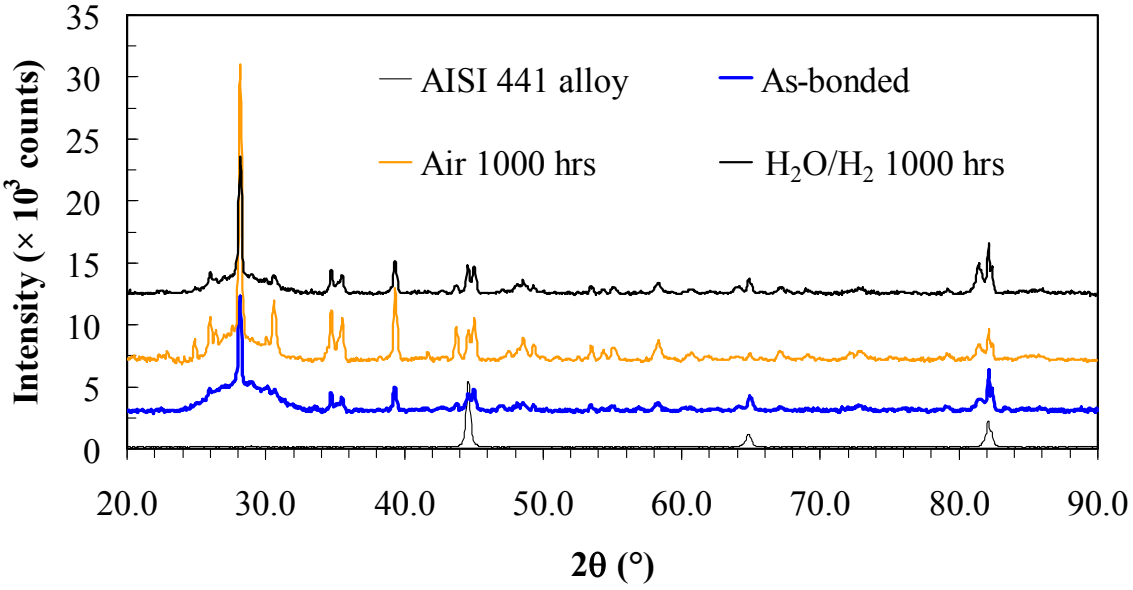

Fig. 6-9. XRD patterns of the AISI 441 alloy and the as-bonded and the thermally treated AISI 441/SABS-0 samples.

6.4. Conclusions

Interfacial stability of the SrO-La_2O_3-Al_2O_3-SiO_2-based seal glass with the AISI 441 alloy is evaluated with respect to argon, air, and H_2O/H_2 atmospheres for 100-1000 hrs at 800°C. The seal glass bonds well with the AISI 441 alloy. Chemical reaction and inter-diffusion of the elements between the seal glass and the AISI 441 alloy contributes to the interface formation. The interface morphology varies with the thermal treatment times and atmospheres but the crystalline phases across the interface are same for all the thermal treatment conditions. The interface of the AISI 441/SABS-0 couple is stable upto 1000 hrs in both air and H_2O/H_2 atmosphere.

References

[1] Z. Yang, G. G. Xia, C. M. Wang, Z. Nie, J. Templeton, J. W. Stevenson, and P. Singh, Investigation of iron-chromium-niobium-titanium ferritic stainless steel for solid oxide cell interconnect applications, Journal of Power Sources 183, 660-667, 2008.

[2] Z. Yang, J. S. Hardy, M. S. Walker, G. Xia, S. P. Simner, and J. W. Stevenson, Structure and conductivity of thermally grown scales on ferritic Fe-Cr-Mn steel for SOFC interconnect applications, Journal of the Electrochemical Society 151, A1825-A1831, 2004.

[3] E. Konysheva, U. Steeling, A. Besmehn, L. Singeiser, and K. Hilpert, Chromium vaporization of the ferritic steel Crofer 22 APU and ODS $Cr5Fe1Y_2O_3$ alloy, Journal of Materials Science 42, 5778-5784, 2007.

[4] N. H. Menzler, D. Sebold, M. Zahid, S. M. Gross, and T. Coppitz, Interaction of metallic SOFC interconnect materials with glass-ceramic sealant in various atmosphere, Journal of Power Sources 152, 156-167, 2005.

[5] B. D. Cullity, Elements of X-ray diffraction, 2nd ed., Addision-Wesley Publishing Company Inc., Philippines, 292–294, 1978.

[6] P. Kumar and V. A. Greenhut, Metal-ceramic joining, TMS Minerals, Metals, Materials, Warrendaley, Pennsylvania, 3-11, 1990.

[7] A. J. Sturgeon, D. Holland, G. Patridge, and C. A. Elyard, Reactions at the interface between a glass ceramic and a metal and their effect on devitrification, Glass Technology 27, 102-107, 1986.

[8] P. Kofstad, High temperature corrosion, Elsevier Applied Science Publishers Ltd, England 1988.

[9] M. G. C. Cox, B. McEnaney, and V. D. Scott, A chemical diffusion model for partitioning of

transition elements in oxide scales of alloys, Philosophical Magazine 2, 839-851, 1972.

[10] R. E. Lobnig, H. P. Schmidt, K. Hennesen, and H. J. Grabke, Diffusion of cations in chromia layers grown on iron-base alloys, Oxidation of Metals 37, 81-93, 1992.

[11] W. D. Kingery, H. K. Bowen, and D. R. Uhlmann, Introduction to Ceramics, John Wiley and Sons, New York, 2nd ed., 1976.

[12] J. Goldstein, D. Newbury, D. Joy, C. Lyman, P. Echlim, E. Lifshin, L. Sawyer, and J. Michael, Scanning electron microscopy and X-ray microanalysis, 3rd ed. Springer, New York, USA, 2007,

[13] M. K. Mahapatra and K. Lu, Interfacial study of Crofer 22 APU interconnect-SABS-0 seal glass for solid oxide fuel/electrolyzer cells, Journal of Materials Science 44, 5369-5378, 2009.

[14] M. K. Mahapatra, and K. Lu, Thermochemical compatibility of a seal glass with different solid oxide cell components, International Journal of Applied Ceramic Technology, Accepted.

[15] K. LU, and M. K. Mahapatra, Network structure and thermal stability study of high temperature seal glass, Journal of Applied Physics 104, 074910, 2008.

[16] L. Cromier, G. Calas, S. Creux, P.H. Gaskell, B. Bouchet-Fabre, and A.C. Hannon, Environment around strontium in silicate and aluminosilicate glasses Physical Review B 59, 13517-13520, 1999.

[17] M. B. Volf, Chemical approach to glass, Glass Science and Technology, Elsevier, Amsterdam, 1984.

CHAPTER SEVEN

SEALING EVALUATION OF $SrO-La_2O_3-Al_2O_3-SiO_2$ (SABS-0) SEAL GLASS

Abstract

Glass is the most suitable material to seal solid oxide fuel/electrolyzer cell components. A suitable seal glass should be hermetic for 5,000-40,000 hrs cell operation periods at 650-900°C with 100-1000 thermal cycles. In this chapter, the sealing performance of the $SrO-La_2O_3-Al_2O_3-SiO_2$ (SABS-0) seal glass has been evaluated. The SABS-0 glass was sandwiched between AISI 441 interconnect alloy and fully stabilized ZrO_2 electrode. The thermal cycling resistance of the tri-layer assembly is tested by gas leakage for 3-20°C/min heating rates. No gas leakage is observed for 100 thermal cycles and 1600 hrs at 800°C. Additionally, the interfacial mechanical strength is evaluated by rupture test.

7.1. Introduction

A hermetic seal is essential for joining different cell components and multiple cells in order to produce enough power or fuel, and to protect gas leakage and mixing of planar SOFCs/SOECs [1,2]. Gas leakage through seals should be less than 1% of the gasses in SOFCs/SOECs for the entire operation period (>5,000 hrs for mobile applications and >40,000 hrs for stationary applications with at least 100 thermal cycles between room temperature and the operating temperature) [3].

Generally, a seal should withstand 13.8-41.4 kPa pressure for sealing and 70.0-210.0 kPa stress for mechanical integrity [4]. Several seal glasses have been extensively investigated but

the pores and cracks at the interconnect-seal glass interface prevent these glasses from being effective[5-11]. Gas-leakage was observed after <5 hrs of sealing test for borosilicate glasses [12-14]. A silicate seal glass showed gas-leakage after 50 hrs [13,15]. No gas-leakage was observed for another silicate seal glass for ~ 3000 hrs but very low (6.7 kPa) gas pressure was used to evaluate the sealing performance [16].

From the previous chapters in this dissertation, it is seen that the SrO-La_2O_3-Al_2O_3-SiO_2 based glass (SABS-0) has all the desired properties. In this chapter, the sealing performances of this glass will be discussed. The sealing performances are evaluated in terms of hermeticity, thermal cycling resistance.

7.2. Experimental procedure

7.2.1. Glass preparation

SABS-0 glass was prepared with conventional glass manufacturing process. $SrCO_3$ (99.9%, Sigma Aldrich, St. Louis, MO), La_2O_3 (99.98%), Al_2O_3 (99.95%), and SiO_2 (99.8%) (all oxides were from Alfa Aesar, Ward Hill, MA) at designed ratios were mixed in a ball mill for overnight. The mixed powders were heated in a platinum crucible in a box furnace (Lindberg, Model No. 51314, Watertown, WI) to 1100°C and kept there for 1 hr for $SrCO_3$ to decompose. After that, the mixture was heated to 1400°C for 4 hrs. The heating rate was 10°C/min. The molten glass was quenched into a graphite mold. Glass powders of ≤ 36 μm particle sizes were prepared by grinding the quenched bulk SABS-0 glass.

7.2.2. Sample preparation for performance evaluation

For the interconnect-seal glass-electrolyte tri-layer assembly preparation, a hole of 6.35 mm diameter was made on AISI 441 interconect alloy (dimension 20 × 20 × 2 mm). A tube was brazed with the AISI 441 alloy at the hole position. The bottom surface of the AISI 441 interconnect alloy was polished with 600 SiC grit papers to remove the surface oxides. The glass powders were mixed with an acrylic-based binder to form a paste. The glass paste of ~ 800 μm thickness was coated on the AISI 441 alloy (except the hole) by a doctor's blade. A fully stabilized zirconia electrolyte (30 μm thick and 25 mm diameter, Nextech Materials, Ohio, USA) was put on the glass paste to cover the hole. Thus the glass sandwiched between the AISI 441 alloy and the zirconia electrolyte forms a tri-layer assembly (Fig. 7-1). The tri-layer assembly is thermally treated at 875°C in air for 30 mins without applying load to bond the glass with the AISI 441 alloy and the zirconia electrolyte. The tri-layer assembly was held at ≤ 250°C for ~ 6 hrs to completely remove water and at 450°C for 2 hrs to burn out the binder during sealing. During the entire sealing process, slow heating and cooling rate of 2°C/min was maintained in order to avoid thermal stress at the interfaces.

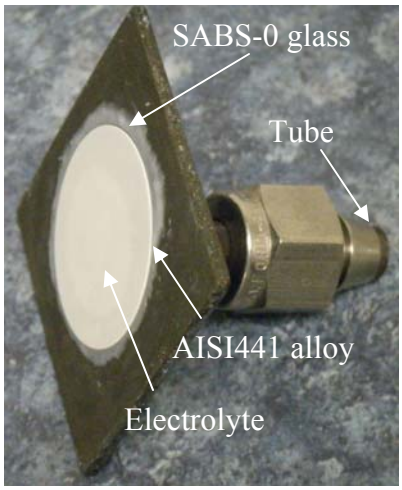

Fig. 7-1. AISI 441/SABS-0 glass/Electrolyte tri-layer assembly after sealing.

7.2.3. Performance evaluation

Gas leakage test was conducted by a pressure leakage method. A differential pressure of 34.5 kPa (5 psi) was created inside the tri-layer assembly by flowing argon gas through the tube. Once the pressure was obtained inside the tri-layer assembly, the gas supply was disconnected. The tri-layer assembly with 34.5 kPa differential pressure was thermally cycled with different heating rates (3-20°C/min) between room temperature and 800°C with 16 hrs dwell time at 800°C. The sealing performance was evaluated by the pressure drop as a function of temperature and time. The thermal cycling resistance was evaluated by the pressure drop as a function of heating rate and the number of thermal cycles.

The rupture strength of the tri-layer assembly was evaluated by a rupture test at room temperature. Argon gas was continuously supplied to increase the pressure inside the tri-layer assembly until rupture.

7.3. Results and Discussion

7.3.1. Sealing performance and thermal cycling resistance

The sealing performance of the SABS-0 seal glass was evaluated in different steps. The gas leakage test for the tri-layer assembly was first tested at room temperature with 34.5 kPa gas pressure for 48 hrs. Then, the sealing performance and the thermal cycling resistance of the same tri-layer assembly were evaluated simultaneously at 34.5 kPa gas pressure. Thermal cycling resistance was first evaluated as a function of heating rate between room temperature and 800°C. Fig. 7-2 shows no gas-leakage (pressure drop) regardless of heating rate. This means the SABS-0

glass can withstand thermal cycles for 3-20°C/min heating rate without degrading the sealing performance.

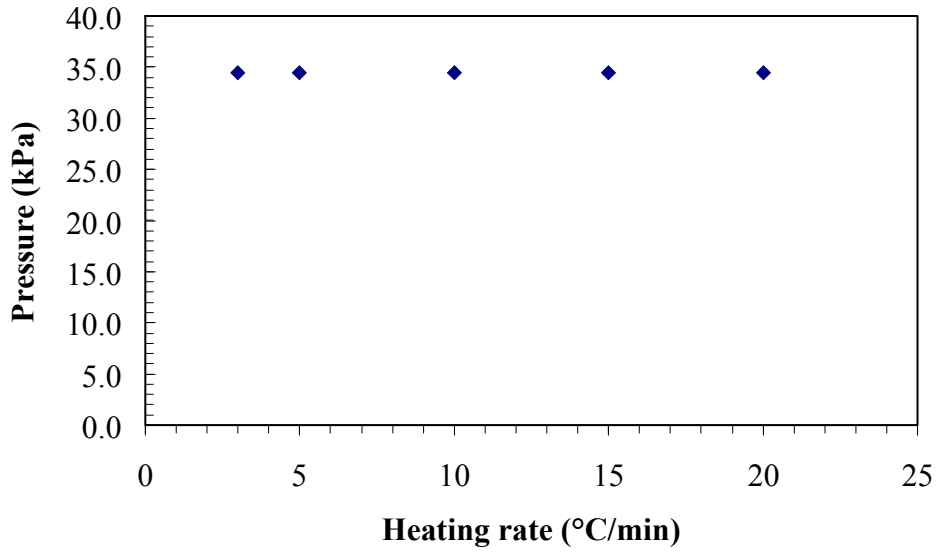

Fig. 7-2. Sealing performance of SABS-0 seal glass with respect to heating rate.

Long-term sealing performance and thermal cycling resistance of the tri-layer assembly are evaluated at the heating rate of 20°C/min between room temperature and 800°C, and cooling rate of 20°C/min in 500-800°C temperature range followed by furnace cooling between 500°C and room temperature (Fig. 7-3). This is the highest heating and cooling rates that can be achieved for the experimental design. The tri-layer assembly was thermally cycled for 100 times before the experiment was aborted. The results are shown in Fig. 7-3. From Fig. 7-3, it is observed that the SABS-0 glass withstood 100 thermal cycles without any gas-leakage. There was no gas-leakage at 800°C for 1600 hrs and 2400 hrs including the heating time, cooling time, and the remaining times at room temperature. Since the same tri-layer assembly was used for all the tests, it withstood total 105 thermal cycles without any gas-leakage for 2568 hrs. A seal is subjected to 13.8-41.4 kPa gas pressure in a planar SOFC/SOEC [4]. It should be mentioned that

the sealing performance and the thermal cycling resistance of other silicate and BaO-borosilicate glasses have been evaluated at relatively low pressure (≤ 13.8 kPa) and slow heating rate (≤ 5°C) using inert gasses [13,16]. The gas leakage rate of a BaO-borosilicate glass increases during cooling from 700°C to 100°C because of thermal stress [17]. This means the SABS-0 glass has high sealing capability for SOFC/SOEC seal applications. However, the actual SOFC/SOEC atmosphere can potentially degrade the sealing performance and thermal cycling resistance due to interfacial reactions.

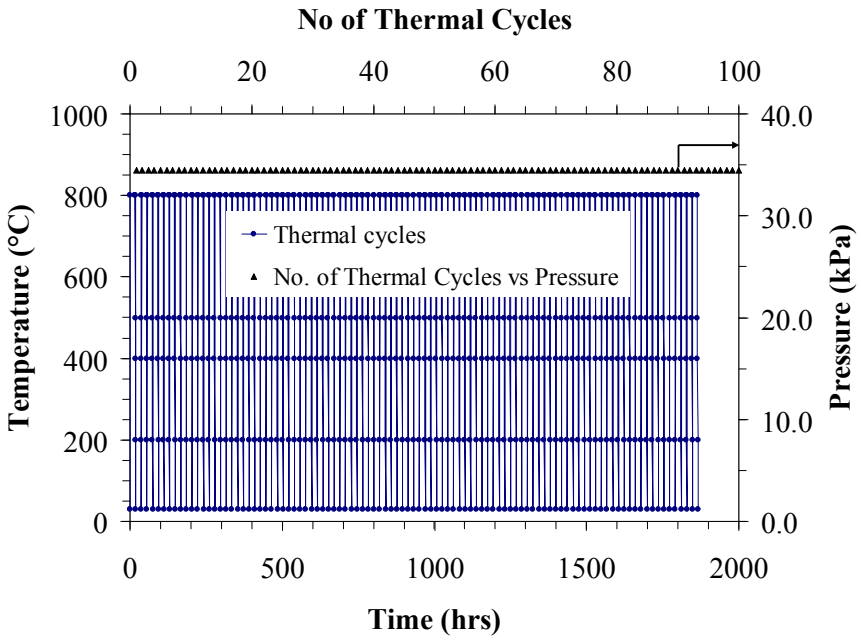

Fig. 7-3. Sealing performance and thermal cycling resistance of the AISI 441 alloy/SABS-0 glass/Electrolyte tri-layer assembly.

7.3.2. Rupture strength

A seal glass should withstand 70-210 kPa stress to maintain the mechanical integrity of SOFC/SOEC [4]. Rupture test has been reported as a quick method to evaluate the strength of a seal glass [7]. Pores and cracks at the interface and severe interfacial reactions degrade the

rupture strength. For example, the rupture strength of a BaO-CaO-borosilicate glass sandwiched between Crofer 22 APU interconnect alloy and electrolyte decreases from 82.7 kPa to 34.5 kPa after 400 hrs thermal treatment at 750°C [7]. The rupture strength of the tri-layer assembly was evaluated at room temperature for the long-term thermally cycled sample. The rupture strength of the thermally cycle sample is 448.5 kPa. The image of the trilayer-assembly after rupture test is shown in Fig. 7-4 for the thermally cycled sample. The failure of the tri-layer assembly occurs mainly at the SABS-0 glass/electrolyte interface as can be observed from Fig. 7-4 (a). Cracks or pores) are observed at the SABS-0 glass/AISI 441 alloy interconnect in Fig. 7-4(b). This means the failure (thermomechanical) stress exceeds the tensile strength of the SABS-0 glass or the interfacial bonding strength of the SABS-0 glass/AISI 441 alloy. The tensile strength of the tri-layer assembly can be calculated from the rupture strength by a conversion factor of 0.231 and is 15 MPa [7]. The tensile strength of the tri-layer assembly is higher than other seal glasses reported in literatures (<10 MPa) [18-21]. It should be mentioned that the thermomechanical stress depends on the thickness, not the width, of the seal glass [22]. The higher rupture stress than the required value for the long-term thermally cycled sample means the SABS-0 glass can maintain the mechanical integrity of SOFC/SOECs. However, only one report is available for the rupture test method and the conversion factor of rupture strength to tensile strength and need to be standardized. In addition, the actual atmosphere during cell operation can degrade the mechanical integrity.

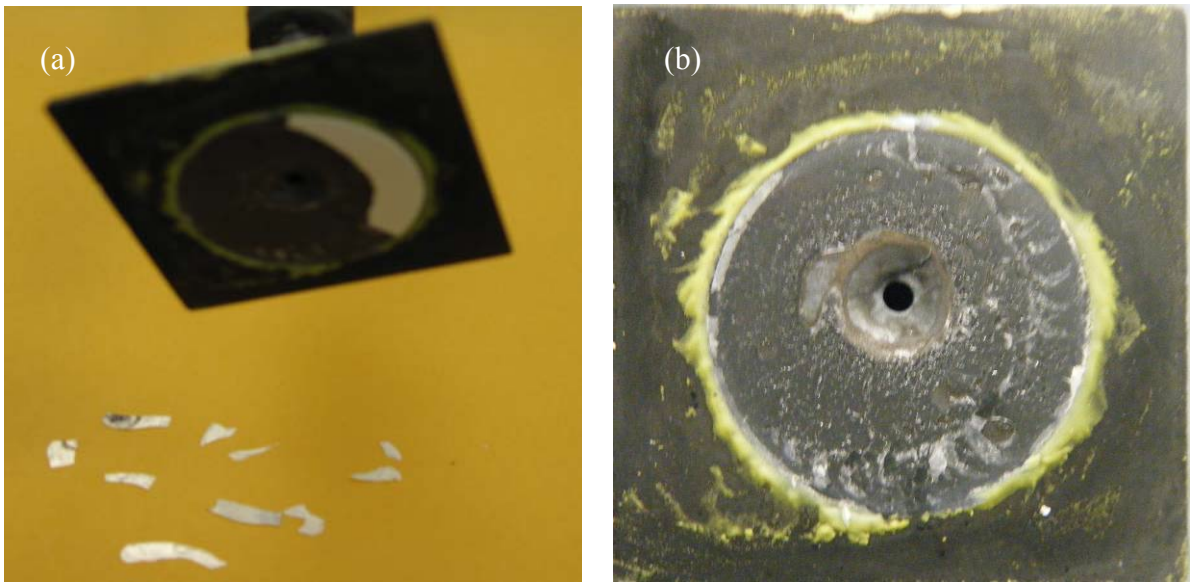

Fig. 7-4. Image of the thermally cycled sample: a) after rupture test and b) the front view of the tri-layer assembly after rupture test.

7.4. Conclusions

The hermeticity, thermal cycling resistance, and the rupture strength of a SrO-La_2O_3-Al_2O_3-SiO_2 (SABS-0) seal glass were evaluated. The SABS-0 glass is hermetic for 2568 hrs, can withstand 100 thermal cycles at 20°C/ min heating rate, and has high rupture strength.

References

[1] J. F. B. Rasmussen, P. V. Hendriksen, andA. Hagen, Study of internal and external leaks in tests of anode-supported SOFCs, Fuel Cells 8, 385-393, 2008.

[2] P. A. Lessing, J. Hartvigsen, and S. Elangovan, Sealants: solid oxide fuel cells: materials properties and performance, edited by J. W. Fergus, R. Hui, X. Li, D. P. Wilkinson, and J. Zhang CRC Press Taylor & Francis Group, Boca Raton, Florida, 213-237, 2009.

[3] D. Stolten, L. G. J. B. d. Haart, and L. Blum, Design criteria for SOFC generators, Ceramic

Engineering and Science Proceedings 24, 263-272, 2003.

[4] K. S. Weil, J. E. Deibler, J. S. Hardy, D. S. Kim, G. G. Xia, L. A. Chick, and C. A. Coyle, Rupture testing as a tool for developing planar solid oxide fuel cell seals, Journal of Materials Engineering and Performance 13, 316-326, 2004.

[5] K. D. Meinhardt, D. S. Kim, Y. S. Chou, and K. S. Weil, Synthesis and properties of a barium aluminosilicate solid oxide fuel cell glass-ceramic sealant. Journal of Power Sources 182, 188-196, 2008.

[6] Z. Yang, G. Xia, K. D. Meinhardt, K. S. Weil, and J. W. Stevenson, Chemical stability of glass seal interface in intermediate temperature solid oxide fuel cells, Journal of Materials Engineering and Performance 13, 327-334, 2004.

[7] V. A. C. Haanappel, V. Shemet, I. C. Vinke, S. M. Gross, T. H. Koppitz, N. H. Menzler, M. Zahid, and W. J. Quadakkers, Evaluation of the suitability of various glass sealant-alloy combinations under SOFC stack conditions, Journal of Materials Science 40, 1583-1592, 2005.

[8] M. J. Pascual, A. Guillet, and A. Durán, Optimization of glass-ceramic sealant compositions in the system MgO–BaO–SiO_2 for solid oxide fuel cells (SOFC), Journal of Power Sources 169, 40-46, 2007.

[9] C. Lara, M. J. Pascual, and A. Durán, Chemical compatibility of RO-BaO-SiO_2 (R=Mg, Zn) glass-ceramic seals with SOFC components, Physics Chemistry of glasses: European Journal of Glass Science and Technology B 48, 218-224, 2007.

[10] K. A. Nielsen, M. Solvang, S. B. L. Nielsen, A. R. Dinesen, D. Beeaff, and P. H. Larsen, Glass composite seals for SOFC application, Journal of the European Ceamic Society 27, 1817-1822, 2007.

[11] Y. S. Chou, J. W. Stevenson, and P. Singh, Novel refractory alkaline earth silicate sealing

glasses for planar solid oxide fuel cells, Journal of the Electrochemical Society 154, B644-B651, 2007.

[12] Y. S. Chou, J. W. Stevenson, and R. N. Gow, Novel alkaline earth silicate sealing glass for SOFC Part II. Sealing and interfacial microstructure, Journal of Power Sources 168, 426-433, 2007.

[13] N. Caron, L. Blanchi, and S. Methout, Development of a functional sealing layer for SOFC Applications, Journal of Thermal Spray Technology 17, (5-6), 598-602, 2008.

[14] S. Ghosh, A. D. Sharma, P. Kundu, and R. N. Basu, Glass-ceramic sealants for planar IT SOFC: A bilayered approach for the joining electrolyte and metallic interconnect, Journal of the Electrochemical Society 155, (5), B473-B478, 2008.

[15] M. M. Seabaugh, K. Sabolsky, G. B. Arkenberg, and J. L. Jayjohn, Composite seal development and evaluation, Ceramic Engineering and Science Proceedings 27, 265-272, 2006.

[16] R. N. Singh, Sealing technology for solid oxide fuel cells (SOFC), International Journal of Applied Ceramic Technology 4, 134-144, 2007.

[17] T. Zhang, Q. Zhu, and Z. Xie, Modelling of cracking of the glass-based seals for solid oxide fuel cell, Journal of Power Sources 188, 177-183, 2009.

[18] K. A. Nielsen, M. Solvang, S. B. L.Nielsen, and D. Beeaff, Mechanical behavior of glassy composite seals for IT-SOFC application, Ceramic Engineering and Science Proceedings 27, 315-323, 2007.

[19] Y. S. Chou, J. W. Stevenson, and P. Singh, Effect of pre-oxidation and environmental aging on the seal strength of a novel high-temperature solid oxide fuel cell (SOFC) sealing glass with metallic interconnect, Journal of Power Sources 184, 238-244, 2008.

[20] Y. S. Chou, J. W. Stevenson, and P. Singh, Effect of aluminizing of Cr-containing ferritic

alloys on the seal strength of a novel high-temperature solid oxide fuel cell (SOFC) sealing glass with metallic interconnect, Journal of Power Sources 185, 1001-1008, 2008.

[21] J. Malzbender, J. Mönch, R. W. Steinbrech, T. Koppitz, S. M. Gross, and J. Remmel, Symmetric shear test of glass-ceramic sealants at SOFC operation temperature, Journal of Materials Science 46, 6297-6301, 2007.

[22] A. Müller, S. Goswami, W. Becker, D. Stolten, L. G. J. D. B. d. Haart, and R. W. Steinbrech, Assessment of the sealing joints within SOFC Stacks by numerical simulation, Fuel Cells 6, 2107-2112, 2006.

CHAPTER EIGHT

CONCLUSIONS AND FUTURE DIRECTIONS

8.1. Conclusions

Several compositions based on SrO-La_2O_3-Al_2O_3-B_2O_3-SiO_2-based glasses have been comprehensively studied. Seal glasses are synthesized based on (25−X)SrO-20La_2O_3-(7+X)Al_2O_3-40B_2O_3-8SiO_2 system and X has been varied from 0 to 10 mol%. All the compositions have glass transition temperatures T_g above 620°C and crystallization temperatures T_c above 826°C. Also, the glasses have thermal expansion coefficients CTE between 9.0 and 14.5×10^{-6}/°C after the first thermal cycle. Suitable increase of Al_2O_3 stabilizes the glass by suppressing devitrification. La_2O_3 and B_2O_3 contribute to devitrification by forming $LaBO_3$. The role of other oxides on the stability of this system is not significant.

The effects of B_2O_3:SiO_2 ratio on the network structure and thermal properties of the SrO-La_2O_3-Al_2O_3-B_2O_3-SiO_2 glass system are studied. Increasing B_2O_3:SiO_2 ratio causes glass network connectivity decrease, non-bridging oxygen increase, glass structural unit local ordering, and glass former distribution inhomogeneity. Increased B_2O_3:SiO_2 ratio degrades the thermal properties. The micro-heterogeneity from different glass structural units also increases the tendency of devitrification and degrades thermal stability. Depending on the bonding affinity with glass modifiers, silicon-containing devitrified phases form for low B_2O_3 content SABS glasses and boron-containing devitrified phases form for high B_2O_3 content SABS glasses. Boron free SABS glass exhibits the best combination of thermal properties and thermal stability.

Effect of nickel addition on the thermal behaviors and the structure of SrO-La_2O_3-Al_2O_3-B_2O_3-SiO_2 (SABS) –based seal glass have been investigated. Nickel decreases SABS glass network connectivity and acts as a modifier in the glass system. Nickel addition does not significantly change the thermal properties but degrades thermal stability by inducing microheterogeneity. Fundamental glass structure evolution with nickel addition has been elucidated by comparing glass network connectivity of different compositions.

Interfacial stability of the SrO-La_2O_3-Al_2O_3-SiO_2-based seal glass (SABS-0) with the Crofer 22 APU and the AISI 441 alloy are evaluated with respect to argon, air, and H_2O/H_2 atmospheres for 0-1000 hrs at 800°C. The seal glass bonds well with the Crofer 22 APU and the AISI 441 alloy. Chemical reaction and inter-diffusion of the elements between the seal glass and the alloys contribute to the interface formation. The interface morphology varies with the thermal treatment times and atmospheres but the crystalline phases across the interface are same for all the thermal treatment conditions. The interface of the Crofer 22 APU/SABS-0 and AISI 441/SABS-0 couples are stable upto 1000 hrs in both air and H_2O/H_2 atmosphere.

Comositional analysis by EDS module attached to SEM are reliable as verified by complentary methods such as WDS module attached to electron proble microscope (EPMA) and EDS of thin samples. However, slight devitation in composition across the thin Crofer 22 APU/SABS-0 interfaces are likely due to the damage during thinning.

Hermeticity and thermal cycling resistance of the SABS-0 seal glass have been evaluated by pressure-leakage method. Hermeticity for at least 2568 hrs and resistance to 100 thermal cycles at 20°C/min heating rate demonstrate the suitability of the SABS-0 seal glass for SOFC/SOEC.

8.2. Future directions

Detailed understanding of composition-structure-property relationships is the main issue in designing seal glass compositions. Composition-structure-property relationship of the SrO-La_2O_3-Al_2O_3-B_2O_3-SiO_2 –based seal glass has been studied but the detailed structural information is needed for better understanding the network structure. Quantitative analysis of network structure, such as the amounts of different structural units and non-bridging oxygen, and the coordination number of constituent cations, can be obtained from nuclear magnetic resonance spectroscopy, X-ray diffraction, and neutron diffraction. More detailed structural information such as cation-oxygen bond length and bond angles can be obtained from neutron diffraction. The role of SrO and La_2O_3 on the SrO-La_2O_3-Al_2O_3-B_2O_3-SiO_2 –based seal glass can be further investigated.

The interfacial reactions depend on the sealing conditions such as temperature and atmosphere. Lack of thermodynamic data for different new phases formed at the interface hinders the understanding of the reaction kinetics. Detailed analysis of the interfacial compositions combined with thermodynamic and reaction kinetics modeling is required in order to address this issue.

The localized stresses cause the degradation of seal glass. CTE mismatch between the seal glass and the interfacing cell component is the main origin for localized stress. Although the SrO-La_2O_3-Al_2O_3-SiO_2 based seal glass shows no sealing performance degradation, the interfacial strength, effect of the interfacial morphology such as pore size and distribution, and devitrified phases on the localized stress should be investigated.

Sealing performances have been evaluated in argon atmosphere. Oxidizing and reducing atmospheres should be used for sealing performance evaluation of the SrO-La_2O_3-Al_2O_3-SiO_2

based seal glass because these atmospheres significantly affect the interface morphology. Differential pressure, seal thickness, leakage area, and gas volume in the tri-layer assembly can significantly affect the sealing performance and should be optimized.

Seal glass failure degrades the performance and durability of SOFCs by affecting the microstructure stability of the electrodes. Deposition of vaporized glass species at electrode grains or grain boundaries and change in overall compositions of electrodes and seal glass are common issues. Insulating phases at the electrode-electrolyte interfaces degrade the cell durability. SrO-La_2O_3-Al_2O_3-SiO_2 based seal glass constituents such as La_2O_3 and SrO can form $La_2Zr_2O_7$ and $SrZrO_3$ insulating phases by reacting with the anode and the electrolyte. Subsequently, cell performance would degrade. The interfacial reaction between the SrO-La_2O_3-Al_2O_3-SiO_2 based seal glass and the electrolyte and electrodes should be studied along with its effect on the electrical performance of the solid oxide fuel/electrolyzer cells.

Seal glass should be stable for 5,000-40,000 hrs for practical applications. The evaluation of seal glass stability for such a long period is not feasible for rapid seal development. A model needs to be developed to predict the life cycle of a seal glass.

Current research trend is to reduce the operating temperature of SOFC/SOECs <700°C by designing and developing new electrodes and electrolytes. Suitable seal glasses for low temperature SOFC/SOECs need to be developed.

List of Publications

Journal articles

1) M. K. Mahapatra and K. Lu, Search of seal glass for solid oxide fuel cells, Energy and Environmental Science, Submitted (Invited article).
2) M. K. Mahapatra and K. Lu, Glass–based seals for solid oxide fuel and electrolyzer cells-A review, Journal of Materials Science and Engineering R: Reports, Accepted.
3) M. K. Mahapatra and K.Lu, Interfacial study of Crofer 22 APU interconnect–SABS-0 seal glass for solid oxide fuel/electrolyzer cells, Journal of Materials Science 44 (2009) 5569-5578.
4) M. K. Mahapatra and K. Lu, Thermochemical compatibility of a seal glass with different solid oxide cell components, International Journal of Applied Ceramic Technology, DOI:10.1111/j.1744-7402.2009.02401.x.
5) M. K. Mahapatra, K. Lu, and R. J. Bodnar, Network structure and thermal property of a novel high temperature seal glass, Applied Physics A 95 (2009) 493-500.
6) K. Lu and M. K. Mahapatra, Network structure and thermal stability study of high temperature seal glass, Journal of Applied Physics 104 (2008) 074910.
7) M. K. Mahapatra and K. Lu, Effect of nickel on network structure and thermal properties of new solid oxide cell seal glass, Journal of Power Sources 185 (2008) 993-1000.
8) M. K. Mahapatra, K. Lu, and W. T. Reynolds. Jr. Thermophysical properties and devitrification of SrO-La_2O_3-Al_2O_3-B_2O_3-SiO_2-based glass sealant for solid oxide fuel/electrolyzer cells, Journal of power sources 179 (2008) 106-112.

Patent filed

K. Lu and M. K. Mahapatra, Barium oxide, calcium oxide, magnesia, and alkali oxide free glass seals for solid oxide fuel/electrolyzer cells (SOFC/SOEC), Serial No.: 61/171,897, 2009

Conference Proceedings

1) M. K. Mahapatra, C. Story, K. Lu, and W. T. Reynolds Jr., Glass-ceramic seal stability study for solid oxide electrolyer/fuel cells, Proceeding of Materials Science and Technology 2007 Conference September 16-20, 2007, Detroit, Michigan, Energy: Fuel Cells: Materials, Processing, Manufacturing and Power Management Technologies, 371-380.2007.

Oral Presentations

1) M. K. Mahapatra and K. Lu, Sealing performance of an alkaline earth silicate glass for solid oxide fuel/electrolyzer cell, 34th International Conference on Advanced Ceramics and Composites January 24-29, 2010 in Daytona Beach, Florida, Accepted.
2) M. K. Mahapatra and K. Lu, Interfacial stability of uncoated and $(Mn,Co)_3O_4$ coated interconnect-glass seal joint, Materials Science and Technology 2009 Conference October 25-29, 2009, Pittsburg, Pennsylvania.
3) K. Lu and M. K. Mahapatra, Compatibility of interconnect/glass seal at different atmospheres for solid oxide cell application, 8th Pacific RIM Conference on Ceramic and Glass Technology May 31-June 5,2009, Vancouver, British Columbia, Canada.
4) M. K. Mahapatra, K. Lu, and W. T. Reynolds Jr., Thermochemical stability of a new glass seal-Crofer 22 APU interface, 33rd International Conference on Advanced Ceramics and Composites January 18-23, 2009, Daytona Beach, Florida.

5) M. K. Mahapatra, K. Lu, and W. T. Reynolds Jr., Diffusion study of a novel glass seal with interconnect and shape memory alloy for solid oxide cell application, Materials Science and Technology 2008 Conference October 5-9, 2008, Pittsburg, Pennsylvania.
6) K. Lu, M. K. Mahapatra, and W. T. Reynolds Jr., $SrO–La_2O_3–Al_2O_3–B_2O_3–SiO_2$ based glass seal phase stability study, 32nd International Conference on Advanced Ceramics and Composites January 28-February 1, 2008, Daytona Beach, Florida.
7) M. K. Mahapatra, K. Lu, and W. T. Reynolds Jr., Glass-ceramic seal stability study for solid oxide electrolyer/fuel Cells, Materials Science and Technology 2007 Conference September 16-20, 2007, Detroit, Michigan.